



**University of
Leicester**

Spectral Properties of AGN in 2XMMi

Amy Elizabeth Scott

Supervisor:

Gordon Stewart

Thesis submitted for the degree of

Doctor of Philosophy

at the University of Leicester.

X-ray & Observational Astronomy Group

Department of Physics and Astronomy

University of Leicester

May 2012

Spectral Properties of AGN in 2XMMi

Amy Elizabeth Scott

ABSTRACT

Studying the emission of Active Galactic Nuclei (AGN), particularly in the X-ray band can offer considerable insights into the accretion process. This is important as AGN activity has a strong effect on the evolution of their host galaxies.

This thesis reports studies of a large sample of type 1 AGN, created by cross-correlating the optical SDSS DR5 quasar catalogue and the catalogue of serendipitous X-ray source detections, 2XMMi. A sample of 761 sources with X-ray spectra of sufficient quality for spectral modelling was obtained. The typical spectral shape of the sources is a power law of $\langle\Gamma\rangle = 1.99 \pm 0.01$ with an intrinsic dispersion of $\sigma_{\langle\Gamma\rangle} = 0.30 \pm 0.01$. However, $\sim 3\%$ were found to have intrinsically flat or steep Γ slopes. Significant trends between Γ and L_X and Γ and Eddington ratio were found. The radio loudness of the sources was also determined and the RLQ show higher L_X values and flatter Γ values than RQQ, suggesting an additional X-ray component is present.

Intrinsic cold absorption was found in $\sim 4\%$ of sources with $N_H \sim 10^{21} - 10^{23} \text{ cm}^{-2}$, despite being unexpected in optically classified type 1 AGN. A soft excess was found in $\sim 8\%$ of sources with an average blackbody temperature of $\langle kT \rangle = 0.17 \pm 0.09 \text{ keV}$. This temperature correlates with L_X and a strong correlation is found between the luminosities in the blackbody and power-law components. The detectability of these additional components is limited by the quality of the spectra. By simulating spectra with typical spectral shapes, the intrinsic percentage of the sample with a soft excess was found to be $75 \pm 23\%$.

The sample is also cross-correlated with archival multiwavelength catalogues and spectral energy distributions are created for each object. The infrared to ultraviolet region is found to be similar between sources regardless of their radio loudness, and the SEDs of low luminosity, low accretion rate sources tend to be flatter, with the optical/UV disc emission becoming more prominent with increases in these parameters.

Acknowledgments

I would like to thank my supervisor Gordon for his guidance and encouragement, Silvia for her contribution to the initial data analysis, and my family and friends for all of their support. I also thank STFC for a postgraduate studentship. This thesis is based on observations obtained with *XMM-Newton*, an ESA science mission with instruments and contributions directly funded by ESA Member States and NASA. It also uses data products from: the Wide-field Infrared Survey Explorer, which is a joint project of the University of California, Los Angeles, and the Jet Propulsion Laboratory/California Institute of Technology, funded by the National Aeronautics and Space Administration; the Two Micron All Sky Survey, which is a joint project of the University of Massachusetts and the Infrared Processing and Analysis Center/California Institute of Technology, funded by the National Aeronautics and Space Administration and the National Science Foundation; the NASA Galaxy Evolution Explorer which is operated for NASA by the California Institute of Technology under NASA contract NAS5-98034; the VLA FIRST Survey; and SDSS, funding for which has been provided by the Alfred P. Sloan Foundation, the Participating Institutions, the National Science Foundation, the U.S. Department of Energy, the National Aeronautics and Space Administration, the Japanese Monbukagakusho, the Max Planck Society, and the Higher Education Funding Council for England.

Declaration

I hereby declare that no part of this thesis has been previously submitted to this or any other University as part of the requirement for a higher degree. The work described herein was conducted by the undersigned except for contributions from colleagues as acknowledged in the text.

Amy Scott

Publications

Some of the work in this thesis has been published in the following papers:

A. E. Scott, G. C. Stewart, S. Mateos, D. M. Alexander, S. Hutton & M. J. Ward
New constraints on the X-ray spectral properties of type 1 AGN,
MNRAS, 417, 992–1012 (2011).

A. E. Scott, G. C. Stewart & S. Mateos
Detectability of low energy X-ray spectral components in type 1 AGN,
MNRAS, 423, 2633–2641 (2012).

©Amy Scott 2012

This thesis is copyright material and no quotation from it may be published without proper acknowledgment.

Contents

1	Introduction	1
1.1	Active Galactic Nuclei	2
1.1.1	Taxonomy and Physical Characteristics	2
1.1.2	Spectral Energy Distributions	11
1.1.3	X-ray Spectra of AGN	15
1.1.4	AGN in a Wider Context	24
1.2	Overview of Thesis	27
2	Data, Instrumentation & Analysis	28
2.1	X-ray Data	29
2.1.1	<i>XMM-Newton</i> Observatory	29
2.1.2	EPIC	32
2.1.3	Data Processing	35
2.1.4	2XMMi Catalogue	36
2.2	X-ray Spectral Analysis	37
2.2.1	Principles of XSPEC	37
2.2.2	Main Models	38
2.3	Optical Data	43
2.3.1	Sloan Digital Sky Survey	43
2.3.2	DR5 Quasar Catalogue	44
2.4	Multiwavelength Data	45
2.4.1	FIRST	45
2.4.2	<i>GALEX</i>	46
2.4.3	2MASS	46
2.4.4	<i>WISE</i>	47
3	X-ray Spectra of Type 1 AGN	48
3.1	Introduction	49
3.2	Procedure	50
3.2.1	Sample Creation	50

3.2.2	Extraction of Spectral Products	51
3.2.3	Spectral Fitting	52
3.2.4	General Properties of the Sample	56
3.3	Results	60
3.3.1	Distribution of Power-Law Slopes	60
3.3.2	Redshift Dependence of the Power-Law Slope	64
3.3.3	Luminosity Dependence of the Power-Law Slope	73
3.3.4	Intrinsic Cold Absorption	77
3.3.5	Soft X-ray Excesses	81
3.3.6	Radio Properties	88
3.3.7	Accretion Properties	97
3.4	Summary	106
4	Extreme Sources in the SDSS/2XMMi Sample	108
4.1	Introduction	109
4.2	Full Extreme Sample	109
4.2.1	Extreme Sources With the Best Quality Spectra	115
4.3	Alternative Explanations	119
4.3.1	Unmodelled Spectral Complexities	119
4.3.2	Complex Absorption Models	122
4.3.3	Extremes From Other Populations	127
4.3.4	Other Considerations	132
4.4	Intrinsic Extremes	134
4.4.1	Physical Properties	141
4.5	Discussion	146
5	Detectability of Spectral Components	148
5.1	Introduction	149
5.2	Data	149
5.3	Soft Excess Components	154
5.3.1	Intrinsic Percentage	154
5.3.2	Joint Spectral Fitting	162
5.4	Absorption Components	166
5.5	Discussion	170
5.6	Conclusions	172

6	Broadband SED Properties	173
6.1	Introduction	174
6.2	Data	176
6.2.1	X-ray	176
6.2.2	Optical	177
6.2.3	Radio	177
6.2.4	Near-Infrared (NIR)	178
6.2.5	Mid-Infrared (MIR)	178
6.2.6	Ultraviolet (UV)	179
6.3	Flux Correlations	182
6.3.1	UV and X-ray	185
6.3.2	X-ray and IR	187
6.3.3	UV and IR	189
6.3.4	X-ray and Radio	191
6.4	Spectral Energy Distributions	193
6.4.1	Luminosity Sub-samples	198
6.4.2	Eddington Ratio Sub-samples	201
6.4.3	Narrow-line Seyfert 1	202
6.4.4	Radio Loudness Sub-samples	207
6.4.5	X-ray Power-law Slope Sub-samples	208
6.4.6	Normalised SEDs	209
6.5	Conclusions	211
7	Conclusions	213
7.1	Summary	214
7.2	Future Work	218
A	Spectral Fitting Results	221
	References	246

List of Tables

2.1	A comparison of the properties of the current major X-ray telescopes.	31
2.2	Principal characteristics of the two EPIC detectors	33
2.3	Details of the different serendipitous source catalogue releases.	37
3.1	XSPEC models used and the number of sources best-fit with each.	54
3.2	Correlations between Γ and z for the binned data and null hypothesis probabilities for both the linear and constant models.	68
3.3	Correlations between Γ and L_X for the binned data and null hypothesis probabilities for both the linear and constant models.	76
3.4	Correlation coefficients and significances for correlations between kT and z , L_X , L_{bb} and M_{BH}	84
3.5	Best-fitting linear trends between R_L and λ_{Edd} for the combined RQ and RL populations, and just the RLQ on their own.	103
4.1	Best-fitting parameters for the po, zxi and po+bb $\Gamma = 2.0$ models, as applied to three of the steep extreme sources.	126
4.2	Table of intrinsic extreme sources	135
5.1	The samples and results of the joint fitting to recover a soft excess feature in low count spectra.	165
5.2	The results of the joint fitting on the samples defined according to λ_{Edd}	167
5.3	Joint fitting results for the apo+bb model in order to recover absorption in addition to the soft excess.	170
6.1	The percentage of sources with a flux measurement at each frequency.	181
6.2	Correlations between fluxes in different wavebands.	183
6.3	Flux correlations considered in broad z bins.	184
6.4	The α_{OX} values derived from the flux values in the mean SEDs of sources binned by λ_{Edd}	201
A.1	Spectral fitting results.	245

List of Figures

1.1	A typical optical spectrum of a type 1 AGN	5
1.2	The production of power-law synchrotron emission.	8
1.3	The Unified Model of AGN.	9
1.4	The spectral energy distribution of a typical quasar.	11
1.5	Bolometric corrections as a function of frequency (from Richards et al. 2006).	14
1.6	Typical features in an AGN X-ray spectrum.	15
1.7	Power-law production from inverse Compton scattering.	17
1.8	The effect of absorption on a power-law spectrum.	19
1.9	The Done et al. (2012) model of the soft excess.	24
2.1	An artist’s impression of <i>XMM-Newton</i>	29
2.2	An internal view of <i>XMM-Newton</i>	30
2.3	MOS and pn detectors.	33
2.4	The CCD layout in the MOS and pn detectors.	33
2.5	The different observing modes of the EPIC detectors.	34
2.6	The effective area of the MOS and pn detectors.	34
2.7	The main models used in the spectral fitting of the sample.	41
2.8	Partially covering absorption model	42
2.9	Ionised absorption model	42
2.10	Photometric and spectroscopic sky coverage of the SDSS DR5 data release.	44
3.1	Plot of Chi-squared vs degrees of freedom for each of the X-ray spectra.	55
3.2	Spectrum for SRCID 73222 which includes an iron line.	56
3.3	The redshift, counts and luminosity distributions of the sample.	57
3.4	The redshift distribution of sources in the full quasar catalogue and in the final sample	58
3.5	The distribution of absolute <i>i</i> band magnitudes for sources in the full quasar catalogue and in the final sample	59
3.6	The distribution of Γ values for the serendipitously detected sources and the targeted sources.	59

3.7	The spectrum of SRCID 75084 which is best-fit with the simple power law model, po.	60
3.8	The distribution of best-fitting photon indices.	62
3.9	The variation in reduced χ^2 for increasing intrinsic dispersion levels.	63
3.10	The distribution of photon indices, modelled with two Gaussians.	65
3.11	A scatter plot of Γ vs z	66
3.12	Plots showing Γ distributions of sources fit with different models, and how the percentage fit with each varies with redshift.	67
3.13	A binned plot of Γ vs z	69
3.14	The power-law slope determined from the 0.5–12.0 keV detector energy range compared with the value from the 2.0 – 6.0 keV rest frame energy range. . .	72
3.15	A scatter plot of Γ vs L_X	74
3.16	A binned plot of Γ vs L_X	75
3.17	X-ray spectrum for SRCID 71597 which is best-fit with the absorbed power law model, apo.	77
3.18	The distribution of intrinsic absorbing column densities.	78
3.19	The optical spectrum of SRCID 141541.	79
3.20	The relations between N_H and z , and N_H and L_X	80
3.21	The change in the percentage of absorbed sources with L_X and z	81
3.22	X-ray spectrum of SRCID 141491 which is best-fit with the power law model and a soft excess, po+bb.	82
3.23	Figures testing the po+bb modelling.	84
3.24	The distribution of best-fitting kT values.	85
3.25	The relations between kT and z , L_X , L_{bb} and M_{BH}	86
3.26	A plot of L_{bb} vs M_{BH}	88
3.27	A plot comparing the luminosity in each of the separate components of the po+bb fits, calculated over the 0.5 – 10.0 keV range.	89
3.28	Radio loudness, R_L , against optical extinction, A_V	91
3.29	Comparison of the M_i , z , Γ and L_X distributions for RQQ and RLQ.	93
3.30	Plots of R_L vs Γ and R_L vs $\log L_X$	95
3.31	Binned plots of R_L vs Γ and R_L vs $\log L_X$	96
3.32	Black hole mass distribution	98
3.33	The relationship between Γ and Eddington ratio	100
3.34	A comparison of the X-ray and optically derived Eddington ratios	101
3.35	The relationship between kT, L_{bb} , M_{BH} and the Eddington ratio.	102
3.36	Comparison of the black hole mass distributions in RQQ and RLQ	104

3.37	A comparison of the Eddington ratio distributions in RQQ and RLQ and the trend between R_L and λ_{Edd}	105
4.1	The full sample of extreme sources in relation to the original distribution of best-fitting power law slopes.	110
4.2	The counts/redshift distribution of the extremes in relation to the full sample.	111
4.3	The percentage of extreme sources in each redshift bin.	112
4.4	The distributions of X-ray luminosities, black hole masses and Eddington ratios for the extreme and non-extreme sources.	113
4.5	The measured Γ values vs total number of counts in the spectra	114
4.6	Spectra of the flattest extreme sources with > 1000 counts.	117
4.7	Spectra of the steepest extreme sources with > 1000 counts.	118
4.8	The unfolded spectra of SRCID 138635, with the original simple power-law fit and the ‘po+bb fix’ model in which Γ is not extreme.	119
4.9	The unfolded spectra of SRCID 76393, with the original simple power-law fit and the ‘apo fix’ model in which Γ is not extreme.	120
4.10	The distribution of Γ values before and after the results of the fixed Γ models are taken into account.	121
4.11	The counts/redshift distribution of the sources which can be well fit with a fixed Γ model.	122
4.12	The unfolded spectra of SRCID 80946 with the original power-law fit plus blackbody and the zxi model in which Γ is not extreme.	123
4.13	The unfolded spectra of SRCID 124986 with the original power-law fit and the zpcfabs model in which Γ is not extreme.	124
4.14	The distribution of Γ values before and after the results of the complex absorber fits are taken into account.	125
4.15	The counts/redshift distribution of the sources which can be well fit with a complex absorption model.	126
4.16	The distribution of Γ values for the 16 sources defined as BALQSOs by the Scaringi et al. (2009) catalogue compared with non-BAL quasars.	129
4.17	The distribution of Γ values and Eddington ratios for the 17 sources defined as NLS1s by Zhou et al. (2006) and the confirmed non-NLS1 quasars.	131
4.18	X-ray and optical spectra of SRCIDs 82106, 94995, 95096 and 96674, some of the intrinsically flat extremes.	139
4.19	X-ray and optical spectra of SRCIDs 27218, 84741 and 210692, some of the intrinsically steep extremes.	140
4.20	The Γ distribution of the intrinsic extreme sources in relation to the full sample.	141
4.21	The distributions of Γ , counts, z , L_X , M_{BH} and λ_{Edd} for the intrinsic and non-extreme sources.	143

4.22	The counts/redshift distribution of the intrinsic extremes compared to the non-extreme sources.	144
4.23	The location of the intrinsic extremes in M_{BH} , L_{X} , λ_{Edd} parameter space. . .	145
5.1	The counts and redshift distribution of the sample.	150
5.2	The percentage of sources requiring an absorption or soft excess component as a function of the number of counts in the spectra.	151
5.3	The redshift dependence of the detected percentages.	153
5.4	The blackbody to power-law normalisation ratios for the high count sources with a detected soft excess.	155
5.5	Examples of typical simulated spectra	156
5.6	Detectability curves for a typical soft excess component at different redshifts.	157
5.7	The detected percentage of sources including a soft excess, after a correction for spectral quality has been applied.	158
5.8	Spurious detection simulations.	159
5.9	Comparison of the detectability of a soft excess with a different kT value. . .	160
5.10	Soft excess detectability curves for a lower blackbody to power-law normalisation ratio.	161
5.11	The blackbody to power-law normalisation ratio values for each of the spectra in the 6 samples used in the joint fitting.	164
5.12	The detectability of absorption components with different N_{H} values.	169
6.1	Reproduction of the <i>GALEX</i> PDF presented in Bianchi et al. (2007a)	181
6.2	Correlations between the fluxes and the luminosities in the soft X-ray and UV bands.	186
6.3	Correlations between the fluxes and the luminosities in the W1 band and the X-ray bands.	188
6.4	Correlations between the fluxes and the luminosities in the W2 and the UV bands.	190
6.5	Correlations between the fluxes and the luminosities in the hard X-ray band and the radio band for RL and RQ sources.	192
6.6	An example SED.	194
6.7	The SED and optical spectrum of a high z AGN.	194
6.8	SEDs showing absorption.	196
6.9	The mean SED of sources with the best quality individual SEDs.	197
6.10	A plot of $F_{\text{X}}/F_{\text{O}}$ against F_{O} with values obtained from mean SEDs binned according to L_{X}	199
6.11	Mean SEDs for sources binned by L_{X}	200

6.12	The dependence of α_{OX} on Eddington ratio.	203
6.13	Mean SEDs for sources binned by λ_{Edd}	204
6.14	Mean SEDs for sources binned by $\lambda_{\text{Edd}(\text{opt})}$	205
6.15	Distributions of optically derived Eddington ratios for NLS1 and non-NLS1.	206
6.16	Mean SEDs for NLS1 and non-NLS1.	206
6.17	Mean SEDs for sources binned by R_{L}	207
6.18	Mean SEDs for sources binned by Γ	208
6.19	Mean SEDs normalised at fixed frequency points.	210

1

Introduction

This thesis reports studies of Active Galactic Nuclei (AGN), the most enigmatic objects in the Universe. They are highly luminous and emit over the entire electromagnetic spectrum. Each wavelength we study them at is a diagnostic for the physics occurring and X-ray observations in particular can help us to understand the physics of the inner regions where it is believed a supermassive black hole is accreting matter. Thanks to the successful *XMM-Newton* mission there is now a large amount of archival X-ray data available including serendipitous detections of large numbers of AGN. In this thesis, a large sample of type 1 AGN with X-ray spectra is created. Their X-ray spectral properties, and full spectral energy distributions are studied in order to better understand their behaviour. This is important as these objects have a major role in galaxy formation and evolution, with the growth of the black hole and host galaxy being strongly linked.

1.1 Active Galactic Nuclei

1.1.1 Taxonomy and Physical Characteristics

The term ‘Active Galactic Nuclei’ now generally refers to all accreting supermassive black holes. However, for historical reasons different classes of AGN exist, with characteristics based largely on how they were first discovered. These observational properties are described below.

Quasars were first discovered in the large radio surveys 3C (third Cambridge, Edge et al. 1959) and 3CR (3C revision, Bennett 1962). Some of the radio sources were found to coincide with point like optical counterparts (Schmidt, 1963) and became known as ‘quasi-stellar radio sources’ or ‘quasars’. Whilst these are naturally radio loud, it was later discovered that radio quiet versions exist which are around 10 times more numerous. Quasars are the most luminous sub-class of AGN which outshine the host galaxy, although some starlight from the host may be visible as ‘quasar fuzz’. Quasars are very blue, $U - B < -0.3$, and their optical spectra include broad emission lines such as $H\alpha$, $H\beta$, $MgII$, $CIII]$, CIV and $Ly-\alpha$ (Peterson, 1997).

Seyfert galaxies are spirals which show an unusually high central surface brightness indicative of a ‘quasar-like’ nucleus (Seyfert, 1943). They have lower luminosities than quasars, with the separation formally at $M_B = -21.5 + 5\log h$ (Schmidt & Green, 1983). Their ultraviolet (UV)/optical spectra also show emission lines, and two separate classes are defined based on which lines are visible in the spectra. In type 1, both broad permitted lines which have widths up to 10^4 km s^{-1} and narrow forbidden lines which have narrower widths of $\sim 400 \text{ km s}^{-1}$, are seen. In type 2, only the narrow emission lines are visible. The flux ratio $O[III]/H\beta < 3$ is often used to discriminate between Seyfert 1 and 2 sources, since it measures the relative strength of the narrow to broad lines. A more complicated classification system defining Seyfert 1.5, 1.8 & 1.9 types was introduced by Osterbrock (1981) and considers the relative strength of the broad and narrow components within the lines.

Radio galaxies are AGN typically residing in elliptical hosts. They can have an extended ($\sim 1 \text{ Mpc}$) radio morphology consisting of two radio lobes connected to the compact core by a jet. Such sources are sub-divided depending on where the emission dominates; FRI sources are

core dominated i.e. the surface brightness decreases outwards and they are generally weaker radio emitters with $L_{1.4\text{GHz}} \leq 10^{32} \text{ erg s}^{-1}\text{Hz}^{-1}$ and FR II sources are lobe dominated, i.e. the surface brightness increases outwards and they have higher radio luminosities of $L_{1.4\text{GHz}} \geq 10^{32} \text{ erg s}^{-1}\text{Hz}^{-1}$ (Fanaroff & Riley, 1974). Radio galaxies can also be classified as broad-line radio galaxies (BLRG) or narrow-line radio galaxies (NLRG) based on the emission lines in their optical spectra, in an analogous way to the Seyfert 1 and 2 classification for spiral hosts. Another classification uses the strength of the optical lines; sources with weak optical emission lines (low-excitation radio galaxies, LERGs) tend to have low radio luminosities, whilst those with stronger lines (high-excitation radio galaxies, HERGs) have higher luminosities (Hine & Longair, 1979).

Blazars are radio sources whose optical spectra have a power-law shape indicative of a non-thermal origin. They can be sub-divided into two sub-classes; BL Lacs have very flat optical spectra characterised by the lack of any strong emission or absorption lines and Optically Violent Variables (OVVs) show very strong (about 50%) and rapid (day timescales) optical variability, in addition to a very strong optical polarisation (Peterson, 1997).

Physical Structure

Despite their different observational properties, all of these classes of AGN are thought to have broadly the same physical structure consisting of a supermassive black hole (SMBH) located at the centre of a massive galaxy (Kormendy & Richstone, 1995; Magorrian et al., 1998; Kormendy & Gebhardt, 2001) which is accreting matter (Lynden-Bell, 1969). Accretion is the most efficient process for converting mass to energy and is the only process capable of producing such large luminosities from relatively small regions.

Material falling onto a compact object, such as a black hole, loses gravitational potential energy due to friction within the matter. However it also possesses large amounts of angular momentum which prevents direct accretion. Instead, the matter forms a geometrically thin, but optically thick disc around the black hole, perpendicular to the angular momentum vector (Pringle & Rees, 1972; Shakura & Sunyaev, 1973). Turbulence is created in the disc, driven by the magneto-rotational instability (MRI; Balbus & Hawley 1991). This transfers angular

momentum outwards and the material inwards, allowing it to be accreted with a rate \dot{m} . The luminosity emitted as the source accretes is given by Eqn. 1.1 where M is the mass of the black hole, R_S is the Schwarzschild radius and k is a factor which depends on the spin of the black hole. For a non-spinning black hole, $k = 3$ and for a maximally spinning black hole $k = 0.5$ (prograde) or $k = 4.5$ (retrograde). The efficiency of accretion, η , therefore also depends on the black hole spin ($\eta = 1/4k$) and varies between 0.04 for a retrograde spin, 0.06 for non-spinning and 0.42 for a fully prograde spin.

$$L = \frac{GM\dot{m}}{2kR_S} = \eta\dot{m}c^2 \quad (1.1)$$

The maximum stable luminosity that can be generated from accretion onto a black hole occurs when the gravitational force pulling material in is equalled by the radiation pressure force pushing material away. This is the Eddington luminosity and is given by Eqn. 1.2.

$$L_{\text{Edd}} = \frac{4\pi GMm_p c}{\sigma_T} \quad (1.2)$$

Typical Eddington ratios, L/L_{Edd} , for AGN are 0.001 – 0.1, but some objects do appear to be accreting at a super-Eddington rate. The Eddington luminosity determination is highly simplified and assumes fully ionised hydrogen, that the radiation is emitted spherically and isotropically, the only source of opacity is Thomson scattering, and there is a steady accretion flow. In particular, the Eddington luminosity could easily appear to have been exceeded if the radiation is beamed. Alternative models for the accretion disc such as the ‘slim disc’ model (Abramowicz et al., 1988) or the ‘leaky disc’ model (Begelman, 2002) can also allow super Eddington accretion rates and luminosities.

A characteristic temperature for the accretion disc can be determined by assuming that the dissipated heat is radiated locally as blackbody radiation. A blackbody is an object which completely absorbs all radiation incident upon it and emits a continuous spectrum which depends only upon its temperature (Seward & Charles, 2010). The peak of the spectrum can be determined from Wien’s displacement law, $\lambda_{\text{max}}T = 2.898 \times 10^{-3}\text{m.K}$ and the total luminosity emitted from a spherical blackbody of radius R can be determined from the Stefan-Boltzmann

law, $L_{\text{bb}} = 4\pi R^2 \sigma_B T^4$ where $\sigma_B = 5.67 \times 10^{-8} \text{Wm}^{-2}\text{K}^{-4}$ (Schneider, 2006). Equating this with the accretion luminosity from Eqn. 1.1 gives Eqn. 1.3 after some rearranging, and assuming typical parameters of $\dot{m} = 0.1\dot{m}_{\text{Edd}}$ and $M = 10^8 M_\odot$, gives a disc temperature of $kT \sim 0.02 \text{ keV}$ which peaks in the UV.

$$T = \left(\frac{0.1 m_p c^5}{4\sigma_B \sigma_T G 10^8 M_\odot} \right)^{1/4} \left(\frac{\dot{m}}{0.1\dot{m}_{\text{Edd}}} \right)^{1/4} \left(\frac{M}{10^8 M_\odot} \right)^{-1/4} \quad (1.3)$$

Close to the black hole ($\lesssim 0.1 \text{ pc}$) is the region known as the Broad Line Region (BLR). Within this are typically $\sim 10^{10}$ clouds with sizes $\sim 10^{11} \text{ cm}$ which are photoionised by the central source and have temperatures of $T \sim 20,000 \text{ K}$. Emission lines are created when bound electrons, which have been temporarily excited into a higher energy state by absorbing a photon, decay back down to a lower energy level. In doing so, a photon is emitted with an energy characteristic of the atomic energy level spacing and the lines are Doppler broadened due to the high velocities ($v \sim 5000 \text{ km s}^{-1}$) of the clouds. The high gas densities of the clouds ($n_e \sim 10^9 \text{ cm}^{-3}$) means that mostly only permitted transitions are allowed giving the lines Ly- α , CIV, MgII, H β and H α but some semi-forbidden transitions occur, such as CIII] and NIV] (Peterson, 1997). Fig. 1.1 shows the typical optical spectrum of a quasar, including these emission lines.

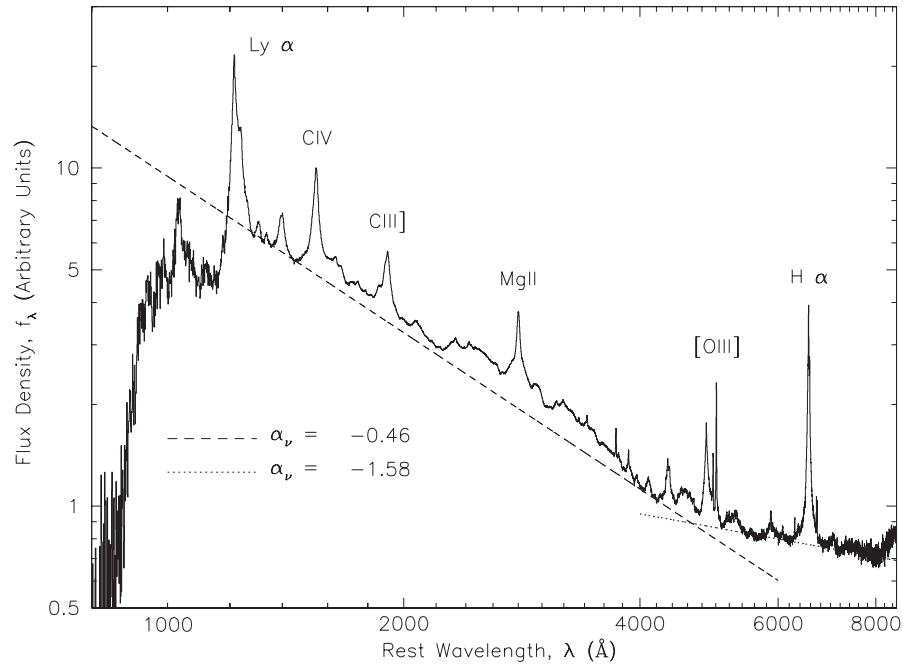


Figure 1.1: A typical optical spectrum of a type 1 AGN (Vanden Berk et al., 2001)

The size of the BLR can be determined from reverberation mapping (Peterson, 1993; Kaspi et al., 2000). This measures the time delay dT between changes in the continuum flux and the line flux which occur due to the finite extent of the region. Typical sizes of the BLR are a few tens of light days corresponding to $\sim 10^{15}$ cm. A less costly and time consuming method is to use empirical correlations with the UV/optical luminosity, such as that found by Kaspi et al. (2000; Eqn. 1.4a), however, there is considerable scatter in the correlation. Similar relations have been found using the luminosity at 3000\AA (Eqn. 1.4b; McLure & Jarvis 2002) and 1350\AA (Eqn. 1.4c; Vestergaard 2002).

$$R_{\text{BLR}} = (32.9_{-1.9}^{+2.0}) \left[\frac{\lambda L_{\lambda}(5100\text{\AA})}{10^{44} \text{ erg/s}} \right]^{0.70 \pm 0.03} \text{ light days} \quad (1.4a)$$

$$R_{\text{BLR}} = (25.2 \pm 3.0) \left[\frac{\lambda L_{\lambda}(3000\text{\AA})}{10^{44} \text{ erg/s}} \right]^{0.47 \pm 0.05} \text{ light days} \quad (1.4b)$$

$$R_{\text{BLR}} = 10.7 \left[\frac{\lambda L_{\lambda}(1350\text{\AA})}{10^{44} \text{ erg/s}} \right]^{0.7} \text{ light days} \quad (1.4c)$$

Knowing the size of the BLR allows the black hole mass to be estimated using the virial method. This assumes that the BLR is gravitationally bound by the potential of the central black hole and that the clouds responsible for the broad emission lines are virialised. If this is the case, the velocity of the gas v_g can be estimated from the Full Width Half Maximum (FWHM) of a broad emission line using the equation $v_{\text{BLR}} = f \times \text{FWHM}$ where f is a geometric factor describing the shape and inclination of the clouds. For an isotropic distribution of randomly orientated clouds, $f = \frac{\sqrt{3}}{2}$ (Netzer, 1990), whereas if the orbits have a flattened disc geometry, $f = \frac{3}{2}$ (McLure & Dunlop, 2001). If magnetic fields or outflows contribute significantly to the dynamics, the estimate of v_g derived from the line width may not be a true estimate of the orbital velocity of the BLR clouds. The mass of the black hole can then be determined using Eqn. 1.5

$$M_{\text{BH}} = R_{\text{BLR}} v_g^2 G^{-1} \quad (1.5)$$

At larger distances from the black hole ($\sim 10 - 100$ pc) is the Narrow Line Region (NLR). This region is also thought to contain clouds, but with a lower filling factor than in the BLR ($\sim 10^{-2}$) and the clouds themselves are also of a slightly lower temperature ($T \sim 16,000$ K), lower velocity (400 km s^{-1}) and lower density ($n_e \sim 10^3 \text{ cm}^{-3}$; Peterson 1997). This lower density means that narrow emission lines caused by forbidden transitions are able to occur before collisional de-excitation, the strongest one being [OIII].

An optically and geometrically thick ‘torus’ of gas and dust surrounding the central regions of AGN was first proposed by Antonucci & Miller (1985) in order to explain why the BLR of the Seyfert 2 galaxy NGC 1608 could be seen via scattered light, but not directly. It was assumed to have a covering factor large enough to block the BLR from sight, but not the NLR and the dust scatters the BLR emission towards the observer. It lies at parsec scales, at the radius where the temperature has dropped to below the sublimation temperature allowing dust grains to form. Infrared (IR) emission from Seyfert 2 galaxies has been observed to be consistent with re-radiation from such a dusty torus (Storchi-Bergmann et al., 1992) and the torus has been imaged with Mid-IR (MIR) observations (Jaffe et al., 2004). However, it is not clear how the torus maintains its required thickness ($\frac{H}{r} \geq 0.5$) for most of the AGN phase rather than collapsing into a thin disc. Many solutions have been proposed to solve the problem, including radiation pressure from IR photons within the torus (Krolik, 2007).

Some AGN have highly collimated jets which emerge from the inner regions with a direction orthogonal to the angular momentum axis of the inner disc. They contain charged particles and magnetic fields and travel close to the speed of light. The jet launching and collimation mechanism is not well understood. It was initially suggested that a magnetic field could extract the spin energy of the black hole (Blandford & Znajek, 1977), but it may originate from the disc itself since any magnetic field threading it would dominate the system (Livio et al., 1999). Jets produce radiation over a wide range of frequencies from radio to γ -rays, most likely a result of synchrotron emission and inverse Compton scattering (Worrall & Birkinshaw, 2006). Synchrotron radiation is emitted by charged particles moving in a magnetic field, and is polarised depending on its emitted direction with respect to the field. The emission spectrum from a population of multiple electrons is the super-position of individual spectra which each

have peaks at different frequencies giving a combined power law shape (see Fig. 1.2). Synchrotron photons generated at low frequencies may be absorbed by the electrons creating them, meaning the spectrum is modified to $F_\nu \propto \nu^{5/2}$. This process is known as Synchrotron Self Absorption (SSA; Rybicki & Lightman 1979). The synchrotron photons can also undergo inverse Compton scattering off the electrons which produced them initially. This is known as Synchrotron Self Compton (SSC) and likely occurs in AGN jets, where the electrons upscatter the synchrotron photons seen in the radio to the X-ray regime (Schneider, 2006).

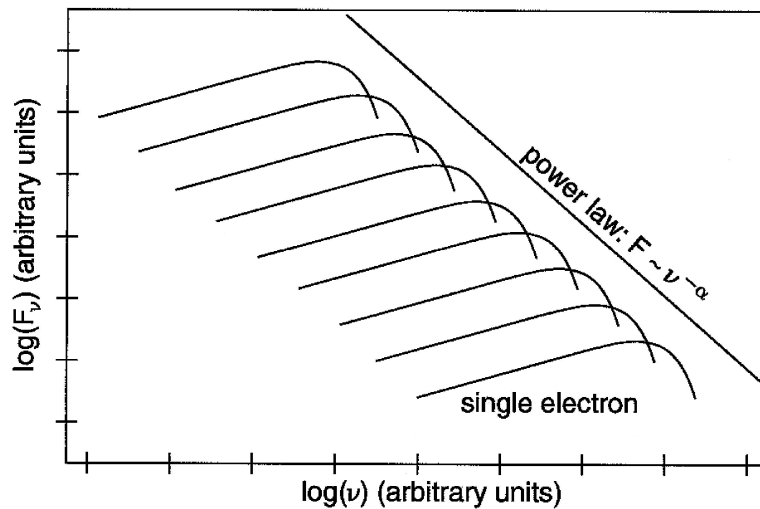


Figure 1.2: This figure shows how the synchrotron emission spectra for individual electrons combine into an overall power law spectrum. Figure taken from Schneider (2006).

Unified Model

The Unified Model (Antonucci, 1993) explains the different observational classes of AGN as being the same type of physical object - an accreting SMBH - with the differences simply due to the observer's line of sight to the source or a difference in luminosity. Fig. 1.3 shows how the physical characteristics of AGN give rise to the different observational classes. Seyfert 1 are AGN in which the observer is able to look directly into the BLR and therefore broad emission lines are seen in their spectra, but in Seyfert 2 the BLR is blocked from view by the torus so only narrow lines are present (Osterbrock, 1978). This scenario also explains why on average Seyfert 2 are less luminous than Seyfert 1 (Lawrence & Elvis, 1982). Radio-quiet quasars (RQQ) are more luminous versions of Seyfert 1 galaxies, in which broad emission lines are also seen. If a jet is present in the source, then there will be increased radio emission.

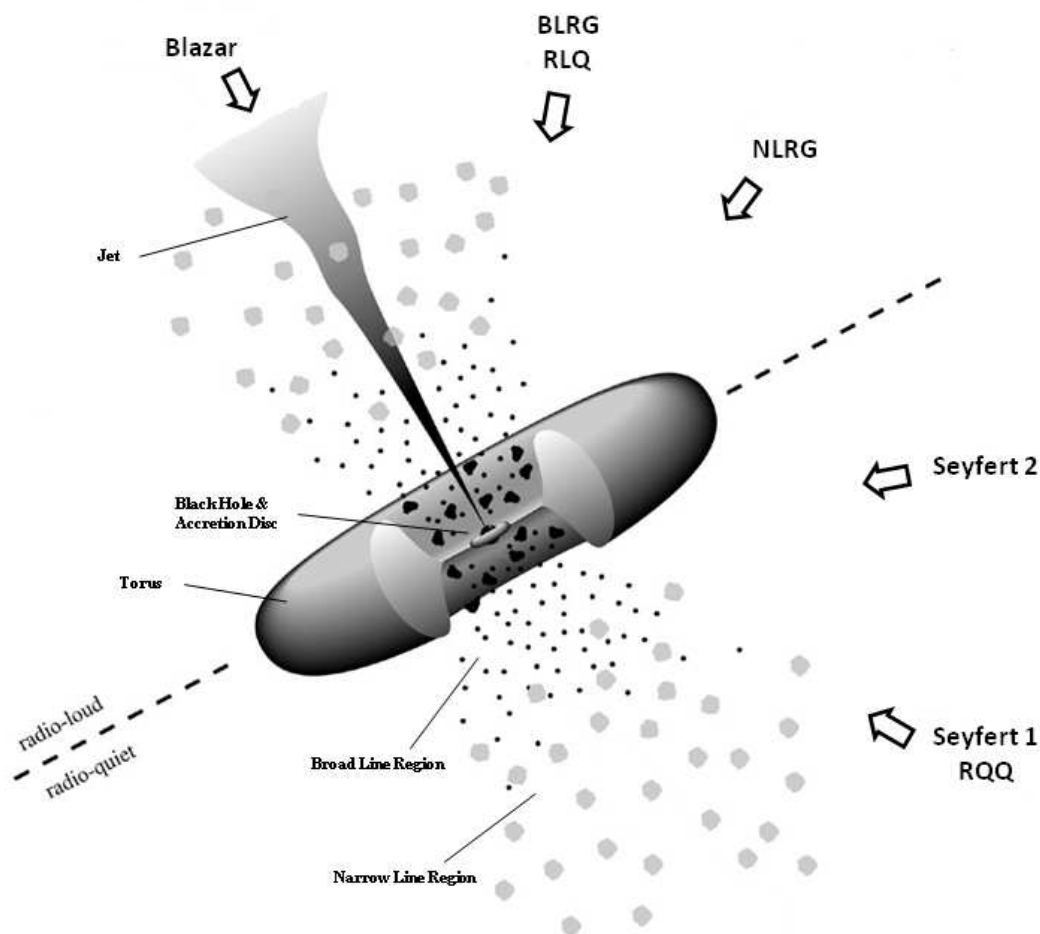


Figure 1.3: This figure shows the Unified Model of AGN proposed by Antonucci (1993). It shows how the physical characteristics of an accreting supermassive black hole, in particular the dusty torus, can give rise to the many different observational classes of AGN. Figure taken from <http://ned.ipac.caltech.edu> and adapted, based on an original image by Urry & Padovani (1995).

The BLRG and NLRG classifications depend upon the observer's viewing angle with respect to the torus alignment in a similar way to radio-quiet sources, and radio-loud quasars (RLQ) are high luminosity analogues of BLRGs. If the observer is looking directly into the jet, then a blazar is seen, in which the flux is dominated by the beamed component (Blandford & Rees, 1978). BL Lacs are thought to correspond to low luminosity FRI sources which are seen face on, rather than edge on, and OVV's correspond to higher luminosity FRII (Padovani & Urry, 1992).

Whilst this picture explains most classes of AGN well, some mis-matches between the type 1 and type 2 classification have been found, suggesting modifications are necessary. Some type 1 AGN, which are expected to be unabsorbed in X-rays, have been found to require intrinsic absorption in the modelling of their X-ray spectra (Page et al., 2003; Perola et al., 2004; Piconcelli et al., 2005; Mateos et al., 2005b; Mainieri et al., 2007; Garcet et al., 2007; Young et al., 2009; Mateos et al., 2010; Corral et al., 2011) and conversely type 2 AGN have been found with no absorption in X-rays (e.g. Panessa & Bassani 2002; Mateos et al. 2005a,b). In addition, variable X-ray absorption or variable optical reddening has made some sources apparently change their classification. One suggestion is that the torus is ‘clumpy’ and consists of individual clouds (Nenkova et al., 2008a,b). However, some X-ray absorption variability is rapid and changes over timescales of days to hours, suggesting it is more likely due to obscuration of the central source by the broad line clouds themselves (e.g. Elvis et al. 2004; Risaliti et al. 2007, 2009a). In these models observing a given source as absorbed depends upon the covering factor of the clouds and is a probability issue rather than one of just orientation (Risaliti et al., 2002). Another suggestion is that a warped accretion disc could be responsible for the obscuration. In this scenario type 2 objects are the ones with larger misalignments, giving larger covering factors (Greenhill et al., 2003; Nayakshin, 2005; Lawrence & Elvis, 2010).

The Unified Model predicts the existence of type 2 quasars as the high luminosity analogue to Seyfert 2 and hence the fraction of absorbed sources should stay constant with changes in luminosity. However, previous studies report the fraction of absorbed sources to decrease with increasing luminosity (Ueda et al., 2003; Hasinger, 2008) and lower levels of absorption are reported in higher luminosity objects and vice versa (Mushotzky, 1982; Lawrence & Elvis, 1982). This suggests that higher luminosity AGN are able to clear their environment, but low luminosity AGN remain surrounded by an obscuring medium. Lawrence (1991) proposed the ‘receding torus’ model, which notes that the dust sublimation radius increases as a function of luminosity and therefore the inner edge of the torus will be further away for higher luminosity sources, resulting in less obscuration. This would explain the apparent lack of type 2 quasars.

1.1.2 Spectral Energy Distributions

AGN have high luminosities across the entire electromagnetic spectrum. The amount of energy output at different frequencies is described by a spectral energy distribution (SED). The SED of an AGN can be broadly described by a power law of the form $F_\nu \propto \nu^{-\alpha}$, where α is the power-law index and takes different values for different frequency ranges. The typical SED of a type 1 AGN is shown in Fig. 1.4. It is made up of features which originate from physical processes occurring in different regions around the black hole.

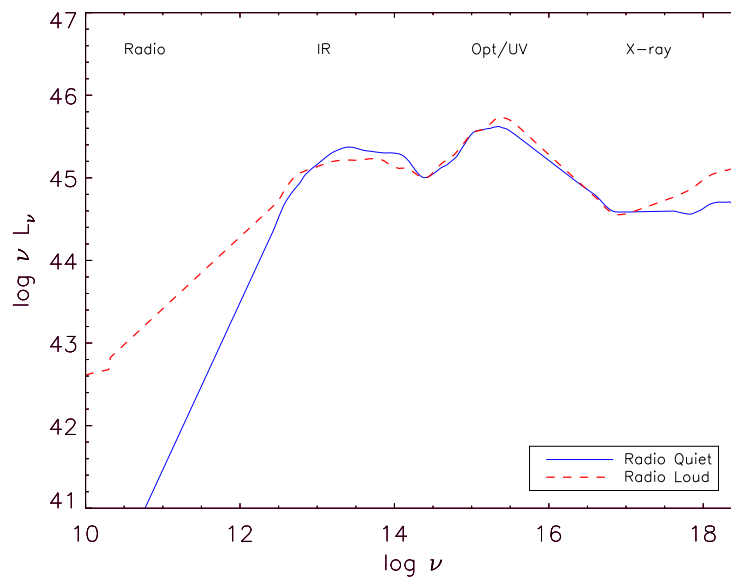


Figure 1.4: A typical SED of a type 1 RL and RQ quasar. Data taken from Elvis et al. (1994).

The radio emission of AGN contributes very little to the bolometric output, even in radio-loud sources where it is typically 100 – 1000 times greater than that of radio-quiet sources. The radio emission of RL sources is due to the synchrotron emission from their relativistic jets but since these are generally not present in RQ sources, the origin of their radio emission is less clear.

The IR emission from AGN constitutes $\sim 15 - 50\%$ of the bolometric luminosity, L_{bol} (Risaliti & Elvis, 2004), and is seen in the SED as a broad ‘IR hump’ covering a range of $1.5 - 100 \mu\text{m}$. It is thought to be due to thermal reprocessing by hot ($50 - 1000 \text{ K}$) dust surrounding the black hole, possibly in the torus (Rees et al., 1969; Rieke, 1978).

The UV and optical emission from AGN is dominated by the ‘big blue bump’ (BBB),

which is attributed to thermal emission from the accretion disc (Shields, 1978; Malkan & Sargent, 1982; Czerny & Elvis, 1987). Fig. 1.1 showed the typical UV/optical spectrum of a quasar. For wavelengths longer than Ly- α the continuum can be approximated as two power laws, one with index $\alpha = -0.46$ up to 5000 \AA and the other with index $\alpha = -1.58$ for longer wavelengths. The break is likely due to contamination from the host galaxy. The continuum bluewards of Ly- α is heavily absorbed creating the ‘Ly- α forest’. Super-imposed on the continuum are emission lines originating from the broad and narrow line regions. Shown in Fig. 1.1 are the broad lines Ly- α (at a rest-frame wavelength of 1216 \AA), CIV (1549 \AA), MgII (2799 \AA), H β (4863 \AA), H α (6565 \AA) and the semi-forbidden line CIII] (at 1909 \AA). The narrow line [OIII] can also be seen at 4364 \AA (Vanden Berk et al., 2001).

X-rays contribute typically $\sim 10\%$ of the total luminous output of AGN. The emission is produced mainly by the inverse Compton scattering of low energy UV photons from the accretion disc by relativistic electrons in the corona (Haardt & Maraschi, 1993) and appears in the spectrum as a simple power law (Mushotzky et al., 1980). In addition, a soft X-ray excess is observed at lower X-ray energies (Arnaud et al., 1985; Turner & Pounds, 1989), and reflected X-rays are observed at higher X-ray energies (Pounds et al., 1990). These features will be discussed in more detail in §1.1.3.

γ -rays have now been detected from a number of AGN (Wagner, 2008). The majority of such sources are blazars, in which the emission is thought to arise inside the jets (Tavecchio et al., 1998) from synchrotron and SSC. This gives a double humped spectrum with one peak in the GeV to TeV regime and the other in the optical to X-ray regime. The radio galaxy M87, whose jet is at 30° to the observer’s line of sight and is therefore not a blazar is also a source of γ -rays. The origin of the emission in this case is most likely from the regions very close to the black hole (Aharonian et al., 2006).

An accurate knowledge of the relative strengths and shapes of the different components in the quasar SED can aid the understanding of the physical processes occurring in the object. The bolometric luminosity of the source can also be derived by integrating under the SED. However, constructing a SED requires many observations at different wavelengths, and it is unlikely that these will be done simultaneously. Therefore intrinsic long-term variability of an

object can lead to a SED which does not accurately represent the energy output of an object at one particular time. It is important to account for the fact that the IR bump is due to reprocessed photons which may have already been considered in the UV range. It is also not clear how to deal with RLQ since some unknown fraction of the X-ray flux may be due to the radio jet.

There have been previous works which have constructed partial SEDs of AGN e.g. Haas et al. (2003), Glikman et al. (2006), Netzer et al. (2007) and Mullaney et al. (2011) who focus on the IR regime; Sanders et al. (1989), Grupe et al. (1998) and Kuraszekiewicz et al. (2009), who also include X-ray data and Trammell et al. (2007), Vasudevan & Fabian (2007) and Jin et al. (2012) who use UV and X-ray data. Full SEDs for 47 quasars (29 RQ and 18 RL) were created by Elvis et al. (1994) using data from *Einstein* & *EXOSAT* (X-ray), the *International Ultraviolet Explorer* (UV), the Multi-Mirror Telescope (Optical), the Infrared Telescope Facility (Near-IR), UKIRT & IRAS (Far-IR) and VLA (radio). A lot of variation in the SEDs of different objects was found, and the mean energy distribution is shown in Fig. 1.4. Richards et al. (2006) constructed SEDs of 259 quasars using data from *ROSAT* (X-ray), *GALEX* (UV), SDSS (Optical), *Spitzer* (IR) and VLA (Radio). More recently, Lusso et al. (2010) constructed SEDs of 545 X-ray selected type 1 AGN from XMM-COSMOS using data from *XMM-Newton* & *Chandra* (X-ray), *GALEX* (NUV & FUV), *Hubble Space Telescope*, Subaru, SDSS (Optical), *Spitzer* (IR), and VLA (radio).

Bolometric correction factors, κ , given by Eqn. 1.6, are used to relate the luminosity observed in a single band to the total bolometric luminosity of the source. These are useful as they allow a quick estimate of L_{bol} to be determined without the need for a comprehensive SED modelling analysis.

$$L_{\text{bol}} = \kappa_{\text{band}} \times L_{\text{band}} \quad (1.6)$$

Elvis et al. (1994) calculated simple bolometric correction factors using their mean energy distribution. The median values are: $L_{\text{bol}} = 5.6 \times L_{2500\text{\AA}}$, $L_{\text{bol}} = 10.7 \times L_{\text{B}}$, $L_{\text{bol}} = 13.2 \times L_{\text{V}}$, $L_{\text{bol}} = 24.8 \times L_{1.5\mu\text{m}}$. This sample is biased towards X-ray bright quasars and bluer quasars, which may result in slightly higher correction factors for the optical bands. Risaliti & Elvis (2004) compiled average bolometric correction factors for PG quasars and found that $\sim 40\%$ of

the bolometric emission is emitted in the IR regime, $\sim 10\%$ is emitted in the optical, $\sim 45\%$ in the UV and $\sim 5\%$ in X-rays. The radio emission is negligible. Richards et al. (2006) created a mean SED of 259 type 1 AGN. The bolometric correction factors they calculated as a function of frequency are reproduced in Fig. 1.5.

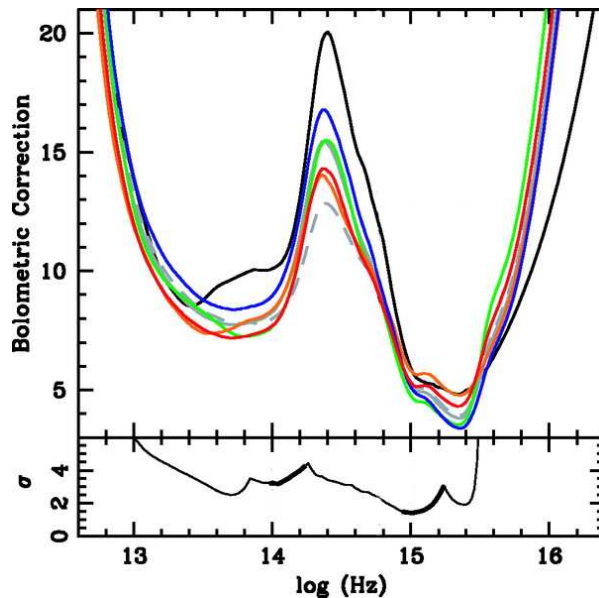


Figure 1.5: Bolometric corrections as a function of frequency for the SEDs determined by Richards et al. (2006). The coloured lines correspond to different sub-sets of quasars used and the bottom panel gives the 1σ error on the bolometric correction factor at each frequency.

Of particular interest to the work in this thesis is the bolometric correction factor for the X-ray band. Wang et al. (2009) find a linear correlation $\log L_{3-20\text{keV}} = (0.91 \pm 0.06)\log L_{\text{bol}} + (3.04 \pm 2.78)$ for hard X-ray selected type 1 AGN. Rather than a simple scaling factor, Marconi et al. (2004) find the correction factor depends upon the X-ray luminosity itself according to Eqn. 1.7, where $\mathcal{L} = \log L_{\text{bol}} - 12$. Similarly, Hopkins et al. (2007) also find luminosity dependent bolometric corrections (see Eqn. 1.8).

$$\log(L_{\text{bol}}/L_{2-10\text{keV}}) = 1.54 + 0.24\mathcal{L} + 0.012\mathcal{L}^2 - 0.0015\mathcal{L}^3 \quad (1.7)$$

$$L_{\text{bol}} = \left[17.87 \left(\frac{L_{\text{bol}}}{10^{10} L_{\odot}} \right)^{0.28} + 10.03 \left(\frac{L_{\text{bol}}}{10^{10} L_{\odot}} \right)^{-0.02} \right] \times L_{0.5-2} \quad (1.8a)$$

$$L_{\text{bol}} = \left[10.83 \left(\frac{L_{\text{bol}}}{10^{10} L_{\odot}} \right)^{0.28} + 6.08 \left(\frac{L_{\text{bol}}}{10^{10} L_{\odot}} \right)^{-0.02} \right] \times L_{2-10} \quad (1.8b)$$

Vasudevan & Fabian (2009) find that the 2 – 10 keV bolometric correction factor is dependent upon the Eddington ratio, with values of $\kappa = 15 - 30$ for $\lambda_{\text{Edd}} < 0.1$, $\kappa = 20 - 70$ for $0.1 < \lambda_{\text{Edd}} < 0.2$ and $\kappa = 70 - 150$ for $\lambda_{\text{Edd}} > 0.2$. This result is confirmed by Lusso et al. (2010; $\kappa_{2-10} \sim 22$ for $\lambda_{\text{Edd}} < 0.1$, $\kappa_{2-10} \sim 27$ for $0.1 < \lambda_{\text{Edd}} < 0.2$ and $\kappa_{2-10} \sim 53$ for $\lambda_{\text{Edd}} > 0.2$). Pozzi et al. (2010) find a large spread in bolometric corrections (6 – 80), with a mean value of $\kappa_{2-10} \sim 20$, and κ_{2-10} is found to be higher for higher luminosity objects and increases for increasing λ_{Edd} . Marchese et al. (2012), using SDSS, *GALEX* and *XMM-Newton* data also find a large spread in the hard X-ray bolometric correction factor (5 – 100) and report a correlation between the correction and Γ . This is also found by Zhou & Zhao (2010), suggesting Γ_{2-10} could be used to estimate κ_{2-10} .

1.1.3 X-ray Spectra of AGN

In this thesis, the X-ray region of the SED is studied in detail. Typical X-ray spectra consist of an underlying power law with multiple spectral features superimposed, as shown by the schematic in Fig. 1.6.

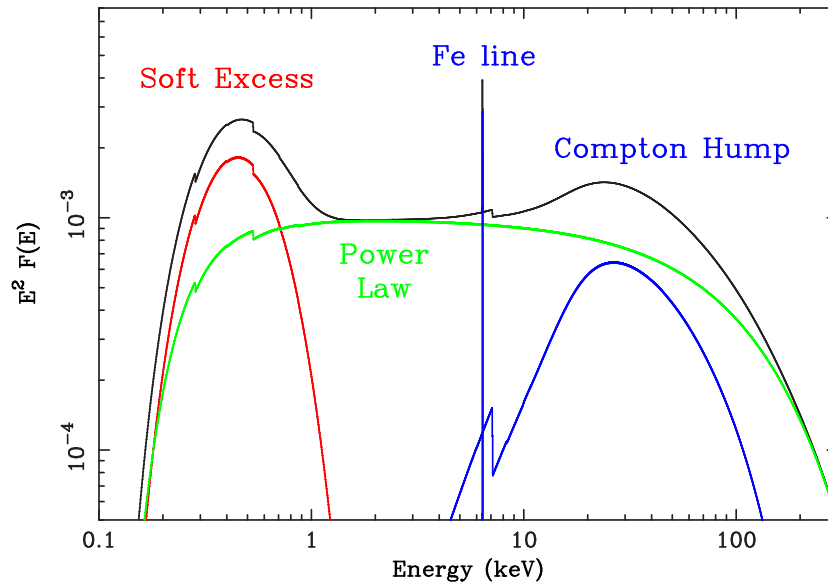


Figure 1.6: This figure shows the main spectral components present in a typical X-ray spectrum. Figure from Fabian & Miniutti (2005)

Power Law

The earliest observations of AGN determined that they had remarkably similar spectra which were well described by a simple power law with a narrow range of energy indices (Mushotzky

et al., 1980) i.e. $F(E) \propto E^{-\alpha}$ where $F(E)$ has units of $\text{ergs cm}^{-2} \text{s}^{-1} \text{keV}^{-1}$. The energy index is related to the more commonly used photon index by $\Gamma = \alpha + 1$. Early observations of Seyfert galaxies with *EXOSAT* showed that their average photon index was $\Gamma = 1.7$ (Turner & Pounds, 1989), but more modern measurements find $\Gamma \approx 1.9 - 2.0$ (Mittaz et al., 1999; Mateos et al., 2005a,b; Page et al., 2006; Just et al., 2007; Mainieri et al., 2007; Young et al., 2009; Green et al., 2009; Mateos et al., 2010; Corral et al., 2011).

This power-law emission is thought to be produced by the inverse Compton scattering of low energy photons by high energy electrons. This process depends upon the optical depth given by $\tau = n_e R \sigma_T$ (where n_e is the electron number density, R is the path length and σ_T is the cross-section for interaction), and the electron temperature, expressed as $\Theta = kT_e/m_e c^2$, as these two properties determine how probable a collision between a photon and an electron will be. The transfer of energy in a collision depends upon the initial energies of the photon and electron and the angle of interaction.

For a thermal distribution the energy exchange of the interaction is given by $E_{\text{out}} \sim (1 + 4\Theta)E_{\text{in}}$. Only a fraction (τ) of the seed photons at the initial energy are scattered but the photons produced can themselves be involved in further scatterings with energy exchange expressed as $E_{\text{out},N} \sim (1 + 4\Theta)^N E_{\text{in}}$. This ‘cascade’ continues until a limiting energy of 3Θ , the initial energy of the electron, and the emission appears as a power law due to the super-position of the N individual scatterings (see Fig. 1.7). The spectrum is described by $F(E) \propto E^{-\alpha}$ where $\alpha = \ln \tau / \ln(1 + 4\Theta)$ and the same spectral index can be created with different combinations of τ and Θ . This degeneracy cannot be broken without observations at higher energies in order to constrain Θ . The spectrum produced is only a smooth power law in the limit where τ is not too small and Θ is not too big (Done, 2010).

In non-thermal Compton scattering, the energy exchange is described by $E_{\text{out}} \sim \frac{4}{3}\gamma^2 E_{\text{in}}$ where $\gamma = 1/\sqrt{1 - (v/c)^2}$. For an initial distribution of electron energies that is given by a power law with index p , i.e. $\frac{dn_e}{d\gamma} \propto \gamma^{-p}$, the resulting inverse Compton spectrum produced will also be a power law with index, $\alpha = (p - 1)/2$ (Holt & McCray, 1982) extending from E_{in} to $\gamma_{\text{max}}^2 E_{\text{in}}$ and consisting of a single scattering order.

The Compton y parameter is defined as the average fractional energy change per scattering,

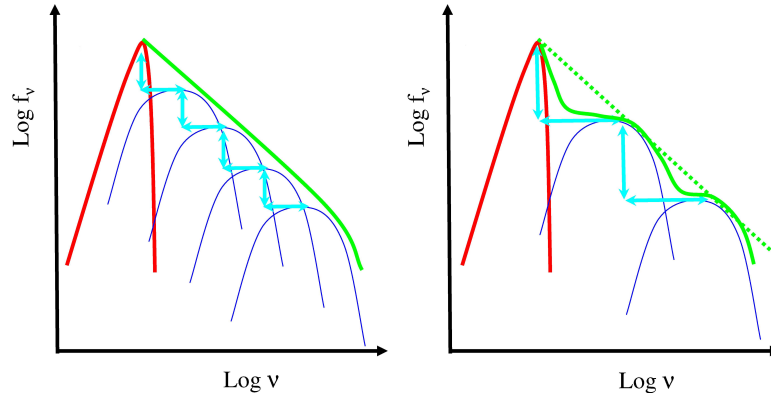


Figure 1.7: These figures show how an apparent power-law emission spectrum (green) can be built up from repeated thermal inverse Compton scatterings (thin blue) from seed photons (red). The same power-law slope index can be obtained with different combinations of Θ and τ values as shown by the two figures. Figure taken from Done (2010).

multiplied by the mean number of scatterings. If $y \ll 1$, the total energy will not be much changed, however if $y \gtrsim 1$ the total photon energy and the spectrum will be significantly altered. The y parameter for both non-relativistic (y_{NR}) and relativistic (y_{R}) electrons are given by Eqn. 1.9 (Rybicki & Lightman, 1979).

$$y_{\text{NR}} = 4\Theta \max(\tau, \tau^2) \quad (1.9a)$$

$$y_{\text{R}} = 16\Theta^2 \max(\tau, \tau^2) \quad (1.9b)$$

It is likely that a mixture of thermal and non-thermal Compton scattering occurs, either with each population of electrons occurring in separate regions or with both thermal and non-thermal distributions existing together.

The pair reprocessing models of Svensson (1994) describe a scenario in which any γ rays produced in the AGN are unlikely to escape without first interacting with an X-ray photon due to the compact nature of the source. In this interaction an electron-positron pair are produced which then cool by inverse Compton scattering with blackbody photons. A particle distribution $N(\gamma) \propto \gamma^{-p}$ gives a radiation spectrum with index $\alpha = (p - 1)/2$ where α is limited by the injection rate of the e^-e^+ pairs and always gives $\Gamma \geq 1.5$. Subsequent Compton scatterings produce photons where $\Gamma_{N+1} = \frac{2+\Gamma_N}{2}$, which tends to the limiting value of $\Gamma = 2$ and is referred to as a ‘saturated’ cascade. In practice the scatterings stop at $N = 3$ or 4, giving

$\Gamma \sim 1.9$. This model implies that Γ can only take values between 1.5 and 2, however, if the radiation density is dominated by X-rays rather than blackbody radiation, the e^-e^+ pairs cool mainly off the X-rays and $\Gamma < 1.5$ can be achieved.

Ishibashi & Courvoisier (2009) propose a model in which shocks between clumps in the accretion flow provide both a mechanism for angular momentum transport and the power-law emission. Optically thick shocks produce UV/optical photons which are then upscattered by hot electrons in optically thin shocks to create the X-ray emission. In Ishibashi & Courvoisier (2010) typical values of Γ are investigated using the parameters from their model and the exact analytical solution for power-law spectra derived by Titarchuk & Lyubarskij (1995) which depends on the physical properties of the plasma (see Eqn. 1.10).

$$\text{Non - relativistic : } \alpha = \sqrt{\frac{9}{4} + \frac{\beta}{\Theta}} - \frac{3}{2} \quad (1.10a)$$

$$\text{Relativistic : } \alpha = \frac{\beta - \ln d_o(\alpha)}{\ln(4\Theta^2)} \quad (1.10b)$$

They define 2 classes of objects, S and Q in order to represent low M_{BH} Seyferts and high M_{BH} quasars, and 2 cases, A and B which have different electron accretion and radiation timescales, and hence act as a proxy for accretion rate (A is low, B is high). For Class S objects the model predicts $\Theta \sim 0.6$, which gives $\alpha \sim 0.9$ ($\Gamma \sim 1.9$) for case A and $\alpha \sim 1.1$ ($\Gamma \sim 2.1$) for case B. For Class Q objects, $\Theta \sim 1.4$, which gives $\alpha \sim 0.5$ ($\Gamma \sim 1.5$) for case A. Therefore the model predicts flatter power-law slopes in sources with higher mass black holes and also a correlation between power-law slope and Eddington ratio.

Photoelectric Absorption

The X-ray spectra of AGN, or any extragalactic source, is modified by photoelectric absorption due to the inter-stellar medium (ISM) of the Milky Way. The total absorbing column can also be greater than the Galactic component, indicating an additional source of absorption intrinsic to the AGN.

When photons collide with atoms, they can be completely absorbed. The photon energy

either causes an electron to be ejected from the atom, giving an absorption edge, or excites an electron to a higher energy level causing absorption lines. The intensity of a beam passing through a material of thickness x decreases according to $I = I_0 \exp(-n\sigma x)$ where n is the number of particles per volume and σ is the absorption cross-section. Absorption therefore depends on the amount of material and its composition. The main contributors in the X-ray band are C, O, Ne, Mg, Al, Si, S, Ca, Fe and an effective cross-section is calculated by summing the cross-section for each element and scaling its contribution by its abundance. Since cross-sections have a strong energy dependence, $\sigma \sim Z^3 E^{-3}$, absorption is also strongly energy dependent and affects lower energies the most. The thickness of the material is usually expressed in terms of an equivalent hydrogen column density, N_{H} , such that $I = I_0 \exp(-\sigma N_{\text{H}})$ (Seward & Charles, 2010). Galactic N_{H} values are available from the HI map of Dickey & Lockman (1990) and typical values out of the plane of the Galaxy are $\sim 10^{20}$ atoms cm^{-2} . The effect of a range of different column densities on power-law spectrum can be seen in Fig. 1.8. The X-ray column density is proportional to optical dust reddening for a given gas/dust ratio which is $N_{\text{H}} = 1.79 \times 10^{21} A_{\text{V}}$ for the Milky Way (Predehl & Schmitt, 1995). However, the ratios found in AGN are much lower, by factors of $\sim 3 - 100$ (Maiolino et al., 2001)

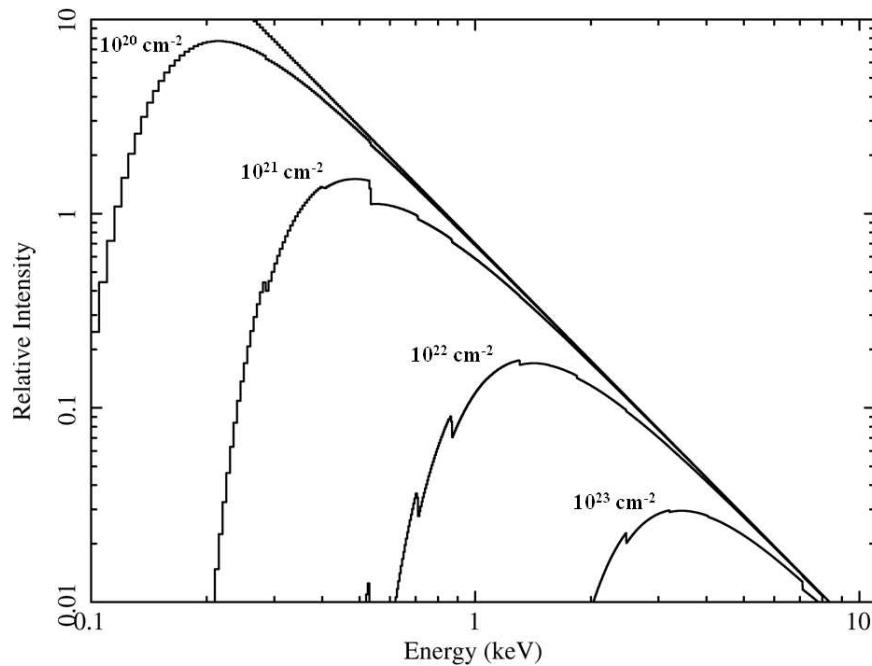


Figure 1.8: This figure shows the effects of absorbers with different column densities (10^{20} , 10^{21} , 10^{22} and 10^{23} cm^{-2}) on a power-law spectrum with slope of $\Gamma = 2$.

The traditional optical classification of AGN based on the presence or absence of broad emission lines generally corresponds to type 1 objects having $N_{\text{H}} < 10^{22} \text{ cm}^{-2}$ and type 2 having $N_{\text{H}} > 10^{22} \text{ cm}^{-2}$. A definition more directly related to the X-ray emission defines Compton-thin sources as those with $N_{\text{H}} < \frac{1}{\sigma_{\text{T}}}$ and Compton-thick as those with $N_{\text{H}} > \frac{1}{\sigma_{\text{T}}}$ (Matt, 2002) where $\frac{1}{\sigma_{\text{T}}} = 1.5 \times 10^{24} \text{ cm}^{-2}$. In Compton-thick sources most of the primary emission is absorbed below 10 keV.

Warm Absorbers

The first warm absorber was found in an *Einstein* observation of MR2251–178, when the strength of the absorption was seen to change with time. This may have been due to neutral absorbing clouds passing across the line of sight, or have been caused by variations in the column density which occur in partially ionised material (Halpern, 1984). Further observations made with *ASCA* found a warm absorber in approximately half of a sample of 24 type 1 RQ and RL AGN, with the more luminous and/or radio-loud objects showing less ionised absorption (Reynolds, 1997). They are thought to be fast ($v \sim 0.2c$), highly ionised ($\log \xi \simeq 3 - 6$) outflows with high column densities ($N_{\text{H}} \simeq 10^{22} - 10^{24} \text{ cm}^{-2}$), possibly radiatively driven outflows from the molecular torus or accretion disc winds (Blustin et al., 2005). They can be identified with X-ray spectroscopy by searching for blueshifted lines (Pounds et al., 2003a,b; Reeves et al., 2003; Lobban et al., 2011; Gofford et al., 2011) and it is now thought that such energetic winds are common (Ganguly & Brotherton, 2008; Tombesi et al., 2010).

Reflection

The strong UV emission observed in AGN spectra is attributed to cold, optically thick material in the vicinity of the black hole such as, but not necessarily, the accretion disc. This is capable of reprocessing some fraction of the hard X-rays giving a reflection component in the spectrum. When the matter is illuminated by the power-law continuum, some photons are absorbed and others undergo Compton scattering to produce a broad reflection hump between 10 and 300 keV, peaking at $\sim 30 \text{ keV}$ with an amplitude approximately a factor of 2 above the underlying power-law emission (Lightman & White, 1988; Guilbert & Rees, 1988).

The first quantitative evidence for the reflection component came from studying a composite of 12 *Ginga* observations of 8 Seyfert AGN. A simple power-law fit gave $\Gamma = 1.7$ in addition to significant residuals attributed to an iron line at 6.4 keV and a reflection bump above 12 keV (Pounds et al., 1990). When reflection was included in the model a Γ value of 1.9 was obtained. Reflection features were then found to be common in further *Ginga* observations of Seyferts (Nandra & Pounds, 1994), but were not detected in *ASCA* observations of bright $z > 1$ quasars (Nandra et al., 1995). If the higher luminosity sources are also accreting at a higher rate, the inner regions of the disc may become ionised, thus reducing the amount of cold material available to produce a reflection feature (Mushotzky et al., 1993). However, *XMM-Newton* observations of the high luminosity RQQ PG1247+267 shows a large, $R = 2$, reflection component where the strength of the reflection is measured in terms of $R = \Omega/2\pi$ where Ω is the solid angle subtended by the reflector at the X-ray source. (Page et al., 2004b).

Iron Line

Evidence for an iron emission line at ~ 6 keV has been found in the X-ray spectra of both nearby Seyferts (Nandra et al., 1989; Pounds et al., 1989) and quasars (Turner et al., 1990; Kii et al., 1991). It is thought to arise when the primary X-ray emission irradiates part of the inner accretion disc, where the iron is not fully ionised even at temperatures of several million degrees. Whilst some of the photons are Compton scattered and produce the reflection component as described above, others can be absorbed by the inner electrons of the iron atoms. When the excited electron then decays from the $n = 2$ to $n = 1$ state, a photon with a rest energy of 6.4 keV is emitted creating the Fe $K\alpha$ emission line. Lines at other energies can occur in atoms of different ionisation states such as 6.9 keV for FeXXVI, which is almost fully ionised (H-like) iron. The Gaussian equivalent widths (EW) of the lines are generally $\sim 50 - 350$ eV (Mushotzky et al., 1993) as the gas velocity approaches the speed of light near to the event horizon of the black hole and relativistic and gravitational redshifts act to smear the line into a broadened feature. Observations of the Seyfert galaxy MCG-6-30-15 showed that the line was asymmetric in addition to being broad (Tanaka et al., 1995) and the shape of iron line profiles can be used to determine the spin of the black hole (Iwasawa et al.,

1996). The equivalent width of the Fe $K\alpha$ line has been shown to be inversely correlated with the X-ray luminosity in the 2 – 10 keV band, i.e. in higher luminosity sources, the line is narrower (Iwasawa & Taniguchi, 1993). Known as the X-ray Baldwin effect, this has been quantified by many people, with consistent results; $EW \propto L^{-0.17\pm0.08}$ (Page et al., 2004a), $EW \propto L^{-0.20\pm0.04}$ (Jiang et al., 2006) and $EW \propto L^{-0.17\pm0.03}$ (Bianchi et al., 2007b). It has been suggested that the primary relationship causing this effect is that between the equivalent width of the iron line and the accretion rate (Bianchi et al., 2007b; Winter et al., 2009).

Soft Excess

Early *EXOSAT* observations of the Seyfert galaxy MKN 841 revealed a soft X-ray component rising above the power law at energies below ~ 1 keV (Arnaud et al., 1985). Further observations with *EXOSAT* found this ‘soft excess’ to be present in 30 – 50% of hard X-ray selected Seyferts (Turner & Pounds, 1989), and observations with *ASCA* found it in $\sim 40\%$ (Reeves & Turner, 2000). It has also been suggested that this may be a ubiquitous feature in optically selected PG quasars (Porquet et al., 2004; Piconcelli et al., 2005), however these samples are biased towards bright and low redshift sources. The origin of this component is still a matter of debate. In particular, it is still not entirely clear whether it is due to an additional physical component, or whether it is just an apparent feature in the spectrum. It was originally explained as the high energy tail of the ‘big blue bump’ seen in the UV and hence blackbody emission from the inner accretion disc. However, as described in §1.1.1, for a $10^8 M_\odot$ black hole accreting at a tenth of the Eddington rate, the disc is expected to have a characteristic temperature of $kT \sim 0.02$ keV. This lies in the UV regime rather than the soft X-ray band and therefore the average kT values found are too high to be consistent with this model (Gierliński & Done, 2004). In addition, if the accretion disc origin is correct, then kT should correlate with the black hole mass and luminosity, but this is not seen (Gierliński & Done, 2004; Crummy et al., 2006; Bianchi et al., 2009; Winter et al., 2009). The soft excess could be generated by Comptonisation of the thermal disc emission. At least one Compton upscattering region consisting of hot electrons ($kT \sim 100$ keV) with a low optical depth ($\tau \sim 1$) has to be present in AGN to produce the hard power-law emission. In order to generate the soft excess, another popula-

tion of electrons is required with a lower temperature, (which remains a remarkably constant ~ 0.2 keV), and a higher optical depth. Therefore models need to include two separate Comptonising regions. This could be a radial transition in the disc (Magdziarz et al., 1998), a warm skin on the disc surface (Róžańska, 1999), a vertical disc-corona model with a two temperature plasma (Kawaguchi et al., 2001) or a hybrid thermal/non-thermal plasma (Vaughan et al., 2002). Recently, Done et al. (2012) have proposed a model in which the soft excess is generated from the intrinsic disc emission which is first shifted into soft X-ray energies due to a colour-temperature correction, required to account for the fact that the radiation may not completely thermalise, and is further Compton upscattered within the disc. Fig. 1.9 shows how the separate locations around the black hole relate to the parts of the spectrum which they produce. The outer accretion disc (red) between R_{out} and R_{corona} generates a colour-temperature corrected blackbody spectrum. These photons become the seeds for Compton upscattering which occurs in the inner disc (green) between R_{corona} and R_{ISCO} . The corona (blue) generates the hard power-law emission, and each of these components combine to generate the overall spectrum, which includes a soft excess, as shown in black in the spectrum. The colour-temperature correction is only substantial enough for this model to produce a soft excess in low mass, high accretion rate AGN.

Alternative explanations for the soft excess describe it as an apparent feature in the spectrum, rather than due to an additional component. Since the kT values observed are rather constant and cover a narrow range of values, $kT \sim 0.1 - 0.2$ keV, atomic processes which have fixed energies such as lines and edges of ionised OVII and OVIII may be responsible. If these features are then smeared by the high velocities and gravitational redshifts found close to a black hole, a smooth feature could be produced. Such a feature may be an artifact of ionised absorption seen through optically thin material in the line of sight, likely from an outflowing disc wind (Gierliński & Done, 2004), or could be due to relativistically blurred photoionised disc reflection from optically thick material out of the line of sight (Ross & Fabian, 2005; Crummy et al., 2006). Distinguishing between the two scenarios is difficult and has been the subject of many works (e.g. Chevallier et al. 2006; Done & Nayakshin 2007; Sobolewska & Done 2007).

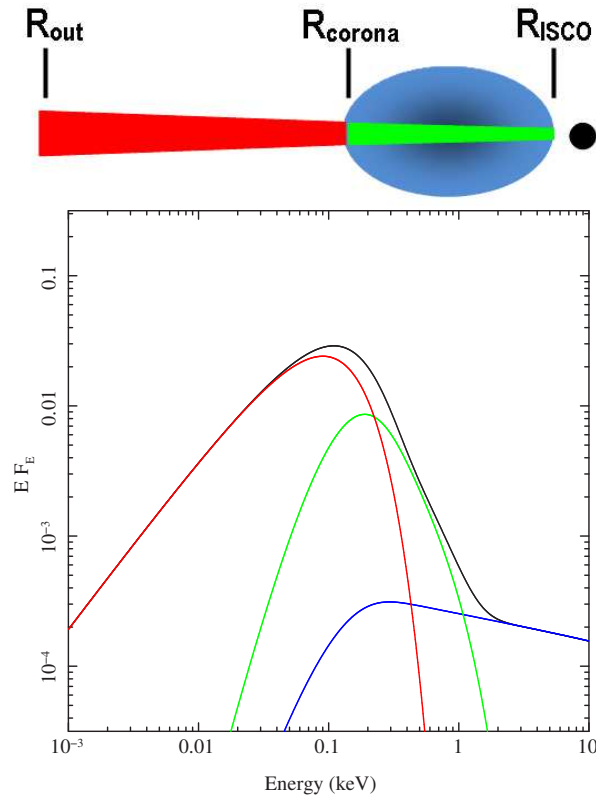


Figure 1.9: The red section of the disc generates a colour-temperature corrected blackbody, shown in red on the spectrum. Compton upscattering occurs within the green section of the disc, giving the green part of the spectrum and the blue corona generates the hard power-law shown in blue. These 3 components combine to make the overall spectrum shown in black. Modified from Done et al. (2012).

An alternative theory involves the high velocity, highly ionised outflows from AGN which can cause a strong shock in the ISM gas of the host galaxy when they interact (King, 2010). Subsequent Compton cooling of this gas may be observable as a soft X-ray component, as suggested in the case of NGC 4051 (Pounds & Vaughan, 2011).

1.1.4 AGN in a Wider Context

AGN have an important role in galaxy evolution. Only $\sim 1\%$ of the SMBH thought to reside in large galaxies are active (Kormendy & Richstone, 1995). Therefore, the process which triggers accretion is an important and unanswered question. It could be achieved by major mergers in which two comparably sized galaxies amalgamate (Kauffmann & Haehnelt, 2000), minor mergers in which a small companion galaxy is disrupted by a much larger one (De Robertis et al., 1998), or harassment in which dynamical instabilities are created in the galaxy as a result of high speed interactions as it passes close to other cluster members (Lake et al., 1998). These

scenarios predict that AGN should lie in high-density environments where the chances of a merger or galaxy interaction are increased. There have therefore been many studies which use clustering measurements in order to investigate the possibility that the large scale environment is responsible for triggering AGN activity. Optically selected AGN are found to be strongly clustered in the Sloan Digital Sky Survey (Shen et al., 2007) and the 2dF QSO redshift survey (Croom et al., 2005), with conflicting evidence for luminosity (Wake et al., 2004; Myers et al., 2006) or redshift dependent clustering (Myers et al., 2006; Shen et al., 2007). X-ray selected AGN were also found to be clustered, albeit less strongly than optically selected (Carrera et al., 1998), however more recent results from the XMM-COSMOS field found a clustering measurement of X-ray selected AGN significant at 18σ (Gilli et al., 2009). Other studies have focused on studying the morphology of the host galaxy to look for signs of a recent galaxy interaction. There is conflicting observational evidence with some studies reporting that host galaxies do show more disturbed morphologies than non-hosts and they have evidence for recent mergers (Rafanelli & Rifatto, 2000; Hutchings et al., 2002, 2009; Koss et al., 2010), and other studies reporting no difference in morphology or no evidence for mergers (Bahcall et al., 1997; Grogin et al., 2005; Gabor et al., 2009; Darg et al., 2010). Whilst a fuel supply is essential for AGN activity, the larger problem is that of angular momentum, as the material must lose 99.9% of it between $r = 10 \text{ kpc}$ and $r = 10 \text{ pc}$. This process is not completely understood, but may include gravitational torques (such as from large-scale bars and nuclear bars), dynamical friction (on gas clumps) or viscous torques and shocks (Jogee 2006; and references therein). In addition to fuelling AGN accretion, this movement of cold gas will also trigger large amounts of star formation which has been observed in the central regions of nearby AGN (e.g. Storchi-Bergmann et al. 2001, and references therein). A link between starburst and AGN activity is also demonstrated by their similar histories, with the peak of both occurring at $z \sim 2$ and the redshift distribution of strongly star-forming galaxies tracing that of optical quasars (e.g. Wardlow et al. 2011). The strength of starbursts has also been shown to correlate with AGN luminosity (Veilleux, 2008) and the AGN fraction is a strong function of star-formation rate (SFR) in distant galaxies (3 – 10% for SFR of $30 - 200 M_{\odot} \text{ yr}^{-1}$ and 10 – 40% for SFR of $100 - 500 M_{\odot} \text{ yr}^{-1}$; Alexander & Hickox 2012).

There are several observational relationships which also suggest that the growth of the black hole is linked to the evolution of its host galaxy. The mass of the SMBH correlates with both the luminosity of the galaxy bulge (Kormendy & Richstone, 1995; Kormendy et al., 2000; Kormendy & Gebhardt, 2001; McLure & Dunlop, 2002) and the mass of the galaxy bulge (Magorrian et al., 1998; Marconi & Hunt, 2003; Häring & Rix, 2004), with $M_{\text{BH}} = 0.006 M_{\text{bulge}}$ (Magorrian et al., 1998). Therefore extraordinary processes must be at work in order for a black hole with just $1/1000^{\text{th}}$ the mass of the galaxy to have a huge effect on its evolution. The $M - \sigma$ relation (see Eqn. 1.11), is a correlation between the mass of the central SMBH and the stellar velocity dispersion of the stars in the bulge of the host galaxy (Gebhardt et al., 2000; Ferrarese & Merritt, 2000).

$$M_{\text{BH}} = \alpha \times 10^8 M_{\odot} \left(\frac{\sigma}{200 \text{ kms}^{-1}} \right)^{\beta} \quad (1.11)$$

where $\alpha = 1.7 \pm 0.3$ and $\beta = 4.8 \pm 0.5$ (Ferrarese & Merritt, 2000)

or $\alpha = 1.2 \pm 0.2$ and $\beta = 3.8 \pm 0.3$ (Gebhardt et al., 2000)

This correlation is unlikely to be caused by a shared formation and evolutionary process alone, and is likely a consequence of regulatory feedback. If such feedback is to operate, a mechanism to transfer energy and momentum from the AGN to the bulge of the galaxy must be present and there is now much evidence for outflows capable of fulfilling this role. The term ‘wind’ is generally used to refer to a wide angle, sub-relativistic outflow and are identified as warm absorbers in the X-ray spectra of AGN (see §1.1.3). Broad Absorption Line Quasars (BALQSOs) are thought to be examples of AGN in which the continuum is viewed through such an outflow. King (2003) showed that super-Eddington accretion will produce outflows as any excess material above that which can be accreted due to the Eddington limit will be expelled in a wind with an outflow rate of $\dot{M}_{\text{out}} v \simeq L_{\text{Edd}}/c$. As the black hole grows, the Eddington limit and hence outflow velocity increases until reaching the escape velocity of the bulge, σ . At this point the gas is expelled and no further accretion is possible. This scenario naturally reproduces $M_{\text{BH}} \propto \sigma^4$, close to observed relation. The co-existence of AGN and starburst activity, and the tight relationships between the growth of the black hole and the

evolution of the host galaxy due to feedback support an overall galaxy evolution sequence in which AGN activity, triggered by a merger, is first obscured by the accompanying starburst. At the peak of the black hole accretion, feedback from the AGN then drives away the gas and dust, revealing an unobscured quasar and suppresses further star formation and black hole growth. When the gas is expelled completely, there is no star formation or AGN activity in the red old galaxy which remains (Sanders et al., 1988).

1.2 Overview of Thesis

In this thesis, the spectral properties of a large sample of type 1 AGN are studied. The sample was created from large archival X-ray and optical catalogues which are described in detail in Chapter 2, along with the various instrumentation used to collect the data, and the main X-ray spectral modelling techniques used. In Chapter 3 the X-ray spectral properties of the sample are studied in detail, with the aim of characterising the shape of a ‘typical’ source. Chapter 4 includes a discussion of a sub-set of sources which have unusual spectral shapes, in particular have either very flat or steep power-law slopes. In Chapter 5 simulations are used in order to quantify the detectability of additional spectral components, with respect to a simple power-law model, in X-ray spectra with a quality typical of that found from serendipitous X-ray surveys. In doing this, the intrinsic percentage of type 1 AGN which require a soft excess feature in the modelling of their X-ray spectra is determined. In Chapter 6 the sample is cross-correlated with multiwavelength archival data sets in order to create SEDs of the objects and investigate changes in their shape with different physical parameters. Chapter 7 summarises the main results of the thesis and offers suggestions for future studies.

2

Data Sources, Instrumentation and Analysis

This thesis studies the spectral properties of a large sample of AGN, created from a cross-correlation of X-ray and optical source catalogues. Chapters 3, 4 and 5 study their X-ray spectral properties, whilst Chapter 6 also uses multiwavelength data to create SEDs. This chapter describes each of the sources of data used, the procedure for generating the X-ray spectra and the main X-ray spectral modelling techniques.

2.1 X-ray Data

2.1.1 XMM-Newton Observatory

The X-ray Multi Mirror Observatory (*XMM-Newton*; Jansen et al. 2001) is a cornerstone mission of ESA's Horizon 2000 project. An artist's impression of the satellite is shown in Fig. 2.1. It was launched on December 10th 1999 into a highly elliptical, 48 hour orbit, which allows for a long period (~ 40 hours) of uninterrupted science observations. The satellite includes 3 X-ray telescopes with a focal length of 7.5 cm, each consisting of 58 nested Wolter I mirrors giving a large collecting area. They consist of a paraboloid and hyperboloid shape in order to give a shallow enough grazing angle to allow the reflection of high energy photons.

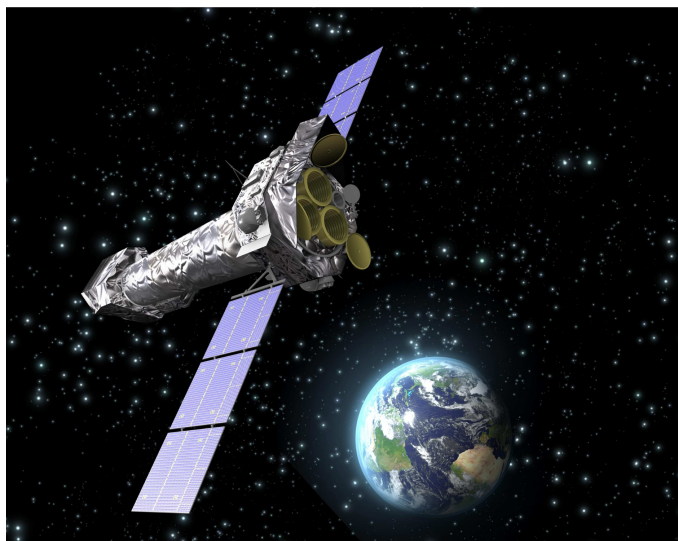


Figure 2.1: An artist's impression of *XMM-Newton*. Image courtesy of C. Carreau and ESA. Taken from <http://xmm.esac.esa.int>

Five detectors lie at the focal planes of the 3 X-ray telescopes. Two have a Reflection Grating Spectrometer (RGS; den Herder et al. 2001) and a Metal Oxide Semiconductor CCD (MOS; Turner 2001), and the remaining telescope has a pn CCD (Strüder et al., 2001), which together with the 2 MOS CCDs makes up the European Photon Imaging Camera (EPIC), described in more detail in §2.1.2. The RGS consists of 2 spectrometers sensitive over the energy range 0.33 – 2.50 keV with an high energy resolution of $E/\Delta E = 200 - 800$. The science instruments are operated simultaneously, although they work independently and can therefore be operated in different modes of data collection, and for different lengths of time.

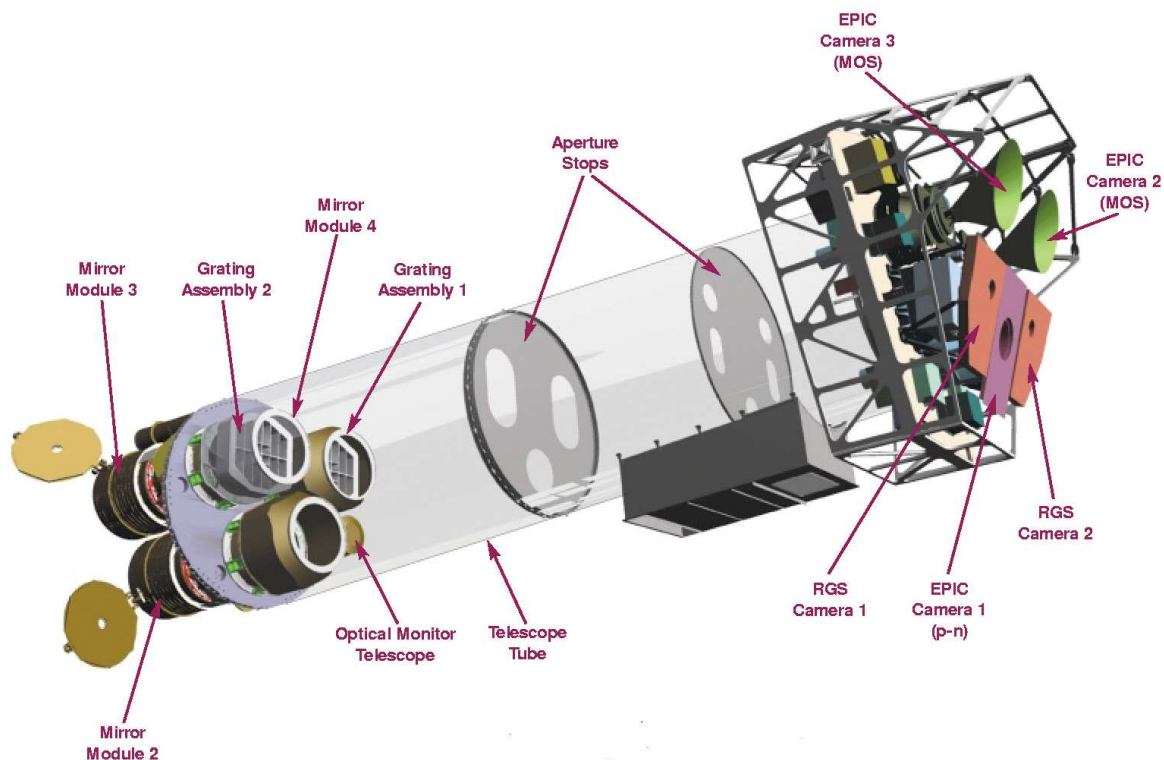


Figure 2.2: An internal view of *XMM-Newton* showing the various scientific instruments. Image courtesy of Dornier Satellitensysteme GmbH and ESA. Taken from <http://esapub.esrin.esa.it/bulletin/bullet100/>

XMM-Newton also includes a UV/Optical telescope, the Optical Monitor (OM; Mason et al. 2001) with a diameter of 30 cm. It is co-aligned with the X-ray telescopes and allows complimentary data to be collected in the wavelength range $\lambda = 1800 - 6000 \text{ \AA}$. An ‘open’ view showing the various telescopes and detectors can be seen in Fig. 2.2.

XMM-Newton is not the only X-ray telescope currently in operation. NASA’s *Chandra* (Weisskopf et al., 2000), also launched in 1999, is a dedicated X-ray telescope with an angular resolution ~ 10 times better than that of *XMM-Newton*. In 2005 JAXA launched the dedicated X-ray telescope, *Suzaku* (Mitsuda et al., 2007) and both the *Swift* (Gehrels et al., 2004) and *INTEGRAL* (Winkler et al., 2003) satellites carry telescopes sensitive in the X-ray regime. A comparison of the main properties of each of these telescopes can be found in Table 2.1. The main advantage of *XMM-Newton* is its large field of view which means that for each observation of a given target, a large number of other X-ray sources are observed serendipitously. This has led to the creation of serendipitous source catalogues which are described in §2.1.4 and are used in creating the sample of objects studied in this thesis.

Table 2.1: A comparison of the properties of the current major X-ray telescopes.

	<i>XMM-Newton</i> ^a (EPIC-MOS)	<i>Chandra</i> ^b (ACIS-I)	<i>Suzaku</i> ^c (XIS)	<i>INTEGRAL</i> ^d (JEM-X)	<i>Swift</i> ^e (XRT)
Energy Range	0.2 – 12 keV	0.2 – 10 keV	0.2 – 12 keV	3 – 35 keV	0.2 – 10 keV
Field of View	30'	16.9'	17.8'	4.8°	23'
Effective Area (at 1.5 keV)	400 cm ²	600 cm ²	350 cm ²	100 cm ² (at 10 keV)	110 cm ²
Energy Resolution (at 6.0 keV)	135 eV	280 eV	130 eV	171 eV	140 eV
Angular Resolution	5" (FWHM)	0.5"	2' (HPD)	3' (FWHM)	18" (HPD)
Timing Resolution	1.5 ms	3.2 s	8 s	0.1 ms	2.5 s (In PC Mode) ^f

ACIS = Advanced CCD Imaging Spectrometer
 XIS = X-ray Imaging Spectrometer
 JEM-X = Joint European X-ray Monitor
 XRT = X-ray Telescope
 HPD = Half Power Diameter
 PC = Photon Counting

^a*XMM-Newton* Users' Handbook
^b<http://cxc.harvard.edu/cal/Acis/index.html>
^cMitsuda et al. (2007)
^dLund et al. (2003)
^eGehrels et al. (2004)
^fhttp://heasarc.nasa.gov/docs/swift/proposals/swift_responses.html

2.1.2 EPIC

The X-ray data used in this thesis comes from the EPIC detectors, described in detail in the *XMM-Newton Users' Handbook* (Ed. M. Ehle). They are sensitive to the energy range 0.15 – 15 keV, have a moderate spectral resolution of $E/\Delta E = 20 - 50$ and an on-axis Point Spread Function (PSF) of $\sim 5'' - 6''$ at Full-Width Half-Maximum (FWHM). At large off-axis angles, the PSF becomes elongated due to aberration (astigmatism) and the effective area decreases as fewer photons entering the telescope actually reach the focal plane (vignetting).

The MOS detectors (shown in Fig. 2.3, left) consist of 7 front-illuminated CCDs, each with 600×600 pixels covering $10.9' \times 10.9'$. The 2 detectors are rotated 90° to each other so that the sky coverage lost due to the outer chip gaps in one detector are covered by the other detector. CCD 6 of MOS1 has been out of operation since March 2005 due to a micrometeoroid impact¹.

The pn detector (shown in Fig. 2.3, right) is a silicon wafer made up of 12 back-illuminated CCDs, each with 200×64 pixels covering an area of $13.6' \times 4.4'$. The pn is offset with respect to the optical axis of the telescope so that the on-axis position does not fall directly onto a chip gap. The layout of the CCDs in both the MOS and pn detectors are shown in Fig. 2.4. A comparison of the principal characteristics of the MOS and pn detectors can be found in Table 2.2.

The EPIC detectors can be operated in a range of different observing modes including large and small window mode, where only half of all 12 pn CCDs, or half of a single pn CCD is used, partial window where only part of the central MOS CCD is used, and timing or burst mode, where the MOS and pn detectors only image in 1D in order to speed up the read out time. Diagrams of these observing modes are in Fig. 2.5.

The EPIC detectors are also sensitive to IR, optical and UV photons which can lead to a contaminated X-ray signal if the target has a high optical flux. Therefore the detectors can be operated with different filters; 2 thin, 1 medium and 1 thick, as required. The use of a blocking filter also limits the response at the softest energies and naturally modifies the effective areas of the detectors as shown in Fig. 2.6.

¹http://xmm.esac.esa.int/external/xmm_news/items/MOS1-CCD6/



Figure 2.3: One of the MOS detectors (left) and the pn detector (right). Images taken from <http://xmm.esac.esa.int/> and courtesy of Leicester University, University of Birmingham, CEA Saclay Service d'Astrophysique, MPI-semiconductor laboratory, MPE, Astronomisches Institut Tübingen, Germany and ESA.

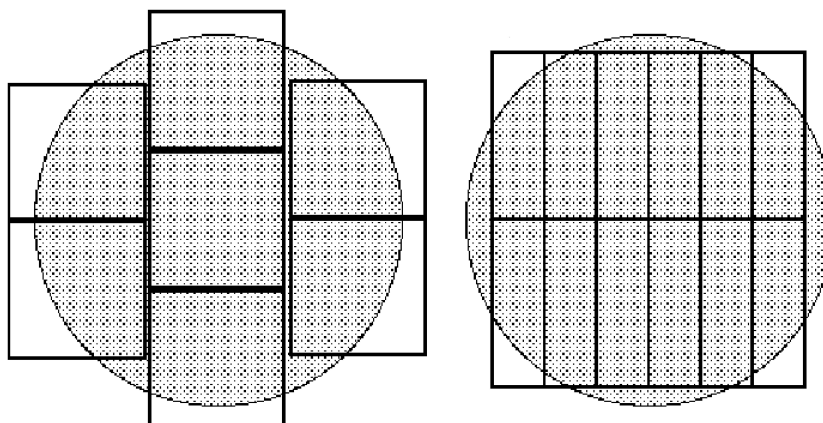


Figure 2.4: The layout of the CCDs in the MOS detectors (left) and in the pn detector (right). Image from <http://xmm.esac.esa.int>

Characteristic	EPIC MOS	EPIC pn
PSF (FWHM)	5''	6''
Pixel Size	1.1''	4.1''
Timing Resolution (in timing mode)	1.5 ms	0.03 ms
Energy Resolution (at 1.5 keV)	~ 90 eV	~ 120 eV
(at 6 keV)	~ 135 eV	~ 160 eV
Readout Time	2.5 s	0.08 s
Effective Area (at 1 keV)	~ 300 cm ²	~ 800 cm ²

Table 2.2: Principal characteristics of the two EPIC detectors

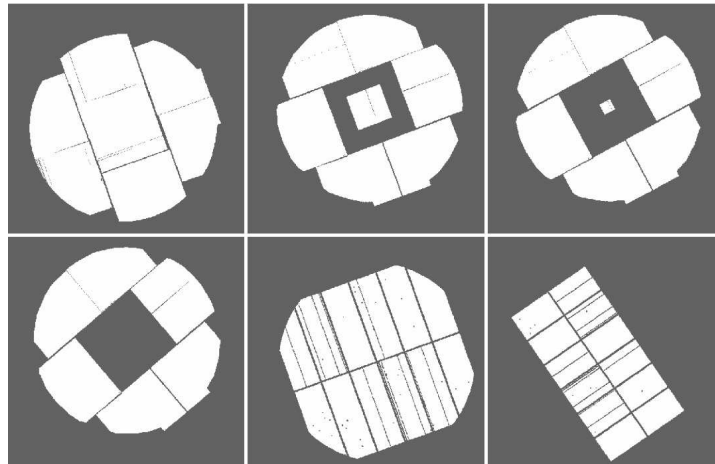


Figure 2.5: The different observing modes of the EPIC detectors. Top row (l-r): MOS full window mode, MOS with large central window, MOS with small central window. Bottom row (l-r): MOS with central CCD in timing mode, pn full window mode, pn large window mode. Image from Watson et al. (2009).

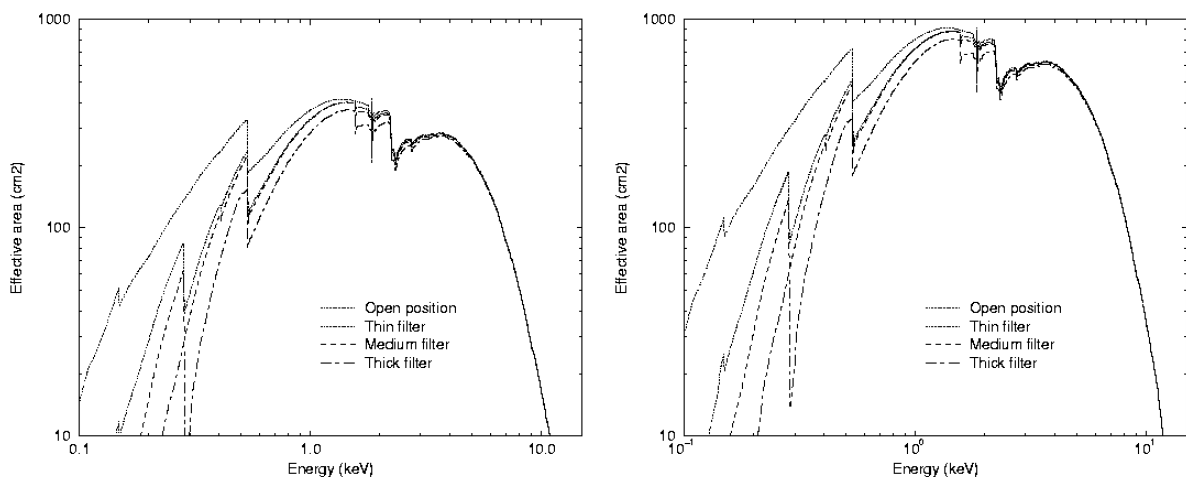


Figure 2.6: These show the effective area of each of the EPIC detectors (Left = MOS, right = pn), and how this varies with the use of each of the different optical blocking filters. Image from http://xmm.esac.esa.int/external/xmm_user_support/documentation/uhb_2.1/node32.html

2.1.3 Data Processing

The data from *XMM-Newton* observations are available both as an ODF (Observational Data File) which contains the uncalibrated science telemetry from all instruments, or as PPS files which are generated by the Pipeline Processing Subsystem created by the SSC (Survey Science Centre²) made up of various SAS³ tasks. In order to convert the files from the ODF to PPS, a CCF (Current Calibration File) is required, which describes the performance of the instruments at the time the observation was made. PPS files include detector and sky images, source lists, exposure maps, background time series, along with cleaned and calibrated event lists.

Such lists include the position of the event (i.e. which pixel the photon arrived at), the arrival time, the pulse height (which relates to the energy), the shape of the event (which can be used to separate X-rays from particles) and the type of event, which describes how the charge cloud generated by the in-falling X-ray is distributed over the pixels. PATTERN = 0 describes a single pixel event, [1 : 4] = double, [5 : 8] = triple and [9 : 12] = quadruple. For the data used in this thesis, all events up to quadruple pixel registered in the MOS cameras are used (i.e. PATTERN ≤ 12) but only single and double events are used from the pn (PATTERN ≤ 4) as the raw pixel size is larger, so any triple and quadruple events are less likely to have been generated by cosmic X-ray photons.

Each event is also assigned a quality flag to allow the removal of photons which hit the detector in a poor location. The best quality events are given FLAG = 0, with events next to a bad pixel or towards the edge of the CCD given FLAG > 0 as these may result in charge loss. In the data reduction, only events with FLAG = 0 are used from the pn camera and #XMMEA_EM is used to screen events from the MOS camera which are near to hot pixels or chip edges and to remove bad rows, edge effects and cosmic ray events.

The EPIC detectors can also suffer from pile-up; the accumulation of events on the same pixel during the read-out time of the CCD. These cases are then interpreted as a single event resulting in spectral distortion and a loss of flux. This is likely to occur if the count rate exceeds 0.7 cts s⁻¹ in the MOS detector or 8 cts s⁻¹ in the pn (both in full frame mode). Out-of-Time (OoT) events can occur if there is a bright source in the field. Stripes leading from the source

²<http://xmmssc-www.star.le.ac.uk/>

³The description and documentation are available online at <http://xmm.esac.esa.int/sas/>

to the CCD readout node appear due to the detector continuing to record data during the brief time when the chip is being read out by the electronics.

The background signal detected by EPIC is due to two main components, the Cosmic X-ray Background (CXB) and an instrumental component, which is itself composed of a relatively quiescent component due to high energy ($E > 100$ MeV) particles interacting with the detector structure, and a flaring component due to soft protons ($E < 100$ keV) which are produced by magnetic reconnection in the Earth's magnetosphere and are funnelled towards the detectors by the X-ray mirrors. Typical values of the quiescent background rate in the 2–7 keV band are ~ 0.002 cts s^{-1} cm^{-2} keV $^{-1}$ in the MOS camera and ~ 0.005 cts s^{-1} cm^{-2} keV $^{-1}$ in the pn. The SAS task `tabgtigen` is used to create a GTI (Good Time Interval) file which specifies the observation time in which no high flaring is occurring and science products can be extracted. This is done by extracting times when the count rate is < 0.35 cts s^{-1} for MOS and < 0.4 cts s^{-1} for pn in a high energy light curve where the contribution from the X-ray source is low.

The SAS task `eregionanalyse` is used to define a region around the source and a background region from which to extract X-ray spectra. They are chosen in order to optimise the signal to noise (S/N). The SAS task `arfgen` is used to generate the auxiliary response file (ARF) describing the instrument's effective area, which is a function of energy and varies depending on any filters used. The redistribution matrix (RMF) describes the probability that a photon of a given energy will be registered in a given channel. This is generated by the SAS task `rmfgen`.

2.1.4 2XMMi Catalogue

The advantage of the 30' field of view of *XMM-Newton* is that during any pointed observation, data from other X-ray sources in the field is collected in addition to that of the target. This data is published in serendipitous source catalogues created by the SSC, and several incremental releases of the catalogue have now been made (see Table 2.3). These catalogues are an invaluable resource for creating large samples of AGN with an X-ray detection.

The version of the catalogue used here is 2XMMi released in August 2008. It includes data

Catalogue	Release Date	Observation Dates	Number of Observations	Number of Detections	Unique Sources	Sky Coverage
1XMM	Apr 2003	Mar 01 – May 02	585	33026	28279	50 deg ²
2XMMp	Jul 2006	Feb 00 – Apr 06	2400	153105	123170	285 deg ²
2XMM	Aug 2007	Feb 00 – Mar 07	3491	246897	191870	360 deg ²
2XMMi	Aug 2008	Feb 00 – Mar 08	4117	289083	221012	420 deg ²
2XMMi-DR3	Apr 2010	Feb 00 – Oct 09	4953	353191	262902	504 deg ²

Table 2.3: Details of the different serendipitous source catalogue releases.

from both the target and non-target sources taken in 4117 pointed *XMM-Newton* EPIC observations from Feb 2000 to March 2008 covering a non-overlapping sky area of ~ 420 deg². It contains 289,083 detections, which due to field duplication by multiple observations, corresponds to 221,012 unique sources. This provides a 17% increase in the number of detections from the 2XMM catalogue and is one of the largest X-ray source catalogues ever produced, although its size has now been surpassed by 2XMMi-DR3⁴. The median flux of the catalogue detections in the 0.2 – 12.0 keV energy band is $\sim 2.5 \times 10^{-14}$ erg cm⁻² s⁻¹ and about 20% of the sources have total fluxes below 1×10^{-14} erg cm⁻² s⁻¹. The catalogue includes the flux detected from the sources in a number of different energy bands, the exposure lengths of the observations, the operating mode of the CCDs, any filters in use and the X-ray positions which have accuracies of typically 1 – 2''.

2.2 X-ray Spectral Analysis

In Chapters 3 & 4, the X-ray spectra of the AGN sample are fit with a number of different models. By comparing such physically motivated models to the spectral shapes observed, the intrinsic properties of the sources can be inferred.

2.2.1 Principles of XSPEC

Raw X-ray spectra consist of a number of photon counts (C) falling within specific channels (I). The observed spectrum $C(I)$ is related to the actual spectrum of the source, $f(E)$ by

⁴3XMM, due for release by the end of 2012 is expected to contain $\sim 330,000$ unique sources and will use an updated processing pipeline.

Eqn. 2.1 where $R(I, E)$ is the instrument response (defined by the RMF and ARF files) and is proportional to the probability that an incoming photon of energy E will be detected in the channel I .

$$C(I) = \int_0^{\infty} f(E)R(I, E) dE. \quad (2.1)$$

An inversion of this equation is required to find $f(E)$, however this is not possible as it returns non-unique solutions. The X-ray spectral fitting in this thesis is carried out using XSPEC version 11.3.2 (Arnaud, 1996) which uses a predicted model spectrum described in terms of a few parameters i.e. $f(E, p1, p2)$, to generate a predicted count spectrum $C_P(I)$, which is compared to $C(I)$ using a least-squared fitting technique⁵. The best-fitting model is found when the χ^2 statistic (see Eqn. 2.2⁶) is minimised by varying the model parameters.

$$\chi^2 = \sum \frac{[C(I) - C_P(I)]^2}{\sigma(I)^2} \quad (2.2)$$

The null hypothesis probability (H0), calculated from both χ^2 and the number of degrees of freedom, ν , is used to determine whether a particular model gives a good fit to the data. In this thesis a probability < 0.01 is chosen to indicate a poor fit. This means that if the model was a good fit to the data, such an extreme value of χ^2 would only be expected to occur 1% of the time by chance. The confidence interval for a given parameter is found by varying its value until χ^2 changes by a fixed amount; $\Delta\chi^2 = 2.706$ for the 90% confidence level on one interesting parameter. In order to ensure that χ^2 statistics are valid, the spectra are first binned to a minimum of 15 counts per bin. This is done using the Ftool⁷ `grppha`.

2.2.2 Main Models

This section describes the main models used in the X-ray spectral fitting procedures described in Chapters 3 & 4.

⁵The default is Levenberg-Marquardt which is based on CURFIT from Bevington (1969).

⁶ $\sigma(I)$ is the error for channel I assuming Poissonian statistics.

⁷<http://heasarc.gsfc.nasa.gov/docs/software/ftools/>

Power Law

The underlying X-ray spectrum of an AGN is thought to be a simple power law. This is described by Eqn. 2.3 where Γ is the dimensionless photon index of the power law and K is the normalisation in photons $\text{keV}^{-1} \text{cm}^{-2} \text{s}^{-1}$ at 1 keV. This is described in XSPEC by the model `pl`. The shape of the model is shown in Fig. 2.7 (top left).

$$A(E) = KE^{-\Gamma} \quad (2.3)$$

Absorption

Photoelectric absorption is modelled by `zphabs` in XSPEC and is described by Eqn. 2.4 where N_{H} is the equivalent hydrogen column density in units of $10^{22} \text{atoms cm}^{-2}$. The abundances used are those of Wilms et al. (2000) and the cross-sections used are those of Balucinska-Church & McCammon (1992). This model is used in a multiplicative way with the underlying power law, the result of which is seen in Fig. 2.7 (top right). In subsequent chapters, `zphabs` is used to model intrinsic absorption at the redshift of the source, however every model also includes a non-redshift dependent component, `phabs`, in order to model the Galactic absorption due to the ISM of the Milky Way.

$$M(E) = \exp[-N_{\text{H}}\sigma(E[1+z])] \quad (2.4)$$

Blackbody

A blackbody component is modelled with the `zbbbody` command and is shown added to a power law in Fig. 2.7 (middle left). This is the model used to model soft X-ray excesses in the sources. It is described by Eqn. 2.5 where $K = L_{39}/[D_{10}(1+z)]^2$ and L_{39} is the luminosity in units of $10^{39} \text{erg s}^{-1}$ and D_{10} is the distance in units of 10 kpc. This model is also added to an absorbed power law as shown in Fig. 2.7 (middle right).

$$A(E) = \frac{8.0525 K [E(1+z)]^2 dE}{(1+z)kT^4 \left[\exp\left(\frac{E(1+z)}{kT}\right) - 1 \right]} \quad (2.5)$$

Gaussian

In order to model any iron lines which may be present in the spectra, a Gaussian is added to the underlying power-law model. This can be seen in Fig. 2.7 (bottom). The Gaussian is described by Eqn. 2.6 where E_L gives the line energy in keV, σ gives the line width in keV and K is the normalisation which gives the total number of photons $\text{cm}^{-2} \text{s}^{-1}$ in the line.

$$A(E) = \frac{K}{\sqrt{2\pi}\sigma^2(1+z)} \exp\left(\frac{1}{2} \left[\frac{E(1+z) - E_L}{\sigma}\right]^2\right) \quad (2.6)$$

Partially Ionised and Partially Covering Absorption

The absorbed power-law model, `apo`, models a neutral, fully covering absorbing material. The model `zpcfabs` allows the effects of a partially covering, neutral absorber to be considered. It is described by Eqn. 2.7 where f is the covering fraction with values ranging from 0 to 1. The models created for different values of f are shown in Fig. 2.8.

$$M(E) = f \exp[-N_H \sigma(E[1+z])] + (1-f) \quad (2.7)$$

The model `zxipcf` (Reeves et al., 2008) models the effects of a partially covering, partially ionised material. It includes the free parameters of z , equivalent hydrogen column density N_H , covering fraction f and ionisation parameter ξ which is given by Eqn. 2.8 where L is the ionising luminosity, n is the electron density and r is the distance to the ionising source.

$$\xi = \frac{L}{nr^2} \quad (2.8)$$

Fig. 2.9 (bottom left) shows the model when $f = 1.0$, $N_H = 5 \times 10^{22} \text{cm}^{-2}$, and $\log \xi = -3$. This models an absorber which is close to neutral and therefore absorbs all the emission in a similar way to the `apo` model. Fig. 2.9 (bottom right) also fixes f and N_H , but sets $\log \xi = +6$ to model a fully ionised absorber. In this case few atoms are left to absorb any photons, and the majority of the emission is let through as if no absorber was present. Fig. 2.9 (top) shows the partially ionised (although fully covering model). A strong jump in opacity can be seen at $\sim 0.7 \text{keV}$ creating an apparent soft excess at low energies.

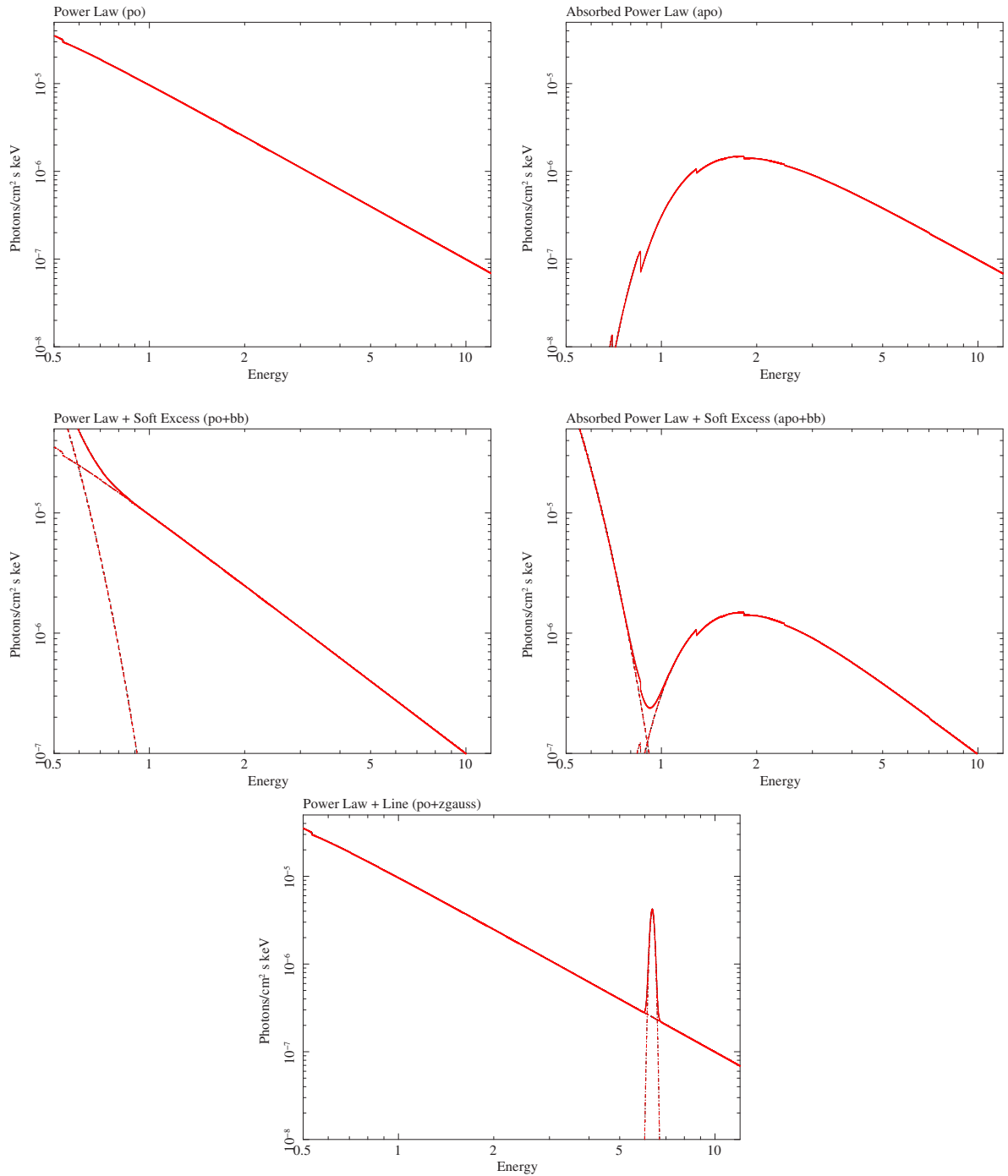


Figure 2.7: Top left - The simple power-law model (po). Top right - The absorbed power-law model (apo). Middle left - The power law + blackbody model (po+bb) used to model the soft excess. Middle right - The absorbed power law + soft excess model (apo+bb). Bottom - The simple power-law model with an additional Gaussian to model the Fe $K\alpha$ line at $E_{\text{rest}} = 6.4$ keV.

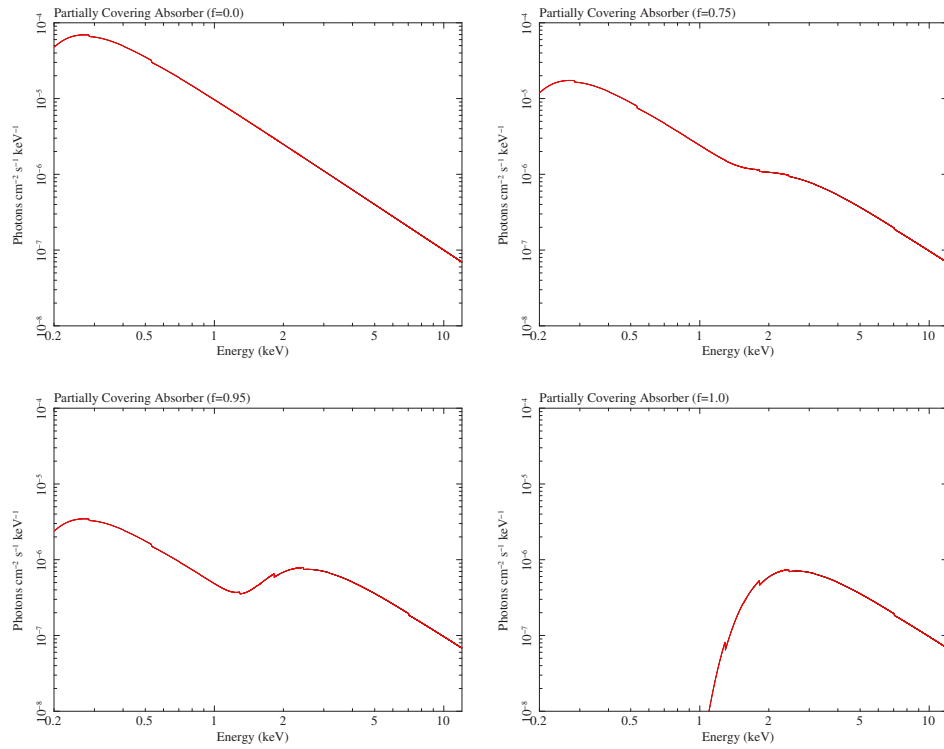


Figure 2.8: This shows the partially covering absorption model for $f = 0.0$ which models no absorption, $f = 0.75$, $f = 0.95$ and $f = 1.0$ which models a fully covering absorber and hence gives the same results as the apo model. N_{H} is fixed at $5 \times 10^{22} \text{ cm}^{-2}$ in each case.

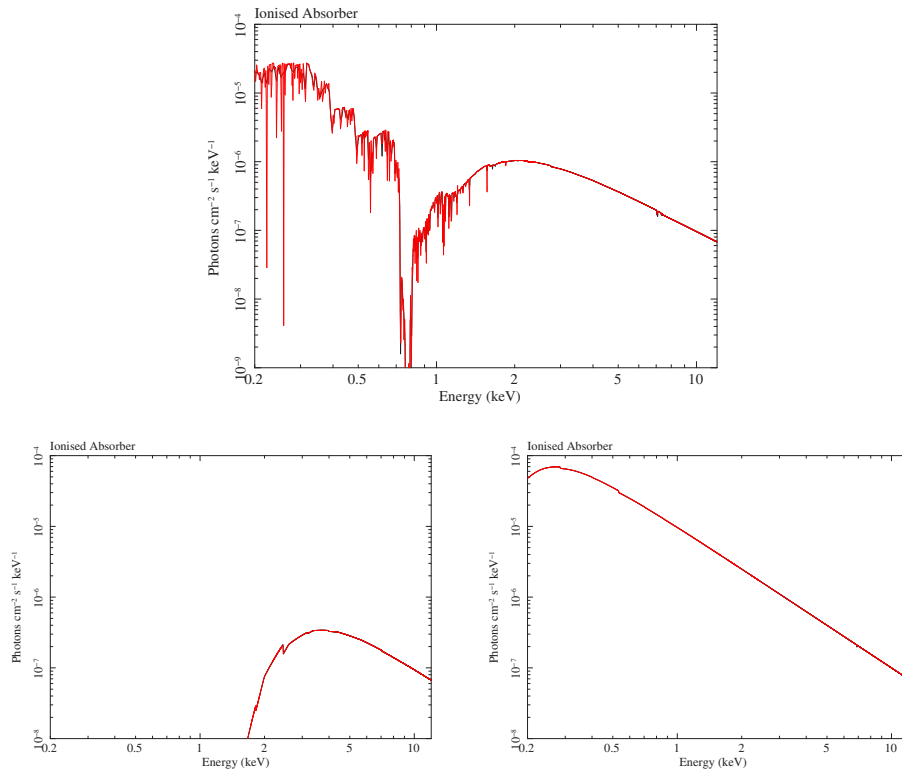


Figure 2.9: This shows the ionised absorber model. In each case f is fixed at 1.0 and N_{H} is fixed at $5 \times 10^{22} \text{ cm}^{-2}$. Top: $\log \xi = 1$, showing a partially ionised absorber. Bottom left: $\log \xi = -3$, showing a neutral absorber. Bottom right: $\log \xi = +6$, showing a fully ionised absorber.

2.3 Optical Data

2.3.1 Sloan Digital Sky Survey

The Sloan Digital Sky Survey (SDSS; York 2000) began in 2000 and has provided optical imaging and spectroscopy over a quarter of the sky. It uses a dedicated 2.5 m wide angle telescope at Apache Point, New Mexico, which has a large secondary mirror and correcting lenses to achieve a 3° field of view without distortion (Gunn et al., 2006).

The photometric camera (Gunn et al., 1998) consists of 30 CCDs with 2048×2048 pixels in each. The CCDs are arranged in 5 rows, such that when the telescope is in drift-scan mode the objects being observed move along the columns of CCDs and the data is read out at the same rate. Each detector row also corresponds to a different filter, so that the camera produces 5 images of each object, one per filter. The 5 SDSS imaging bands, *ugriz*, cover a wavelength range of $3000\text{--}11000\text{\AA}$ with the central wavelength of each filter being 3500\AA , 4800\AA , 6250\AA , 7700\AA and 9100\AA respectively (Fukugita et al., 1996). The 95% completeness limits for the detection of point sources are: $u = 22.0$ mag, $g = 22.2$ mag, $r = 22.2$ mag, $i = 21.3$ mag, $z = 20.5$ mag. The SDSS photometry is intended to be on the AB system (Oke & Gunn, 1983) such that a magnitude 0 object should have same counts as a source of $F_\nu = 3631$ Jy. However in reality the *u* and *z* bands require a slight correction: $u_{AB} = u_{SDSS} - 0.04$ mag, $g_{AB} = g_{SDSS}$, $r_{AB} = r_{SDSS}$, $i_{AB} = i_{SDSS}$, $z_{AB} = z_{SDSS} + 0.02$ mag. Each source is morphologically classified; extended sources as ‘galaxy’, and point sources, which includes quasars, as ‘stars’.

SDSS also has 2 spectrometers⁸ which are each fed light from the focal plane by 320 optical fibers, allowing spectroscopy of more than 600 objects in a single pointing. The light into each spectrograph is split by a dichroic filter directing it into separate blue ($3900\text{--}6100\text{\AA}$) and red ($5900\text{--}9100\text{\AA}$) channels. 4 CCDs of 2048×2048 pixels are used, one for each channel of the spectrograph, giving a spectral resolution of $\lambda/\Delta\lambda = 2000$.

SDSS DR5 (Adelman-McCarthy, 2007) includes all data collected in the first phase SDSS-I, which ran between 2000 and 2005. It is the fifth data release, also incorporating DR1–4. It

⁸<http://www.astro.princeton.edu/PBOOK/spectro/spectro.htm>

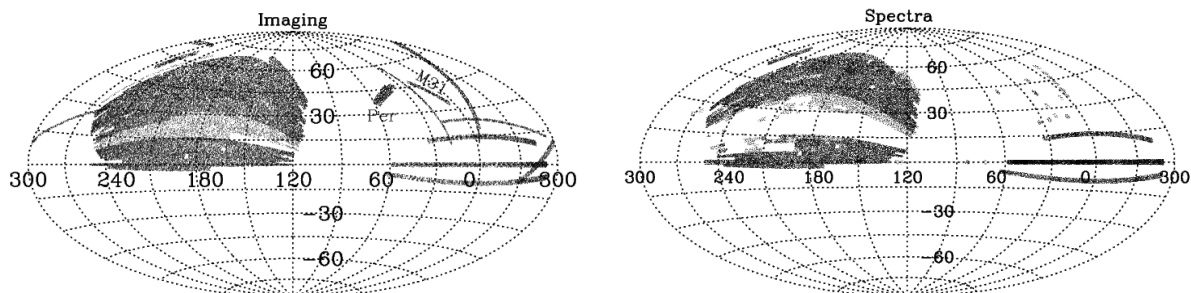


Figure 2.10: This shows the photometric (left) and spectroscopic (right) sky coverage of the DR5 data release, covering the north galactic cap and equatorial stripes. Areas which are new to this release are shown in lighter shading (Adelman-McCarthy, 2007).

includes photometric data for 217 million objects over a sky area of 8000 deg^2 (shown in Fig. 2.10, left) and spectra of ~ 1 million objects covering a sky area of 5713 deg^2 (Fig. 2.10, right). SDSS is now in the third phase of its operation and the latest release DR8 contains ~ 470 million unique objects (SDSS-III collaboration: Hiroaki Aihara et al., 2011).

2.3.2 DR5 Quasar Catalogue

The DR5 quasar catalogue (Schneider et al., 2007) includes 77429 objects selected from the fifth data release of SDSS (Adelman-McCarthy, 2007)⁹. Quasar candidates are primarily selected for spectroscopic follow up based on their location in multidimensional SDSS colour space, however others are selected if they lie within $2.0''$ of a FIRST (Becker et al., 1995) radio source, introducing a possible radio bias into the catalogue. Similarly some sources are included due to their inclusion in the *ROSAT* All Sky Survey's Bright and Faint source catalogues (Voges et al., 1999). A difficulty with the colour selection procedure arises for quasars between redshifts 2.2 and 3.0, where their broadband colours become indistinguishable from early F and late A type stars. To account for this, additional objects are specifically targeted in this range to avoid a low completeness in the catalogue (Richards et al., 2002). The objects are required to have an absolute i band magnitude brighter than -22 , an apparent i band PSF magnitude fainter than 15 and a reliable redshift. They also require at least one emission line in their spectra with a $\text{FWHM} > 1000 \text{ km s}^{-1}$, or interesting/complex absorption features. This means that the catalogue includes type 1 AGN, rather than type 2 or blazars but does include

⁹An updated quasar catalogue based on data from releases DR1-DR7 has now been released containing 105,783 quasars (Schneider et al., 2010).

Broad Absorption Line Quasars (BALQSOs). The catalogue includes spectroscopic redshifts (ranging from 0.08 to 5.41), positions accurate to better than $0.2''$ per co-ordinate, the *ugriz* photometry with a typical accuracy of 0.03 mag, and multiwavelength detections by FIRST (Becker et al., 1995), *ROSAT* (Voges et al., 1999) and 2MASS (Two Micron All Sky Survey; Skrutskie et al. 2006) where available. The spectra for each object cover a wavelength range of $3800 - 9200 \text{ \AA}$ with a spectral resolution of 2000.

2.4 Multiwavelength Data

2.4.1 FIRST

The FIRST (Faint Images of the Radio Sky at Twenty centimetres) survey is produced by the NRAO Very Large Array (VLA) at a frequency of 1.4 GHz, with an angular resolution of $5.4''$ (Becker et al., 1995). The survey covers two areas, chosen to match the footprint of SDSS. The reported source positions are accurate to $\sim 1''$ if the source is detected at the catalogue detection limit ($\sim 1 \text{ mJy}$), increasing to $0.5''$ for a 2 mJy source in a region with a typical noise level. Systematic errors in the positions are less than $0.05''$. The RMS gives an estimate of the local noise at the source position, and is typically $\sim 0.15 \text{ mJy}$ per beam. If a source is detected with a flux greater than $5 \times \text{RMS}$, it is recorded as a significant detection and is included in the FIRST catalogue¹⁰ which includes 816,331 sources. There are ~ 90 sources per square degree, and $\sim 30\%$ have counterparts in SDSS. The catalogue reports both the peak flux density (in mJy per beam) and the integrated flux density (in mJy) for each source, where the uncertainty in the peak flux is given by the RMS noise at that position. The probability that a source is a spurious detection, such as a side-lobe of a nearby source, is also given, with $\sim 78\%$ of sources having probabilities less than 5% , suggesting they are unlikely to be spurious.

¹⁰Available from <http://sundog.stsci.edu>

2.4.2 GALEX

The Galaxy Evolution Explorer (*GALEX*; Morrissey et al. 2007) launched in 2003, is a space-borne telescope operating in the ultraviolet (UV). It has 2 detectors sensitive to different wavelengths; 1344 – 1786Å (Far-UV)¹¹ and 1771 – 2831Å (Near-UV), for which the effective wavelengths are 1538.6 Å (FUV) and 2315.7 Å (NUV). The astrometry is $\sim 0.5'' - 0.6''$ and the image resolution is 4.2'' (FUV) and 5.3'' (NUV). It is conducting whole sky imaging, aided by its large, (1.25 deg²) field of view. The All Sky Imaging Survey (AIS) has a limiting magnitude of $m_{AB} = 20.5$ and covers ~ 26000 deg², whilst the Medium survey (MIS) has a limiting magnitude of $m_{AB} = 23.5$, but only covers ~ 1000 deg², however, the MIS survey footprint was chosen to match the area covered by SDSS. In addition, to the all sky surveys, *GALEX* also conducts pointed observations of interesting targets e.g. the COSMOS and DEEP fields which are covered by the Deep Imaging Survey (DIS) to a magnitude limit of $m_{AB} \sim 25$. A guest observer program is also available. The current data release used in this thesis (GR6) was completed on Nov 11 2010 and includes 28,889 tiles; some new and some re-processed from GR4/5. All *GALEX* observations are expected to end on Sep 30th 2012.

2.4.3 2MASS

The Two-Micron All-Sky Survey (2MASS; Skrutskie et al. 2006) is an all sky survey in the near-infrared (NIR) conducted between 1997/8 and 2001. It was carried out by two 1.3 m telescopes, one in Mt. Hopkins, Arizona to survey the northern hemisphere and another at the Cerro Tololo Inter-American Observatory, Chile to survey the southern hemisphere. The telescopes have a 3 channel camera, with each channel consisting of a 256×256 array of detectors, capable of observing in each of 3 wavebands, J (1.25 μ m), H (1.65 μ m) and K (2.17 μ m), simultaneously. The point source catalogue produced from the All Sky Data released in March 2003, includes positions and photometry for 470,992,970 objects. It comprises 2 sub-sets of data, the ‘high reliability catalogue’ which requires a detection with S/N greater than 10 and is 99.998% complete to the magnitude levels of 15.8 (J), 15.1 (H), 14.3 (K), and the ‘faint extension’ which includes detections with S/N > 7 and thus sources ~ 1 magnitude fainter.

¹¹The FUV camera is no longer operational.

2.4.4 *WISE*

The Wide-field Infrared Survey Explorer (*WISE*; Wright et al. 2010) is a space-borne, 16 inch telescope with a field of view $47'$ wide. It was launched in December 2009 to survey the entire sky in 4 mid-infrared (MIR) wavebands; $3.4 \mu\text{m}$, $4.6 \mu\text{m}$, $12 \mu\text{m}$ and $22 \mu\text{m}$. It has a resolution of $6''$ in $3.4 \mu\text{m}$, $4.6 \mu\text{m}$ and $12 \mu\text{m}$ and $12''$ at $22 \mu\text{m}$ and 5σ point source sensitivities better than 0.08, 0.11, 1 and 6 mJy for each of the bands. The all sky data release made on March 14th 2012 includes all the data taken during the full cryogenic mission phase between 07/01/10 and 06/08/10. The source catalogue includes 563,921,584 objects detected with $S/N > 5$.

3

X-ray Spectral Properties of a Large Sample of Type 1 AGN

The X-ray emission of AGN is produced in the innermost regions of the source, by the accretion of matter onto a supermassive black hole as described in more detail in Chapter 1. Studying the shape of the X-ray spectra produced can aid our understanding of the accretion process and the physical conditions surrounding the black hole, as different features seen in them correspond to different physical processes occurring. In this Chapter a detailed characterization of the X-ray spectral properties of a large sample of type 1 AGN is presented. The aim is to provide a complete description of the spectral shape of a ‘typical’ source and the distribution of spectral properties within the population of type 1 AGN.

3.1 Introduction

The basic X-ray spectral shape of type 1 AGN consists of a power law, $P_E \propto E^{-\Gamma}$, with spectral index, Γ , the value of which is dependent upon the physical process creating the X-ray emission. It is therefore important to constrain the average Γ value for typical sources, and determine the intrinsic spread of values allowed for this parameter in order to understand the physics occurring in the sources. Some spectral indices are found to be significantly different from the majority, and may be indicative of a peculiar form of accretion or interesting physical processes in the system. These objects will be discussed in more detail in Chapter 4, whilst the properties of the main population are described here.

Much of our understanding of the X-ray emission mechanisms of AGN to date has come from detailed studies of individual, bright AGN, which reveal significant spectral complexities (e.g. Pounds et al. 2004). Whilst these high S/N spectra provide very detailed descriptions of the sources, only a handful can be studied in this way, leading to an unrepresentative sample. By considering sufficiently large numbers of objects, the full range of spectral properties possible can be deduced, along with source-to-source variations which are necessary for describing the population as a whole. The main disadvantage of large sample studies, is that the spectra tend to be of a much lower quality which allows only relatively simple models to be fit. The limiting effect of spectral quality on the detectability of spectral components is explored further in Chapter 5.

Previous works have also investigated the X-ray spectral properties of type 1 AGN using large samples. Bianchi et al. (2009) investigate the X-ray spectral properties of ~ 160 AGN from targeted *XMM-Newton* observations. This sample has the advantage of high S/N X-ray spectra, however it is also biased towards sources at low redshift (90% of their sources are at $z < 1$). Since *XMM-Newton* targets have been used, the sample contains objects observed for a number of different reasons, and hence does not represent a uniform sample of AGN. Mateos et al. (2010) present an X-ray spectral analysis of ~ 500 type 1 AGN from the *XMM-Newton* Wide Angle Survey (XWAS). The overall broad-band properties and their dependences on X-ray luminosity and redshift are investigated, offering a complete picture of the X-ray spectral properties of an X-ray selected sample of type 1 AGN. Young et al. (2009)

present an optically selected sample of ~ 500 objects by cross-correlating the Sloan Digital Sky Survey (SDSS; York 2000) and the *XMM-Newton* archive. They fit only simple power law and absorbed power-law models to their spectra and include only ~ 300 sources in their investigation of Γ with L_X . It is possible that by restricting their sample to the higher S/N sources, they have introduced a bias towards lower redshift objects, or the most X-ray luminous higher redshift sources.

This Chapter describes the analysis of the X-ray spectra of the largest sample of type 1 AGN to date (~ 750). They are optically selected from SDSS and also have observations taken by *XMM-Newton*. Spectral models are fit to each of the sources over an energy range of 0.5 – 12.0 keV, including ones to model any soft excess components or intrinsic cold absorption. The best-fitting model is chosen for each source via the F-test. The average power-law slope and intrinsic dispersion are discussed in §3.3.1. The sample covers a large range in redshift, with sources up to $z \sim 5$, allowing a possible trend between Γ and z to be investigated in §3.3.2. The sample also covers around 4 orders of magnitude in L_X , and the relationship between Γ and L_X is described in §3.3.3. Sources which require any intrinsic absorption in the modelling of their X-ray spectra are discussed further in §3.3.4, and those found to require a soft excess component are studied in §3.3.5. The radio properties of the sample are discussed in §3.3.6 and in §3.3.7 black hole mass estimates from the literature are used to consider correlations with the Eddington ratio.

3.2 Procedure

3.2.1 Sample Creation

The sample of AGN was created from the optical SDSS DR5 quasar catalogue (Schneider et al., 2007) and the X-ray catalogue of serendipitous detections, 2XMMi (Watson et al., 2009), which were described in Chapter 2. A positional cross-correlation of the two catalogues using a $10''$ matching radius yielded 2013 initial matches, corresponding to 1281 unique objects.

The optical positions of the quasars in the DR5 quasar catalogue are accurate to $\sim 0.1''$ in each co-ordinate (Schneider et al., 2007), smaller than the typical errors on the X-ray positions,

which are $\sim 1 - 2''$ (Watson et al., 2009). A combined X-ray and optical positional error was defined by adding the contribution from each in quadrature. 97% of detections had a separation less than the 3σ combined positional error (88% for 2σ , 49% for 1σ) which is lower than is expected from a Gaussian distribution. This suggests that the systematic errors on the X-ray positions may be underestimated. Nine detections were matched to the optical position with a separation greater than the 5σ X-ray positional error. These were visually checked and in the majority of cases the X-ray source had a high number of counts resulting in a low X-ray positional error but the optical position was close enough to make them very likely to be counterparts.

There were 9 cases in which two different 2XMMi sources were within the $10''$ matching radius of a single quasar's optical position. Since the spectral extraction regions would encompass the PSFs of both sources, the resulting spectrum would be contaminated if they were different X-ray sources. However, in the majority of cases one of the detections was found in the wings of the brighter source with a large extent, and hence was regarded as a spurious detection. In other cases the alternative SRCID detections were on the edge of the field of view where the PSF was elongated (astigmatism), resulting in a slightly different X-ray position being determined and was hence identified as a separate source during the creation of the catalogue.

3.2.2 Extraction of Spectral Products

The general procedure for the reduction of *XMM-Newton* data was outlined in §2.1.3. Here, the specific details relating to the spectral extraction for this sample are described.

The X-ray spectra of all 2013 detections were extracted from the *XMM-Newton* Science Archive (XSA)¹ using an automated pipeline written by Dr Silvia Mateos incorporating tasks from the Science Analysis Software v6.6.0 (SAS²). In particular the task `eregionanalyse` was used to select the spectral extraction regions so as to optimize the S/N. Circular regions with an average radius of $\sim 17''$ were used for the source spectra. A circular background region with a radius of $50''$ was automatically chosen in the same CCD and close to the source,

¹<http://xmm.esac.esa.int/xsa/>

²The description and documentation are available online at <http://xmm.esac.esa.int/sas/>

but excluding any other nearby sources. Auxiliary response files and redistribution matrices were generated using `arfgen` and `rmfgen`, respectively.

Each of the 2013 detections were manually screened using the LEDAS thumbnails³ available for each detection in the catalogue. The detections were flagged if there was likely to be significant contamination of the source due to another nearby bright source or if the camera showed a significant Out-of-Time (OoT) event from a bright source in the field. Once the source and background extraction regions had been defined, some of the detections were then retained if neither extraction region was affected directly by the OoT event or contamination. In the case of some detections, redefining the position or size of the extraction regions meant that they could also be retained. The number of good pixels in each of the source extraction regions was determined, to help remove sources which fell partially outside of the camera's field of view or into chip gaps. Any detections with 95 – 100% of good pixels were automatically retained, any with 0 – 50% were automatically rejected, and any between 50 – 95% were subjected to another manual screening. If the majority of the source PSF was judged to fall onto the chip it was assumed that a reliable spectrum could be obtained from it and the detection was kept. 6% of the detections were excluded based on the screening flags, leaving a final sample of 1201 unique AGN. Multiple detections of the same source were merged into a single spectrum and the data from the two MOS cameras was combined. A separate MOS and pn spectrum for each source were generated, assuming that data from both detectors was available (for 278 sources data from only one detector was available or hadn't been rejected in the screening process). Finally, objects with < 75 total (MOS+pn) background subtracted counts were excluded from the sample in order to allow spectral fitting to be conducted with Γ left as a freely varying parameter. This gave a final sample of 761 unique sources.

3.2.3 Spectral Fitting

The spectra were binned using the `grppha Ftool`⁴, to ensure that Chi-squared (χ^2) statistics could be used. The minimum number of counts per bin was varied depending on the S/N of the spectra, with 15 being used for sources with ~ 100 counts, increasing up to 30 counts per

³<http://ledas-www.star.le.ac.uk/>

⁴<http://heasarc.gsfc.nasa.gov/docs/software/ftools/>

bin for sources with a few thousand counts. The spectra were then fit using XSPEC v11.3.2 (Arnaud, 1996) over the energy range 0.5 – 12.0 keV. Where available, the MOS and pn data were fit simultaneously with the same parameters, but a freely varying constant was added to the model to account for calibration offsets between the two cameras (Mateos et al., 2009). Each model included an absorption component fixed at the value of the Galactic column density in the direction of the source, as determined from the n_{H} Ftool⁴ which uses the HI map of Dickey & Lockman (1990). It was modelled using `phabs` with abundances from Wilms et al. (2000) and cross-sections from Balucinska-Church & McCammon (1992).

All 761 sources were fit with a simple power law (`po`) and an absorbed power law (`apo`), in which Γ and an intrinsic N_{H} component at the redshift of the source were allowed to vary freely. For 680 sources with more than 100 counts, models including a blackbody component were also considered. This component was introduced to model any soft excess, and was added to both the simple power-law (`po+bb`) and absorbed power-law (`apo+bb`) models. A summary of the different models considered, along with their XSPEC terminology can be found in Table 3.1.

The best-fitting model for each source was chosen via an F-test at 99% significance. The best-fit was assumed to be a simple power law unless an F-test determined that an additional intrinsic absorption component or blackbody component was required. These sources now assumed to be best-fit with the `apo` or `po+bb` models were then tested to see if the best-fitting model was in fact `apo+bb` i.e. both components were required. The number of sources best-fit with each model can also be found in Table 3.1. As expected, the majority of the sources, $\sim 90\%$, are best-fit with the simple power-law model and do not require any additional spectral components. However, $\sim 4\%$ are found to require an intrinsic absorption component and $\sim 8\%$ require a soft excess component. These percentages represent lower limits as the detectability of such additional spectral features is limited by the quality of the spectra. This will be considered further in Chapter 5.

Whilst the F-test determined the *best-fit* to the data, a model was deemed to be a *good fit* to the data if the null hypothesis probability, H_0 , was $> 1\%$. The majority (96%) of the sample were well fit by the model chosen by the F-test and the numbers of good fits for each

Table 3.1: This describes the different models used to fit the X-ray spectra of the sources. The spectral components included in each particular model are listed in column 2. Galactic absorption is also included in each, modeled by the additional `phabs` component. The 4th column lists the total number of sources in the sample which were *best-fit* by that particular model as chosen by an F-test at 99% significance. The final column lists the number of those sources which are also *well fit* by the best-fitting model i.e. $H0 > 1\%$.

Model	Components	XSPEC terminology	No. of sources	
			F-test > 99%	No. of good fits $H0 > 1\%$
po	Power law	phabs*po	672	650 (89%)
apo	Power law + intrinsic absorption	phabs*zpha*po	29 ^a	28 (4%)
po+bb	Power law + soft excess	phabs*(zbody+po)	55	52 (7%)
apo+bb	Power law + intrinsic absorption + soft excess	phabs*(zbody+zpha*po)	5 ^b	4 (<1%)
			761	734

Notes: ^a1 source shows an iron line and is fit with the model `pha*(zpha*po+zgauss)`. ^b2 sources show iron lines and are fit with the model `pha*(zgauss+zbody+zpha*po)`

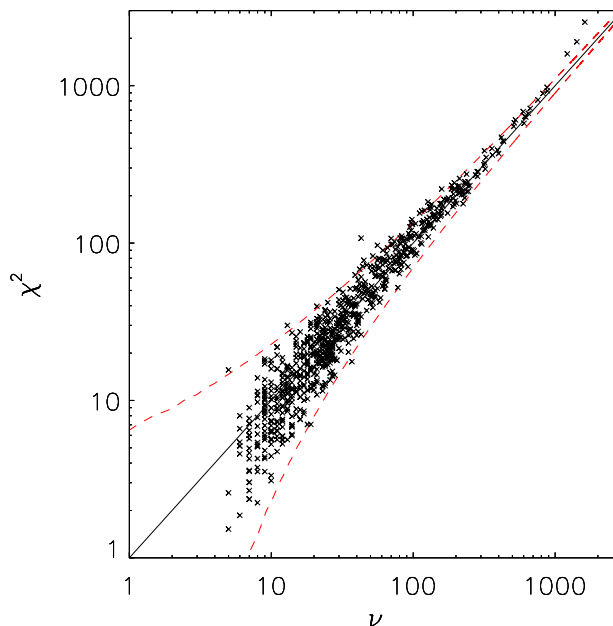


Figure 3.1: Plot of Chi-squared value (χ^2) vs Degrees of freedom (ν) for each of the X-ray spectra. The solid black line indicates the location of $\chi^2/\nu = 1$. The dashed red lines represent the locus outside of which that particular χ^2 value is expected to be observed only 1% of the time if the fit is correct.

type of model can be seen in Table 3.1. By defining the level for a good fit at 1%, ~ 8 sources would be expected to have a bad fit from purely statistical considerations. However, 27 sources have a bad fit. These include some sources with high numbers of counts (i.e. > 1000 degrees of freedom) for which the models are not sufficient to deal with the complexities shown to exist from studies of bright, nearby AGN (e.g. Pounds et al. 2004). For a good fit, reduced chi-squared (χ^2/ν), is expected to be approximately 1, which is shown in Fig. 3.1 as the solid black line and is compared to the actual quality of the fits. The region in which the best-fit model is considered correct at the 99% confidence level is shown between the red dashed lines.

The spectral fits of each source, particularly those with a bad original fit, were visually inspected and revealed 3 sources with clear evidence for an iron emission line. A Gaussian component, `zgauss`, was manually added to the model for these sources. This component could exist in more of the source spectra, but a systematic search for this component is beyond the scope of this study. The 3 Gaussian components have energies (E) and equivalent widths (σ) as follows: $E = 6.718 \pm 0.002$ keV and $\sigma = 0.07 \pm 0.01$ keV (SRCID 211185), $E = 6.67 \pm 0.03$ keV and $\sigma = 0.22 \pm 0.03$ keV (SRCID 73222), $E = 6.40 \pm 0.05$ keV and $\sigma = 0.13 \pm 0.02$ keV (SRCID 94028), which are typical of those found for nearby, bright AGN. An example of a source requiring this component can be seen in Fig. 3.2.

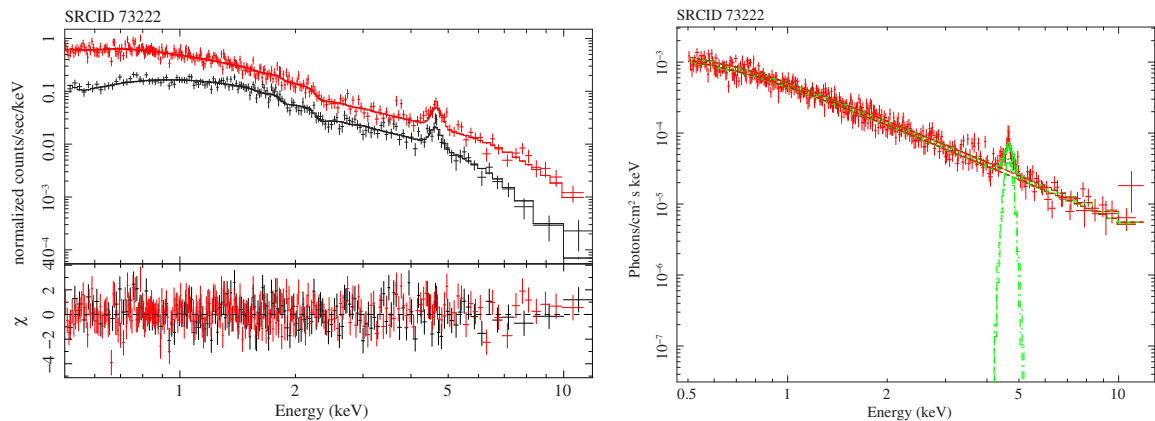


Figure 3.2: This figure includes the raw (left) and unfolded (right) spectra for SRCID 73222 which is best-fit with the apo+gauss model with the parameters $\Gamma = 1.95 \pm 0.02$, $N_{\text{H}} = 0.14 \pm 0.02 \times 10^{22} \text{ cm}^{-2}$, $E_{\text{Rest}} = 6.67 \pm 0.03 \text{ keV}$ and $\sigma = 0.22 \pm 0.03 \text{ keV}$. The source has ~ 15000 counts in total and is at $z = 0.44$.

The full spectral fitting parameters for each source can be found in Appendix A. Fluxes and rest frame luminosities for the sources were computed from the best-fit model. They were corrected for Galactic absorption, and where necessary, intrinsic absorption.

3.2.4 General Properties of the Sample

The final sample covers a large range in redshift (0.11 to 5.41) and 2–10 keV X-ray luminosity ($10^{43} - 10^{46} \text{ erg s}^{-1}$), better enabling an investigation into the dependencies of Γ on these quantities. The redshift and counts distribution can be seen in Fig. 3.3 (top) and the luminosity-redshift dependence can be seen in Fig. 3.3 (bottom).

The redshift distribution of sources in the full quasar catalogue is shown in Fig. 3.4 (solid, blue). A dip in the number of sources between $z = 2.2 - 3.0$ where the colours of quasars become indistinguishable from early F and late A type stars can be clearly identified. This dip is also evident in the final sample analysed here, also shown in Fig. 3.4 (red, dashed). A Kolmogorov-Smirnov (KS) test finds that the two distributions are significantly different (KS statistic = 0.13, significance = 9×10^{-12}) largely because the sample presented here includes relatively more low-redshift objects, as shown by the bottom panel of the figure, which plots the difference between the two redshift distributions. The distribution of absolute magnitudes in the i band which are taken from the quasar catalogue are plotted in Fig. 3.5. The magnitude cut-off limit of the quasar catalogue can be clearly seen at $M_i = -22$. The

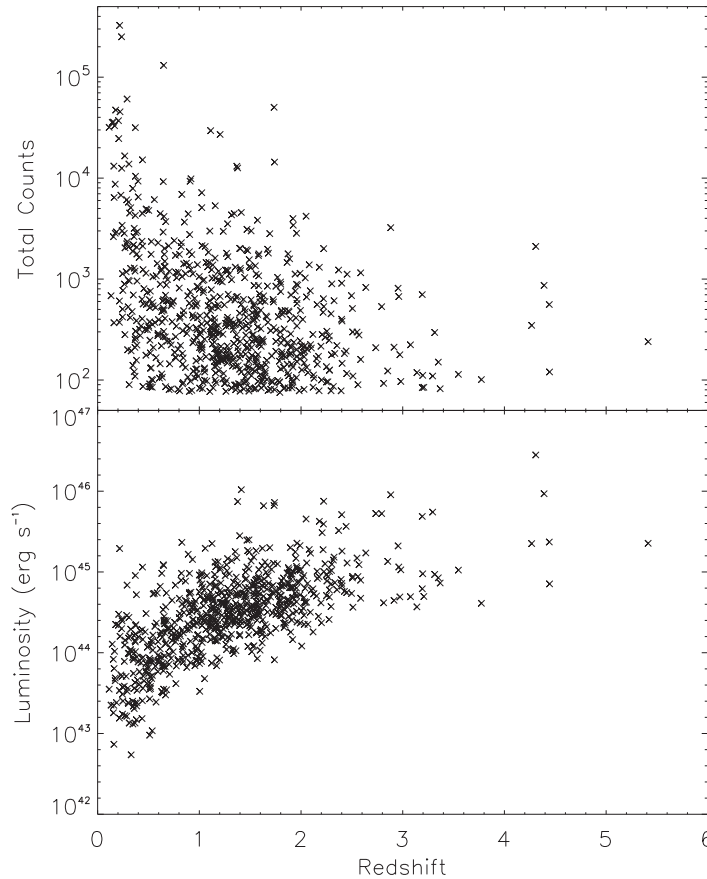


Figure 3.3: Plots showing the general properties of the final sample of 761 objects with X-ray spectral fits. Top - The redshift and counts distribution. Bottom - The luminosity (2 – 10 keV) and redshift range of the sample.

solid blue line shows the distribution of values for the full DR5 quasar catalogue, whilst the dashed red line shows the distribution for the sample studied here. A KS test finds them to be significantly different (KS statistic = 0.095, significance = 3×10^{-6}). Therefore the sample studied here is not consistent with the full DR5 quasar catalogue in terms of z and M_i , however their average values are not very different; for this sample $\bar{z} = 1.31 \pm 0.03$ (median = 1.26) and $\bar{M}_i = -25.24 \pm 0.06$ (median = -25.34) and for the full catalogue $\bar{z} = 1.538 \pm 0.003$ (median = 1.48) and $\bar{M}_i = -25.411 \pm 0.005$ (median = -25.60).

2XMMi includes both target and serendipitous source detections. Since observations with *XMM-Newton* can be requested for a variety of reasons, including the target detections in the sample could add bias towards ‘interesting’ objects. The final sample includes 62 sources which were the target of an observation (8% of the sample), which are naturally the ones with the highest number of counts and the sources fit with the most complex models. Since the subsequent analysis deals primarily with the distribution of Γ values and trends of Γ with

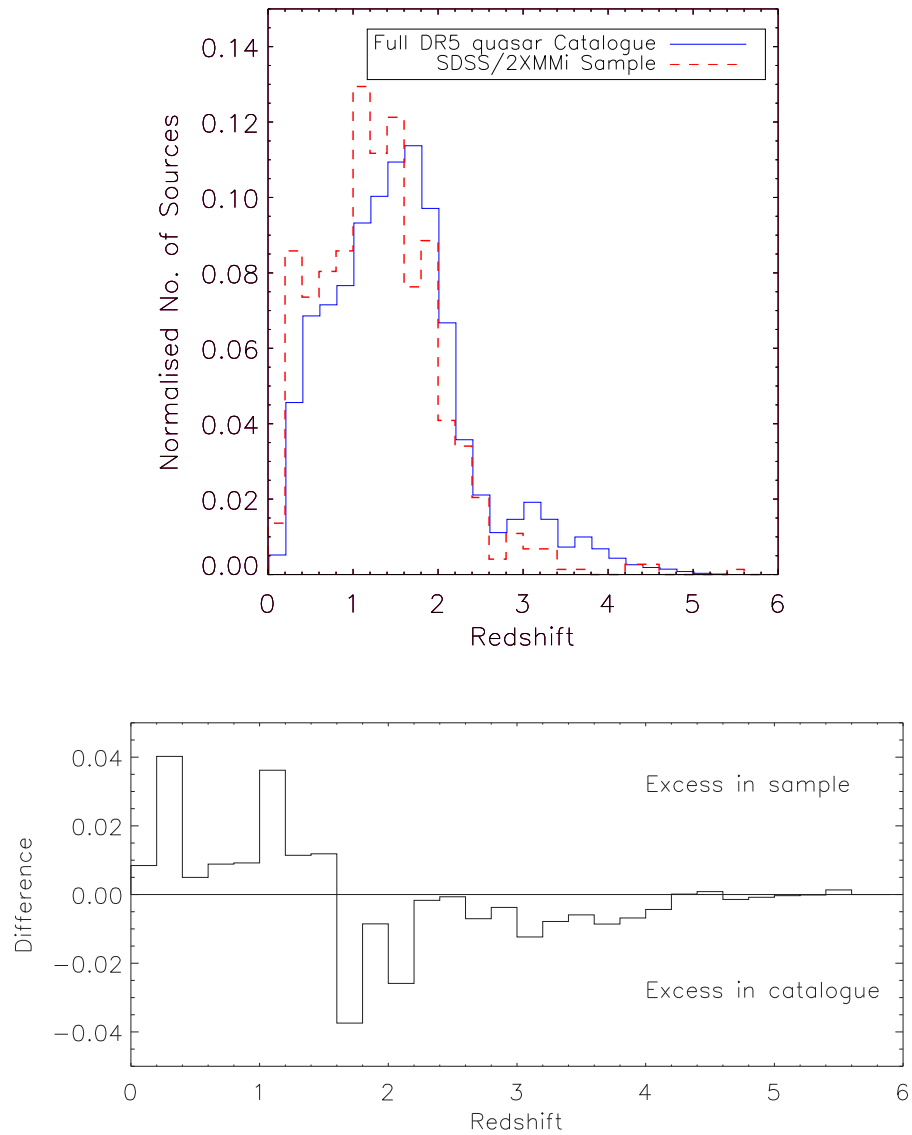


Figure 3.4: The redshift distributions of sources in the full quasar catalogue (solid, blue) and in the final sample (red, dashed). The bottom panel shows the difference between the 2 distributions above. Above the zero line represents an excess of sources in the sample at that redshift, compared with what is expected from the redshift distribution of the full catalogue.

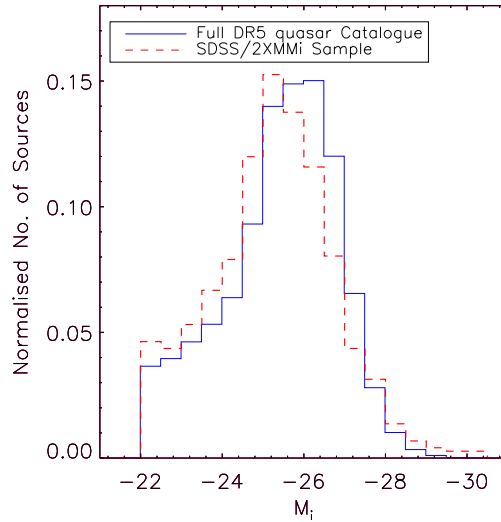


Figure 3.5: The distribution of absolute magnitudes in the i band for sources in the full quasar catalogue (solid, blue) and in the final sample (red, dashed).

various quantities, the Γ distribution of the target sources is compared with the sample of serendipitously detected sources in order to determine whether they are significantly different. The average Γ value of the target sources is $\Gamma = 1.92 \pm 0.05$ which is consistent with the average Γ value of the serendipitous sources, $\Gamma = 1.97 \pm 0.01$. Histograms showing the Γ distributions for these 2 sub-samples can be seen in Fig. 3.6 (serendipitous sources are shown with the solid blue line and the targets are shown with the dashed red). The KS statistic indicates that the Γ distributions are consistent (0.16, sig = 0.14) and therefore the use of the target detections should not significantly affect the findings of the subsequent sections.

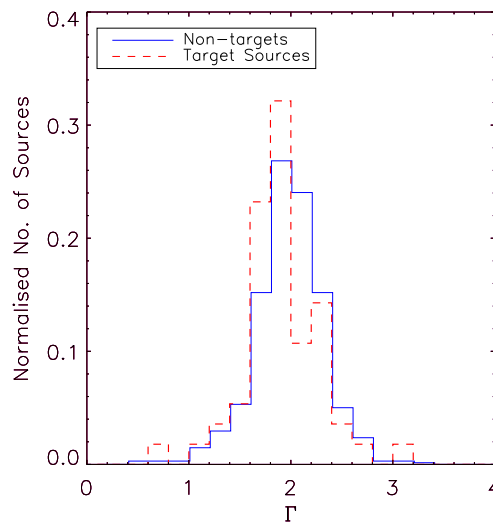


Figure 3.6: The distribution of Γ values for the serendipitously detected sources (solid, blue) and the targeted sources (dashed, red).

3.3 Results

3.3.1 Distribution of Power-Law Slopes

The majority of the sources in this sample are best-fit with the simple power-law model. An example spectrum of such a source is shown in Fig. 3.7.

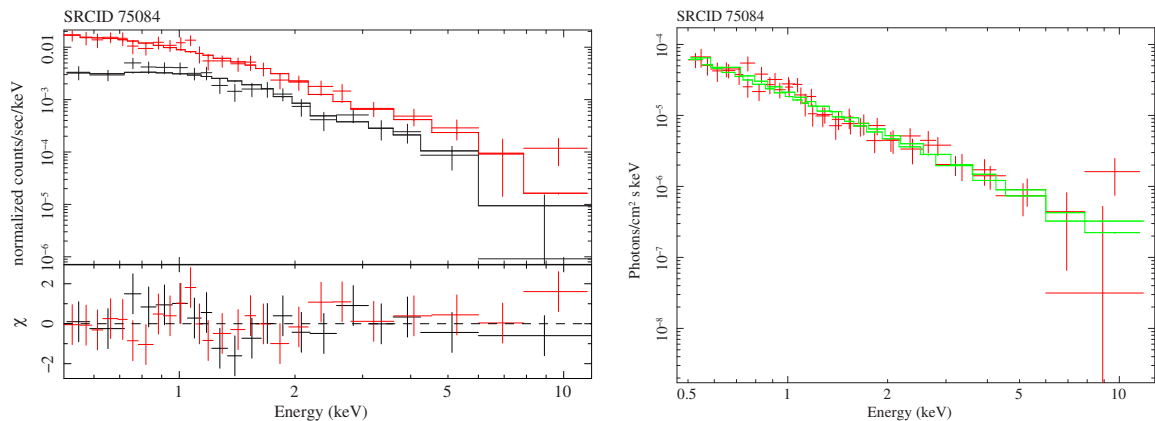


Figure 3.7: This figure includes the raw (left) and unfolded (right) spectra for SRCID 75084 which is best-fit with the simple power-law model (po), where $\Gamma = 1.98 \pm 0.07$.

In this section, the distribution of power-law slopes is described, where the Γ value used for each source is taken from its best-fitting model.

In general, previous studies have found an average Γ value of 1.9–2.0 (Mittaz et al., 1999; Mateos et al., 2005a,b; Page et al., 2006; Just et al., 2007; Mainieri et al., 2007; Green et al., 2009; Young et al., 2009; Mateos et al., 2010; Corral et al., 2011) and an intrinsic dispersion of $\sigma \sim 0.2 - 0.3$ (Reeves & Turner, 2000; Dai et al., 2004; Mateos et al., 2005b; Tozzi et al., 2006; Mainieri et al., 2007; Young et al., 2009; Mateos et al., 2010). However, using satellites with different band passes can give different values. For example, samples selected in hard X-rays by *INTEGRAL* or *Swift* yield generally lower average spectral indices of ~ 1.7 (Molina et al., 2009; Winter et al., 2009), likely because there is a bias towards detecting flatter sources at higher X-ray energies. The Γ value reported is dependent upon the energy range it is considered over, particularly if some spectral components are not properly modelled, for example, the presence of a warm absorber or unmodelled reflection component can produce a slope flatter than the true intrinsic value. Bianchi et al. (2009) suggest that the difference in photon index found between different populations of AGN could be due to varying amounts

of Compton reflection present in the sources. For their sample, quasars were found to have steeper power-law slopes ($\Gamma = 1.80 \pm 0.05$) than Seyferts ($\Gamma = 1.66 \pm 0.05$), which may be indicative of a larger reflection component present in the Seyfert population. When a reflection component was included in the models, the Γ values of both populations increased, but more so for the Seyferts. Different Γ values in other populations of AGN are likely due to real physical differences. For example, RLQ are known to have flatter power-law slopes than their radio-quiet counterparts (e.g. Reeves & Turner 2000) and NLS1s are also observed to have steeper power-law slopes than their broad-line counterparts (e.g. Brandt et al. 1997).

The distribution of best-fitting power law slope values, Γ , can be seen in Fig. 3.8 (top). It shows that most sources have a power-law slope value ~ 2 , with the arithmetic average value being $\Gamma_{\text{av}} = 1.97 \pm 0.01$. The typical (68%) error on a Γ measurement is $\Delta\Gamma = 0.13$, significantly smaller than the spread of Γ values, indicating that the observed dispersion of values is truly intrinsic. The panel showing the enlarged distribution indicates that there are some sources with extremely flat ($\Gamma < 1.4$) or steep ($\Gamma > 2.6$) power-law slopes which will be discussed in Chapter 4.

By assuming that the distribution of Γ values can be represented by a Gaussian function of mean $\langle\Gamma\rangle$ and dispersion $\sigma_{\langle\Gamma\rangle}$, simultaneous estimates of these values are obtained using a χ^2 minimization technique. Fig. 3.8 (bottom) shows the 1σ , 2σ and 3σ confidence contours, along with the derived best-fitting values $\langle\Gamma\rangle = 1.99 \pm 0.01$ and $\sigma_{\langle\Gamma\rangle} = 0.30 \pm 0.01$. The best-fitting Gaussian can be seen over-plotted on Fig. 3.8 (top).

This analysis does not take into account the individual errors on each of the Γ estimates, so here their contribution to the total dispersion is investigated. This is done by assuming that the observed dispersion can be expressed as the sum of the intrinsic dispersion and the individual errors on Γ added in quadrature, i.e. $\sigma^2 = \sigma_{\text{int}}^2 + \sigma_{\text{err}}^2$. χ^2 is then calculated for a range of different values of σ_{int} , assuming the expected Γ value for each point to be equal to the average value for the entire sample and the error on each point to be the 68% error derived from its spectral fit. The results of these fits can be seen in Fig. 3.9. As expected, a ‘poor’ fit is found for low intrinsic dispersions, while the fit becomes ‘too good’ for much higher levels. The point at which reduced χ^2 becomes equal to 1 is taken as the best-fitting

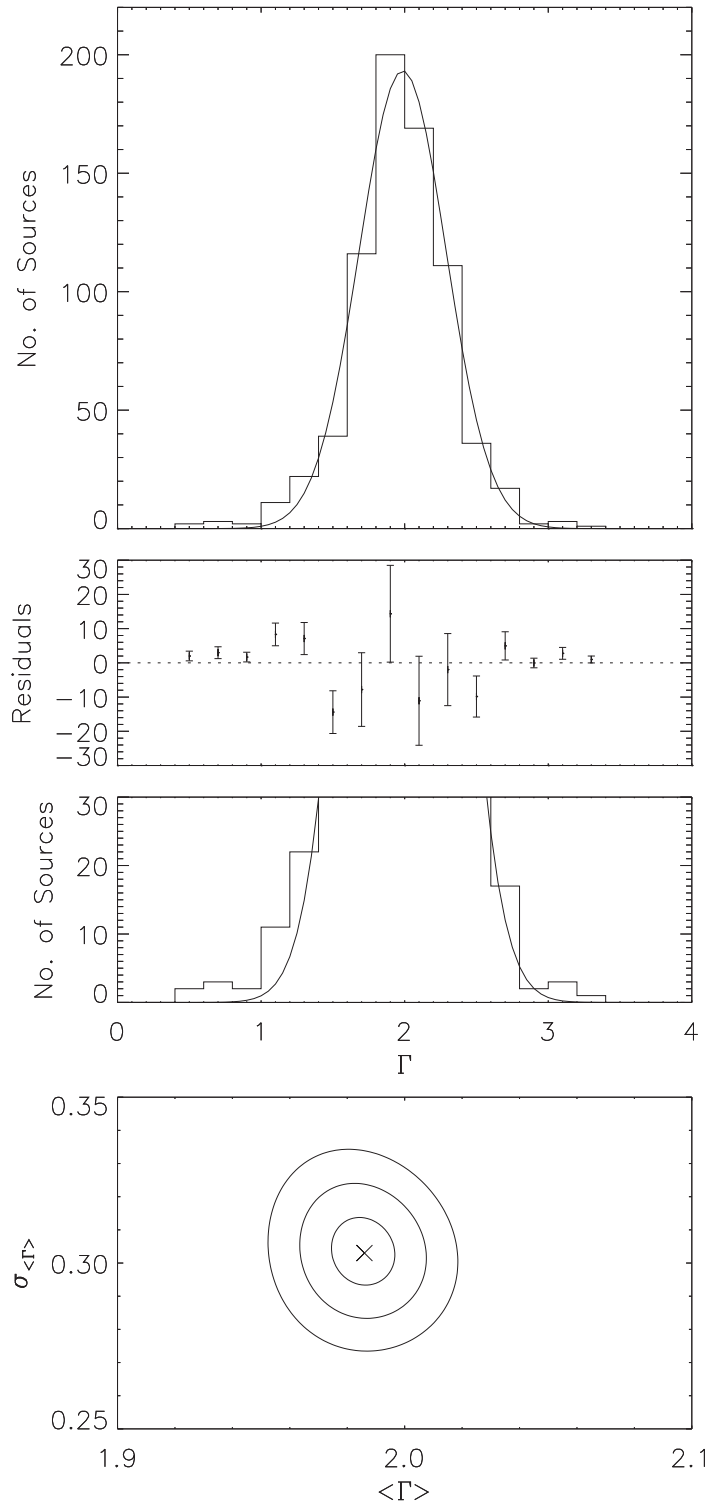


Figure 3.8: The histogram (top) shows the distribution of best-fitting photon indices where the required model gives an acceptable fit to the data. The smooth line is the best-fitting Gaussian distribution, as determined by χ^2 minimization and is described by $\langle \Gamma \rangle$ and $\sigma_{\langle \Gamma \rangle}$. Also included is a plot of the residuals, comparing the data to the model, and an enlarged version of the lower regions of the histogram to better highlight the presence of extreme sources. The bottom figure shows the best-fitting values, indicated by the cross, and the 1σ , 2σ and 3σ confidence contours for the derived values of $\langle \Gamma \rangle$ and $\sigma_{\langle \Gamma \rangle}$.

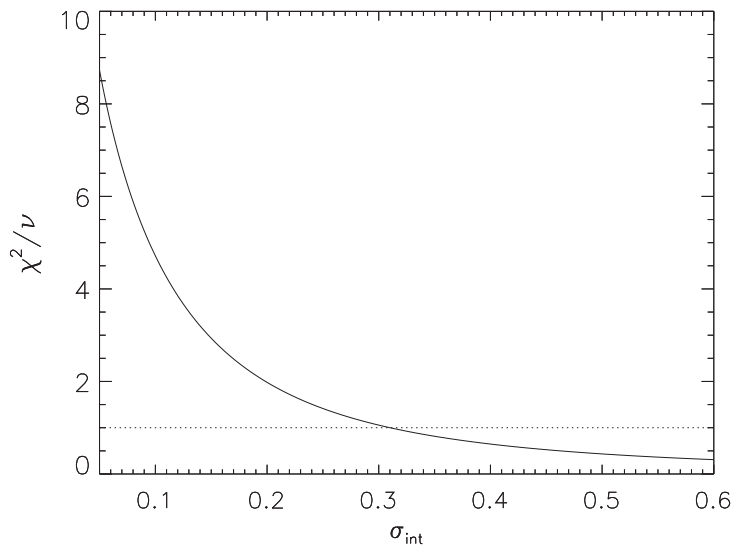


Figure 3.9: This shows how the reduced χ^2 of the fit varies when increasing levels of intrinsic dispersion are added in quadrature to the individual errors on the Γ values for each source in the sample.

value which is $\sigma_{\text{int}} = 0.31 \pm 0.01$, the same result as that obtained from the single Gaussian fit above. Therefore the individual errors on Γ contribute very little to the overall dispersion. This is not entirely unexpected since the typical 68% error on Γ is $\Delta\Gamma \sim 0.13$, which will contribute much less than an intrinsic dispersion of 0.30 when added in quadrature.

This value of Γ agrees with those found by previous studies, including the XWAS sample, $\Gamma = 1.96 \pm 0.02$, $\sigma = 0.27^{+0.01}_{-0.02}$ (Mateos et al., 2010) and the *XMM-Newton* COSMOS sample, $\Gamma = 2.06 \pm 0.08$ (Mainieri et al., 2007). Young et al. (2009), using a subset of objects from the same data presented here, find $\Gamma = 1.91 \pm 0.08$ and that their typical 68% errors, $\Delta\Gamma = 0.15$ result in an intrinsic dispersion of $\sigma = 0.37$.

When fitting a single Gaussian to the Γ distribution, a null hypothesis probability value of $p = 0.43\%$ was found. Since this is $< 1\%$, it suggests that the model does not provide an acceptable fit to the data. A two Gaussian model gives a better fit to the data (null hypothesis probability, $p = 15.4\%$) and an F-test comparing the two Gaussian and one Gaussian models suggests that the inclusion of the second Gaussian is statistically valid (F-test probability of 99%). In this fit the average value of the two Gaussians, which were kept equal, was $\mu = 1.98 \pm 0.01$, consistent with the previous single Gaussian fit, and the best-fitting dispersions of the Gaussians were found to be $\sigma_1 = 0.27 \pm 0.01$ and $\sigma_2 = 0.59 \pm 0.04$. The fit can be seen in Fig. 3.10. The two Gaussian model should not be taken as a physically motivated fit to the

Γ distribution since it models both the flat and steep sources as a single ‘extreme’ population, when in reality they are likely to be different sub-samples. However, since a multiple Gaussian model can produce an acceptable fit, where the single Gaussian is inadequate, it does highlight the existence of extreme sources in the distribution.

3.3.2 Redshift Dependence of the Power-Law Slope

In this section the data is tested for evidence supporting an intrinsic variation of the spectral index, Γ , with redshift. If a trend with redshift was found it may indicate that the accretion mechanism is different for objects in the past. This possibility has been widely investigated, but no clear consensus has been reached. Many studies of large samples of AGN report no evolution of Γ with redshift (Reeves & Turner, 2000; Piconcelli et al., 2003; Perola et al., 2004; Mateos et al., 2005a,b; Page et al., 2006; Tozzi et al., 2006; Just et al., 2007; Mainieri et al., 2007; Green et al., 2009; Young et al., 2009) which agrees with some results of studies specifically targeting a few high redshift objects and measuring Γ values consistent with those for lower redshift objects (Vignali et al., 2005; Shemmer et al., 2005). However, some report Γ flattening for higher redshift sources (Vignali et al., 1999; Bechtold et al., 2003; Kelly et al., 2007).

Fig. 3.11 includes 734 sources for which the best-fitting model provides an acceptable fit to the data i.e. $H0 > 1\%$. The sources are plotted with different colours/symbols according to their model. The correlation coefficients (Kendall’s τ and Spearman’s rank, ρ) are calculated for both the entire population of 734 sources, and the subset of 650 sources whose best fit is a simple power-law model (po). Considering the entire population gives a $\sim 3\sigma$ anticorrelation of Γ with z ($\tau = -0.08$, prob = 0.001 and $\rho = -0.11$, prob = 0.002). Considering only the sources fit by po, gives a tighter $\sim 5\sigma$ anticorrelation ($\tau = -0.13$, prob = 3×10^{-7} and $\rho = -0.20$, prob = 4×10^{-7}).

These two cases are considered because the percentage of sources best-fit with each of the spectral models is not constant with redshift. In particular, a large percentage of sources in the redshift bins $z < 0.6$ are those fit with po+bb, as the blackbody component is easier to detect in these sources (see Fig. 3.12, top). Since the absorption and soft excess components

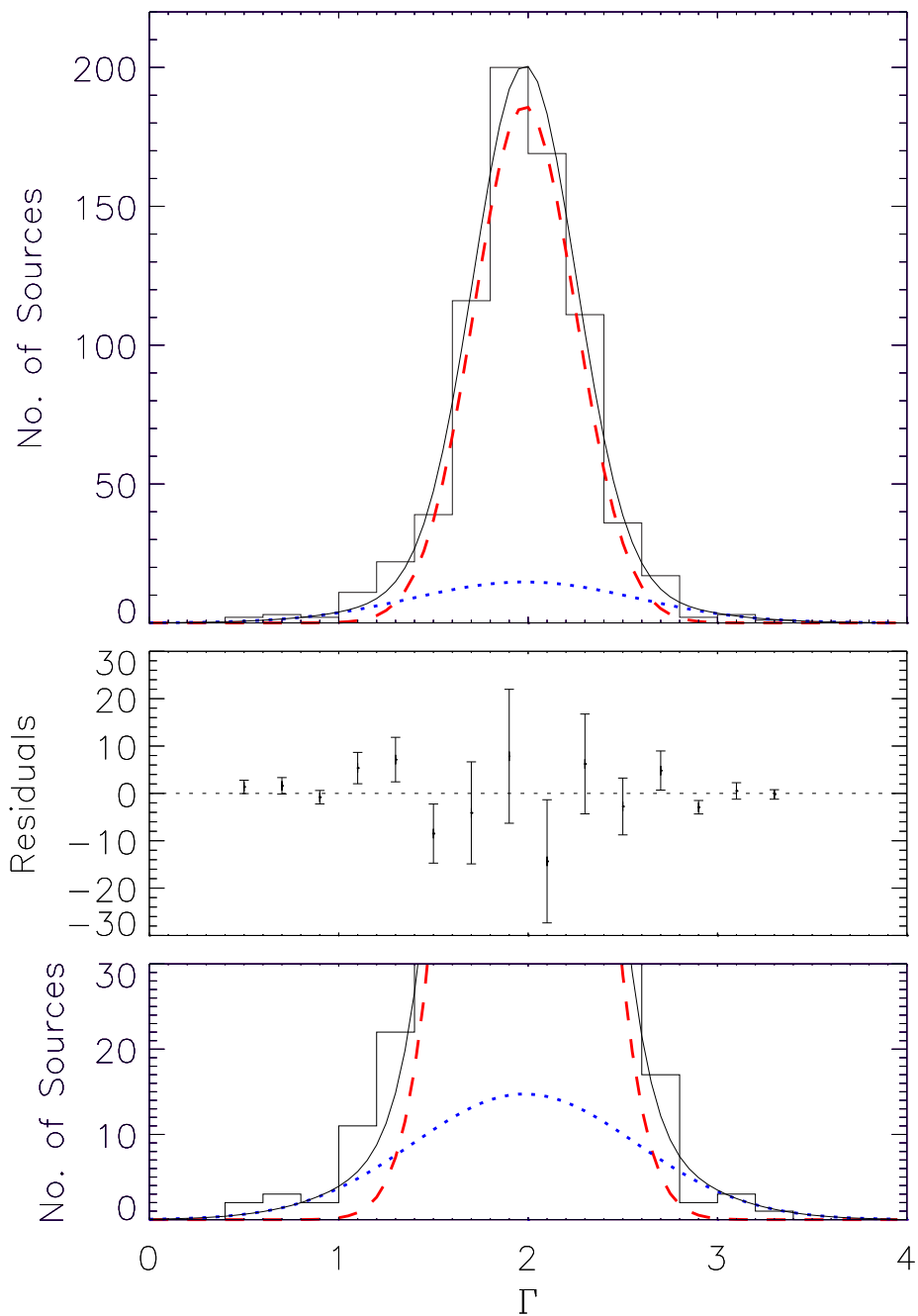


Figure 3.10: The red, dashed and blue, dotted lines show the two constituent Gaussians, while the black, solid line shows the overall model, produced by the addition of the two.

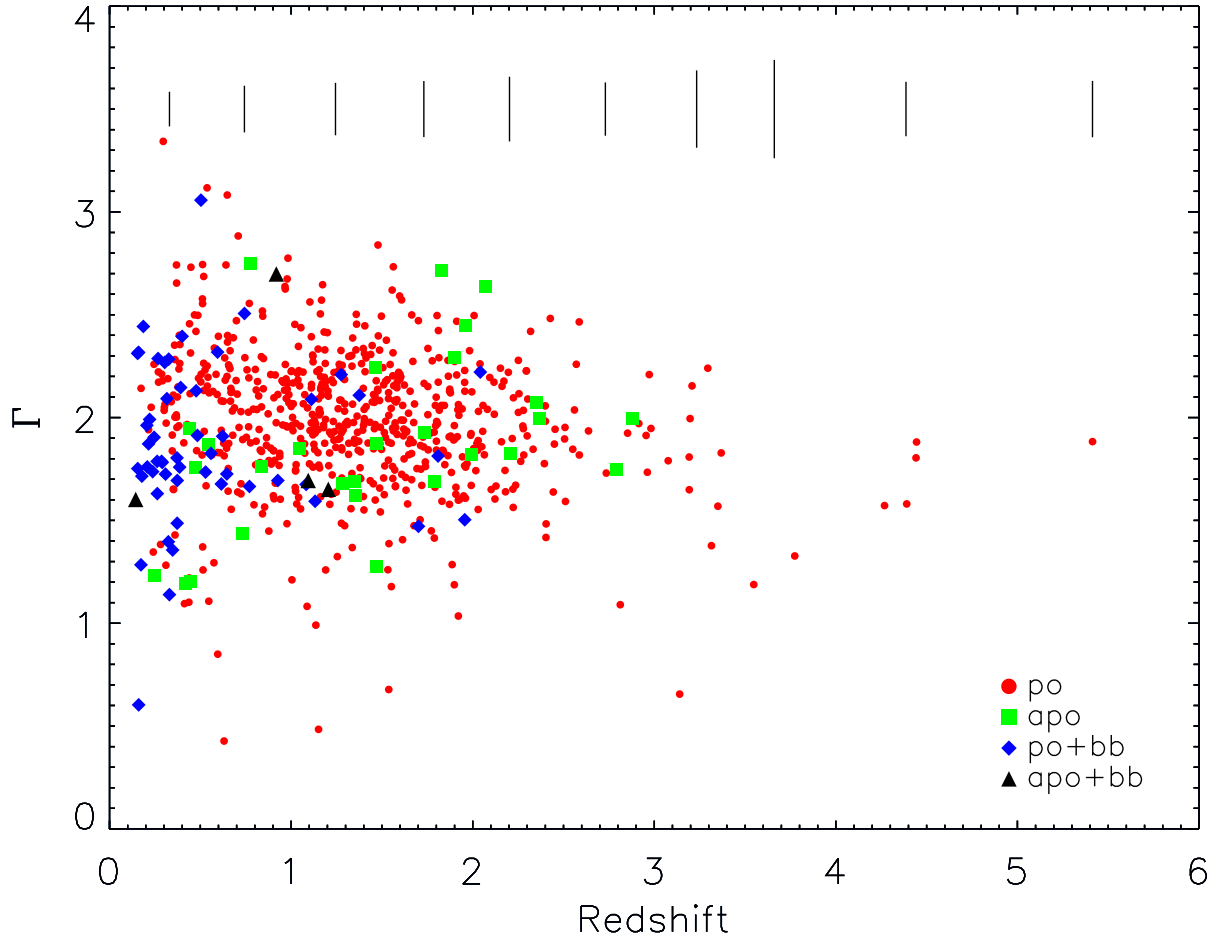


Figure 3.11: This plot includes the 734 sources with $H0 > 1\%$. The different colours/symbols correspond to the best-fitting model; red circles are po, green squares are apo, blue diamonds are po+bb and black triangles are apo+bb. The error bars shown at the top of the plot correspond to the average of each of the 1σ errors on the individual sources, calculated in $dz = 0.5$ bins.

have been included in the models so as to correctly account for the spectral complexities, the Γ values obtained should be consistent with those seen in the simple power-law sources. The sample is separated into sub-samples of sources best-fit with each of the models po, apo and po+bb and their Γ distributions can be seen in Fig. 3.12 (bottom). KS tests comparing the Γ values of the sub-samples find that the apo sources have a similar distribution to that of the po sources (significance = 0.02), but the po+bb sources have significantly different Γ values (significance = 0.0003). They tend to have flatter power-law slopes than expected, which may be an artifact of the spectral fitting in which a large soft excess component is added, forcing the power-law slope to a flatter value than would be necessary if a smaller soft excess component was used.

Fig. 3.13 shows binned versions of Fig. 3.11. The top plot includes sources fit with all

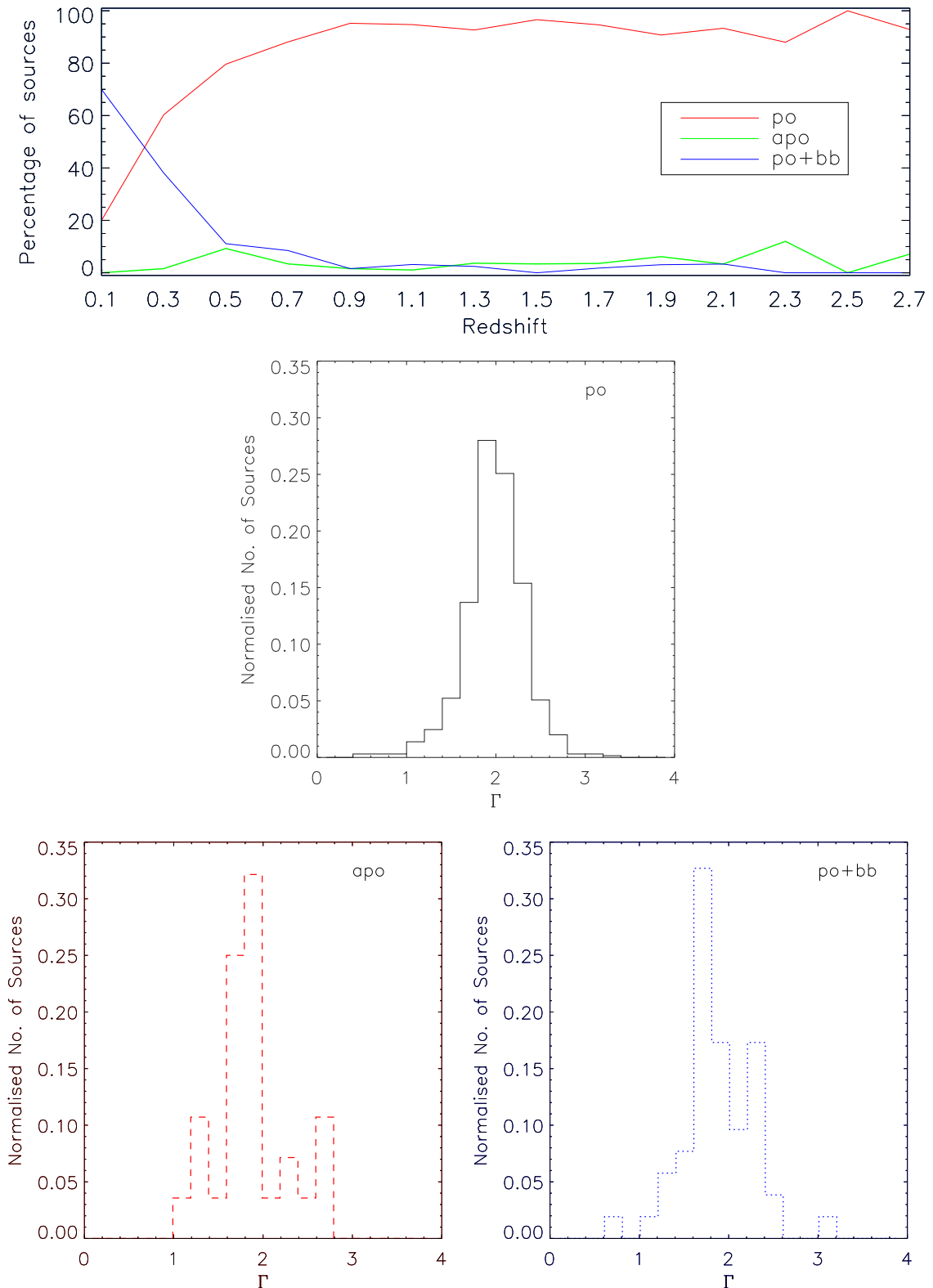


Figure 3.12: Top - This plot shows how the percentage of sources fit with each of the different models varies with redshift. Bottom - These histograms compare the distribution of Γ values for each of the sub-samples of sources fit with the different models, po, apo and po+bb (apo+bb is not included as there are only 4 sources best fit with this model). The histograms have been normalised to account for the different numbers of sources that are best-fit with each model.

Correlated Properties	Sources Included	Model	p -value %
Γ and z	All	$\langle \Gamma \rangle = (-0.04 \pm 0.02)z + (1.94 \pm 0.03)$	14.2
		$\langle \Gamma \rangle = 1.87$	4
	po only	$\langle \Gamma \rangle = (-0.07 \pm 0.02)z + (1.99 \pm 0.03)$	12
		$\langle \Gamma \rangle = 1.90$	0.012

Table 3.2: Listed are the best-fitting linear correlations between Γ and z for the binned data, found by χ^2 minimization. The errors on the values are 1σ . The null hypothesis probabilities (p -values) for both the linear models and constant $\langle \Gamma \rangle$ models are listed, where $p > 1\%$ is taken to be an acceptable fit.

models, whilst the bottom plot only considers sources best-fit with the simple power-law model. Narrow redshift bins ($dz = 0.2$) are used up to $z = 2.6$. Above this point, the data is binned so as to ensure at least 8 sources per bin (or 6 in the case of the po only plot) due to decreased numbers of sources. A weighted mean value of Γ is calculated for each bin according to the equation,

$$\langle \Gamma \rangle = \sum P_i \times \Gamma_i \quad \text{where} \quad P_i = \frac{1/\sigma_i^2}{\sum (1/\sigma_i^2)}, \quad (3.1)$$

which takes into account the individual errors (σ_i) on the Γ estimates (Γ_i). The errors on $\langle \Gamma \rangle$ are calculated as standard errors on the mean, $\alpha = \sigma/\sqrt{N}$, where,

$$\sigma = \sqrt{\frac{1}{N-1} \sum (\Gamma_i - \langle \Gamma \rangle)^2}. \quad (3.2)$$

The data was fit with 2 models; a linear trendline where a gradient inconsistent with zero would indicate Γ values evolving with redshift, and a model where $\langle \Gamma \rangle$ was fixed at the value of the weighted mean for the sample to represent a non-evolving Γ . The models and corresponding null hypothesis probabilities (p -values) can be found in Table 3.2.

For the sources fit with all types of spectral model, a non-evolving Γ gives a good fit to the data and the linear trend gives a gradient consistent with zero. This suggests no significant trend for decreasing Γ with increasing redshift. However, when only the sources best-fit with a simple power-law model are considered, the non-evolving Γ model does not provide a good fit to the data and the linear trend gives a gradient inconsistent with zero. This suggests that for this sub-set of sources, a significant, but slight, trend of Γ with redshift is present.

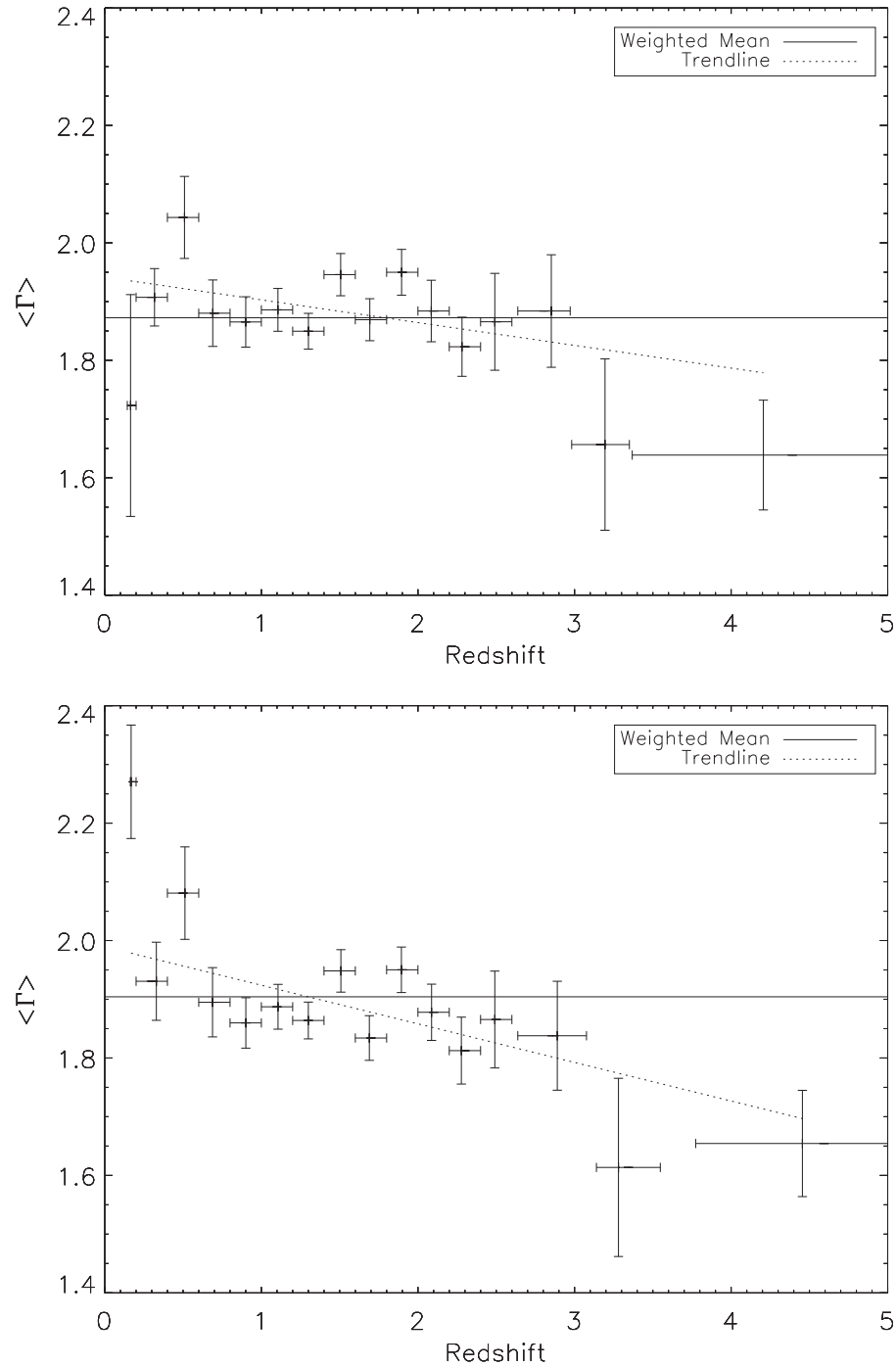


Figure 3.13: These plots show the dependence of weighted Γ values on redshift. The sources are binned in redshift ($dz = 0.2$), up until $z = 2.6$ and then after this, to ensure at least 8 sources per bin (or 6 for the po only plot). The y error bars are standard errors on the mean, $\alpha = \sigma/\sqrt{N}$, where the standard deviation is based on deviations from the weighted mean. The x errors indicate the width of the bin. The solid horizontal lines indicate the weighted mean values of each sample and the dotted lines show the linear fits to the data. The top plot includes data from 734 sources with good fits and shows a linear fit of $\langle \Gamma \rangle = (-0.04 \pm 0.02)z + (1.94 \pm 0.03)$. The bottom plot includes data from 650 sources best-fit using a simple power-law model and shows a linear fit of $\langle \Gamma \rangle = (-0.07 \pm 0.02)z + (1.99 \pm 0.03)$.

The estimate of $\langle\Gamma\rangle$ for the entire sample is lower than the arithmetic value determined without considering the individual errors on Γ measurements. This is not due to any particular source with vastly underestimated errors, but is a general effect created because the slopes of flatter sources are easier to constrain and therefore have lower associated errors than the steeper sources. If the top 2.5% of sources with weights above 0.01 are removed, the weighted mean value steepens to 1.93.

The lowest redshift bin of Fig. 3.13 has a large error in $\langle\Gamma\rangle$ due to a low number of sources with a large scatter of Γ values, which also causes the $\langle\Gamma\rangle$ value to change considerably between the 2 plots. Similarly the higher redshift bins also include low numbers of sources and are likely unrepresentative of the entire sample as the percentage of sources that were targets of the *XMM-Newton* observation is higher (for $z > 2.6$: $25 \pm 11\%$, for $z < 2.6$: $7 \pm 1\%$). When the lowest bin and top bins are removed from consideration the overall conclusions remain the same, i.e. there is no dependence of Γ on z when all sources are considered, but a marginal trend is apparent when just those sources best-fit with a simple power law are. Since it is suggested that RLQ tend to have flatter spectra than RQQ, it is possible that an increased fraction of RL sources in high redshift bins may be a contributing factor to the flatter Γ values observed. However, all the sources in the sample above $z = 2.6$ are found to be radio quiet from the definition of radio loudness, as will be described in §3.3.6.

Since a trend between Γ and z is found, it is investigated whether this could be due additional spectral complexity at higher energies in the sources. When the power-law slope over the observed range of the EPIC detectors (0.5 – 12.0 keV) is considered, it probes higher rest frame energies for sources at higher redshift. In these cases a contribution from the reflection component is expected. If this is not modelled separately, and just a simple power-law model is used for the entire spectrum, its presence will make the slope of the power law appear flatter. This could explain the slight decrease in the power-law slopes seen for sources at higher redshift. To test this hypothesis simple power-law models are fit to spectra over the rest frame energy range 2.0 – 6.0 keV, with the upper limit chosen so as to exclude any contribution from such a reflection component and the lower limit of 2 keV chosen to exclude any absorption component thus giving a cleaner representation of the power law.

While attempting to fit spectra over a reduced rest frame energy range, particularly for high redshift sources, the detector energy range being used can become very small. Therefore a new minimum counts threshold is imposed to ensure a reliable spectral fit. Also as the counts that fall into the reduced energy range are still binned to a minimum of 15 counts per bin, with any incomplete bins at the higher energies being disregarded, sources with low numbers of counts are not actually analysed over the entire reduced energy range. The true range being probed was determined and the percentage loss from what is expected was considered. If the sample is restricted to sources containing at least 300 counts in the reduced energy range, the average percentage loss is $< 5\%$ and the maximum loss of range is $\sim 20\%$. This cut also ensures that there are enough counts available in the reduced energy range to generate a reliable spectral fit. This necessary limit in the number of counts reduces the number of sources to 211. Also requiring that both fits were acceptable i.e. $\text{HO}_{\text{part}} > 1\%$ and $\text{HO}_{\text{full}} > 1\%$, and considering only the sources whose original best-fit model was a simple power law reduces the number of sources considered here to 128.

Fig. 3.14 plots the power-law slope value measured over the reduced range, 2.0 – 6.0 keV in the rest frame (Γ_{part}) against the slope measured over the full 0.5 – 12.0 keV observed frame (Γ_{full}), for a reduced sample of 128 sources described above. They are divided into 3 broad redshift bins and the typical 68% error size is indicated to the left of the figure. If an unmodelled reflection component is being removed when considering the spectral fits over the reduced range, Γ_{part} should be steeper than Γ_{full} and hence the sources should lie in the top left corner, above the $\Gamma_{\text{part}} = \Gamma_{\text{full}}$ line. The χ^2 statistic is calculated between the points and the null hypothesis line of $\Gamma_{\text{part}} = \Gamma_{\text{full}}$. All 3 redshift bins are found to be consistent with this line indicating that there is no significant difference between Γ_{full} and Γ_{part} . This suggests no strong reflection component is present in these sources and therefore cannot be used to explain the flattening of Γ with increasing redshift.

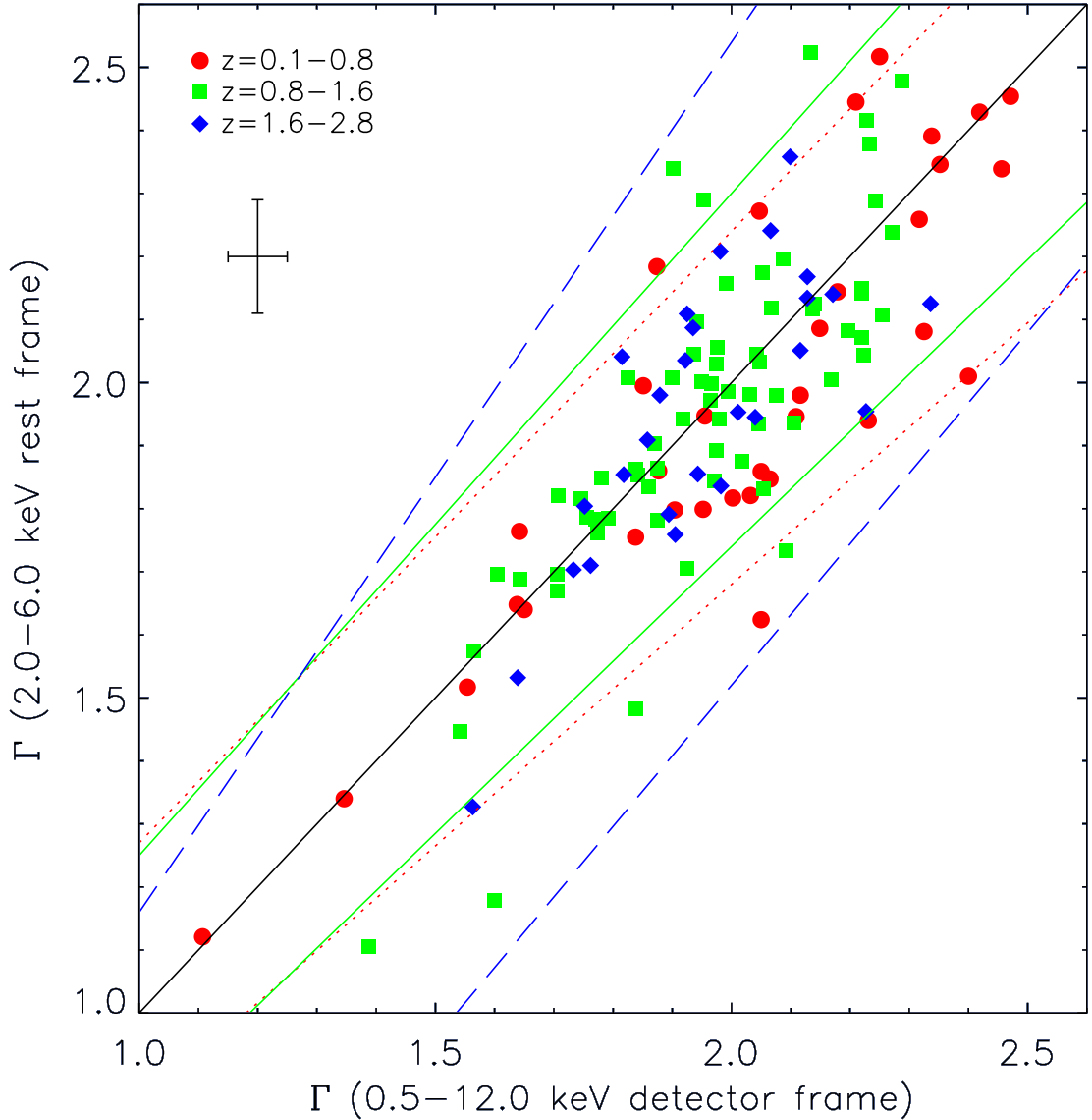


Figure 3.14: This figure plots the power-law slope value as determined from a spectral fit over the entire 0.5 – 12.0 keV detector energy range against the value determined from a spectral fit over the reduced 2.0 – 6.0 keV rest frame energy range for 128 sources as detailed in the text. They are divided into 3 broad redshift bins, red circles: $z = 0.1 - 0.8$, green squares: $z = 0.8 - 1.6$, blue diamonds: $z = 1.6 - 2.8$. An indication of the typical 68% error is shown offset from the real data points. The line where $\Gamma_{\text{part}} = \Gamma_{\text{full}}$ is marked on the figure for reference and does not represent a particular linear fit. The dotted red/solid green/dashed blue lines represent 68% error bounds on the best-fitting trendline for the $z = 0.1 - 0.8/z = 0.8 - 1.6/z = 1.6 - 2.8$ sources respectively. It can be seen that all sources lie within these boundaries, suggesting the sub-samples are consistent with each other.

3.3.3 Luminosity Dependence of the Power-Law Slope

Although it is natural to assume that the X-ray production must be related to the black hole mass, accretion rate and luminosity, this dependence is poorly understood and it is not clear whether there is any intrinsic variation of Γ with X-ray luminosity, despite having been widely investigated. Some studies report a correlation with luminosity that is positive, implying steeper spectral slopes in higher luminosity sources, possibly with a redshift or luminosity dependence (Dai et al., 2004; Saez et al., 2008), some studies report no correlation (Reeves & Turner, 2000; Shemmer et al., 2005; Mateos et al., 2005a,b; Tozzi et al., 2006; Winter et al., 2009) whilst some studies report a negative correlation (Reeves et al., 1997; Young et al., 2009; Corral et al., 2011) implying that the X-ray spectral slope flattens as the X-ray luminosity of the sources increases.

Fig. 3.15 plots the spectral index, Γ , as a function of hard (2 – 10 keV) X-ray luminosity. The hard band is used since this energy range is less affected by any intrinsic absorption that may be present in the source. Correlation coefficients (Kendall's τ and Spearman's rank, ρ) are calculated for both the entire population of 734 sources, and the subset of 650 sources whose best-fit is a simple power-law model (po). Considering the entire population gives a negative correlation of Γ with $\log L_X$ ($\tau = -0.167$, prob = 0.000001 and $\rho = -0.24$, prob = 3×10^{-11}). Considering only the sources fit by po, gives a tighter negative correlation ($\rho = -0.29$, prob = 2×10^{-14}). These correlations imply that it is the sources with higher hard X-ray luminosities that tend to have flatter Γ values.

As previously discussed, the higher redshift objects in the sample may be present due to pre-selection. Since these sources are also likely to be the sources with the highest luminosities, the correlation coefficients are determined again, this time omitting sources with $z > 2.6$. The correlation of Γ with L_X remains present at high significance.

Fig. 3.16 shows binned versions of Fig. 3.15, with each bin size being approximately $\log L_X = 0.5$, and including at least 18 sources. A weighted mean value of Γ is calculated for each bin using Eqn. 3.1 as before. The top plot includes sources which are best-fit with any of the spectral models, whilst the bottom plot includes only those best-fit with the simple power-law model. As in the previous section, linear trends to the data are calculated using χ^2

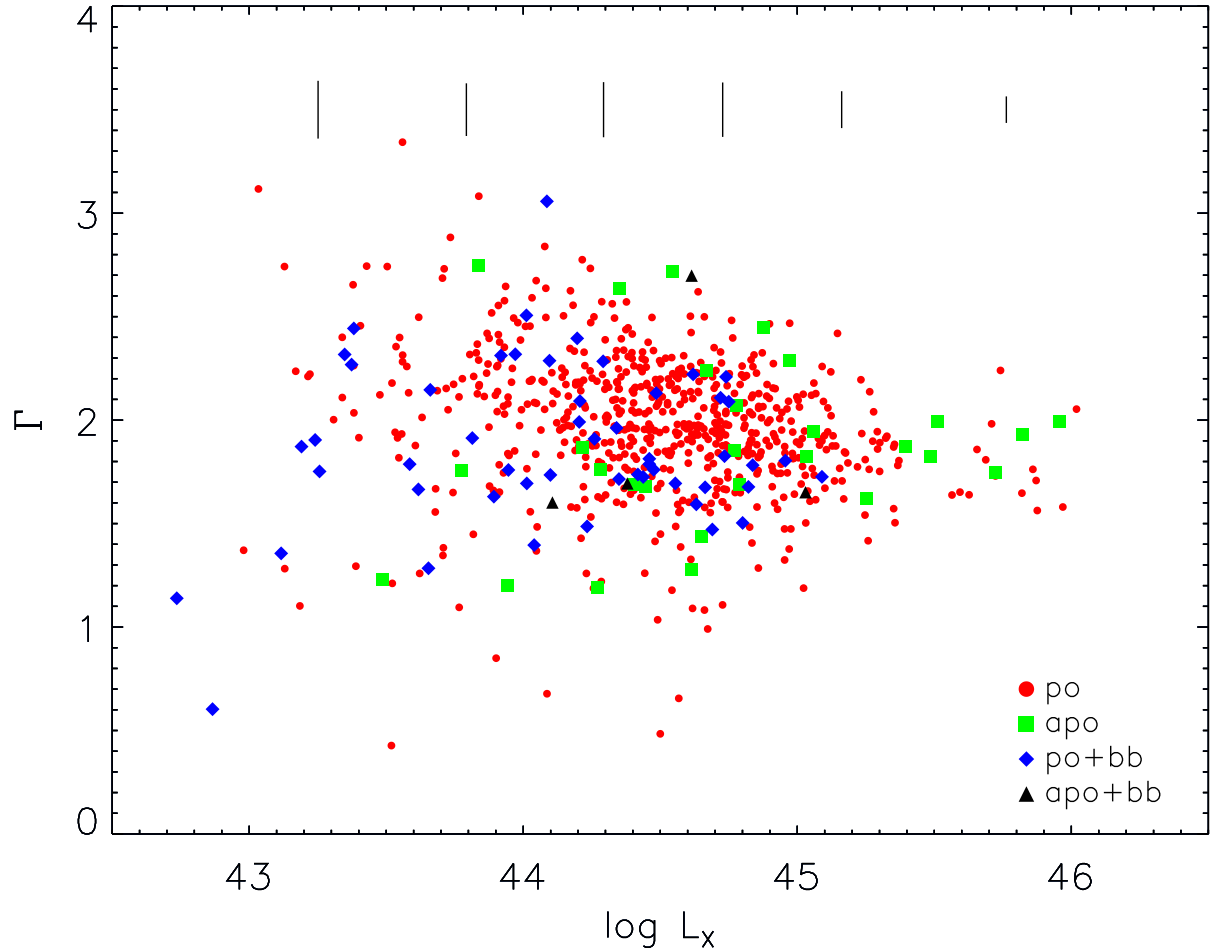


Figure 3.15: This plot includes the 734 sources with $H0 > 1\%$. The different colours/symbols correspond to the best-fitting model; red circles are po, green squares are apo, blue diamonds are po+bb and black triangles are apo+bb. The error bars shown at the top of the plot correspond to the average of each of the 1σ errors on the individual sources.

minimization and fits to a constant value are also considered to determine whether the data are consistent with a $\langle \Gamma \rangle$ that is constant with L_x . These trends along with the null hypothesis probabilities for each model can be found in Table 3.3. Considering sources best-fit with all types of spectral model, the linear trend gives a gradient only consistent with zero at 3σ . However, a constant Γ also gives an acceptable fit to the data meaning that a non-evolving Γ model cannot be ruled out. When only the sources fit with a simple power-law model are considered, the non-evolving Γ model does not provide a good fit to the data and the linear trend gives a gradient inconsistent with zero at 5σ . This suggests that for this sub-set of sources, a significant trend of Γ with L_x is present.

The trends observed are still present in the data when the sample is restricted to sources above certain count levels. For the un-binned data, a significant correlation is still present

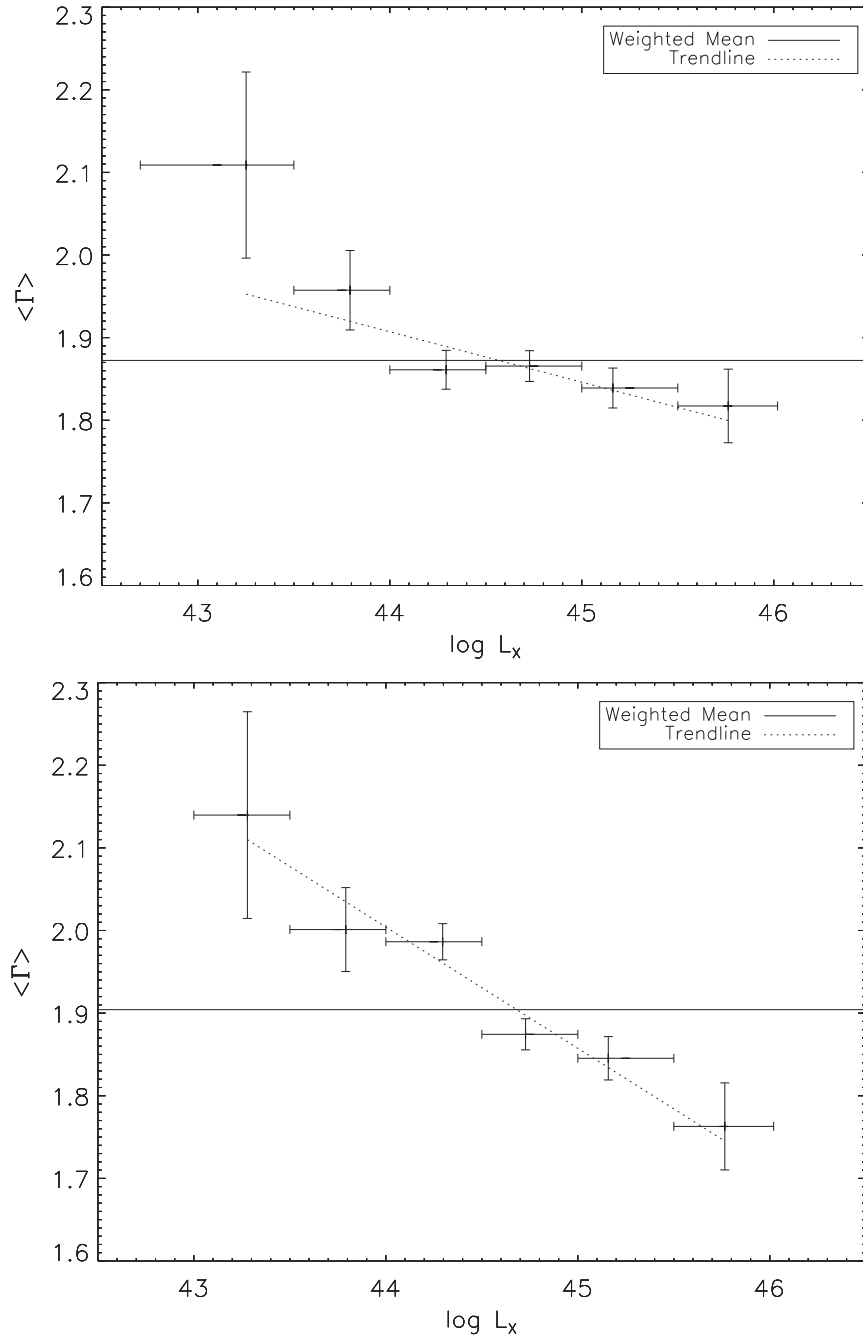


Figure 3.16: These plots show the dependence of weighted Γ values on hard (2 – 10 keV) luminosity. The sources are binned in approximately $\log L_X = 0.5$ bins, although the lower and upper bins do include sources slightly below 43.0 and above 46.0 respectively. The solid horizontal lines indicate the weighted mean values of each sample and the dotted lines show the linear fits to the data. The top plot includes data from 734 sources with good fits using all models and shows a linear fit of $\langle \Gamma \rangle = (-0.06 \pm 0.02) \log L_X + (4.6 \pm 1.1)$. The bottom plot includes data from 650 sources best-fit using the simple power-law model and shows a linear fit of $\langle \Gamma \rangle = (-0.15 \pm 0.03) \log L_X + (8.5 \pm 1.2)$. The y error bars are standard errors on the mean and the x errors indicate the width of the bin.

Correlated Properties	Sources Included	Model	p -value %
Γ and L_X	All	$\langle \Gamma \rangle = (-0.06 \pm 0.02)\log L_X + (4.6 \pm 1.1)$	38.6
		$\langle \Gamma \rangle = 1.87$	4.5
	po only	$\langle \Gamma \rangle = (-0.15 \pm 0.03)\log L_X + (8.5 \pm 1.2)$	45.4
		$\langle \Gamma \rangle = 1.90$	9×10^{-5}

Table 3.3: Listed are the best-fitting linear correlations between Γ and L_X for the binned data, found by χ^2 minimization. The errors on the values are 1σ . The null hypothesis probabilities (p -values) for both the linear models, and constant $\langle \Gamma \rangle$ models are listed, where $p > 1\%$ is taken to be an acceptable fit.

between L_X and Γ even when all the sources with < 1000 counts have been removed, although the significance level does fall. The binned data shows similar results for all count levels i.e. a trend that is only consistent with zero at 3σ (all models) and 5σ (po model). The correlation is still present (5σ) when the RLQ are removed from the sample, tested since it has been suggested that they have flatter spectra than RQQ.

As the sample is flux limited, it is biased towards higher luminosity objects in the higher redshift range. Therefore, the flatter power-law slopes that are observed in higher redshift objects may actually be a consequence of their higher luminosities. Since the stronger correlation is found to be between Γ and L_X , it may be this trend which causes the weaker correlation with redshift. The $\Gamma - L_X$ correlation is also considered in broad redshift bins ($z < 1.0$, $1.0 < z < 1.5$, $z > 1.5$), containing ~ 250 sources in each. A negative correlation is still found in each of the bins, including the highest redshift sources, although the significance of the correlation is lower. This disagrees with the result of Dai et al. (2004) who found a positive correlation for high redshift sources.

A correlation of Γ and L_X is perhaps expected from a consideration of the spectral shapes and how the luminosity is calculated. For example, a source with a steep spectral slope will have less emission over the hard X-ray range, compared with a source with a flat spectral slope but with the same total luminosity. As an example a power-law spectrum with $\sim 10,000$ counts and $\Gamma = 2.4$ was simulated. 52% of the source's luminosity is emitted in the 2.0 – 10.0 keV hard band. A simulated source with the same number of counts, but a flatter slope of $\Gamma = 1.6$ emits a much larger proportion of its luminosity in the hard band, 71%.

Young et al. (2009) report no correlation with redshift, but a strong correlation with luminosity. They report strong correlations between Γ and rest-frame monochromatic luminosities at 0.7, 2.0, 10.0 and 20.0 keV, with the strength of the correlation increasing towards higher energies. However, since the monochromatic luminosity determination depends directly on the Γ value, a correlation between the two quantities is expected. As a flat source has more emission at higher energies than a steep source, it is the flatter sources that will have the higher monochromatic luminosities at these energies. This effect will decrease between $L_{20 \text{ keV}}$ and $L_{2 \text{ keV}}$, until a pivot point at which the steeper sources start to have more emission at the energy at which the monochromatic luminosity is calculated, than the flat sources.

3.3.4 Intrinsic Cold Absorption

Whilst the majority of the sources were well fit by a simple power-law model, some sources were better fit by an absorbed power law which includes an additional intrinsic absorption component at the redshift of the source (modelled by `zphabs` in XSPEC). The requirement of this component was tested by the F-test at 99% significance. An example of a source which is best-fit by this model is shown in Fig. 3.17.

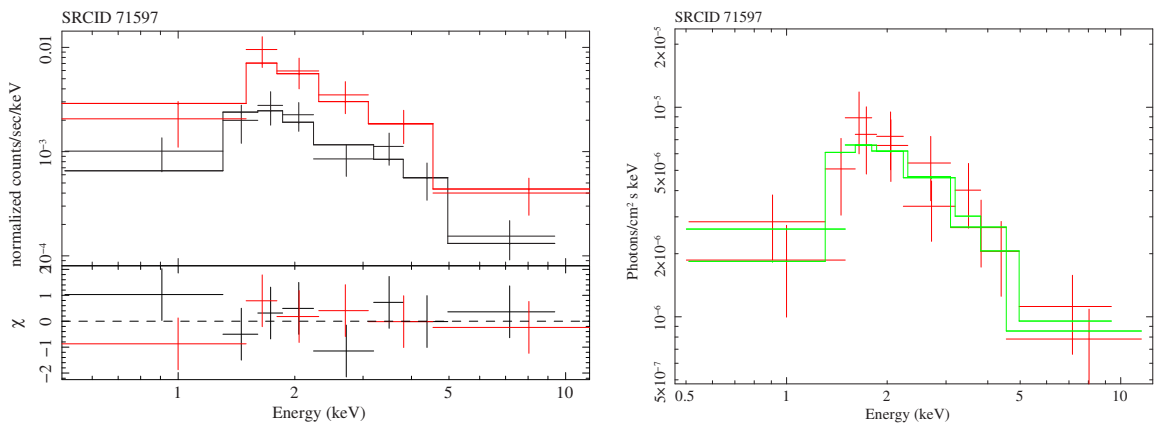


Figure 3.17: This figure includes the raw (left) and unfolded (right) spectra for SRCID 71597 which is best-fit with the absorbed power-law model (apo), where $\Gamma = 1.85 \pm 0.36$ and $N_{\text{H}} = (9.8 \pm 3.6) \times 10^{22} \text{ cm}^{-2}$.

In the sample of 734 sources which have $\text{H0} > 1\%$, 32 sources required an additional absorption component. Setting the F-test confidence level at 99% implies that 1% of detections could be spurious. Taking those into account gives $\sim 3.4\%$ absorbed sources. This represents

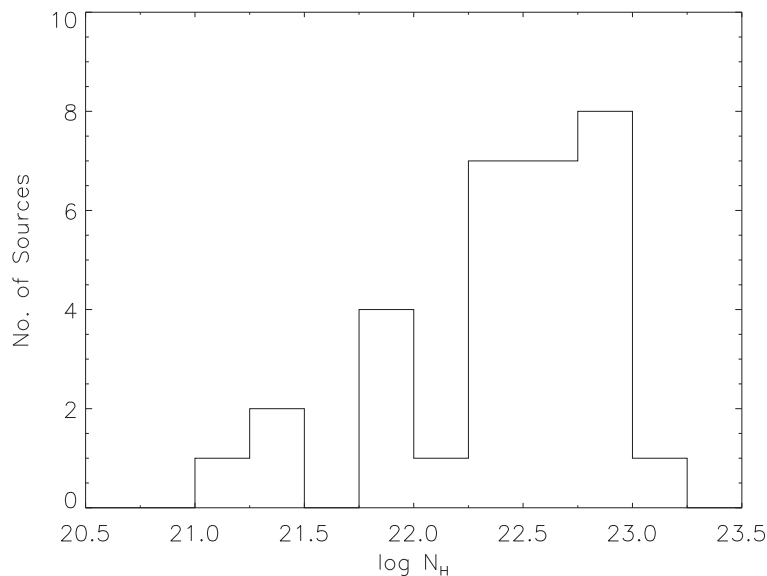


Figure 3.18: The distribution of intrinsic absorbing column densities for the 32 sources in the sample which require an additional absorption component.

only a lower limit since the detection of absorption at the required significance is more difficult in spectra with lower numbers of counts (this will be discussed further in Chapter 5). This value is lower than those in the literature, with many studies reporting absorbed fractions of $\sim 10\%$, albeit for lower F-test significances (Mateos et al., 2005a,b; Mainieri et al., 2007; Young et al., 2009; Corral et al., 2011). Mateos et al. (2010) uses the more stringent significance threshold of 99% as used here, but still find a greater absorbed fraction of $\sim 8\%$.

Both the result presented here, and those found in the literature are at odds with the standard orientation based Unified Model (Antonucci, 1993), which does not predict sources that are optically classified as type 1 to require an absorbed power-law model in X-rays. The typical levels of absorption in the sources range from 10^{21} cm^{-2} to 10^{23} cm^{-2} , higher than is expected for an AGN defined as type 1. Fig. 3.18 shows the distribution of $N_{\text{H}}^{\text{intr}}$ values for all of the absorbed sources in the sample. A visual inspection of the optical spectra of the absorbed sources hints that some may be of an intermediate type (e.g. Sy 1.5), and others may be BALQSOs, offering a possible explanation for their apparent high levels of absorption. Fig. 3.19 shows the optical spectrum of SRCID 141541 (SDSS 154359.44+535903.2) which is was best-fit with an absorbed power-law model and was defined as a BALQSO by Scaringi et al. (2009; see Chapter 4).

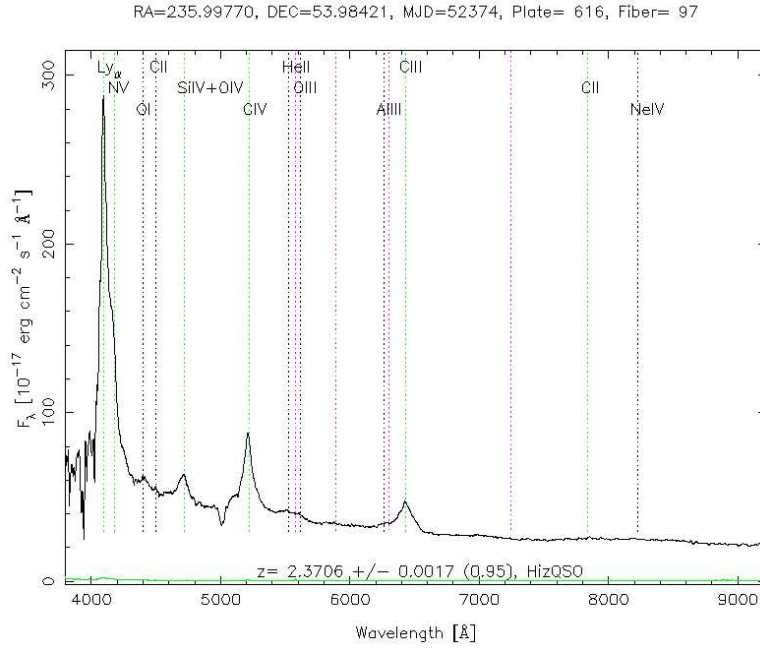


Figure 3.19: The optical spectrum of SRCID 141541 (SDSS 154359.44+535903.2) which is defined as a BALQSO by Scaringi et al. (2009). Its X-ray spectrum was best-fit with an absorbed power-law model with $N_{\text{H}} = (2.6 \pm 0.6) \times 10^{22} \text{ cm}^{-2}$.

Fig. 3.20 (top) investigates the dependence of the intrinsic column densities of the absorbed sources, measured in the rest frame of the source, on redshift. Although it perhaps shows a slight trend for higher absorption levels in higher redshift sources, this can be explained as an observational bias, since sources with low levels of absorption will not be detected at higher redshifts as their absorption signature falls outside of the *XMM-Newton* EPIC bandpass. Absorption is not detected in any sources above $z = 3$ where the detectable lower energy limit corresponds to a source rest-frame energy of $\sim 2 \text{ keV}$. At $z = 2$, where this limit falls to $\sim 1.5 \text{ keV}$, some absorbed sources with the highest column densities become detectable. Considering correlation coefficients, no significant trend between intrinsic column density and redshift is found (Kendall: $\tau = 0.28$, prob = 0.03, Spearman: $\rho = 0.42$, prob = 0.02).

The relationship between $N_{\text{H}}^{\text{intr}}$ and hard X-ray luminosity is considered in Fig. 3.20 (bottom). The X-ray luminosity in the hard band (2 – 10 keV) is used rather than the soft band (0.5 – 2.0 keV) as any intrinsic absorption present in the source would suppress the emission at softer energies. There is no correlation apparent between $N_{\text{H}}^{\text{intr}}$ and L_{X} (Kendall: $\tau = 0.02$, prob = 0.87, Spearman: $\rho = 0.0007$, prob = 1.0).

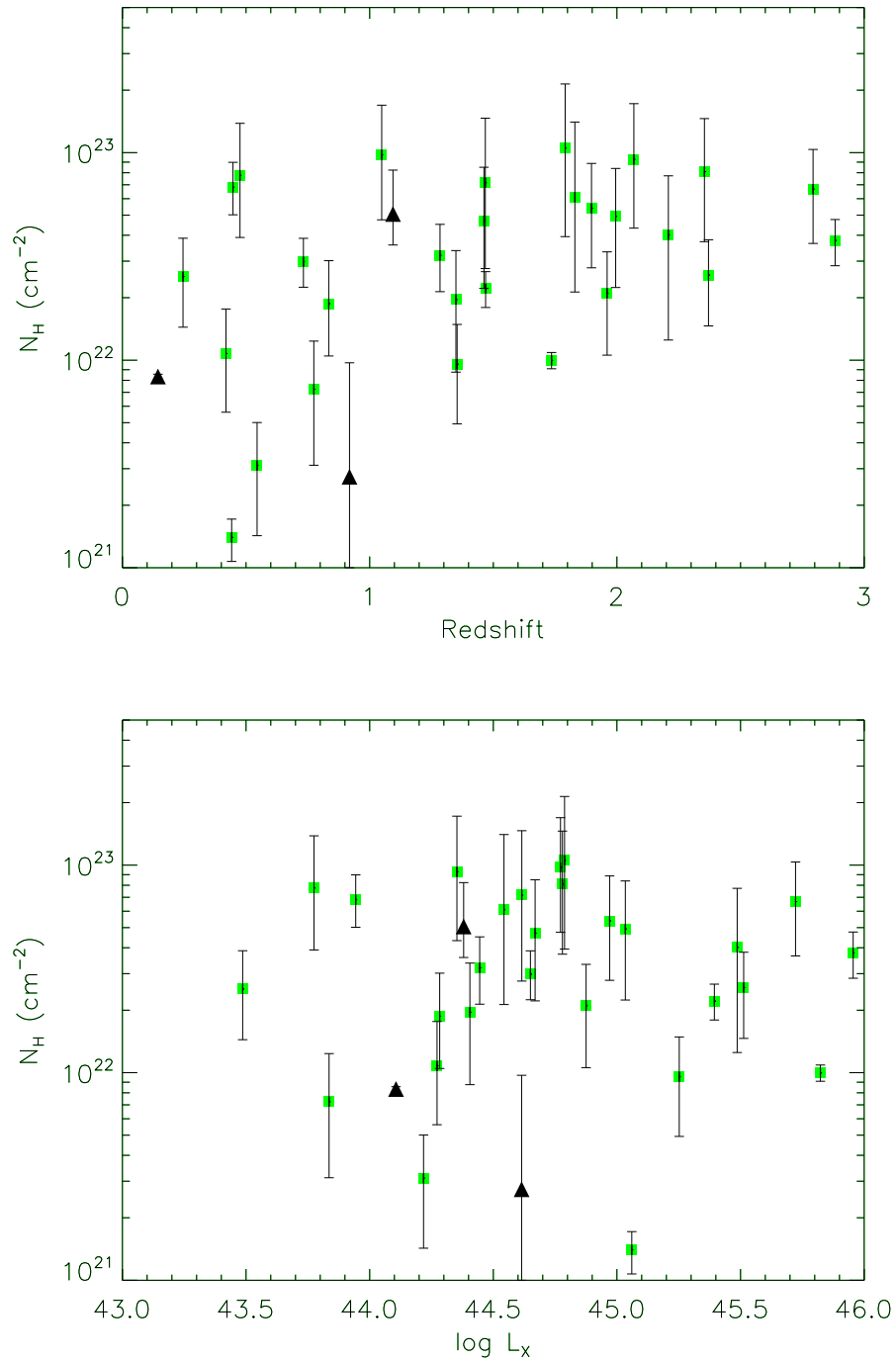


Figure 3.20: The relations between the intrinsic absorbing column density and redshift (top) and 2 – 10 keV X-ray luminosity (bottom). Green squares indicate the sources best-fit with the apo model and black triangles indicate the apo+bb model. The error bars correspond to the 68% confidence range.

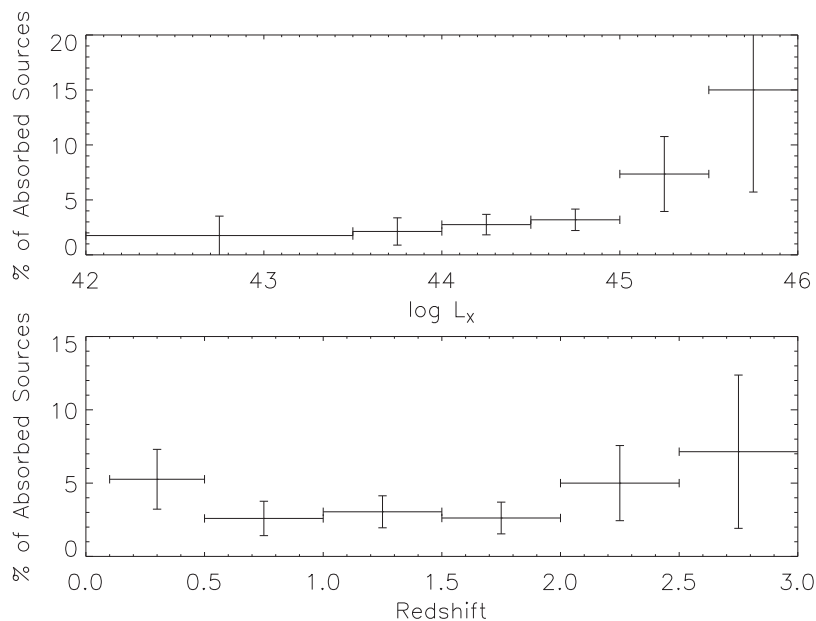


Figure 3.21: These figures show how the percentage of sources that require an intrinsic absorption component in their best-fitting model varies for different luminosity and redshift bins. The x error bars indicate the width of the bins, and the y error bars come from Poissonian counting statistics.

The change in the fraction of absorbed sources with increasing luminosity and redshift is also investigated. This can be seen in Fig. 3.21 and the fraction is found to be constant across the different luminosity and redshift bins. Previous studies (e.g. Hasinger 2008) which include both ‘unabsorbed’ type 1 and ‘absorbed’ type 2 objects find the percentage of absorbed sources decreases with increasing luminosity, which supports the receding torus model of Lawrence (1991). Although the sample here includes only type 1 objects, a small percentage of these have been shown to include intrinsic absorption, which might be expected to behave in a similar way to the absorption found in type 2 objects. However, since the percentage of absorbed objects is shown to remain constant with increasing luminosity, the receding torus model is not supported and the absorption present in these type 1 sources may be of a different nature.

3.3.5 Soft X-ray Excesses

The sources were also fit with models including a soft excess component, modelled with `zbody` in `XSPEC`. Although using a blackbody to model the soft excess component is not strictly physical, it provides a good representation of the spectral signatures and allows a comparison with other studies. An example spectrum of a source best-fit with this model can be

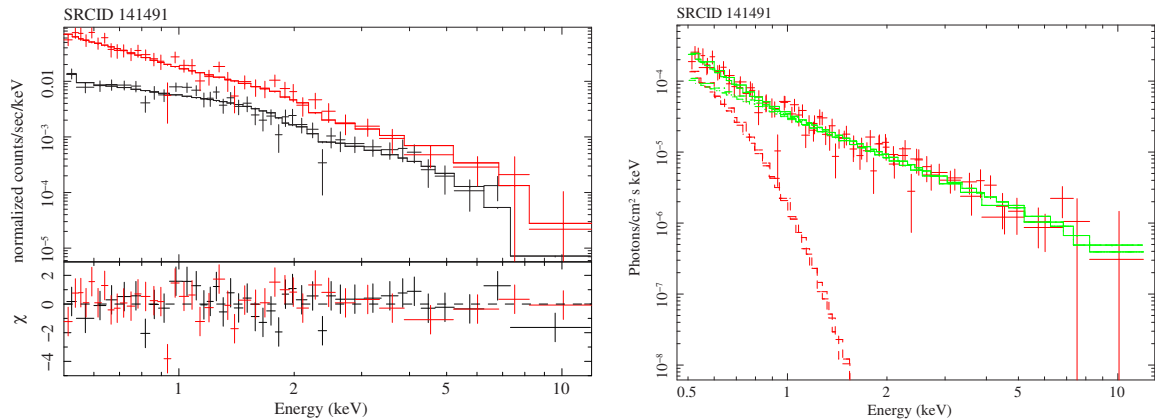


Figure 3.22: This figure includes the raw (left) and unfolded (right) spectra for SRCID 141491 which is best-fit with a power-law model and a soft excess (po+bb), where $\Gamma = 1.90 \pm 0.09$ and $kT = 0.10 \pm 0.02$ keV.

seen in Fig. 3.22. This component is only searched for in sources with X-ray spectra containing at least 100 counts. Using the F-test at 99% significance, this component is detected in 60 of 680 sources. Accounting for spurious detections, the soft excess component is found in 7.8% of the sample. This fraction agrees with previous studies of type 1 AGN (Mateos et al., 2005a, 2010).

In the automatic fitting process, XSPEC is left to fit the po+bb model, which has 5 free parameters, with few constraints. Therefore in some cases a flat power law and a large blackbody component could be chosen as the best-fit since it has a lower value of χ^2 , despite being less physically realistic. Each of the sources best-fit with the po+bb model were also re-fit over the 0.5 – 12.0 keV detector frame energy range with the po+bb model, but with Γ fixed to the value obtained from a simple power-law fit over the 2 – 10 keV rest frame energy range. The Γ and kT values obtained from this fitting were compared to the original fit carried out without constraint (see Fig. 3.23, top). For the majority of sources there was little change between the values, however 7 outliers were identified (as indicated by the red dots). The best spectral fit for these sources was taken to be the new manual fit but the remainder of the sources were left with their automatic fittings. Γ and kT values more consistent with the other sources are then obtained. An F-test between the manual fits and the simple power-law fits is not appropriate since the new fit utilizes a result already obtained from the data. It is therefore assumed that the blackbody component is still statistically required, based on the original best-fit classification. When considering these new fits, the average Γ value steepens to $\Gamma = 1.87 \pm 0.05$ (from Γ

$= 1.80 \pm 0.06$), however a KS test still shows that the distribution is significantly different from that of the entire population (see Fig. 3.12). The Γ values are plotted against the kT values in Fig. 3.23 (bottom) for each of the fits to check for any remaining dependencies. No trend is apparent in this plot, however the sources with the highest kT values (> 0.2 keV) do have $\Gamma < 2$. Spectral fits of the po+bb sources are also considered over the $0.3 - 12.0$ keV range in order to attempt to better constrain the blackbody component. In this instance the benefit of having more bins at lower energies where the soft excess is present, may outweigh the known noise issues of the pn detector, which are highest below 0.3 keV. When these fits are considered, 12 sources would not require the addition of the soft excess component. The average Γ value steepens to $\Gamma = 1.93 \pm 0.05$ and the average kT value falls to $kT = 0.15 \pm 0.01$ keV. This shows the large difference in results that can be obtained when the spectra are modelled over a different energy range, which is usually arbitrarily chosen as a matter of personal preference. Comparisons with results in the literature are therefore only valid when the same energy range has been used.

The mean temperature of the soft excess component when fitted with a blackbody is $\langle kT \rangle = 0.17 \pm 0.09$ keV, obtained from modelling the distribution with a single Gaussian. This is slightly higher than results in the literature (Gierliński & Done, 2004; Mateos et al., 2005b; Winter et al., 2009; Mateos et al., 2010), although consistent within errors. The range in temperatures is observed to be rather small, with 68% of the sources having kT values in the range $0.1 - 0.25$ keV. The full distribution of kT values can be seen in Fig. 3.24.

Correlations between the soft excess temperature $\log(kT)$, and redshift (z), hard X-ray luminosity (L_X), the luminosity of the blackbody component (L_{bb}) and the black hole mass (M_{BH}) are considered⁵. The correlation values and best-fitting linear trends can be found in Table 3.4. No significant correlation with z is found, which is consistent with previous results (e.g. Mateos et al. 2010). Fig. 3.25 (top left) shows the presence of some soft excess components detected even in sources at $z > 1$.

One explanation for the soft excess, and the motivation for modelling it with a blackbody is that it is thermal emission from the inner accretion disc. The standard description predicts

⁵For 29 of the sources that required a blackbody component in the spectral fit, a black hole mass estimate is available from the Shen et al. (2008) catalogue (see §3.3.7 for details).

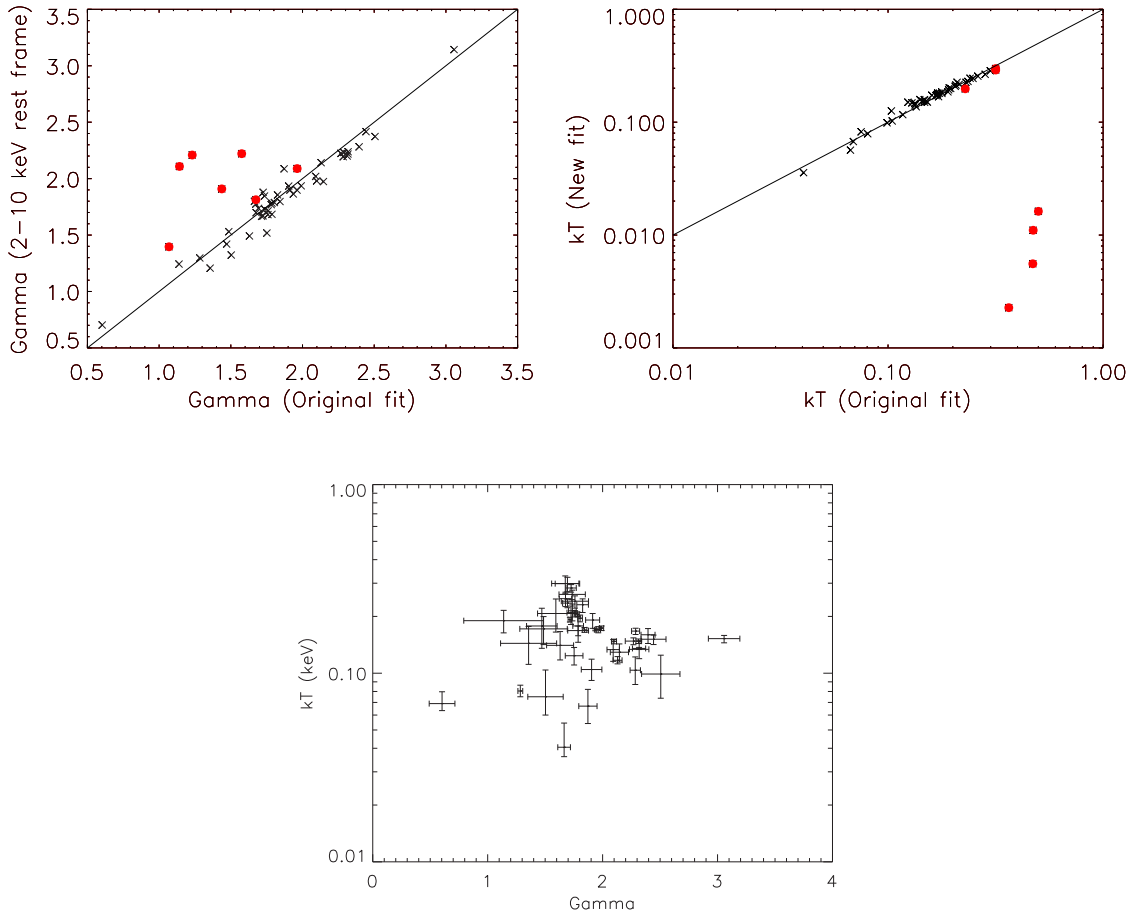


Figure 3.23: Top left - A comparison of the Γ values obtained from the automatic po+bb fit over the 0.5 – 12.0 keV detector frame range and the 2 – 10 keV rest frame range. Top right - A comparison of the kT values from the same fits as described above. The 1:1 lines are included on each plot as a visual aid only and do not represent any particular fit to the data. Bottom - A plot of the Γ values against the kT values for each of the new po+bb fits.

Correlated Properties	Strength of Correlation	Best-fitting Linear Trend
kT and z	2.6σ , $\rho = 0.37$, sig= 0.009	$\log(\text{kT}) = (0.61 \pm 0.01)z - (1.059 \pm 0.004)$
kT and L_X	4.4σ , $\rho = 0.59$, sig= 0.00001	$\log(\text{kT}) = (0.08 \pm 0.01)\log(L_X) - (4.3 \pm 0.2)$
kT and L_{bb}	2.2σ , $\rho = 0.33$, sig= 0.03	$\log(\text{kT}) = (0.15 \pm 0.01)\log(L_{\text{bb}}) - (7.4 \pm 0.5)$
kT and M_{BH}	3.0σ , $\rho = 0.57$, sig= 0.003	$\log(\text{kT}) = (0.18 \pm 0.01)\log(M_{\text{BH}}) - (2.3 \pm 0.1)$

Table 3.4: The Spearman rank correlation coefficients and significances for correlations between the characteristic blackbody temperature used to model the soft excess, kT, and the parameters z , L_X , L_{bb} and M_{BH} . The best-fitting linear trends were determined by χ^2 minimization.

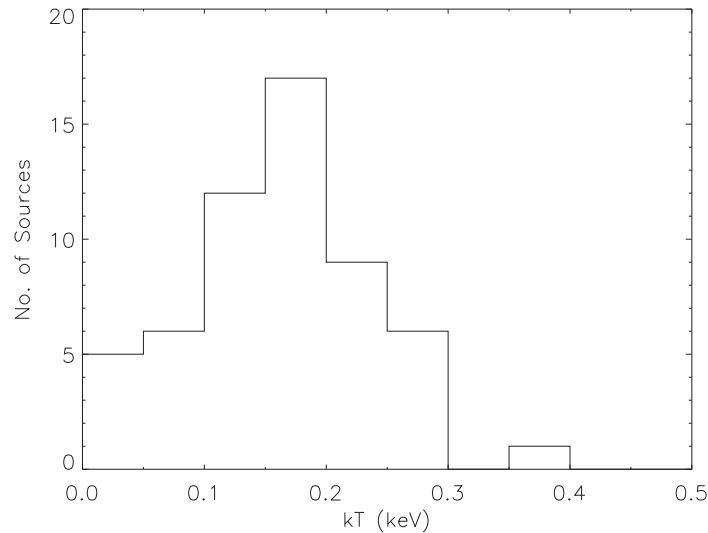


Figure 3.24: The distribution of kT values for the 56 sources in the sample which require the additional soft excess component and whose best-fit provides an acceptable fit to the data.

characteristic temperatures of the order $kT \sim 0.02$ keV for a $10^8 M_{\odot}$ black hole, as determined from $T_{\text{disc}} \propto M^{-1/4}(L/L_{\text{Edd}})^{1/4}$ (Shakura & Sunyaev 1973, see Chapter 1). Therefore the average kT value for this sample is too high to be consistent with the standard disc origin. This also implies that the kT values should show variations with black hole mass and luminosity, with negative and positive linear trends, respectively.

For each of the sources fit with a po+bb model, the luminosities in the separate blackbody and power-law components were computed, both over the 0.5 – 10.0 keV energy range. A significant correlation between kT and L_X is found (see Fig. 3.25 bottom left), but no significant correlation with L_{bb} is present (see Fig. 3.25 top right). A 3σ correlation is found between kT and M_{BH} , but the best-fitting linear trend shows a positive, rather than a negative gradient as would be expected. This result disagrees with that of Bianchi et al. (2009) who report the temperature of the blackbody component used to model the soft excess to be unrelated to the mass of the black hole.

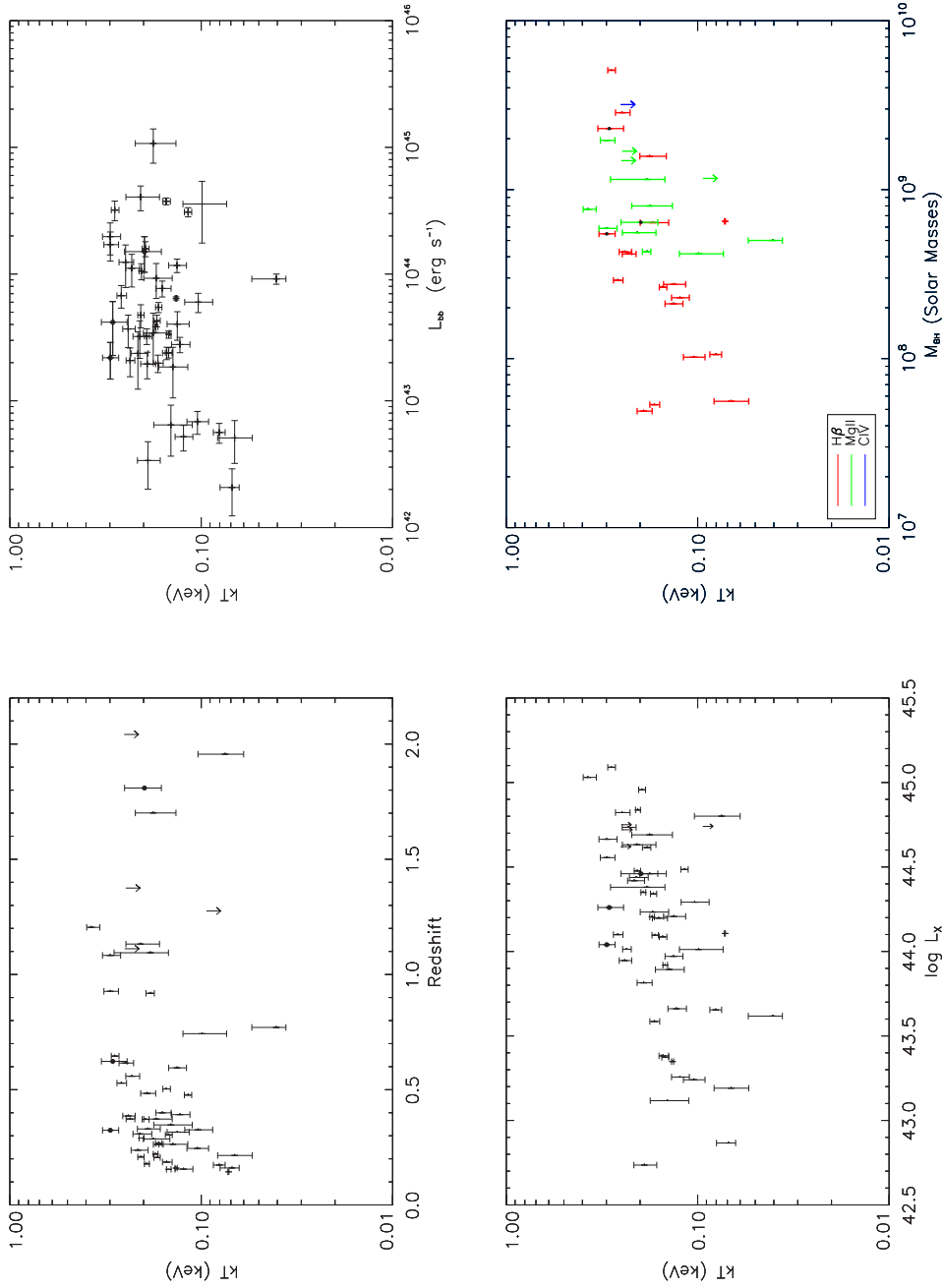


Figure 3.25: The relations between the characteristic soft excess temperature, kT , and redshift (top left), hard X-ray luminosity (bottom left), blackbody luminosity (top right) and black hole mass (bottom right). The error bars correspond to the 68% confidence range. Only sources for which $H0 > 1\%$ are included on these plots. Sources indicated by the filled black circles or upper limits are the ones fit with a manual $po+bb$ model as described in the text. These sources are not included in the determination of any correlations or linear trends, however they are shown to be consistent with the rest of the sample.

Previous studies have reported no trend of kT with luminosity (Bianchi et al., 2009; Winter et al., 2009). This problem was first highlighted by Gierliński & Done (2004), and led to the development of new theories, moving away from the accretion disc origin. They invoke the idea that since the soft excesses display a narrow range of kT values, the physical process behind their origin is likely to be one of constant energy, such as atomic transitions. At ~ 0.7 keV, lines and edges of ionized OVII and OVIII produce a strong jump in opacity. If these features are smeared by high velocities or gravitational redshifts, as found close to a black hole, a featureless soft excess would be produced. Therefore the soft excess component could be an artefact of ionized absorption, likely from an outflowing disc wind (Gierliński & Done, 2004). Alternatively, the partially ionized material could be out of the line of sight and seen via reflection. In this scenario, the hard X-ray source needs to be at a small height above the disc so that light bending can illuminate the inner disc. In this case the soft excess component is an artefact of relativistically blurred photoionized disc reflection (Ross & Fabian, 2005).

It is possible that the observed relation between kT and L_X is due to an observational bias. As the sample is flux limited, the higher luminosity sources tend to be the ones at higher redshifts where the soft excess feature starts to be redshifted out of the *XMM-Newton* EPIC bandpass. Therefore the lowest temperature soft excesses may not be detected in higher redshift (and higher L_X) sources, leading to an apparent trend. However, Fig. 3.25 (top, left) shows this effect is not strong.

In Fig. 3.26, the black hole mass is plotted against the blackbody luminosity and a $\sim 3\sigma$ correlation is found. This suggests that regardless of the origin of the soft excess, its luminosity is likely related to the mass of the black hole.

Fig. 3.27 shows a strong ($\sim 8\sigma$) correlation between the luminosity of the blackbody component and the luminosity of the power-law component with a best-fitting trend of $\log L_{\text{bb}} = (0.78 \pm 0.02)\log L_{\text{PL}} + (9.2 \pm 1.0)$. This indicates a link between the energy production in these two components and supports the idea of inverse Compton scattering where the low energy photons from the disc are up-scattered to X-ray energies creating the power-law emission. However it could also imply a reverse process in which the power-law emission is re-processed into the lower energy soft excess.

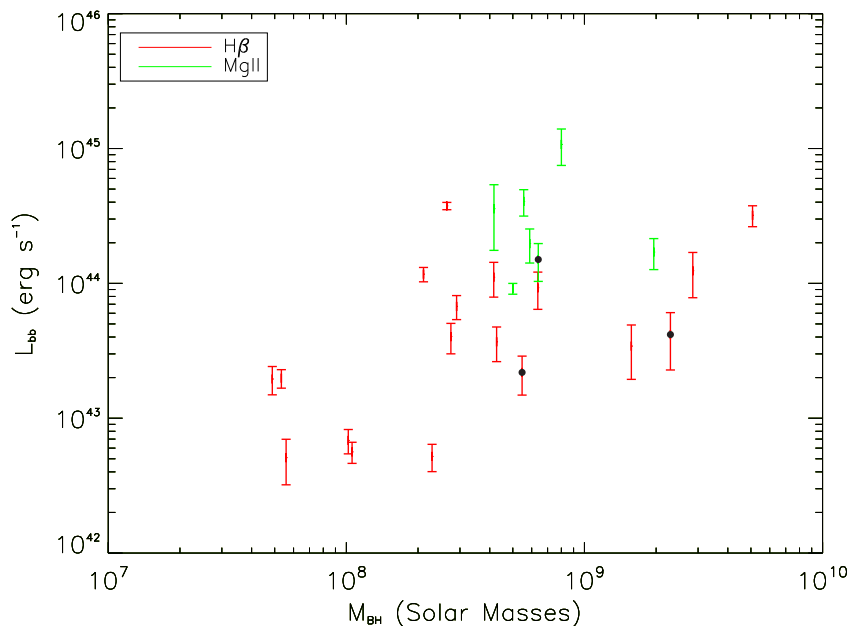


Figure 3.26: This figure includes the 25 sources best-fit with the po+bb model, for which a black hole mass estimate is available and L_{bb} can be determined. The different colours correspond to the different emission lines used in the mass determination (red - $\text{H}\beta$, green - MgII). It shows the dependence of the black hole mass on the luminosity of the blackbody component, determined over the 0.5 – 10.0 keV range. The errors shown on L_{bb} correspond to the 68% confidence range. The black circles indicate the sources fit with the manual po+bb model.

This correlation has been previously reported in Winter et al. (2009) and a similar correlation is seen in Mateos et al. (2010) where the power-law luminosity over 2 – 10 keV is plotted against the blackbody luminosity over 0.5 – 2 keV. It is suggested that the lack of sources in the bottom right of the plot is a selection effect due to the fact that a low luminosity blackbody component will be difficult to detect over a high luminosity power-law component and the lack of sources in the top left of the plot is due to an apparent upper limit to the soft excesses allowed in AGN. These linear relationships, each with gradients close to 1, imply that the fraction of converted emission is constant for sources of all luminosities. However all 3 data sets show that in the luminosity range $10^{42} - 10^{46} \text{ erg s}^{-1}$, the luminosity in the power law is greater than that in the blackbody component.

3.3.6 Radio Properties

In order to determine the radio loudness of the objects, the sample was cross-correlated with the FIRST (Becker et al., 1995) catalogue (see Chapter 2 for details). The optical source positions were used in the matching, since they have lower errors than the X-ray positions. A

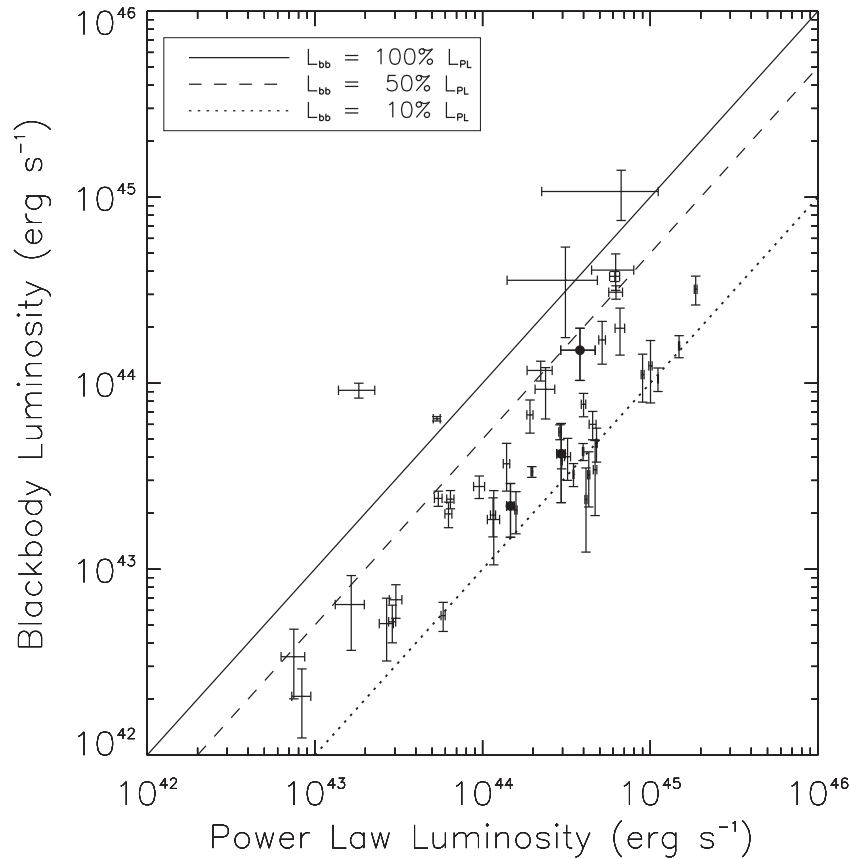


Figure 3.27: This plot compares the luminosity included in each of the separate components of the po+bb fits, calculated over the 0.5 – 10.0 keV range. The linear trendline is $\log L_{\text{bb}} = (0.78 \pm 0.02)\log L_{\text{PL}} + (9.2 \pm 1.0)$. The errors shown in these plots correspond to the 68% confidence range. The black circles indicate the sources fit with the manual po+bb model and are consistent with the rest of the sources. The lines indicate the locations of $L_{\text{bb}} = L_{\text{PL}}$ (solid), $L_{\text{bb}} = 50\%L_{\text{PL}}$ (dashed) and $L_{\text{bb}} = 10\%L_{\text{PL}}$ (dotted) but do not represent any particular fit to the data.

20'' matching radius was used so as to ensure that any extended radio emission such as jets and lobes would be included. However, this larger search radius increases the possibility of matching to a physically unrelated source. 128 unique AGN were matched to at least one source in FIRST, with 25 of these having more than one match. In these cases, the flux was taken to be the sum of each of the integrated fluxes. For the remaining AGN, $5 \times \text{RMS}$ value at each particular source position was used as an upper limit, this level being chosen to match the requirement for a source to be included in the FIRST catalogue (i.e. this is the maximum flux that a source could have if it was present at that location, but was not detected as a source). The flux at 1.4 GHz ($F_{1.4\text{GHz}}$) measured by FIRST was extrapolated to a flux at 5 GHz ($F_{5\text{GHz}}$, F_{R}) by assuming the radio emission is described by a power law with spectral index $\alpha = -0.8$ (see Eqn. 3.3). Although this offers a good approximation for extended radio sources, compact

radio sources tend to have flatter spectral indices of $\alpha \sim 0$.

$$F_{5 \text{ GHz}} = F_{1.4 \text{ GHz}} \left(\frac{5 \text{ GHz}}{1.4 \text{ GHz}(1+z)} \right)^{-0.8} \quad (3.3)$$

The optical SDSS magnitudes were converted to fluxes in mJy using Eqn. 3.4⁶ after first being corrected for Galactic extinction and converted to the AB system. The flux at 4400Å (F_O) was determined from a linear interpolation of the optical fluxes in each of the *ugriz* bands. The radio loudness was then calculated as $R_L = F_R/F_O$, and a source was considered to be radio loud if $R_L > 10$ (Kellermann et al., 1989).

$$\text{Flux} = 3631000 \times 10^{\frac{\text{magnitude}}{-2.5}} \text{ mJy} \quad (3.4)$$

552 (72%) were found to be radio-quiet quasars, 75 (10%) radio-loud quasars, 90 (12%) were sources whose upper limits are too high to determine their radio loudness with confidence and 44 (6%) sources lay outside the FIRST coverage area and therefore a radio loudness could not be determined. If the sources with radio upper limits are assumed to be either all radio quiet or all radio loud, the radio-loud fraction lies between $\sim 10\%$ and $\sim 22\%$, respectively, in broad agreement with previously reported values (e.g. Kellermann et al. 1989). The properties of the RQQ and RLQ sub-samples are investigated in this section.

There are 5 radio-loud quasars whose X-ray spectra are best-fit with an absorbed model which suggests optical obscuration may also be present. Determining the radio loudness using the parameter R_L , which depends on the optical emission makes it susceptible to extinction effects and in the case of heavily optically obscured sources the determined radio loudness may appear unusually high. Fig. 3.28 considers the optical extinction value, A_V , as a function of radio loudness. A similar range of R_L values are found for a range of both positive and negative extinction values suggesting no strong bias is present. The A_V values are taken from Hutton et al. (in preparation) and are obtained via a comparison of the optical spectra with a composite de-reddened spectrum. Therefore in this case, the negative extinction values are obtained when the source is bluer than expected.

⁶www.sdss.org/dr5/algorithms/fluxcal.html#counts2mag

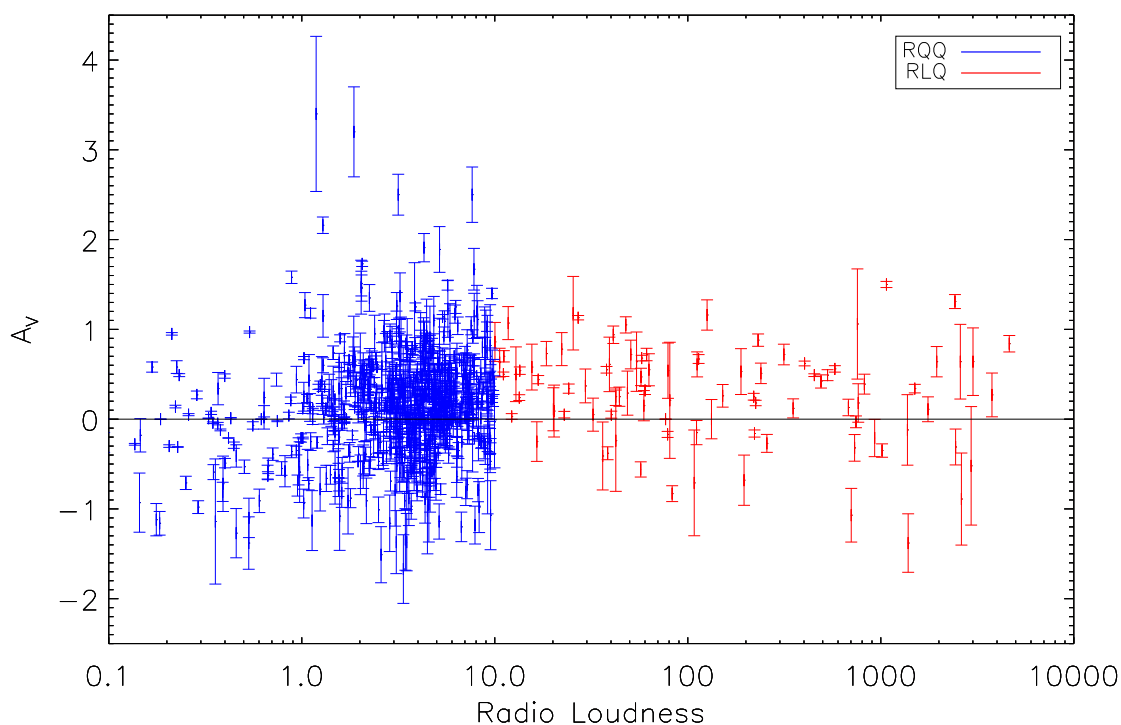


Figure 3.28: This figure plots the radio loudness parameter, R_L , against the optical extinction, A_V .

The distributions of absolute i band magnitudes for the RQQ and RLQ sub-samples are found to not be significantly different (KS significance = 0.39, Fig. 3.29 top left). In addition, the redshift distributions are not significantly different (KS significance = 0.87, Fig. 3.29 top right). The X-ray luminosity distributions are found to be significantly different (KS significance = 8×10^{-9} , Fig. 3.29 middle left), with RLQ having higher 2–10 keV X-ray luminosities. Since the redshift distributions are the same, this is likely due to a physical difference in the sources rather than an observational bias from the sample being flux limited. This suggests that an additional mechanism of producing X-rays is present, which increases the total X-ray emission. This idea has been previously suggested by Reeves & Turner (2000). The additional component is perhaps related to the jet and may be Synchrotron Self Compton (SSC) scattering where the radio photons produced as synchrotron emission from electrons spiralling in a magnetic field, undergo inverse Compton scattering off the same electrons, up to X-ray energies (Band & Grindlay, 1986). It is thought that the synchrotron emission produced in RLQ will contaminate the power law produced by inverse Compton scattering, making the X-ray spectrum appear flatter. The Γ distribution of the sub-samples of RLQ and RQQ (see Fig. 3.29,

middle right), are found to be significantly different (KS significance = 3×10^{-5}). When modelled with a single Gaussian, the RQQ distribution has a mean value of $\Gamma = 2.01 \pm 0.01$, whereas the RLQ distribution has a lower mean value of $\Gamma = 1.86 \pm 0.02$, however the two populations cover a similar range of Γ values. Flat Γ values in RLQ are noted in the literature, although the actual values found here are steeper than those reported. Reeves & Turner (2000) found an average of $\Gamma = 1.66 \pm 0.04$ for a sample of 35 RLQ and $\Gamma = 1.89 \pm 0.05$ for 27 RQQ. The intrinsic dispersion of Γ values is $\sigma_{\langle\Gamma\rangle} = 0.31 \pm 0.01$ for the RQQ, which is similar to that for the entire original sample and $\sigma_{\langle\Gamma\rangle} = 0.20 \pm 0.02$ for the RLQ, which is considerably lower. The typical 68% error on Γ for the RLQ is 0.08, significantly lower than the intrinsic dispersion. Fig. 3.29 (bottom) shows the best-fitting $\langle\Gamma\rangle$ and $\sigma_{\langle\Gamma\rangle}$ values and 1σ , 2σ and 3σ confidence contours from the Gaussian fitting of the Γ distributions. This clearly shows that the Γ distribution for RLQ has a lower dispersion than that for RQQ and the average $\langle\Gamma\rangle$ value is also lower.

Fig. 3.30 (top) plots Γ against the radio loudness parameter R_L . The solid line shows the average Γ value for the RLQ sample whilst the dashed line shows the best-fitting linear trend to the RLQ. Flatter Γ values are expected for increasing levels of radio loudness as suggested from Fig. 3.29 and the idea that the power-law spectrum will become contaminated by emission from the radio jet. Such an anticorrelation has been seen in previous works for low redshift quasars (e.g. Wilkes & Elvis 1987; Reeves & Turner 2000) and a recent study including observations of $z > 4$ RLQ also finds a strong anticorrelation, suggesting that the $\Gamma - R_L$ relation does not change with redshift (Saez et al., 2011). The data is inconsistent with a constant Γ fit ($p = 0\%$), but the F-test shows that the linear fit is not statistically required. This is also the case when the combined RQ and RL populations are considered. Since both the constant and linear fits give poor fits to the data due to the large spread in values, the data is also considered when it is binned by radio loudness as shown in Fig. 3.31 (top). In this case the data is well fit by the constant Γ model ($p = 15.3\%$) and an F-test does not require the linear model. This is again also true for the combined RQ and RL populations and therefore there is no significant trend observed between R_L and Γ , contrary to results in the literature.

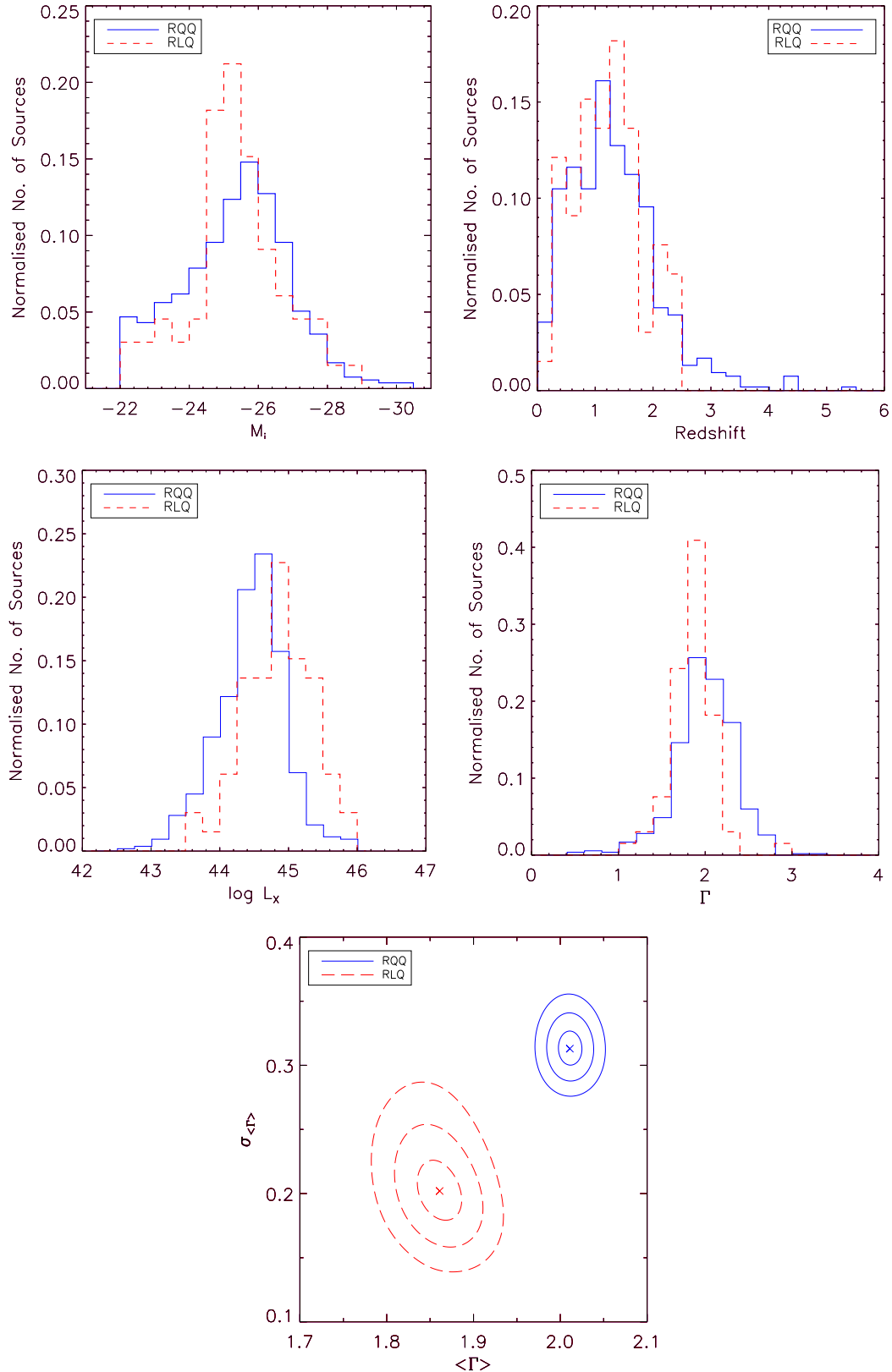


Figure 3.29: These plots compare the absolute i band magnitudes (top left), redshift (top right), 2 – 10 keV luminosity (middle left) and Γ (middle right) distributions of the confirmed radio-quiet (solid blue) and radio-loud (dashed red) sources. The bottom figure shows the best-fitting $\langle \Gamma \rangle$ and $\sigma_{\langle \Gamma \rangle}$ values (crosses) and 1 σ , 2 σ and 3 σ confidence contours from the Gaussian fitting of the Γ distributions for the RQQ and RLQ sub-samples.

Fig. 3.30 (bottom) plots L_X against the radio loudness parameter R_L . The solid line shows the average L_X value for the RLQ and the dashed line shows the best-fitting linear trend to the RLQ sample. The result from Fig. 3.29 and works in the literature suggests that the more radio-loud objects also tend to be more X-ray luminous. RLQ were found to be more X-ray luminous than their RQQ counterparts with similar optical/UV luminosities (Zamorani et al., 1981) and the X-ray luminosity was found to increase with increasing radio luminosity (Worrall et al., 1987). Recent work suggests that for very radio-loud quasars ($\log R_L \sim 4$), the X-ray luminosity can be a factor of ~ 10 brighter than in RQQ (Miller et al., 2011). The data is inconsistent with a constant luminosity model ($p = 0\%$), but a linear fit is not statistically required. For the combined RQ and RL populations, the linear trend is required, but this model still does not provide a good fit to the data ($p = 0\%$). When binned data is considered (shown in Fig. 3.31, bottom), the constant $\log L_X$ model is still a poor fit to the RLQ ($p = 5 \times 10^{-11}$), but the linear model is now statistically required. However, the gradient of the linear trend is 0.17 ± 0.08 which is only significant at $\sim 2\sigma$. For the combined RQ and RL populations, the linear trend is not required for the binned data.

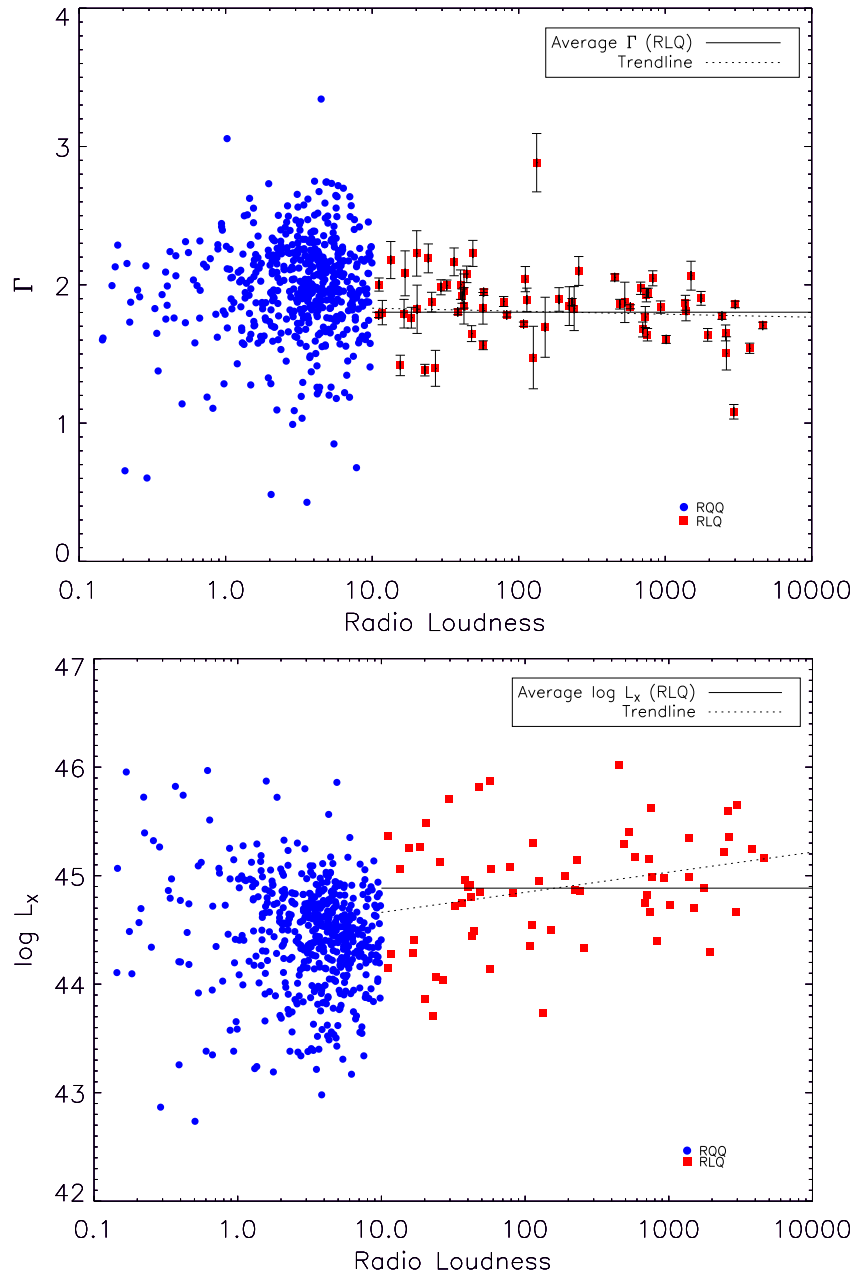


Figure 3.30: This plots the radio loudness, R_L , as a function of the best-fitting Γ values (top) and $\log L_X$ (bottom). The RLQ are shown as red squares and the errors on Γ correspond to the 68% confidence level. The RQQ are shown as blue circles, for which the errors on Γ have been omitted for reasons of clarity. The solid lines show the average Γ (1.80) and $\log L_X$ (44.88) values for the RLQ sample, which represent the non-evolving models. The dashed lines show the best-fitting linear trends to the RLQ: $\Gamma = (-0.022 \pm 0.006)\log R_L + (1.85 \pm 0.02)$ and $\log(L_X) = (0.17 \pm 0.002)\log R_L + (44.5 \pm 0.003)$.

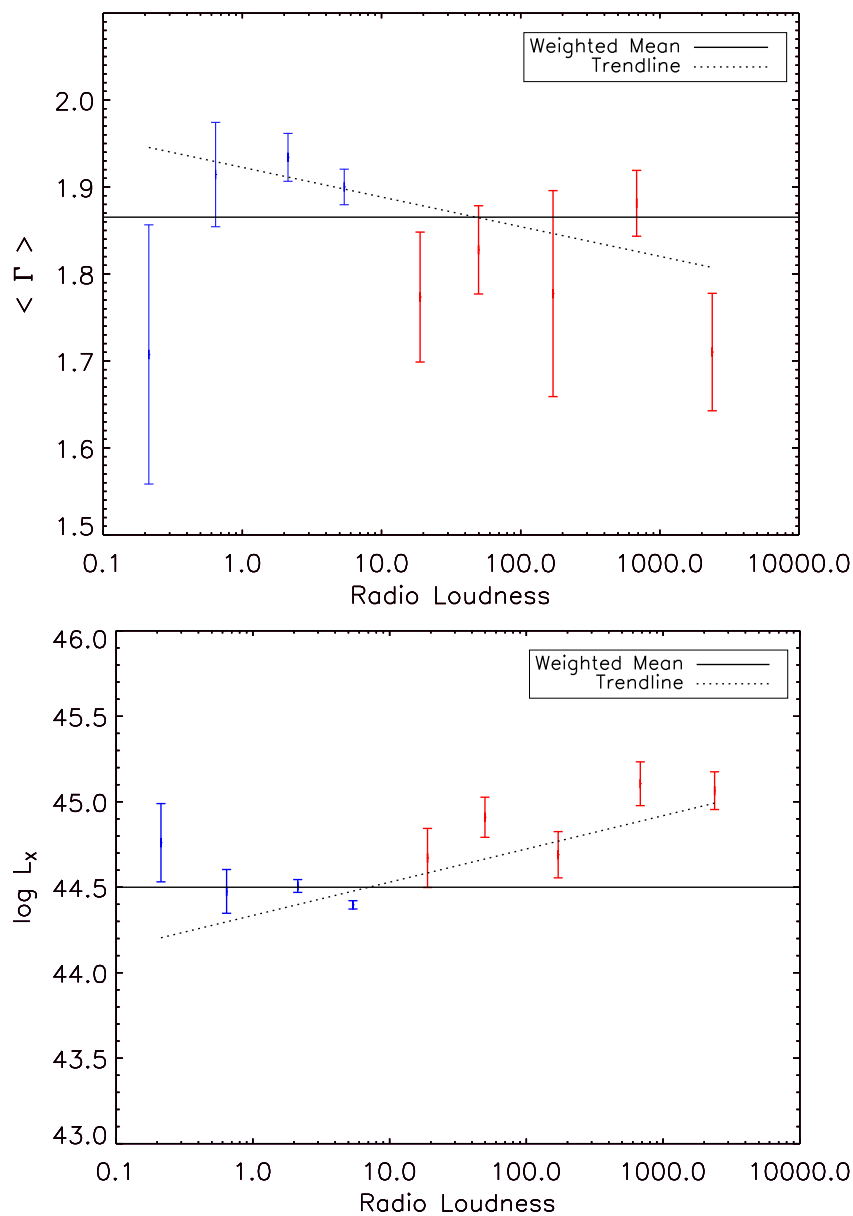


Figure 3.31: This shows the trend between R_L and $\langle \Gamma \rangle$ (top) and R_L and $\log L_X$ (bottom) binned by radio loudness.

3.3.7 Accretion Properties

Since the X-ray emission is believed to originate from the accretion process, relationships between the X-ray spectral properties and the physical properties of the central engine are expected. In this section correlations between the Eddington ratio and both the broadband continuum and the soft excess properties are considered. Differences in the Eddington ratios between the radio-loud and radio-quiet sub-samples are also investigated.

As described in Chapter 1, virially determined black hole mass estimates can be obtained by using optical spectra to estimate the widths of the broad emission lines and the monochromatic luminosity at a particular wavelength. This method was used by Shen et al. (2008) to provide black hole mass estimates for $\sim 58,600$ quasars in the SDSS DR5 quasar catalogue. A power-law continuum and iron emission template are subtracted from the optical spectra to leave isolated broad lines which are fit with two Gaussians to model both the broad and narrow components in order to determine the FWHM. Monochromatic luminosities are determined at 5100\AA , 3000\AA and 1350\AA using the calibrations of McLure & Dunlop (2004) and Vestergaard & Peterson (2006). Three mass estimates are calculated using a different broad line and monochromatic luminosity and the best estimate is chosen depending upon the redshift of the source; $H\beta$ is used for $z < 0.7$, $MgII$ for $0.7 < z < 1.9$ and CIV for $z > 1.9$. The $H\beta$ and $MgII$ masses are reported to be consistent, with a dispersion of 0.22 dex, but the $MgII$ and CIV masses show a larger scatter of 0.34 dex. Mass estimates are available for 581 (79%) sources in the sample and are shown in Fig. 3.32. The bolometric luminosity is also calculated from the monochromatic luminosity using bolometric correction factors determined by Richards et al. (2006) from a composite SED of DR3 quasars.

The Eddington luminosity is calculated using Eqn. 3.6. The bolometric luminosity is calculated from the observed X-ray luminosity in the $2-10$ keV band, L_X , using the luminosity dependent bolometric correction of Marconi et al. (2004) described by Eqn. 3.7 where $\mathcal{L} = \log L_{\text{bol}} - 12$ and L_{bol} is in units of L_{\odot} . The Eddington ratio is then defined as:

$$\lambda_{\text{Edd}} = \log \left(\frac{L_{\text{bol}}}{L_{\text{Edd}}} \right). \quad (3.5)$$

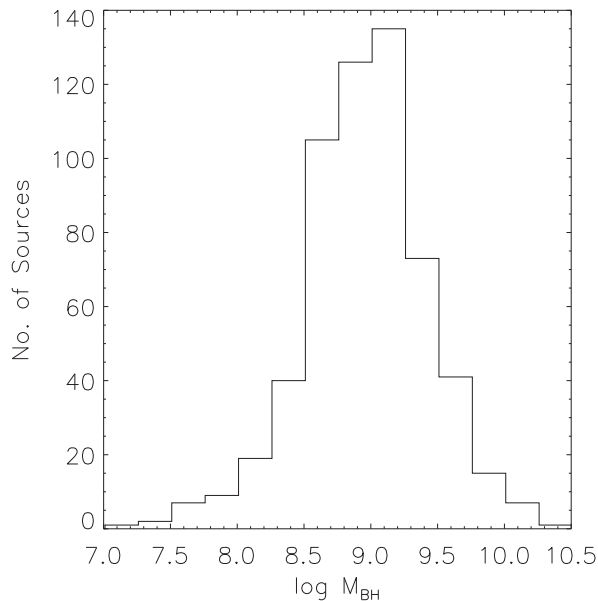


Figure 3.32: The distribution of black hole mass estimates taken from Shen et al. (2008) for 581 sources in the sample.

$$L_{\text{Edd}} = \frac{4\pi GMm_{\text{p}}c}{\sigma_{\text{T}}} \sim 1.3 \times 10^{38} \frac{M}{M_{\odot}} \text{erg s}^{-1} \quad (3.6)$$

$$\log(L_{\text{bol}}/L_{\text{X}}) = 1.54 + 0.24\mathcal{L} + 0.012\mathcal{L}^2 - 0.0015\mathcal{L}^3 \quad (3.7)$$

Fig. 3.33 (left) shows the relationship between Γ (as determined from the 0.5 – 12.0 keV detector frame) and the Eddington ratio, separated depending on which broad line was used to estimate the black hole mass. A positive correlation is found for the $\text{H}\beta$ data (Spearman rank correlation coefficient, $\rho = 0.26$, 2.8σ), there is no correlation for the MgII data ($\rho = -0.10$, 2.0σ) and a negative correlation is found for the CIV data ($\rho = -0.32$, 2.9σ), however the reliability of the CIV line as a mass estimator has been widely questioned (e.g. Shen et al. 2008). The virial method for determining black hole masses is calibrated using results from reverberation mapping studies. These are only widely available for low redshift objects, giving a well calibrated method using the $\text{H}\beta$ broad line but a less reliable calibration for the MgII and CIV lines which are simply scaled to match the $\text{H}\beta$ results. Shen et al. (2008), from whom the black hole mass estimates are taken, note that the estimates determined from the $\text{H}\beta$ and MgII lines tend to agree with each other, but the masses estimated from the CIV

line do not. The C_{IV} lines can be severely affected by a disc wind component and therefore may be asymmetric and blueshifted, leading to an overestimate of the width of the line and a FWHM which is not representative of the virial velocity of the broad line region (e.g. Baskin & Laor 2005). However, some authors have reported consistency between black hole masses determined with the H β , MgII and C_{IV} lines (Greene et al., 2010; Assef et al., 2011). Whilst the different correlations seen may be due to a calibration effect, the possibility of a hidden physical effect cannot be ruled out. By necessity different broad lines are used for sources at different redshifts and the C_{IV} line is used for sources at high redshifts and likely high X-ray luminosities. Therefore the difference in these parameters may be the true driver behind the different trends seen with Eddington ratio.

The result differs slightly from that of Risaliti et al. (2009b) who find a highly significant, positive correlation with estimates based on the H β line, a significant, although weaker positive correlation with MgII and no significant correlation with C_{IV}. However, in their analysis they use the bolometric luminosity given by Shen et al. (2008). Therefore Fig. 3.33 (right) shows the relationship between Γ and the Eddington ratio, where the Eddington ratio is determined from the optically derived bolometric luminosity given in the Shen et al. (2008) catalogue. In this case significant positive trends are found when the H β and MgII lines are used to determine the black hole mass (8σ and 4σ , respectively), but no significant correlation is found when the C_{IV} line is used (1.9σ). This result is in agreement with Risaliti et al. (2009b) and suggests that the waveband used in determining the bolometric luminosity can have a considerable impact on the conclusions of such studies. Fig. 3.34 compares the distributions of the X-ray and optically derived Eddington ratios, which a KS test finds to be significantly different (significance = 3×10^{-7}).

Previous studies of PG Quasars with *XMM-Newton* have also reported a positive correlation between Γ and Eddington ratio (Porquet et al., 2004; Piconcelli et al., 2005) and Shemmer et al. (2006) show that this is the dominant correlation, as opposed to the known relation between accretion rate and line width. This correlation suggests that the sources with flatter power-law slopes found at high redshift in §3.3.2 could be due to a low Eddington ratio. Of the 4 sources at $z > 3.5$ for which a black hole mass estimate is available, two have signif-

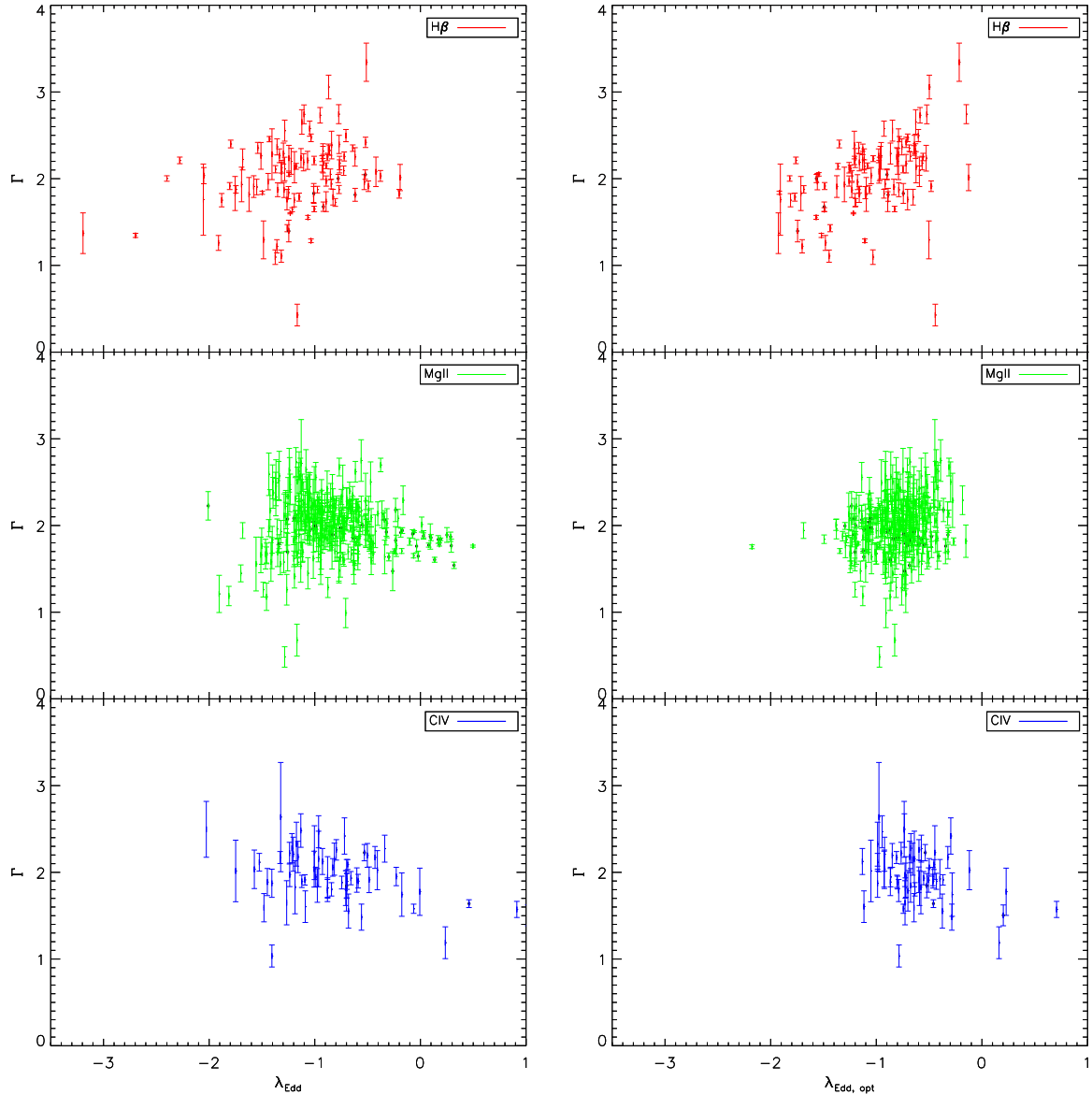


Figure 3.33: This figure shows the relationship between Γ and the Eddington ratio, where the latter is based on mass estimates obtained using different broad emission lines. Top: 117 sources for which the $H\beta$ line was used. Middle: 385 sources for which the $MgII$ line was used. Bottom: 79 sources for which the CIV line was used. The error bars correspond to 68% errors. Sources indicated with the black dots are RLQ. The left hand panel uses the X-ray derived bolometric luminosity to determine the Eddington ratio, whilst the right hand panel uses an optically derived bolometric luminosity.

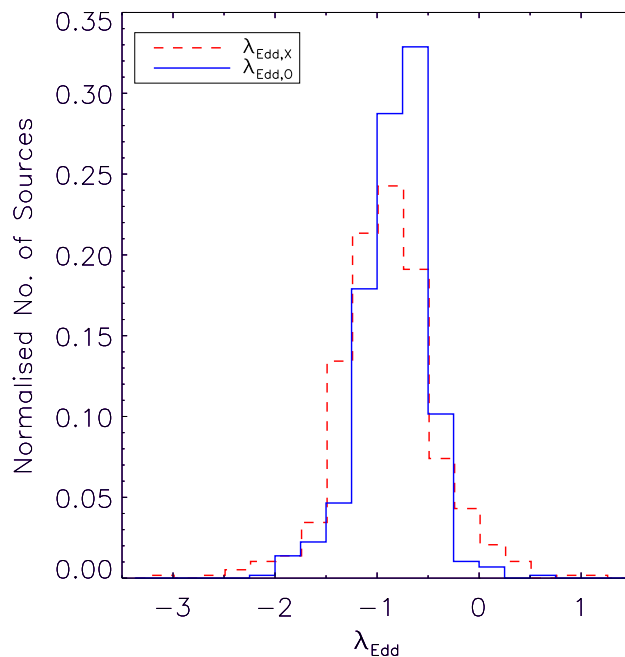


Figure 3.34: A comparison of the X-ray derived (dashed red) and optically derived (solid blue) Eddington ratios, $\lambda_{\text{Edd}} = \log(L_{\text{bol}}/L_{\text{Edd}})$

icantly lower optically derived Eddington ratios than the rest of the sample. The other two sources have masses significantly higher than the rest of the sample, consistent with the anti-correlation between Γ and M_{BH} found by Risaliti et al. (2009b). However, not all sources with a flat power-law slope have a high M_{BH} and/or a low Eddington ratio. This is shown in Fig. 4.4 where the distributions of black hole masses and optically derived Eddington ratios for sources with flat power-law slopes are found to not be significantly different from the rest of the sample.

Since §3.3.5 indicated a strong relationship between the luminosities in the blackbody component and the power-law component, and the properties of the power-law component have been shown to correlate with the Eddington ratio, the dependence of the blackbody properties on Eddington ratio are also investigated. Fig. 3.35 considers the dependence between kT (top), blackbody luminosity (middle) and black hole mass (bottom) and both the X-ray derived (left) and optically derived (right) Eddington ratio. No significant correlations are found ($kT = 1.8\sigma$, $L_{\text{bb}} = 2.5\sigma$, $M_{\text{BH}} = 0.3\sigma$ for $\lambda_{\text{Edd}, X}$ and $kT = 1.5\sigma$, $L_{\text{bb}} = 0.8\sigma$, $M_{\text{BH}} = 2.5\sigma$ for $\lambda_{\text{Edd}, \text{opt}}$). This agrees with Shemmer et al. (2008) who also find the soft excess does not depend strongly on Eddington ratio.

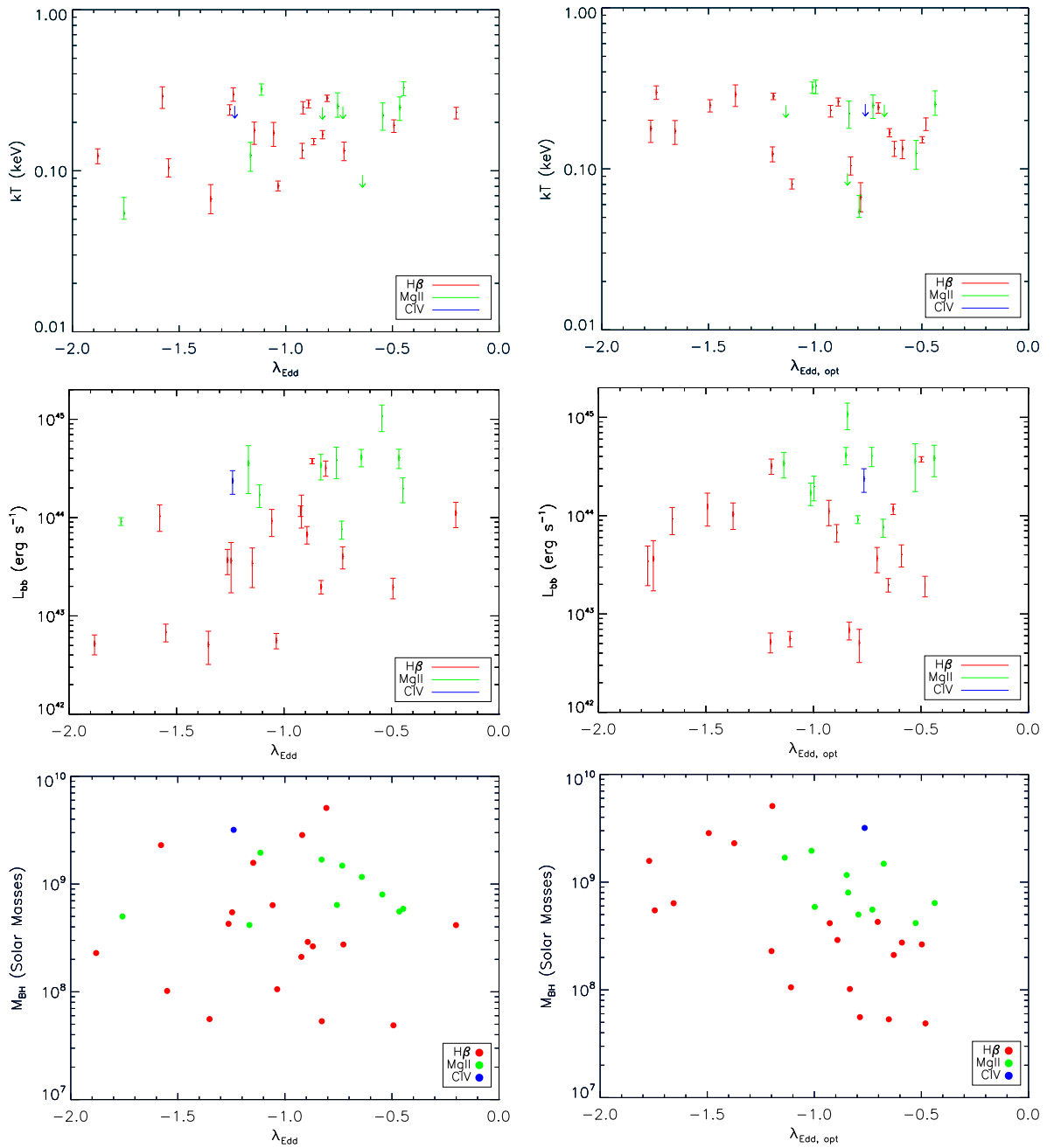


Figure 3.35: These figures show the relationship between kT (top), L_{bb} (middle), M_{BH} (bottom) and the Eddington ratio. The left plots use the X-ray derived Eddington ratio, whilst the plots on the right use the optically derived Eddington ratio.

Sources included		Best-fitting linear trend
X-ray	RLQ & RQQ	$\log(\lambda_{\text{Edd}, \text{X}}) = (0.19 \pm 0.03)\log R_{\text{L}} - (1.03 \pm 0.03)$
	RLQ	$\log(\lambda_{\text{Edd}, \text{X}}) = (0.4 \pm 0.1)\log R_{\text{L}} - (1.3 \pm 0.2)$
Optical	RLQ & RQQ	$\log(\lambda_{\text{Edd}, \text{opt}}) = (-0.02 \pm 0.02)\log R_{\text{L}} - (0.81 \pm 0.02)$
	RLQ	$\log(\lambda_{\text{Edd}, \text{opt}}) = (0.09 \pm 0.07)\log R_{\text{L}} - (1.05 \pm 0.17)$

Table 3.5: Listed are the best-fitting linear trends between radio loudness, R_{L} , and Eddington ratio (derived from both X-ray and optical bolometric luminosities), for the combined RQ and RL populations, and just the RLQ on their own.

In order to investigate a possible link between radio jet production and accretion rate, the distribution of Eddington ratios for the confirmed RLQ and RQQ sub-samples are compared (see Fig. 3.37, top) and a possible trend between radio loudness and Eddington ratio is investigated (see Fig. 3.37, bottom). Both an X-ray derived Eddington ratio and an optically derived Eddington ratio using the bolometric luminosities derived by Shen et al. (2008) are considered. The best-fitting linear trends are listed in Table 3.5.

The distribution of X-ray derived Eddington ratios is significantly different between the RQQ and RLQ sub-samples (KS significance = 2×10^{-10}), with RLQ having higher Eddington ratios. However, when the optically derived Eddington ratios are compared, no significant difference is found (KS significance = 0.50). Similarly, a significant trend towards higher X-ray derived Eddington ratios in sources with a higher radio loudness is suggested. This trend is not found when optically derived Eddington ratios are used. Since RLQ have higher X-ray derived Eddington ratios, there is an inherent bias present in the consideration of R_{L} with Eddington ratio when both the RQQ and the RLQ are included which could be causing the observed trend. However, a trend for increased R_{L} with higher X-ray derived Eddington ratio is also present within just the RLQ sub-sample. This might argue for models in which jet formation and hence radio emission depend on the accretion mode/Eddington ratio in analogy with Galactic stellar mass black holes. The lack of a correlation between radio loudness and an optically derived Eddington ratio is in disagreement with previous results which find an anti-correlation suggesting lower Eddington ratios in more radio-loud sources (Ho, 2002; Sikora et al., 2007). The differences found between using X-ray derived and optically derived Eddington ratios could be an artefact of the additional X-ray component which may be present in RLQs (see

§3.3.6). Whereas the optical emission of RQQ and RLQ is similar (the distributions of M_i were not found to be significantly different), the X-ray luminosity of the radio-loud sources was found to be higher, which results in relatively higher X-ray derived Eddington ratios for these sources. Since any difference in black hole mass would result in different Eddington ratios, the distributions are compared in Fig. 3.36. They are found to be consistent between RQQ and RLQ sources (KS significance = 0.68). There is no clear consensus in the literature as to whether the black hole masses of RQQ and RLQ are consistent. A dependence of the amount of radio flux on the mass of the black hole was first suggested by Franceschini et al. (1998) and the black hole masses of RLQ were found to be, on average, a factor of 2 higher than those of RQQ (McLure & Dunlop, 2002; Metcalf & Magliocchetti, 2006) with the highest black hole masses ($> 10^9 M_\odot$) being found solely in RLQ (Laor, 2000). Strong correlations between both the radio luminosity and the radio loudness parameter with the mass of the black hole have been reported (Lacy et al., 2001; Liu et al., 2006) suggesting that jet production may be related to the black hole mass. However, other studies have found there to be no correlation between black hole mass and radio power or the radio loudness measure (Oshlack et al., 2002; Woo & Urry, 2002; Ho, 2002; Snellen et al., 2003).

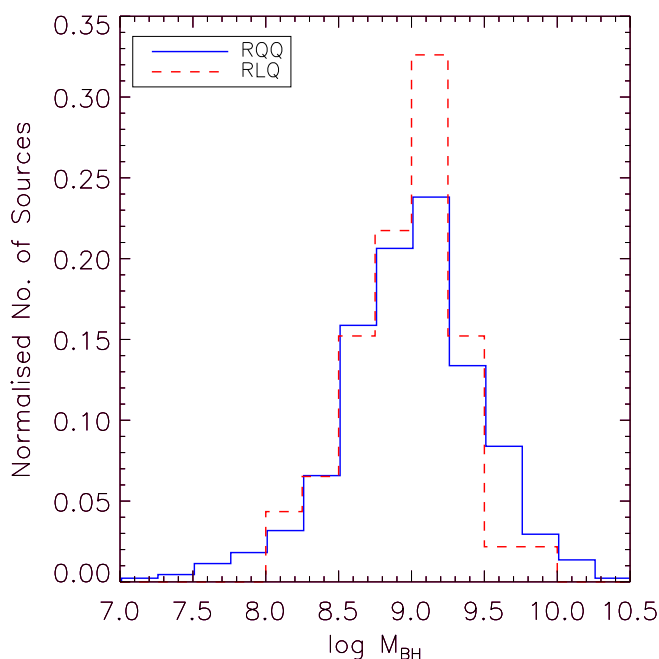


Figure 3.36: This compares the black hole mass distributions of the confirmed radio-quiet (solid blue) and radio-loud (dashed red) sources.

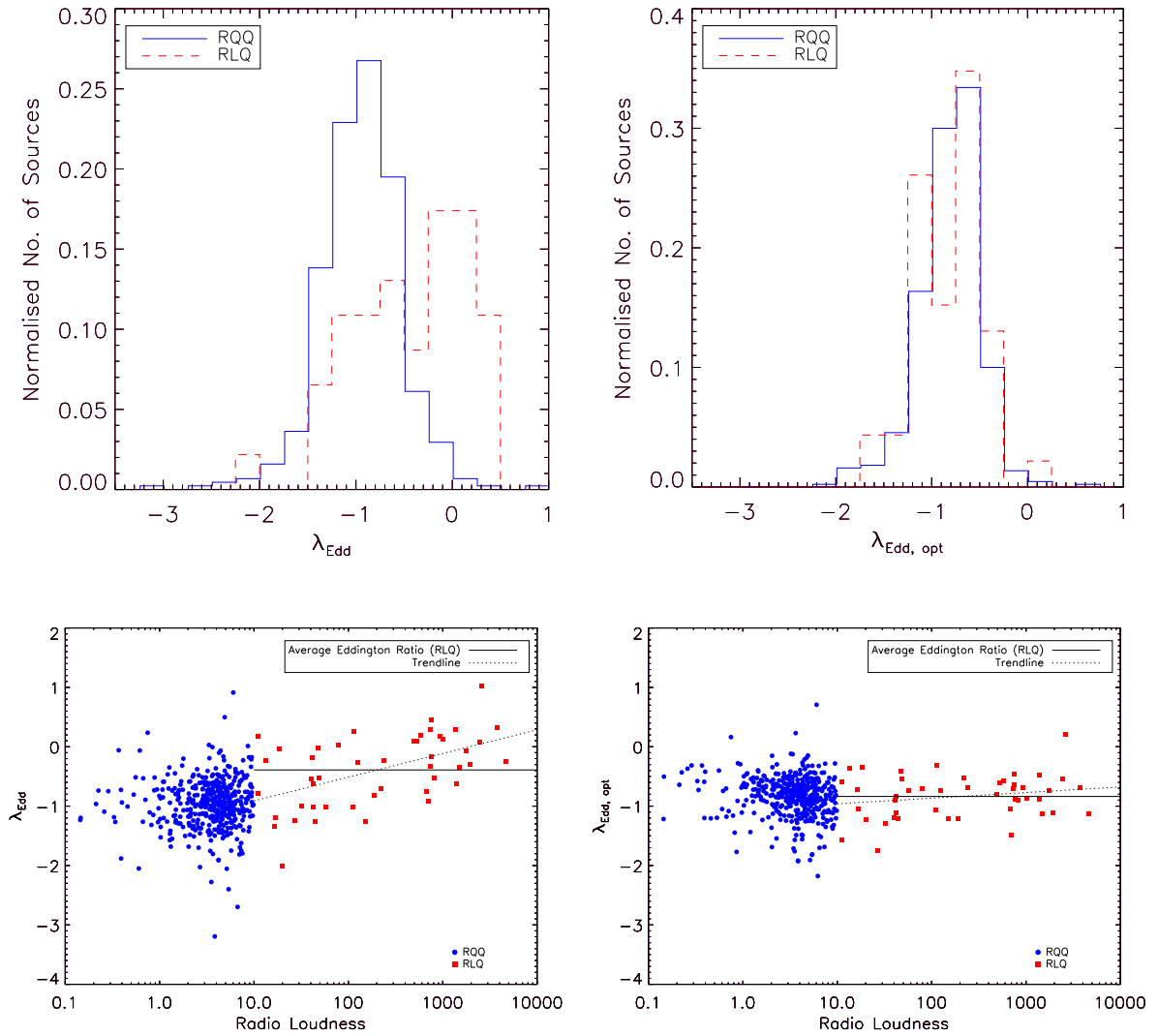


Figure 3.37: The top figures show the Eddington ratio distributions of the confirmed radio-quiet (solid blue) and radio-loud (dashed red) sources. The bottom figures show the trend of R_L with the Eddington ratio with the best-fitting trend to the RLQ is shown by the dashed line. The figures on the left use Eddington ratios defined from the observed 2 – 10 keV X-ray luminosity and the luminosity dependent bolometric correction of Marconi et al. (2004). The figures on the right use Eddington ratios defined from monochromatic luminosities in the optical and UV by Shen et al. (2008), and bolometric correction factors from Richards et al. (2006).

3.4 Summary

In this Chapter the X-ray spectra of a sample of 761 type 1 AGN from a cross-correlation of the SDSS DR5 quasar catalogue and 2XMMi have been analysed. The main conclusions are summarized below:

1. When the distribution of best-fitting power-law slopes is modelled with a single Gaussian, the best-fitting values are found to be $\langle\Gamma\rangle = 1.99 \pm 0.01$ with an dispersion of $\sigma_{\langle\Gamma\rangle} = 0.30 \pm 0.01$. The typical 68% error on a source is $\Delta\Gamma = 0.13$, which is much lower than the intrinsic dispersion of values. The distribution is better modelled with a combination of two Gaussians due to the presence of extreme sources with flat or steep Γ values.
2. A marginal trend ($\sim 3\sigma$) for flatter Γ values in higher redshift sources is found, but only when just those sources best-fit by a simple power-law model are used. This apparent flattening does not appear to be due to the presence of a reflection component in the spectrum at higher energies.
3. A significant trend ($\sim 5\sigma$) for flatter Γ values in higher X-ray luminosity sources is found.
4. Evidence for intrinsic neutral absorption is found in 3.4% of the sample, however, this is a lower limit (see Chapter 5). The levels of absorption ($N_{\text{H}} = 10^{21} - 10^{23} \text{ cm}^{-2}$) are higher than those expected for objects defined in the optical as type 1. No trend is found between $N_{\text{H}}^{\text{intr}}$ and redshift or X-ray luminosity. The fraction of absorbed sources does not appear to vary with luminosity or redshift.
5. Evidence for a soft excess component is found in $\sim 8\%$ of the sample, but again this is a lower limit. The average blackbody temperature used to model the soft excess is $\langle\text{kT}\rangle = 0.17 \pm 0.09 \text{ keV}$. This temperature is shown to correlate with hard (2 – 10 keV) luminosity (4.4σ).
6. A strong correlation ($\sim 8\sigma$) is found between the blackbody luminosity and power-law luminosity for those sources best-fit with the po+bb model with the soft excess

luminosity being $\sim 10 - 50\%$ that of the power-law luminosity.

7. A positive correlation ($\rho = 0.26, 2.8\sigma$) between Γ and the X-ray derived Eddington ratio is found when the broad $H\beta$ line is used in the determination of the black hole mass. No such trend is found when the MgII line is used and a negative correlation ($\rho = -0.32, 2.9\sigma$) is found when the CIV line is used. However, these results change when an optically derived Eddington ratio is considered. The blackbody properties kT , L_{bb} and M_{BH} are not found to correlate with Eddington ratio.
8. 10% of the sample are RLQ and 72% are RQQ. The RLQ have higher X-ray luminosities compared to the RQQ. This may be due to an additional X-ray component, perhaps related to a jet, which also causes RLQ to show flatter Γ values and higher Eddington ratios if L_{bol} is calculated from the X-ray luminosity.

4

Extreme Sources in the SDSS/2XMMi AGN

Sample

Chapter 3 characterised the X-ray spectral shape of a typical type 1 AGN. The majority of sources were found to consist of a simple power law with index $\Gamma \sim 2$, however, some sources with particularly flat or steep Γ values were also identified. In this Chapter these sources are studied in more detail.

4.1 Introduction

In Chapter 3, the X-ray spectral properties of a sample of 761 type 1 AGN were studied in detail. The underlying spectrum was found to consist of a power law; the average spectral index being $\Gamma = 1.99 \pm 0.01$ with an intrinsic dispersion of $\sigma = 0.30 \pm 0.01$. Section 3.3.1 described how the distribution of best-fitting power-law slopes was not well modelled with a single Gaussian distribution, but a combination of two Gaussians, in which the second Gaussian was statistically required, did give an acceptable fit. This suggested the presence of extreme sources in the wings of the Γ distribution with particularly flat or steep Γ values.

Since the X-ray emission of AGN comes from the central regions of the source, changes in this emission, particularly the power-law slope are likely to be related to the accretion process. Therefore, objects with intrinsically flat or steep Γ values are interesting to study in more detail. They may be displaying an extraordinary state of accretion and the production mechanism for the X-ray power law must be able to explain them. The extreme sources in the SDSS/2XMMi sample of Chapter 3 are studied in this chapter in order to investigate their properties and determine their nature.

4.2 Full Extreme Sample

The creation of the initial sample of 761 type 1 AGN and subsequent X-ray spectral fitting were described in §3.2. A Gaussian fit to the resulting distribution of best-fitting power-law slopes suggested an excess of extreme sources with flat or steep Γ values. This excess is apparent at $\pm 1.5\sigma$, where $14.9 \pm 1.1\%$ of sources are found in wings, compared with an expected 13.4%. A ‘full sample’ of extreme sources is defined such that any source with a Γ value outside of the $\Gamma_{\text{av}} \pm 1.5\sigma$ range is included. This gives 58 flat sources with $\Gamma < 1.54$ and 51 steep sources with $\Gamma > 2.44$, as shown in relation to the original Γ distribution in Fig. 4.1.

The counts/redshift distribution of the extreme sources can be seen in Fig. 4.2 (top), where the flat sources are shown with red circles and the steep with blue circles. The black crosses are the sources which do not have extreme Γ values. In general the extreme sources are found at lower count levels than the non-extreme population, although there are 10 extreme sources

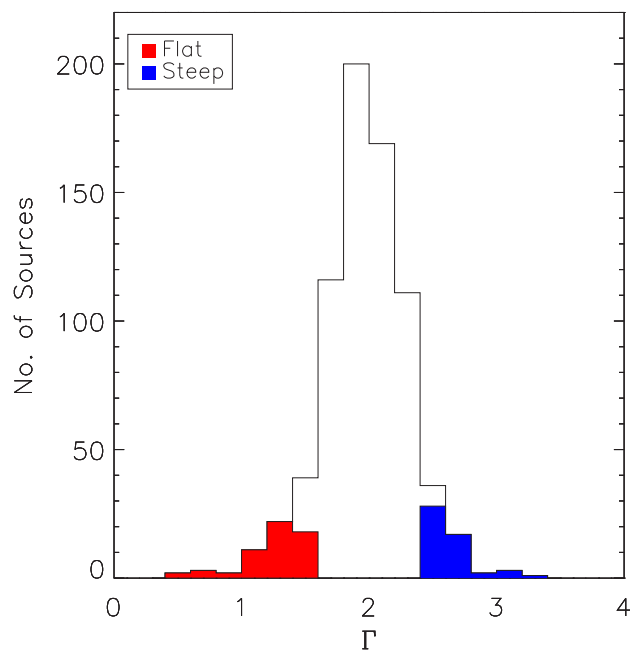


Figure 4.1: This figure shows the distribution of Γ values of the 734 sources for which $H0 > 1\%$ (see Chapter 3). The sources defined as flat ($\Gamma < 1.54$) are shown in red and the sources defined as steep ($\Gamma > 2.44$) are shown in blue.

with $> 10^3$ counts. This is also shown by Fig. 4.2 (bottom left) which compares the normalised count distributions of the two extreme populations (flat: dashed red; steep: dotted blue) with the non-extreme population (solid black). A KS test finds the count distributions of the two extreme samples to be similar, but both to be significantly different from the population of non-extreme sources. This is expected since a reliable fit to spectra with fewer counts is more difficult to achieve. The presence of an intrinsic spectral complexity may also remain undetected, skewing the power-law slope value obtained. These effects are discussed further in §4.3.

Fig. 4.2 (top) also shows that whilst extreme sources are generally found in a similar redshift range to the non-extreme sources, flat extremes are found up to $z \sim 3.8$, whilst the highest redshift steep extreme is only at $z \sim 2.6$. The redshift distributions of the 3 sub-samples are shown in Fig. 4.2 (bottom right). Flat extreme sources at $z > 3$ are clear in this plot, along with an excess of both flat and steep extremes at $z \lesssim 0.8$. Despite these features, KS tests find the redshift distributions of all 3 sub-samples not to be significantly different from each other. At higher redshifts it becomes increasingly easier to detect sources with flat

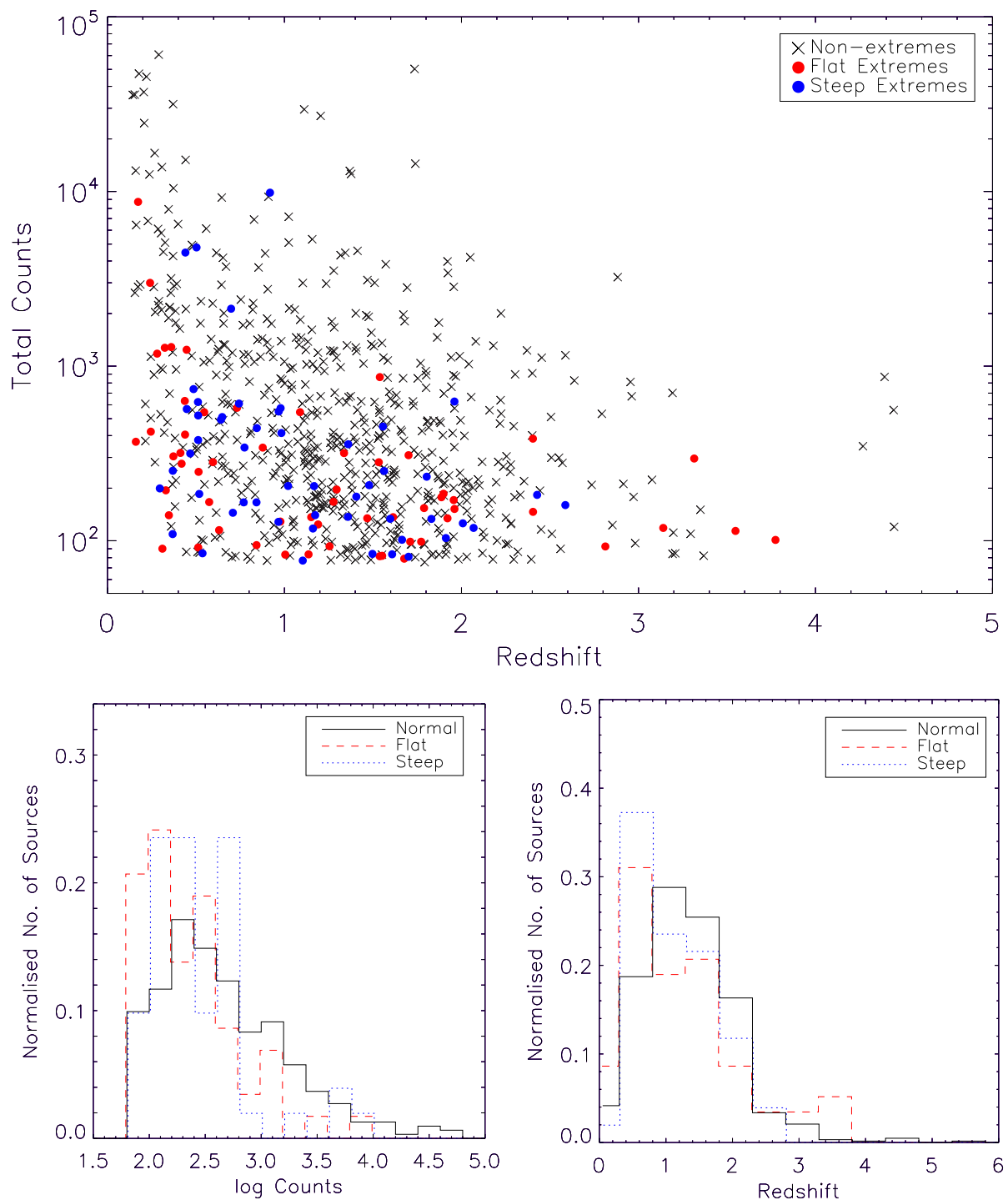


Figure 4.2: The top figure shows the counts/redshift distribution for the original sample of 734 sources (see Chapter 3). The red circles indicate the 58 flat sources and the blue circles show the 51 steep sources. The bottom figures show the normalised counts (left) and redshift (right) distributions of the non-extreme sources (solid black), the flat extreme sources (dashed red) and steep extreme sources (dotted blue).

Γ values, and relatively harder to detect sources with steep Γ values (Mateos et al., 2010) which may explain why flat extremes are found at higher redshifts than steep extremes. Fig. 4.3 plots the percentage of extreme sources found in different redshift bins. χ^2 values are calculated for constant percentages, and in both cases the best-fitting constant percentages are $\sim 6 \pm 1\%$, which give a good fit to the data and suggest no variation in the percentage of extremes with redshift.

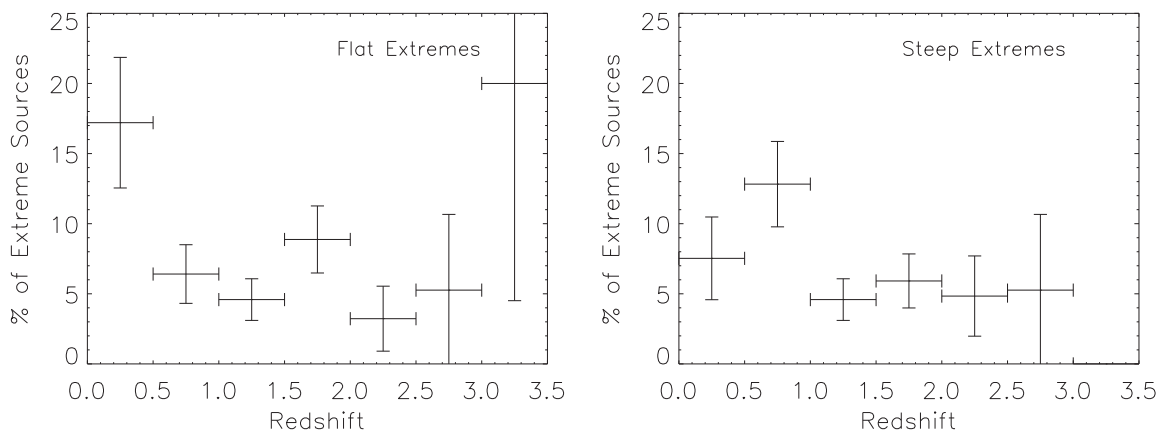


Figure 4.3: This plots the percentage of sources in each redshift bin which are defined as extreme.

The distribution of 2 – 10 keV luminosities, black hole masses and X-ray derived Eddington ratios are also compared for the 3 sub-samples (see Fig. 4.4). KS tests find the luminosities of all 3 sub-samples to be significantly different from each other, particularly that the steep sources have lower luminosities than the non-extreme sample (KS significance = 4×10^{-9}). The distribution of black hole masses for steep sources is significantly different to both non-extreme (KS significance = 0.001) and flat extreme sources (KS significance = 0.01), as it includes relatively more black holes at lower masses ($\lesssim 3 \times 10^8 M_{\odot}$). This likely relates to the lower luminosities seen in the steep sources since $L_X \propto M_{\text{BH}}$. The distribution of X-ray derived Eddington ratios for extreme sources (both flat and steep) is also significantly different to non-extreme sources (KS significance = 7×10^{-5} for steep, KS significance = 2×10^{-5} for flat), with the peak of the distributions occurring at lower Eddington ratios. For optically derived Eddington ratios, the extremes are not significantly different from non-extreme sources, but they are different to each other (KS significance = 0.0002)

The sample of objects considered here was defined based on a Γ value *observed* to be extreme. However, there are likely to be some of these sources whose *intrinsic* Γ value is

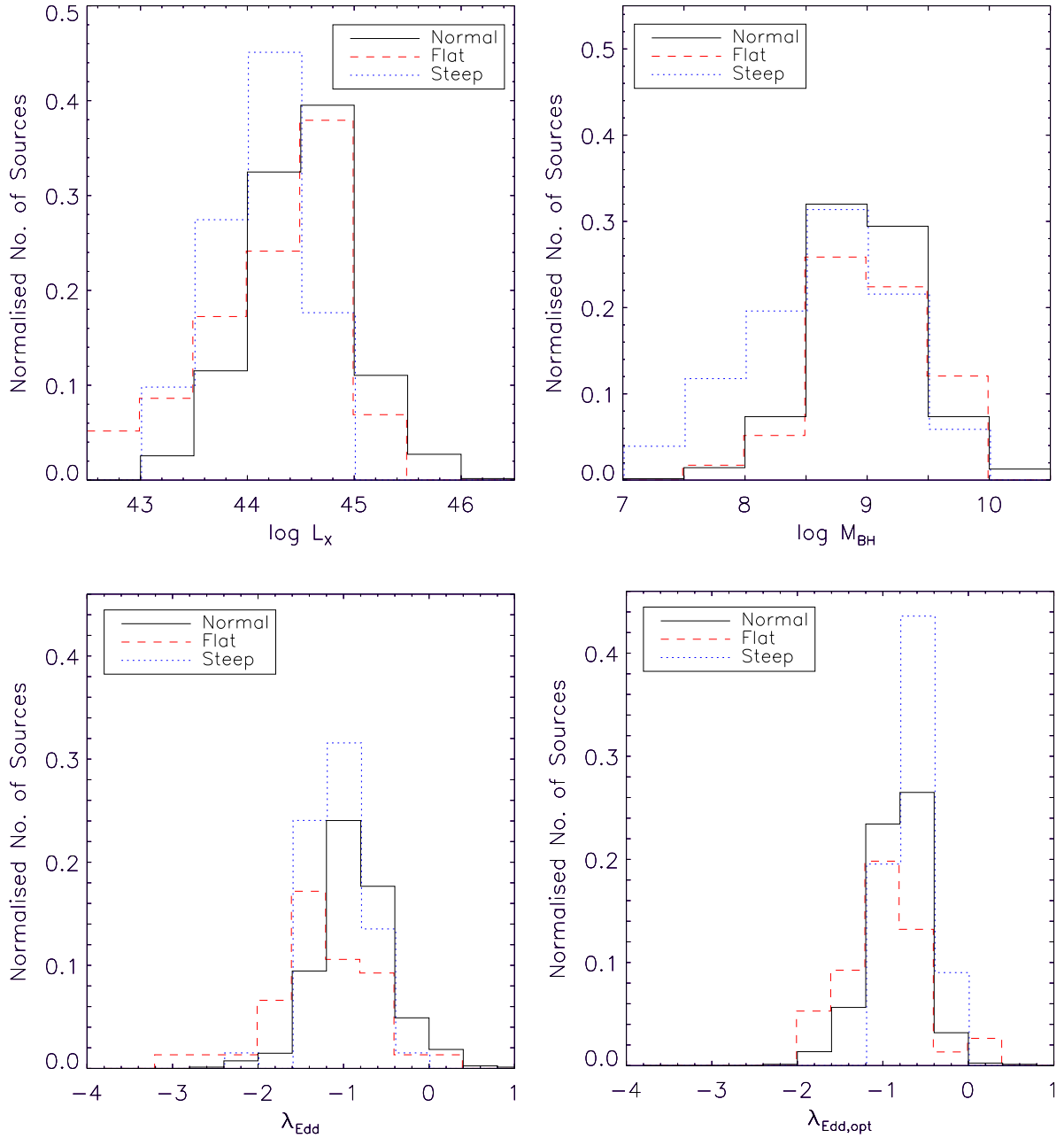


Figure 4.4: Top left - The distribution of $\log 2 - 10$ keV X-ray luminosities; top right - The distribution of \log black hole masses; Bottom - The distribution of X-ray (left) and optically (right) derived Eddington ratios (as calculated in §3.3.7). In each plot the non-extreme distribution is shown by the black solid line, the flat extremes by the red dashed line, and the steep extremes by the blue dotted line.

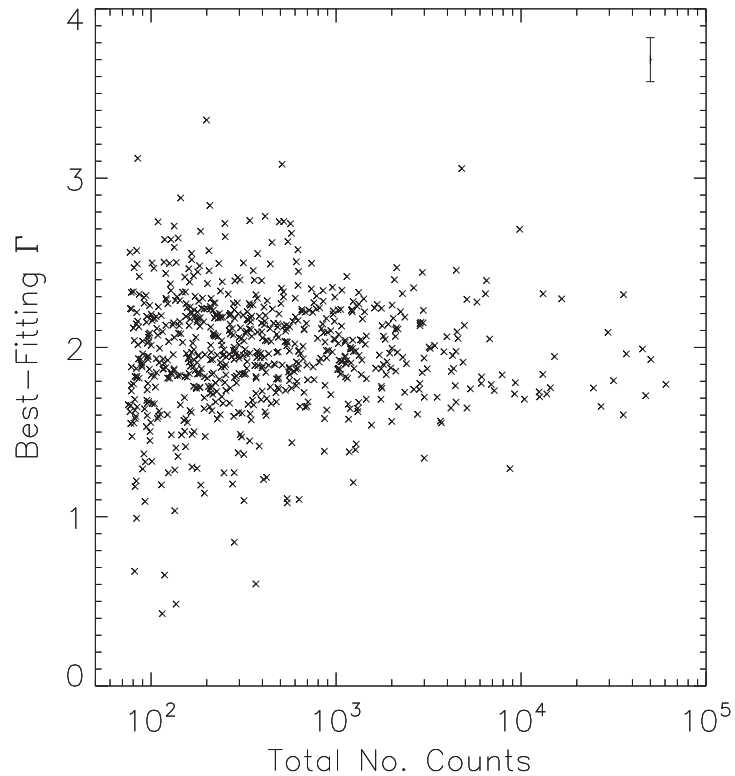


Figure 4.5: This shows the measured Γ values against the total number of counts in each of the X-ray spectra for which $H0 > 1\%$. The error bars have been omitted from this plot for reasons of clarity but an error of typical size can be seen in the top right hand corner.

not necessarily extreme. Since it is the intrinsic power-law slope which is expected to be dependent upon physical quantities such as luminosity, black hole mass and Eddington ratio, significant relationships are not expected for these sources.

As the sample was created from a serendipitous source catalogue, the majority have X-ray spectra with low numbers of counts. In these cases a reliable spectral fit is more difficult to obtain and may result in sources with apparently extreme Γ values. Fig. 4.5 shows the dependence of the derived Γ value on the number of counts in the spectra for the entire sample described in Chapter 3. It shows that many of the extremely flat or steep sources are those with the lowest numbers of counts. Similarly it is known that that the Γ value obtained is dependent upon which spectral components are modelled in the spectra. An unmodelled reflection component or intrinsic absorption can lead to a flatter Γ , while an unmodelled soft excess can lead to a steeper Γ (e.g. Pounds et al. 1990, Bianchi et al. 2009, Mateos et al. 2010). In low count spectra, these additional components may not be formally detected in the spectra with enough significance to be included in the model.

4.2.1 Extreme Sources With the Best Quality Spectra

Within the sample of 109 extreme sources, 10 have > 1000 counts in their spectra. Due to their relatively good quality, it is more likely that these will have a good spectral fit and that any additional spectral complexities will have been detected significantly. They could therefore provide the best evidence for intrinsically flat or steep power-law slopes and are hence studied in more detail.

Flat

SRCID 81225 has a flat power-law slope of $\Gamma = 1.35 \pm 0.02$ shown in Fig. 4.6 (top left). In §3.3.6 this source was identified as a RLQ and might be expected to have a flatter power-law slope because of contamination from synchrotron emission related to the radio jet. Since the observed power law is therefore perhaps not a direct measure of the emission from the inner regions, the source is not considered to be *intrinsically* flat. SRCID 101676 has a flat power-law slope of $\Gamma = 1.40^1$ as shown in Fig. 4.6 (middle left), but is also classed as a RLQ. Similarly SRCID 93253 shown in Fig. 4.6 (bottom left) is also a RLQ and has a flat power-law slope of $\Gamma = 1.38 \pm 0.04$.

Due to the statistical nature of the study in Chapter 3, the sources were only fit with 4 simple models. However it is known that complexities do exist and some of the sources in the sample may require a more complex model to correctly model their features. In particular, some AGN are known to have more complex absorbers in which the material is partially ionised or only partially covering the emitting region (Halpern, 1984). Some of the extreme sources may be better modelled using a complex absorption model rather than the neutral, fully covering apo model, and may no longer require an extreme power law. SRCID 16734 has a flat power-law slope of $\Gamma = 1.43 \pm 0.04$ as shown in Fig. 4.6 (top right). The original best-fitting model was a simple power law for which $\chi^2/\nu = 111/83$ and $p = 2.2\%$. The source spectrum can be better fit ($\chi^2/\nu = 105/81$ and $p = 4.0\%$) with a neutral, but partially covering absorber (zpcfabs in XSPEC). The best-fitting parameters are $N_{\text{H}} = 0.72_{-0.33}^{+0.49} \times 10^{22} \text{ cm}^{-2}$, $f = 0.52_{-0.15}^{+0.48}$ and the power-law slope is no longer extreme at $\Gamma = 1.69 \pm 0.13$. SRCID

¹There is no error on the Γ value as it was obtained from the po+bb model in which Γ was fixed at the value obtained from a simple power-law fit over the rest-frame energy range 2 – 10 keV (see §3.3.5).

84914 has a flat power-law slope of $\Gamma = 1.28 \pm 0.02$ as shown in Fig. 4.6 (middle right). The original best-fitting model was po+bb for which $\chi^2/\nu = 216/224$ and $p = 63\%$. However, the spectrum can be well fit, if not necessarily better fit, ($\chi^2/\nu = 268/224$, $p = 2.4\%$) with a fully covering, but partially ionised absorber (referred to as the model zxi). The best-fitting parameters are $N_{\text{H}} = 64_{-5}^{+4} \times 10^{22} \text{ cm}^{-2}$, $\log \xi = 3.18 \pm 0.02$ and the power-law slope is no longer extreme at $\Gamma = 1.54 \pm 0.02$. Similarly SRCID 141208, shown in Fig. 4.6 (bottom right), was originally best-fit with an absorbed power law in which the absorber was fully covering and fully neutral and $\Gamma = 1.20 \pm 0.12$. However, a good fit can be obtained with either the zpcfabs or zxi models, resulting in a non-extreme power-law slope.

Steep

SRCID 88367 has a steep power-law slope of $\Gamma = 3.06 \pm 0.14$ as shown in Fig. 4.7 (top left) and was best-fit with the po+bb model. However, Zhou et al. (2006) define this source as a Narrow-line Seyfert 1 (NLS1) which are known to have steeper power-law slopes. SRCID 127306 which has a steep power-law slope of $\Gamma = 2.70 \pm 0.08$ and was best-fit with the apo+bb model as shown in Fig. 4.7 (top right) is also defined as a NLS1 by Boller et al. (1996). These sources are therefore not considered to be *intrinsically* extreme, as they are from a different sub-population of type 1 AGN.

SRCID 109409 has a steep power-law of $\Gamma = 2.46 \pm 0.03$ as shown in Fig. 4.7 (bottom left). It was originally best-fit with the simple power-law model for which $\chi^2/\nu = 203/219$ and $p = 77\%$. The F-test comparing the po and po+bb models gave 98%, just below the 99% significance threshold used to accept the blackbody component as statistically required in the fit. When the po+bb model is considered keeping Γ fixed at 2.0 (the average value for the entire sample; see §3.3.1) $\chi^2/\nu = 201/218$ and $p = 80\%$, with a kT value of $0.20 \pm 0.01 \text{ keV}$. Since this model can provide a good fit to the spectrum without requiring an extreme power-law slope, this source is not classed as intrinsically extreme. The same is also true of SRCID 79444 which has a steep power-law of $\Gamma = 2.47 \pm 0.04$ as shown in Fig. 4.7 (bottom right). It was originally best-fit with a simple power-law model for which $\chi^2/\nu = 152/140$ and $p = 23\%$, but it can be well fit with the po+bb model keeping Γ fixed at 2.0 with $\chi^2/\nu = 161/139$,

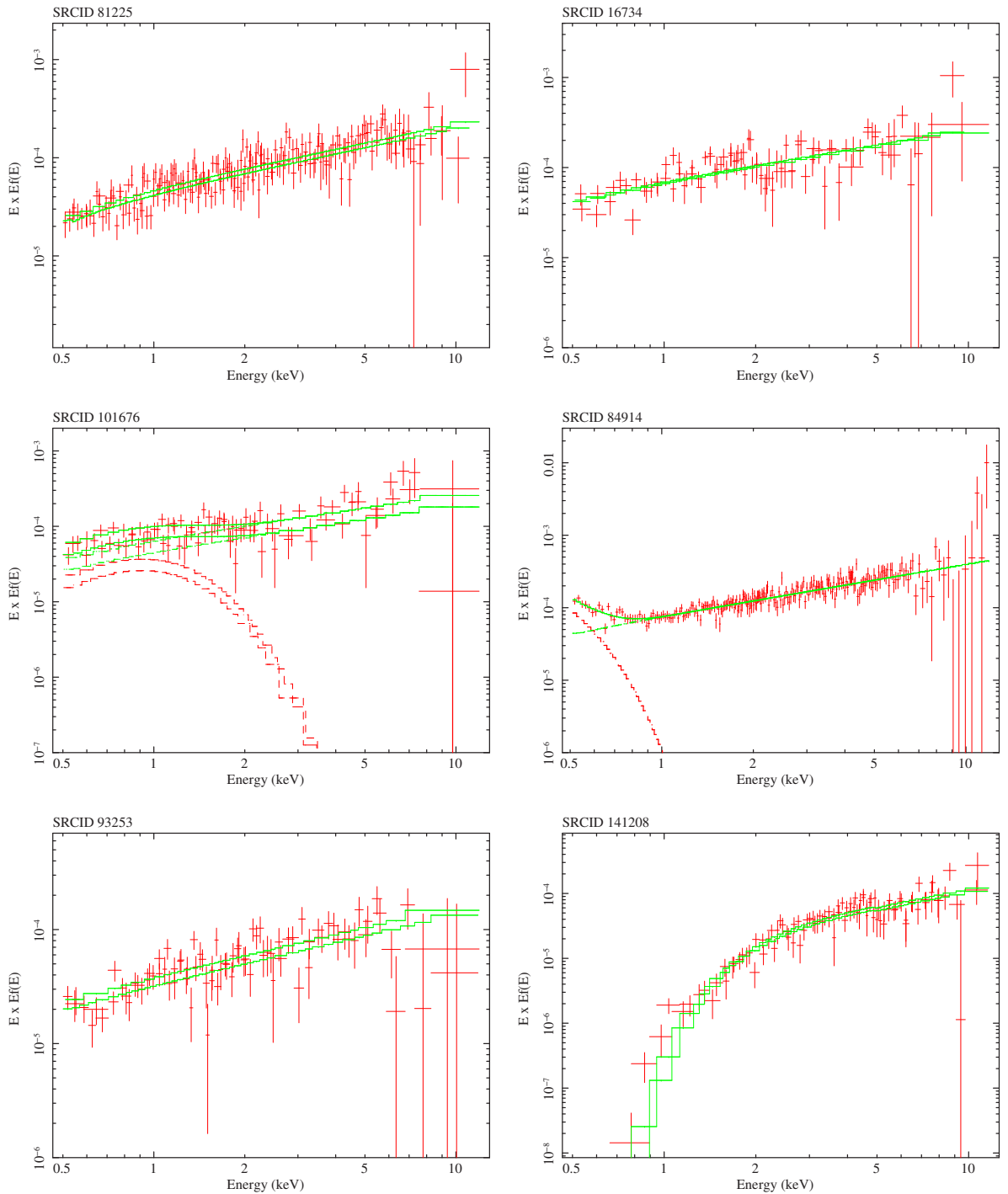


Figure 4.6: This figure shows the X-ray spectra of 6 sources with $\Gamma < 1.54$ in their original best-fitting model, making them extremely flat. The 3 sources in the left hand column were all identified as RLQ. The 3 sources in the right hand column can all be well fit with a complex absorption model in which the Γ value is no longer classed as extreme.

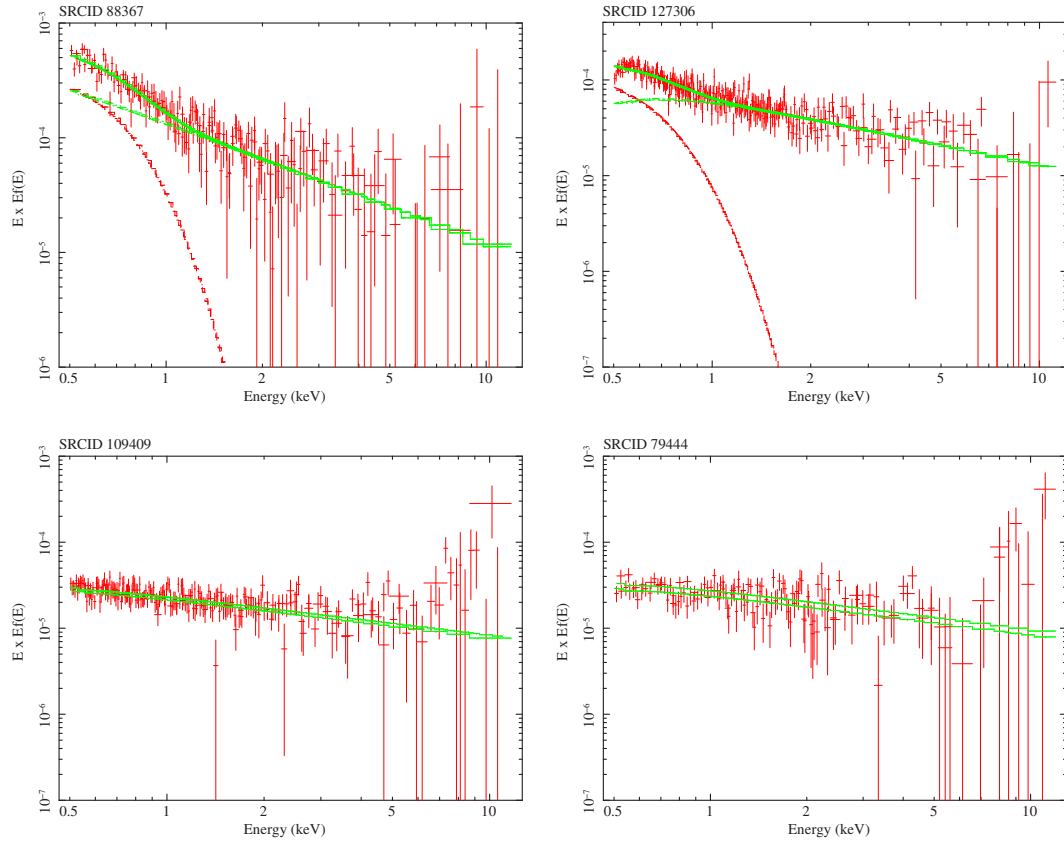


Figure 4.7: This figure shows the X-ray spectra of the 4 sources with $\Gamma > 2.44$ in their original best-fitting model, making them extremely steep. The top 2 sources were identified as NLS1s and the bottom 2 can all be well fit with a $po+bb$ model if the power-law slope is fixed at 2.0.

$p = 9.6\%$ and $kT = 0.26 \pm 0.02$ keV. Even though this model is not necessarily a better fit to the spectrum, it does provide a good fit without requiring an extreme power-law slope. Therefore this source is also not taken to be intrinsically extreme.

For each of the 10 sources described above, there exists an alternative explanation for their apparently extreme power law. Therefore, in §4.3 a systematic analysis of the full extreme sample is carried out. Each source is fit with models including spectral components which may have not been detected in the original fits with enough significance. All sources are also fit with complex absorption models to test whether these can give a good fit to the spectra. The sample is cross-correlated with catalogues of NLS1 from Zhou et al. (2006) and BALQSO from Scaringi et al. (2009) in order to exclude these objects from consideration. RLQ and sources of unknown radio loudness as determined in §3.3.6 are also removed from consideration. After this rigorous selection process, only sources thought to have intrinsically flat or steep power-law slopes remain, and will be discussed in §4.4.

4.3 Alternative Explanations

4.3.1 Unmodelled Spectral Complexities

The steep extreme sources are re-fit with the po+bb model, keeping Γ fixed at 2.0. A source is considered to be well fit by this model if $H0 > 1\%$ and the kT value obtained in the fit is constrained. The fits are considered to be consistent if kT lies within the range $0.08 - 0.26$ keV, the range of values obtained in the full sample. There are 23/51 sources which are well fit, of which 17 have consistent fits. Fig. 4.8 shows the unfolded spectra of SRCID 138635 which was originally fit with a simple power-law model where $\Gamma = 2.7 \pm 0.1$ (shown on the left), but can also be well fit with the po+bb model (shown on the right) with Γ fixed at 2.0, a non-extreme value. In this case $kT = 0.18_{-0.02}^{+0.03}$ keV which is consistent with the values found in §3.3.5. When the source was originally fit with the po+bb model, Γ was steeper ($\Gamma = 2.32 \pm 0.24$), kT was smaller ($kT = 0.16 \pm 0.05$ keV) and the F-test probability was only 89%, below the 99% significance threshold needed to adopt the blackbody component into the original fit. Fixing the Γ value to 2.0, reduces the number of free parameters in the spectral fit, making it easier to model the additional spectral components. However any Γ value in the range $1.7 - 2.3$ would be classed as non-extreme. Three sources have a consistent fit with the po+bb model with Γ values in this range.

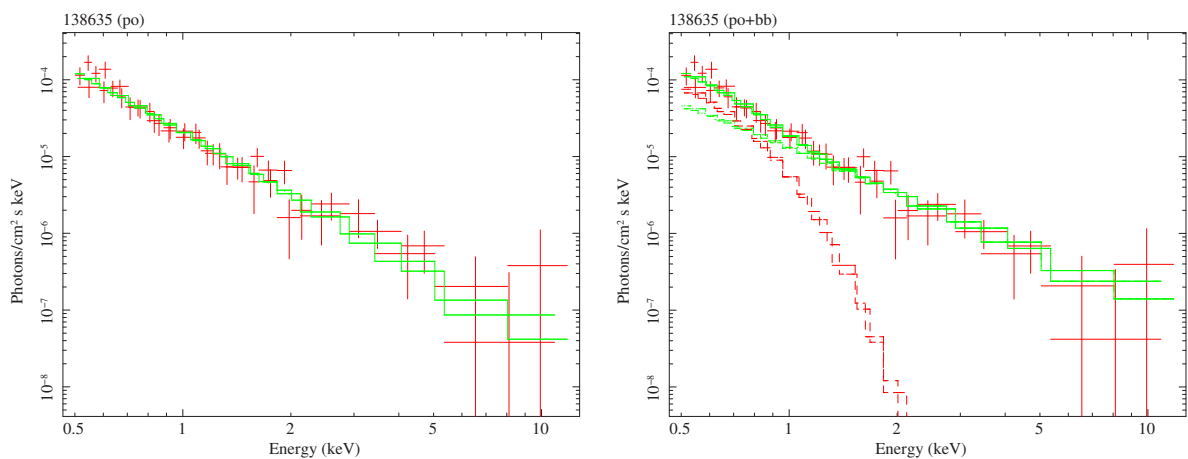


Figure 4.8: These figures show the unfolded spectra of SRCID 138635. On the left is the original simple power-law fit in which Γ is classed as extreme ($\Gamma = 2.7 \pm 0.1$). On the right is the po+bb model in which Γ is fixed at the non-extreme value of 2.0. For this fit $kT = 0.18_{-0.02}^{+0.03}$ keV.

The flat extreme sources are re-fit with the apo model, keeping Γ fixed at 2.0. A source is considered to be well fit by this model if $H0 > 1\%$ and the N_H value obtained is well constrained. 20/58 sources are well fit by this model, all with values of N_H consistent with the range of values obtained previously in the full sample, i.e. $\sim 2 \times 10^{21} - 5 \times 10^{23} \text{ cm}^{-2}$. Fig. 4.9 shows the unfolded spectra of SRCID 76393 which was originally fit with a simple power-law model where $\Gamma = 1.41_{-0.12}^{+0.14}$ (shown on the left), but can also be well fit with the apo model (shown on the right) with Γ fixed at 2.0, a non-extreme value. In this case $N_H = 2.55_{-0.72}^{+1.05} \times 10^{22} \text{ cm}^{-2}$ which is consistent with the values found in §3.3.4. The apo model was rejected in the original analysis as the F-test probability was only 61%. This fit had a steeper Γ value (although a large associated error; $\Gamma = 1.61 \pm 0.27$) and an unconstrained column density; $N_H \leq 3.8 \times 10^{22} \text{ cm}^{-2}$.

An F-test is not appropriate in either of these cases since the new models fix Γ rather than leaving it free and simply adding spectral components. However, this analysis merely aims to test whether a fit with a non-extreme Γ value is possible; the presence of the additional complexity is not expected to be formally required.

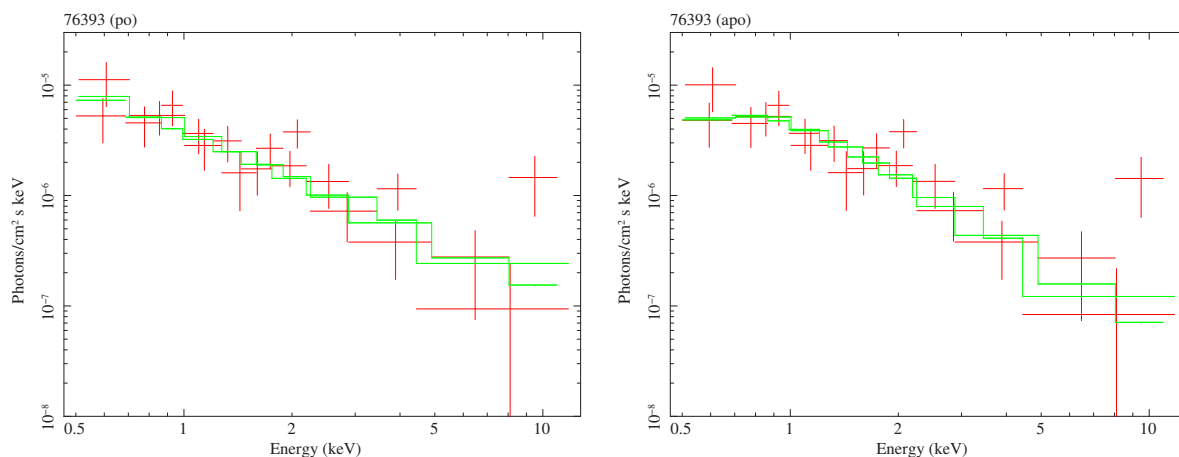


Figure 4.9: These figures show the unfolded spectra of SRCID 76393. On the left is the original simple power-law fit in which Γ is classed as extreme ($\Gamma = 1.41_{-0.12}^{+0.14}$). On the right is the apo model in which Γ is fixed at the non-extreme value of 2.0. For this fit $N_H = 2.55_{-0.72}^{+1.05} \times 10^{22} \text{ cm}^{-2}$.

Fig. 4.10 shows the original distribution of Γ values (red, dotted line), clearly showing the extreme sources in the wings. The black solid line shows what the new distribution would look like if the Γ values of the 37 sources which can be adequately modelled with $\Gamma = 2.0$ and a spectral complexity are adjusted. This reduces the number of sources in the wings, but does

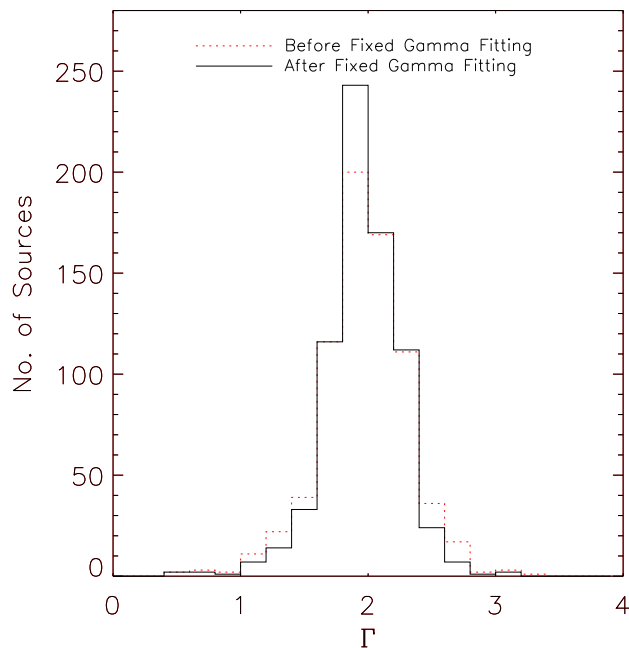


Figure 4.10: The distribution of Γ values before (red, dashed line) and after (black, solid line) the results of the $\Gamma = 2.0$ fits are taken into account. The original Γ distribution clearly shows the extreme sources in the wings of the distribution. $\sim 39\%$ of these sources are then moved into the central population after the fixed Γ fits are considered.

not remove them completely. This explanation of unmodelled spectral complexities is able to account for $\sim 39\%$ of the extreme sources and it does so in a way as to suggest that they are part of the same physical population of sources rather than a unique subset, and that it is merely the limitations of the spectral fitting which gives them their initial extreme classification.

Fig. 4.11 shows the counts/redshift distribution of the 109 original extreme sources, with the sources which can be better fit with $\Gamma = 2.0$ and a spectral complexity shown by the coloured circles. The better fit steep sources are generally found at $z < 1$. This is expected as for higher redshift sources the spectral signature of the soft excess will be shifted out of the EPIC bandpass and become difficult to detect. The sources cover a range of count levels from ~ 100 to ~ 4000 , showing that even in spectra with high numbers of counts, spectral complexities are not always accurately modelled by automatic spectral fitting techniques as will be discussed in Chapter 5. The better fit flat sources are generally found at low count levels (< 400), but at all redshifts from $0.3 - 2.8$. This could be because the detection of absorption components is less dependent upon the number of counts in the spectra than in the case of the soft excess and absorption components of differing N_{H} values can be detected in spectra with a wide range in redshift.

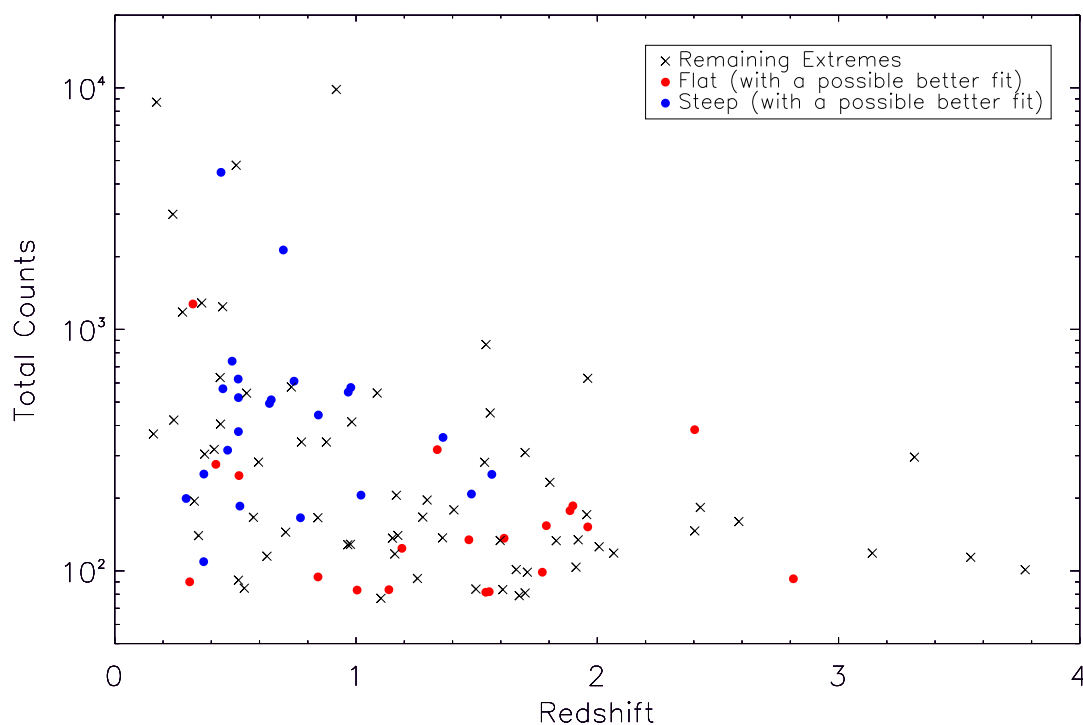


Figure 4.11: This shows the counts/redshift distribution of the initial sample of 58 flat and 51 steep extreme sources (shown by black crosses). The 20 flat sources which can be well fit with the apo, $\Gamma = 2.0$ model are shown by the red circles and the 23 steep sources which can be well fit with the po+bb, $\Gamma = 2.0$ model are shown by the blue circles.

4.3.2 Complex Absorption Models

In §4.2.1, three of the extremes with the best quality spectra, SRCIDs 16734, 84914 and 141208 with ~ 1300 , ~ 9000 and ~ 1200 counts respectively, were all well fit with a complex absorption model in which the absorber was either partially covering the emitting region, or partially ionised. In these models, the Γ value obtained was no longer classed as extreme. In this section, the extreme sources are modelled with complex absorbers.

The zpcfabs model (described in Chapter 2) can be used to model a neutral, but partially covering absorber and is implemented as `phabs*(zpcfabs*po)` in XSPEC. The zxicpf model (Reeves et al. 2008; Chapter 2) is implemented in XSPEC as `phabs*(zxicpf*po)`, and was considered with both the covering factor f fixed at 1.0 to model a partially ionised, but fully covering absorber (hereafter known as the model zxi), and with f left free to vary so as to model a partially ionised and partially covering absorber (model zxicpf). Fits were deemed acceptable if $H0 > 1\%$, and all of the model parameters Γ , N_H , f and $\log \xi$ were constrained.

Although an F-test could be performed between the original simple power-law model and `zxi` or `zpcfabs`, it is known that the sources in the sample are unlikely to pass a stringent statistical test due to their low counts, else they may have already required an absorbed model in the original analysis. It is more instructive to identify the sources for which a model with a complex absorber and non-extreme Γ are possible, if not statistically required. 20 of the flat sources were better fit with a complex model; `zxi` = 3, `zxi` or `zxicf` = 3, `zxi` or `zpcfabs` = 5, `zpcfabs` = 9 and 3 steep extreme sources could also be well fit with the `zxi` model.

Fig. 4.12 shows unfolded spectra of SRCID 80946 which was originally fit with the `po+bb` model (left) and an extreme power-law slope, $\Gamma = 0.6 \pm 0.1$, and $kT = 0.07 \pm 0.01$ keV. When the spectra were re-fit with a simple power law fixed at 2.0, curvature could clearly be seen in the residuals, suggesting complex absorption was present. The `zxi` model provides a good fit to the data (right) and the model no longer requires an extreme Γ value; $\Gamma = 1.58 \pm 0.06$, $N_H = 64_{-25}^{+7} \times 10^{22} \text{ cm}^{-2}$ and $\log \xi = 2.82_{-0.04}^{+0.02}$. This source was also studied by Schartel et al. (2005) and they find the *XMM-Newton* spectrum to be well fit with an ionised absorber. The XSPEC model `absori` was used with the best-fitting parameters $N_H = 19.2_{-7.3}^{+11.9} \times 10^{22} \text{ cm}^{-2}$, $\log \xi = 2.73_{-0.13}^{+0.08}$, $\Gamma = 1.97_{-0.14}^{+0.17}$.

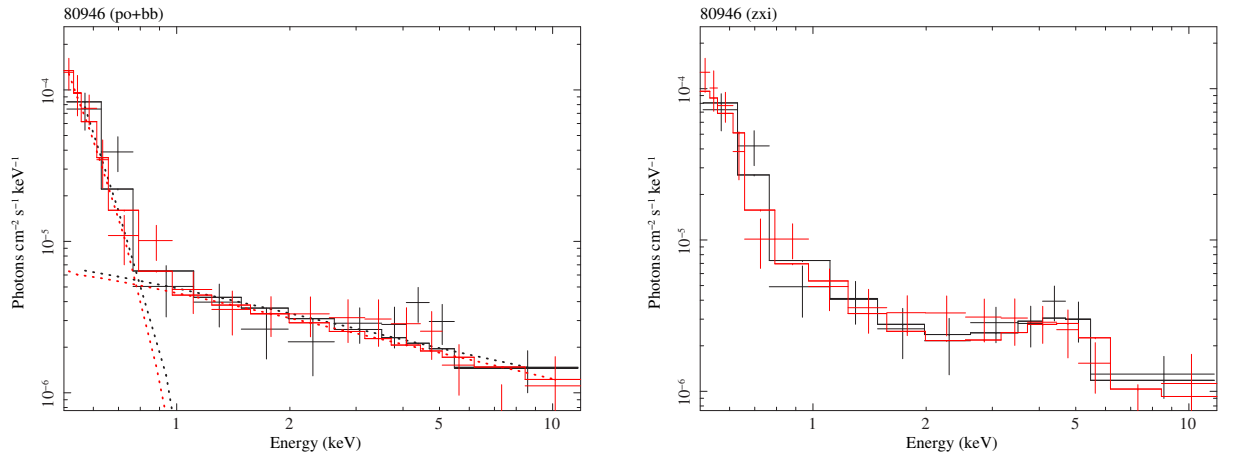


Figure 4.12: These figures show the unfolded spectra of SRCID 80946. On the left is the original power law fit plus blackbody in which Γ is classed as extreme, $\Gamma = 0.6 \pm 0.1$, and $kT = 0.07 \pm 0.01$ keV. On the right is the `zxi` model in which Γ is no longer extreme; $\Gamma = 1.58 \pm 0.06$, $N_H = 64_{-25}^{+7} \times 10^{22} \text{ cm}^{-2}$ and $\log \xi = 2.82_{-0.04}^{+0.02}$.

Fig. 4.13 shows unfolded spectra of SRCID 124986 which was originally fit with a simple power law (shown on the left) with an extreme Γ value of $\Gamma = 1.23 \pm 0.08$. Shown on the right is the fit using the *zpcfabs* model which no longer requires an extreme Γ value. The best-fitting parameters are $\Gamma = 1.73 \pm 0.25$, $N_{\text{H}} = 8.92^{+12.9}_{-1.66} \times 10^{22} \text{ cm}^{-2}$ and $f = 0.59^{+0.11}_{-0.27}$.

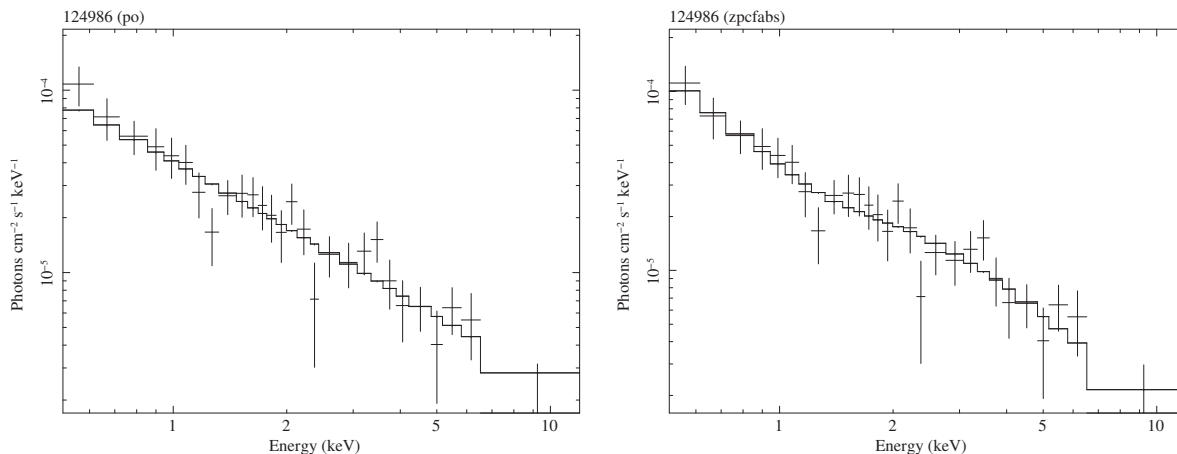


Figure 4.13: These figures show the unfolded spectra of SRCID 124986. On the left is the original power law fit in which Γ is classed as extreme; $\Gamma = 1.23 \pm 0.08$. On the right is the *zpcfabs* model in which Γ is no longer extreme; $\Gamma = 1.73 \pm 0.25$, $N_{\text{H}} = 8.92^{+12.9}_{-1.66} \times 10^{22} \text{ cm}^{-2}$ and $f = 0.59^{+0.11}_{-0.27}$.

The effect of the new Γ values from these fits on the Γ distribution is shown in Fig. 4.14. The original distribution (red, dotted line) clearly shows extreme sources in the wings and the final distribution (black, solid line) shows that $\sim 21\%$ of the extreme sources are moved into the central population.

Fig. 4.15 shows the counts/redshift distribution of the original sample of extreme sources, with the flat/steep sources which can be better fit with a complex absorption model shown by the red/blue squares. In general, the sources which can be well modelled with a complex absorption component are found at a lower redshift than the rest of the sample as more of the absorption signature will be detectable in the observed spectrum for these sources.

There are 3 steep extreme sources which can be well fit with both the *zxi* model and the power-law plus blackbody model when Γ is fixed at 2.0. The *po+bb* model was used in the original analysis to model any soft excess emission that may be present in the spectra and assumes that it is an additional feature, perhaps from upscattered emission from the accretion disc. However, it has also been suggested that the soft excess may be an apparent feature in the spectrum, caused by ionised absorption material creating a dip in the spectrum at $\sim 0.7 \text{ keV}$.

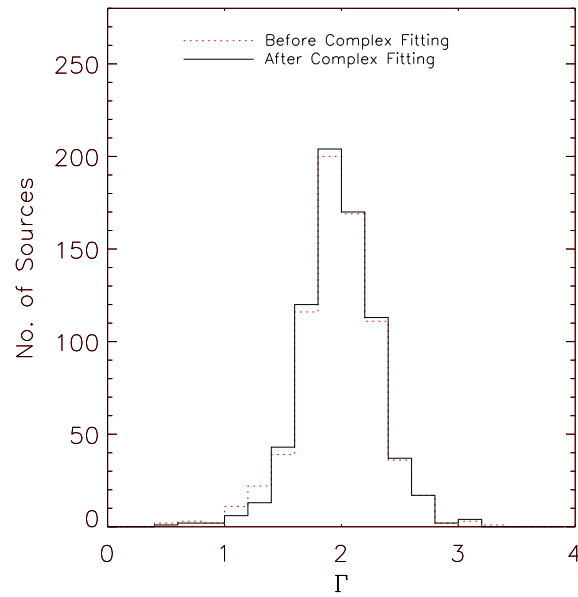


Figure 4.14: The distribution of Γ values before (red, dotted line) and after (black, solid line) the results of the complex absorber fits are taken into account. $\sim 21\%$ of the extreme sources are moved into the central population after the complex absorber fits are considered.

Therefore it is interesting that these sources can be well fit by either model. In Table 4.1, the best-fitting parameters for each model, along with original power-law model which gave the sources their extreme classification are listed. For each of the sources, the *zxi* model gives the best-fit (lowest *p* value), but still requires a steep Γ . The *p* values for the *po+bb*, $\Gamma = 2.0$ fits are not quite as good as for *zxi*, but do offer an improved fit over the simple power-law model. In this case the power-law slope does not have an extreme value and the blackbody temperatures obtained are consistent with those found in §3.3.5.

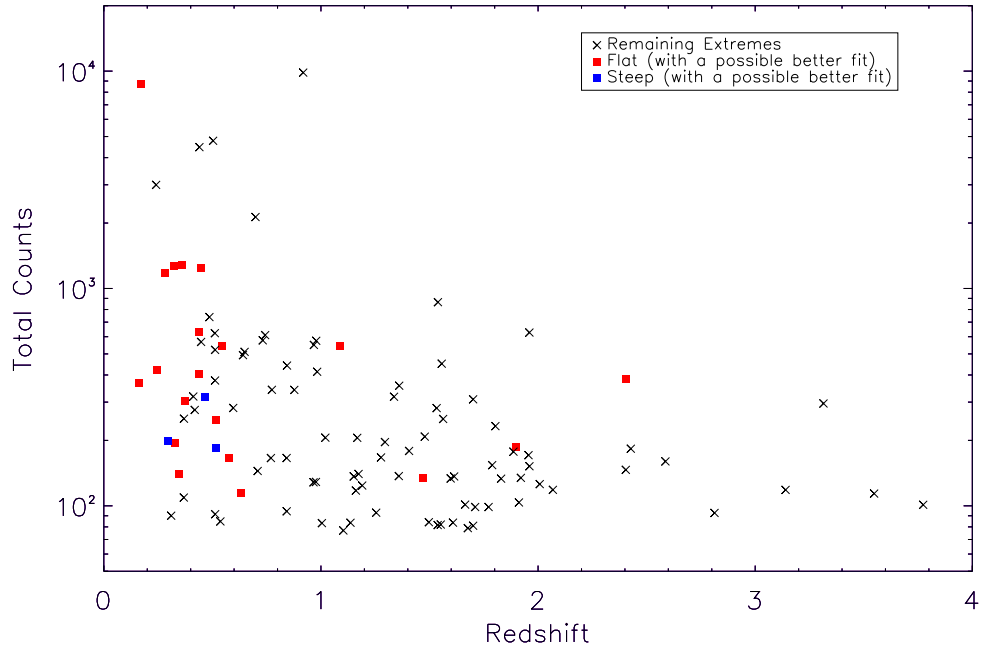


Figure 4.15: This shows the counts/redshift distribution of the initial sample of 58 flat and 51 steep extreme sources (shown by black crosses). The 20 flat sources which can be well fit with a complex absorption model, *zxi*, *zxipecf* or *zpcfabs* are shown by the red squares and the 3 steep sources which can be well fit by the *zxi* model are shown by the blue squares.

SRCID	po	zxi	po+bb, $\Gamma = 2.0$
62350	$\chi^2/\nu = 17/13$ $p = 22\%$ $\Gamma = 3.3 (2.9 - 3.8)$	$\chi^2/\nu = 13/11$ $p = 32\%$ $\Gamma = 3.0 (2.7 - 3.5)$ $N_{\text{H}} = 38 (6 - 129) \times 10^{22} \text{cm}^{-2}$ $\log \xi = 3.0 (2.8 - 3.5)$	$\chi^2/\nu = 14/12$ $p = 31\%$ $\Gamma = 2.0$ $kT = 0.14 (0.10 - 0.18) \text{ keV}$
196974	$\chi^2/\nu = 23/20$ $p = 28\%$ $\Gamma = 2.5 (2.3 - 2.7)$	$\chi^2/\nu = 20/18$ $p = 35\%$ $\Gamma = 2.6 (2.3 - 2.8)$ $N_{\text{H}} = 97 (17 - 298) \times 10^{22} \text{cm}^{-2}$ $\log \xi = 3.0 (2.8 - 4.1)$	$\chi^2/\nu = 22/19$ $p = 31\%$ $\Gamma = 2.0$ $kT = 0.11 (0.07 - 0.22) \text{ keV}$
210769	$\chi^2/\nu = 23/17$ $p = 15\%$ $\Gamma = 2.7 (2.3 - 3.1)$	$\chi^2/\nu = 20/15$ $p = 20\%$ $\Gamma = 2.8 (2.5 - 3.1)$ $N_{\text{H}} = 23 (9 - 126) \times 10^{22} \text{cm}^{-2}$ $\log \xi = 3.0 (2.5 - 3.5)$	$\chi^2/\nu = 21/16$ $p = 18\%$ $\Gamma = 2.0$ $kT = 0.16 (0.11 - 0.23) \text{ keV}$

Table 4.1: The best-fitting parameters for the po, *zxi* and po+bb, $\Gamma = 2.0$ models, as applied to three of the steep extreme sources. The errors on the parameters represent the 90% confidence range.

4.3.3 Extremes From Other Populations

The sample includes particular types of AGN such as radio-loud quasars (RLQ), Narrow-line Seyfert 1s (NLS1s) and Broad Absorption Line Quasars (BALQSOs) which are thought to display different X-ray spectral properties from the non-BAL, broad-line, radio-quiet AGN that the majority of the sample consists of.

It is widely accepted that all types of AGN are accreting supermassive black holes, but the presence or absence of features such as jets and outflows can make them appear as different classes in observations. It could therefore be assumed that the intrinsic X-ray emission from the very inner regions surrounding the black hole is similar in each object, but becomes modified before observations are made meaning the X-ray emission observed from sub-populations of AGN is different. Such sources are therefore not classified as ‘intrinsic extremes’ in the sense that it is not the true intrinsic emission that is being observed.

Broad Absorption Line Quasars (BALQSOs)

BALQSOs are a subclass of AGN which show strong, broad, blueshifted absorption features, which are thought to be the signatures of fast ($\sim 0.1 - 0.2c$), highly ionised, powerful outflows, also observed in the X-ray spectra of some non-BAL quasars (Pounds et al., 2003a,b). BALQSOs make up 15% of quasars in general (e.g. Foltz et al. 1990; Reichard et al. 2003) and Weymann et al. (1991) proposed that the differences between BAL and non-BAL quasars was simply an orientation effect. Elvis (2000) proposed a detailed model for quasars in which all have a highly ionised, high velocity outflow and the source is only observed as a BALQSO if the viewing angle to the source is directly through the outflowing material. BALQSOs are important for understanding AGN feedback since the mechanical energy of the outflows is thought to be large enough to interrupt the growth of the host galaxy (Pounds & Reeves, 2009). The first X-ray observations of BALQSOs revealed them to be significantly weaker in X-rays than non-BAL quasars with similar redshifts and luminosities, with some being entirely undetected (Green & Mathur, 1996). Studies of the X-ray spectra of BALQSOs suggest that their intrinsic Γ values are no different from those of type 1, non-BAL, radio-quiet quasars (Gallagher et al., 2002; Giustini et al., 2008; Streblyanska et al., 2010), and therefore any flattening

of the power-law slope is likely due to the absorption component being either unmodelled or under-estimated in the spectral fit.

The sample is cross-correlated with existing BALQSO catalogues; the Trump et al. (2006) catalogue containing 4784 objects from SDSS DR3 and the Scaringi et al. (2009) catalogue containing 3552 sources in the redshift range $1.7 < z < 4.2$ from the DR5 quasar catalogue. The Trump et al. (2006) catalogue defined 6 of the flat sample and 10 of the normal sources to be BALQSOs, whilst the Scaringi et al. (2009) catalogue defines 8 of the extreme sample and 8 of the normal sources to be BALQSOs. In addition to this, a visual inspection of the optical spectra of the sources suggests 3 other sources may be BALQSOs due to the presence of the characteristic absorption features (an example of which can be seen in Fig. 3.19). In total, 24 unique sources are defined as BALQSOs; 11 flat, 1 steep and 12 non-extreme.

The percentage of BALQSOs best-fit with the absorbed power law model in the original analysis where complex absorption was not considered is considerably higher ($29 \pm 13\%$) than the percentage of non-BAL sources requiring absorption ($4 \pm 2\%$). However, only 1/12 extreme BAL sources are found to have an acceptable fit with the models *zxi* (or *zxipcf*) which include an ionised absorber. This is likely due to the low quality of the X-ray spectra being considered; the average number of counts for the BALQSOs is ~ 160 . Some of the sources are also at such high redshifts (at least $z > 1.7$ by definition) that an absorption signature will be largely redshifted out of the *XMM-Newton* bandpass.

The Scaringi et al. (2009) catalogue only includes sources in the redshift range $1.7 < z < 4.2$ as the optical spectra must include the CIV line to be used in the classification process. This restricted redshift range covers only $\sim 25\%$ of the sample studied here, giving a raw BAL fraction of $8.7 \pm 2.3\%$ (16/188 sources), lower than that found by Scaringi et al. (2009). 550 sources, including 84 in the extreme sample are not covered by the catalogue, so it is possible that some may be undefined BALQSOs.

Fig. 4.16 compares the Γ distribution for BAL and non-BAL quasars. It includes only the sources in the redshift range covered by the Scaringi et al. (2009) catalogue (184) and only the sources which are defined as BAL by the same catalogue (16). A KS test comparing the Γ values of BAL and non-BAL quasars shows that they are significantly different

(KS significance = 0.0077) with the Γ values of BALQSOs being generally flatter.

The Γ distribution of the BALQSOs appears to consist of two peaks, one of which is more consistent with the non-BAL sources and one with flatter power-law slopes. The sources in the steeper of the two peaks are those that were best-fit with an absorbed power-law model, whilst the flatter peak corresponds to the sources which were best-fit with the simple power-law model, suggesting the flat Γ values measured are likely a result of unmodelled absorption in the spectra.

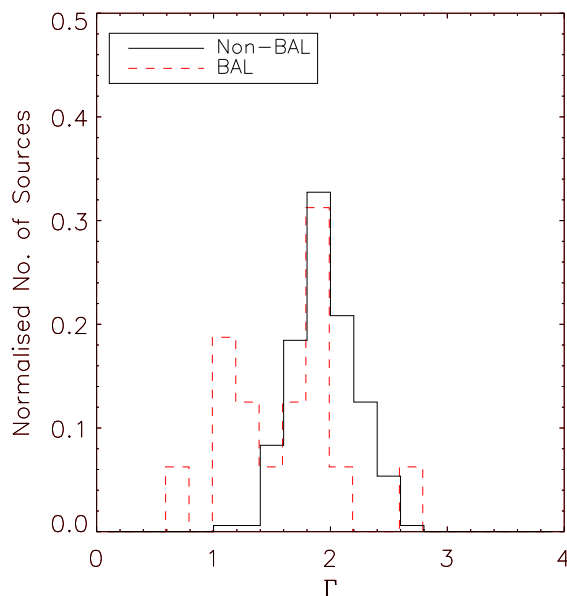


Figure 4.16: The distribution of Γ values for the 16 sources defined as BALQSOs by the Scaringi et al. (2009) catalogue (red, dashed) and the rest of the non-BAL quasars (black, solid) covered by the Scaringi et al. (2009) catalogue and therefore confirmed non-BALs. This shows that the Γ values of BALQSOs are generally flatter than those of the non-BALs.

Narrow-line Seyfert 1s (NLS1s)

NLS1s are a subclass of AGN defined by Osterbrock & Pogge (1985) as having $\text{FWHM}(\text{H}\beta) < 2000 \text{ km s}^{-1}$ (to distinguish from Seyfert 1) and $[\text{OIII}]/\text{H}\beta < 3$ (to distinguish from Seyfert 2). Boller et al. (1996) found that objects with narrow $\text{H}\beta$ lines tend to have steeper X-ray spectra, so it naturally follows that NLS1s should show steep spectra. This was observed by Brandt et al. (1997) who compared the Γ values of NLS1s to Seyfert 1 and found them to be steeper (NLS1: $\Gamma = 2.15 \pm 0.05$, BLS1: $\Gamma = 1.87 \pm 0.04$). Since the mass of the black hole is

proportional to the FWHM of the observed $H\beta$ lines, it was suggested that NLS1s were AGN with lower mass black holes (Boller et al., 1996). They may also be objects accreting at high rates. If NLS1 have the same luminosities as BLS1 but their black hole masses are smaller, their accretion rates must naturally be larger (Eqn. 1.1). Section 3.3.7 suggested that the power-law slope is related to the accretion process. At higher mass accretion rates, a stronger soft X-ray/UV component from the disc is created, which in turn causes more Compton cooling, producing a steeper X-ray spectrum. This scenario was offered as an explanation for the NLS1 RE 1034+39, which has an unusually soft power law of $\Gamma \sim 2.6$ (Pounds et al., 1995). This was noted to be similar to the high/soft spectral state observed in Galactic black hole binaries that are accreting close to the Eddington limit (Remillard & McClintock, 2006).

The sample is cross-correlated with the Zhou et al. (2006) catalogue, consisting of 2011 NLS1s identified in SDSS DR3 at $z \leq 0.8$. To be defined as a NLS1 in this catalogue, only the FWHM of the broad component of $H\alpha$ or $H\beta$ must be detected at $> 10\sigma$ and be narrower than 2200 km s^{-1} ; there is no requirement based on the $[\text{OIII}]/H\beta$ flux ratio. 18 sources in the sample are defined as NLS1s; 17 by the Zhou et al. (2006) catalogue, and another by Boller et al. (1996) which is at $z = 0.92$ and therefore not covered by the Zhou et al. (2006) catalogue. 8 of the NLS1s do not have extreme Γ values. 7 are steep sources, as expected, but 3 are part of the flat sample. Two of the sources, SRCIDs 73154 and 80946, are classed as flat at the 3σ level; these sources have low numbers of counts in their spectra (115 and 369, respectively). Only $\sim 25\%$ of the full sample is covered by the Zhou et al. (2006) catalogue due to the redshift limit meaning 548 sources, including 66 of the extremes, could be undefined NLS1s. Restricting the sample to just those covered by the catalogue gives a NLS1 fraction of $9.0 \pm 2.3\%$.

The Γ distributions of the NLS1 and non-NLS1s are compared in Fig. 4.17 (left) and a KS test reveals them to be significantly different (KS significance = 0.0004). In general the NLS1s appear to have steep Γ values, with the exception of some sources with particularly flat Γ values as mentioned above. The distributions of Eddington ratios are shown in Fig. 4.17 (right). A KS test finds them to not be significantly different, despite suggestions in the literature that NLS1s are high accretion rate objects (Pounds et al., 1995; Boroson, 2002; Grupe,

2004). Although the peaks of the two distributions occur at a similar Eddington ratio, the spread of values for the non-NLS1s is broader, particularly with more objects at low accretion rates.

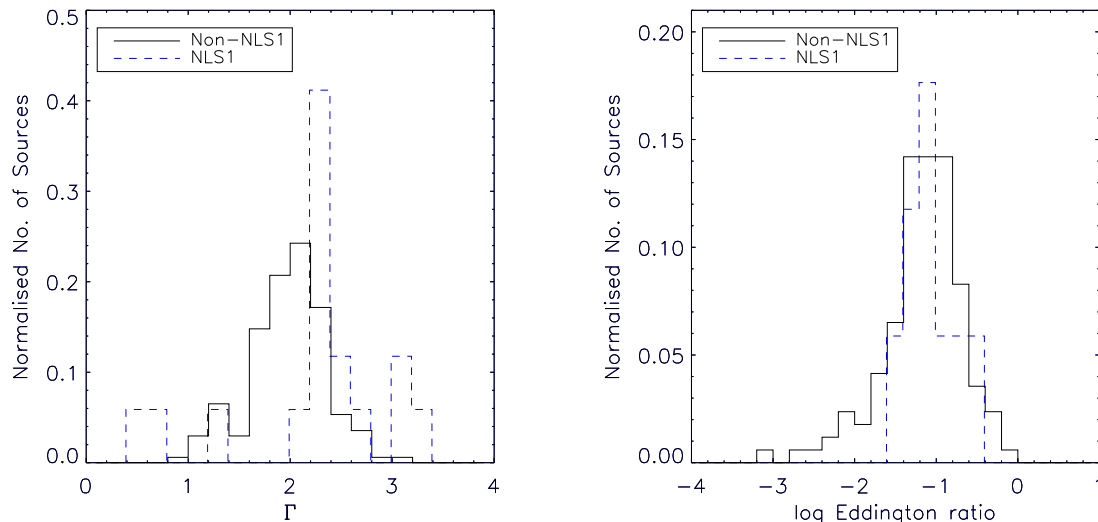


Figure 4.17: The distribution of Γ values (left) and Eddington ratios (right) for the 17 sources defined as NLS1s by (Zhou et al. 2006; blue, dashed) and the confirmed non-NLS1 quasars (black, solid). This shows that some of the NLS1s have extremely flat Γ values, although in general they tend to be steeper. There is no significant difference between the distribution of Eddington ratios. The peaks of the distributions occur at a similar value, although the spread in Eddington ratios for the non-NLS1 objects is broader.

Radio-Loud Quasars (RLQ)

The radio loudness of the objects in the sample was calculated from the optical SDSS magnitudes and the radio flux from FIRST (Becker et al., 1995), as described in detail in §3.2. Section 3.3.6 shows that the Γ values of the radio-loud sources in the sample are significantly flatter than those of radio-quiet sources (see Fig. 3.29, middle right). This effect agrees with the literature (e.g. Reeves & Turner 2000) and is generally attributed to contamination of the Comptonised power law by synchrotron emission (Sambruna et al., 1999). Using only those sources which are confirmed as RQQ and RLQ, the radio-loud percentage in the flat extreme sample is $12.8 \pm 5.5\%$ (6/47 sources), whilst the steep extreme sample does not include a significant percentage of radio-loud sources, $2.4 \pm 2.4\%$ (1/42). It would be interesting to establish whether the underlying power law slope of RLQ was similar to that of RQQ. However, removing the X-ray contribution from the jet, whose size is unknown, is difficult.

4.3.4 Other Considerations

Other possible explanations for apparently extreme Γ values are considered below.

Large Scale Environment

It has been suggested that AGN activity could depend upon the large scale environment of the host galaxy (Georgakakis et al., 2007) and it is still not clear what causes the SMBHs at the centre of galaxies to become active (see §1.1.4).

The SDSS Navigate tool² was used to examine the optical images of each of the sources in the full sample and $7.0 \pm 1.0\%$ were determined to have a disturbed morphology. This is much lower than the $\sim 25\%$ value reported by Koss et al. (2010) as their sources lie at much lower redshifts $z < 0.05$, where a disturbed morphology can be more easily detected. The DR5 quasar catalogue includes a morphology flag for each source which can be set to ‘point like’ or ‘extended’ as classified by the SDSS photometric pipeline. $7.2 \pm 1.0\%$ sources in the full sample are classed as extended, slightly higher than the value for the entire DR5 catalogue, $4.5 \pm 0.1\%$. Although the percentage of disturbed sources found by these two indicators are consistent, they include different sources, with the overlap being $\sim 40\%$.

In order to investigate whether the extreme sources have their unusual Γ values due to differences in their environment, the percentage of disturbed morphologies is considered for each of the flat and steep subsamples using both morphology indicators. The samples are restricted to sources at $z < 1$ since disturbed morphologies are unlikely to be detected at higher redshifts. The percentage of disturbed sources are consistent between each of the flat, steep and non-extreme sub-samples. Therefore there is no evidence that their morphology influences their X-ray power-law slope. However, as a precaution any source marked as ‘disturbed’ (from the visual inspection) was removed from the sample of intrinsic extremes. This applies to 1 steep source and 4 flat sources, only 1 of which would not have been eliminated for a previous reason.

²<http://cas.sdss.org/dr5/en/tools/chart/navi.asp>

Previous Literature Results

Lines can be seen in quasar spectra due to absorption by neutral hydrogen along the line of sight to the source. Damped Lyman Alpha (DLA) systems occur for column densities $N_{\text{H}} > 2 \times 10^{20} \text{ cm}^{-2}$, while Lyman Limit systems (LLS) have $N_{\text{H}} > 2 \times 10^{17} \text{ cm}^{-2}$. BALQSOs can also be thought of as absorption line systems (AbLS) as their spectra include wide absorption troughs caused by outflowing material. Four of the extreme sources were defined in the literature as including an absorption line system. Whilst these lines are detected in the optical spectra, they indicate the presence of absorbing material along the line of sight to the source, which would affect the X-ray spectrum as well.

SRCID 80352 (SDSS 100205.36+554257.9) is a flat extreme and was originally best-fit with the simple power-law model suggesting unmodelled absorption in the spectrum. Absorption lines with a lower redshift than the source were identified by Ryabinkov et al. (2003). SRCID 15981 (SDSS 015309.12+005250.1) was defined as a DLA by Rao et al. (2006) using the MgII absorption doublet as a tracer. SRCID 78672 (SDSS 095822.18+014524.1) was defined as an Associated Absorption line (AAL) system by Ganguly et al. (2007). They tend to have a narrow velocity dispersion, $\lesssim 500 \text{ km s}^{-1}$, and a low velocity separation from the background quasar, $\lesssim 5000 \text{ km s}^{-1}$, suggesting the absorption system is more likely to be physically associated. SRCID 122068 was defined as a DLA by Prochaska et al. (2005) and also as a BALQSO by both Scaringi et al. (2009) and Trump et al. (2006).

Multiple X-ray Detections

The X-ray spectra of the sources in the sample were created by merging spectra from separate detections of the sources by *XMM-Newton*, providing they passed the screening criteria described in §3.2. The spectra from the two MOS cameras were also combined. This has the advantage of creating higher S/N spectra, but the potential disadvantage associated with using data taken at different epochs. Whilst any differences in calibration state will have been taken into account by the appropriate ccf file (see §2.1.3), any intrinsic variation in the spectral properties of the source itself will not be accounted for. Spectral state changes, such as those observed in Black Hole Binaries (BHBs) would occur on timescales of $\sim 10^5$ years (Sobolewska

et al., 2011) and are therefore not observed in individual AGN. However, in order to eliminate variations between observations as a possible reason for a slightly unusual spectrum, sources created from multiple detections are not included in the intrinsic extreme sample unless the individual spectra created before the merging were consistent with each other. 9 flat sources and 7 steep sources are removed as a result. Only 1 flat and 3 steep sources would have not been removed for another reason.

4.4 Intrinsic Extremes

The full sample of extremes included 58 flat sources with $\Gamma < 1.54$. However, 20 of these can be fit with a model where Γ is fixed at 2.0 and an absorption component is added, and a further 15 are better fit with a complex absorption model. 8 are found to be RLQ (or unknown radio loudness) and 3 are BALQSOs. Another 2 sources were removed due to possible problems with multiple detections or mentions in the literature. Removing these sources gives a sample of 10 sources whose flat Γ values cannot be explained, and are therefore assumed to be intrinsically flat.

The full extreme sample included 51 steep sources with $\Gamma > 2.44$. 23 of these were better fit with a model where Γ was fixed at 2.0 and a soft excess was added and another was better fit with the po+bb model in which Γ was free to vary between 1.7 and 2.3. 6 were RLQ, 1 was a BALQSO and 2 were found to be NLS1. A further 5 were removed due to the literature search or complications with multiple detections. Removing these sources leaves 13 sources whose power-law slopes are assumed to be intrinsically steep.

The remaining intrinsic sample includes 23 sources; 10 flat and 13 steep. This sample represents $\sim 21\%$ of the initial extreme sample and $\sim 3\%$ of the entire initial sample of 761 objects. Details of each source are included in Table 4.2 and the optical and X-ray spectra are presented for some interesting sources below.

These remaining intrinsic extreme sources all have low (< 350) numbers of counts in their X-ray spectra. Therefore, the spectra are binned to 1 count per bin and re-fit using the Cash statistic to check if the extreme Γ obtained is a consequence of using the χ^2 statistic and

SRCID	SDSSName	Γ	σ_{Γ}	z	$\log(L_X)$	CTS	$\log(M_{\text{BH}})$	$\log\left(\frac{L_{\text{bol}}}{L_{\text{Edd}}}\right)$	A_V
81596	101148.98+5541.016	1.260	0.085	1.5329	44.44	282	9.515	-1.488	0.39 ± 0.03
82106	101616.77+391143.3	1.095	0.084	0.4123	43.77	318	8.508	-1.375	-0.52 ± 0.10
85135	103357.21+005324.8	1.503	0.178	1.7103	45.03	99	9.448	-0.629	0.67 ± 0.26
85331	103518.53+392934.9	1.448	0.098	0.8773	43.82	341	8.901	-1.700	0.27 ± 0.28
94995	112020.96+432545.1	1.188	0.183	3.5479	45.02	114	8.573	0.236	-0.02 ± 0.01
95096	112048.99+133821.9	1.371	0.234	0.5128	42.98	92	9.324	-3.194	-0.35 ± 0.14
96674	113342.72+490025.8	1.474	0.116	1.2949	44.98	197	9.518	-0.772	0.75 ± 0.03
105706	122853.71+441152.8	1.486	0.149	1.2769	44.56	167	8.950	-0.772	-0.09 ± 0.20
134510	143506.62+033257.2	1.483	0.150	2.4042	44.83	146	9.100	-0.558	0.50 ± 0.22
137426	150152.76+014837.4	1.327	0.294	3.7738	44.61	101			-0.47 ± 0.00
12003	011824.28-010832.0	2.637	0.252	0.9660	44.08	128	8.790	-1.242	-0.40 ± 0.09
17998	021449.10-005040.9	2.591	0.245	1.5977	44.03	134	8.916	-1.435	0.00 ± 0.04
24188	023451.43-084005.1	2.572	0.284	1.6082	44.29	87	9.154	-1.336	-0.06 ± 0.07
27218	030220.46+001937.4	2.749	0.240	0.7741	43.84	342	7.785	-0.561	0.03 ± 0.49
68864	083748.99+254412.9	2.468	0.185	1.9119	44.97	104	9.704	-0.964	0.23 ± 0.01
75475	093205.68+284343.9	2.571	0.206	1.1673	44.38	206	9.074	-1.136	-0.45 ± 0.10
78393	095726.33+411628.7	2.471	0.313	1.7010	44.25	81	9.002	-1.238	0.19 ± 0.14
84741	103114.20+051718.3	2.482	0.193	2.4273	44.76	183	9.585	-1.132	0.25 ± 0.14
93708	111512.44+525601.5	2.562	0.288	1.1034	44.32	77	9.017	-1.148	-0.12 ± 0.07
123468	133314.81+504526.1	2.646	0.229	1.1734	43.94	140	8.438	-1.083	0.15 ± 0.22
124759	133735.65+520530.7	2.518	0.221	0.8419	43.88	166	8.630	-1.342	0.14 ± 0.12
139000	151403.00+365700.6	2.446	0.163	1.4059	44.38	179	8.992	-1.046	-0.03 ± 0.08
210692	144003.78+023805.7	2.493	0.265	1.4971	44.33	84	9.247	-1.367	0.18 ± 0.03

Table 4.2: The sample of intrinsic extreme sources including 10 flat (top) and 13 steep (bottom). Γ = best-fitting power-law slope value, σ_{Γ} = 68% error on Γ , z = spectroscopic redshift from the SDSS DR5 quasar catalogue, $\log(L_X)$ = log X-ray luminosity in the 2 – 10 keV band determined in XSPEC from the best-fitting spectral model and corrected for Galactic absorption, CTS = Total number of MOS+pn background subtracted counts in the X-ray spectra, $\log(M_{\text{BH}})$ = log black hole mass estimate from Shen et al. (2008) where available, $\log\left(\frac{L_{\text{bol}}}{L_{\text{Edd}}}\right)$ = X-ray derived Eddington ratio (as determined in §3.3.7), A_V = optical extinction estimate from Hutton et al. (in preparation).

binned spectra when there aren't enough counts for this to be appropriate. The majority of the flat sources give consistent results in which the best-fitting Γ value is still extreme. However, there are 2 notable exceptions; SRCID 105706 when fit with Cash statistics has a power-law slope of $\Gamma = 1.64 \pm 0.14$, which is both steeper than the original flat slope of $\Gamma = 1.49 \pm 0.15$ and no longer extreme. SRCID 134510 retains a flat Γ value when fit using a simple power-law model and Cash statistics. However, a non extreme value of $\Gamma = 1.62 \pm 0.16$ can be obtained when using an absorbed power-law model with $N_{\text{H}} = 0.72_{-0.32}^{+0.48} \times 10^{22} \text{ cm}^{-2}$. The majority (9/13) of the steep sources have a non-extreme Γ value when re-fit using the Cash statistic, with 5 sources having values inconsistent with those obtained using χ^2 . This likely occurs due to the large errors on the Γ parameter which allow the value to change considerably between fittings. The large errors on Γ , occurring due to the low numbers of counts in the spectra, mean that only 1 steep (27218) and 3 flat (81596, 82106 & 94995) sources can be regarded as *significantly* extreme when their 1σ errors are also considered. These sources all have counts much lower than the threshold required to significantly detect a spectral complexity in the spectrum. However, by checking if a good fit is possible when the features are forced to be included, this possibility should have been largely eliminated.

SRCID 82106 (SDSS 101616.77 +391143.3)

This source is the flattest of the intrinsic extremes, with a photon index of $\Gamma = 1.095 \pm 0.084$, significantly flatter than the average for the entire original sample at the 2σ level (see Fig. 4.18, top). This source is interesting as the optical spectrum shows a very blue continuum, supported by the measured optical extinction value, $A_V = -0.52 \pm 0.10$, the most blue of any of the extremes. This is unexpected considering the flat X-ray spectrum.

SRCID 94995 (SDSS 112020.96 +432545.1)

This source has a flat photon index of $\Gamma = 1.188 \pm 0.183$, significantly flatter than the average for the entire original sample at the 1.5σ level (see Fig. 4.18, second). The source is at high redshift, $z = 3.5$, so the Ly- α forest can be seen in the optical spectrum. It has a high luminosity, $L_X = 1.05 \times 10^{45} \text{ erg s}^{-1}$, a black hole mass of $M_{\text{BH}} = 3.7 \times 10^8 M_{\odot}$ and a high

(log) Eddington ratio of 0.236, likely due to the high X-ray luminosity. The optically derived Eddington ratio is 0.16, which is still apparently super-Eddington.

SRCID 95096 (SDSS 112048.99+133821.9)

This source has a flat photon index of $\Gamma = 1.371 \pm 0.234$ (see Fig. 4.18, third). It has an Eddington ratio of -3.194 , making it a distinct outlier from the rest of the sample, both extreme and non-extreme. This occurs despite having a fairly large black hole mass of $M_{\text{BH}} = 2.1 \times 10^9 M_{\odot}$, as the source has a low X-ray luminosity; $L_{\text{X}} = 9.5 \times 10^{42} \text{ erg s}^{-1}$. The optically derived Eddington ratio is -1.93 .

SRCID 96674 (SDSS 113342.72+490025.8)

This source has been previously studied by Young et al. (2008) using an *XMM-Newton* spectrum and it is identified as an intrinsically red quasar. They report $\Gamma = 1.4_{-0.4}^{+0.5}$, in agreement with the measured value of $\Gamma = 1.474 \pm 0.116$ from this analysis (see Fig. 4.18, bottom). A flat X-ray spectrum is in agreement with the measured value of $A_{\text{V}} = 0.75 \pm 0.03$.

SRCID 27218 (SDSS 030220.46+001937.4)

This source is the steepest of the extreme sources with a power-law slope of $\Gamma = 2.749 \pm 0.240$ (see Fig. 4.19, top). However, the optical spectrum does not appear to have a particularly blue continuum, as expected for a quasar, particularly one with a steep Γ value. The best-fitting model for the X-ray spectrum is an absorbed power-law. If absorption is present in the source this would explain the redder optical continuum. It is possible that the Γ value has been artificially steepened by adding a column density to the model which is too high. The simple power law model po gives $\Gamma = 2.16 \pm 0.19$, which does not classify the source as extreme, however, absorption is required by the F-test at 99.69% significance and there is an improvement in the fit from $p = 20\%$ to $p = 65\%$ when the column density of $N_{\text{H}} = (0.72 \pm 0.26) \times 10^{22} \text{ cm}^{-2}$ is added.

SRCID 84741 (SDSS 103114.20 +051718.3)

This source has a steep power-law slope of $\Gamma = 2.482 \pm 0.193$ (see Fig. 4.19, middle). The optical extinction estimate, $A_V = 0.25 \pm 0.14$, suggests the optical spectrum is particularly red, unexpected for a source with a steep X-ray power law. However, this source is at a high redshift of $z = 2.4$ meaning Ly- α and some of the Ly- α forest can be seen in the optical spectrum. When the Cash statistic is used, $\Gamma = 2.24^{+0.23}_{-0.09}$, which is no longer extreme.

SRCID 210692 (SDSS 144003.78 +023805.7)

This source has a steep power-law slope of $\Gamma = 2.493 \pm 0.265$ (see Fig. 4.19, bottom). The optical extinction estimate, $A_V = 0.18 \pm 0.03$, suggests the optical spectrum is particularly red, unexpected for a source with a steep X-ray power law. As this source only includes 84 counts, the spectra were also binned to a minimum of 1 count per bin. When the Cash statistic is used, $\Gamma = 2.26^{+0.3}_{-0.14}$. In this case the Γ value is no longer extreme, although there is a large error on the estimate, particularly in the direction of a steeper value.

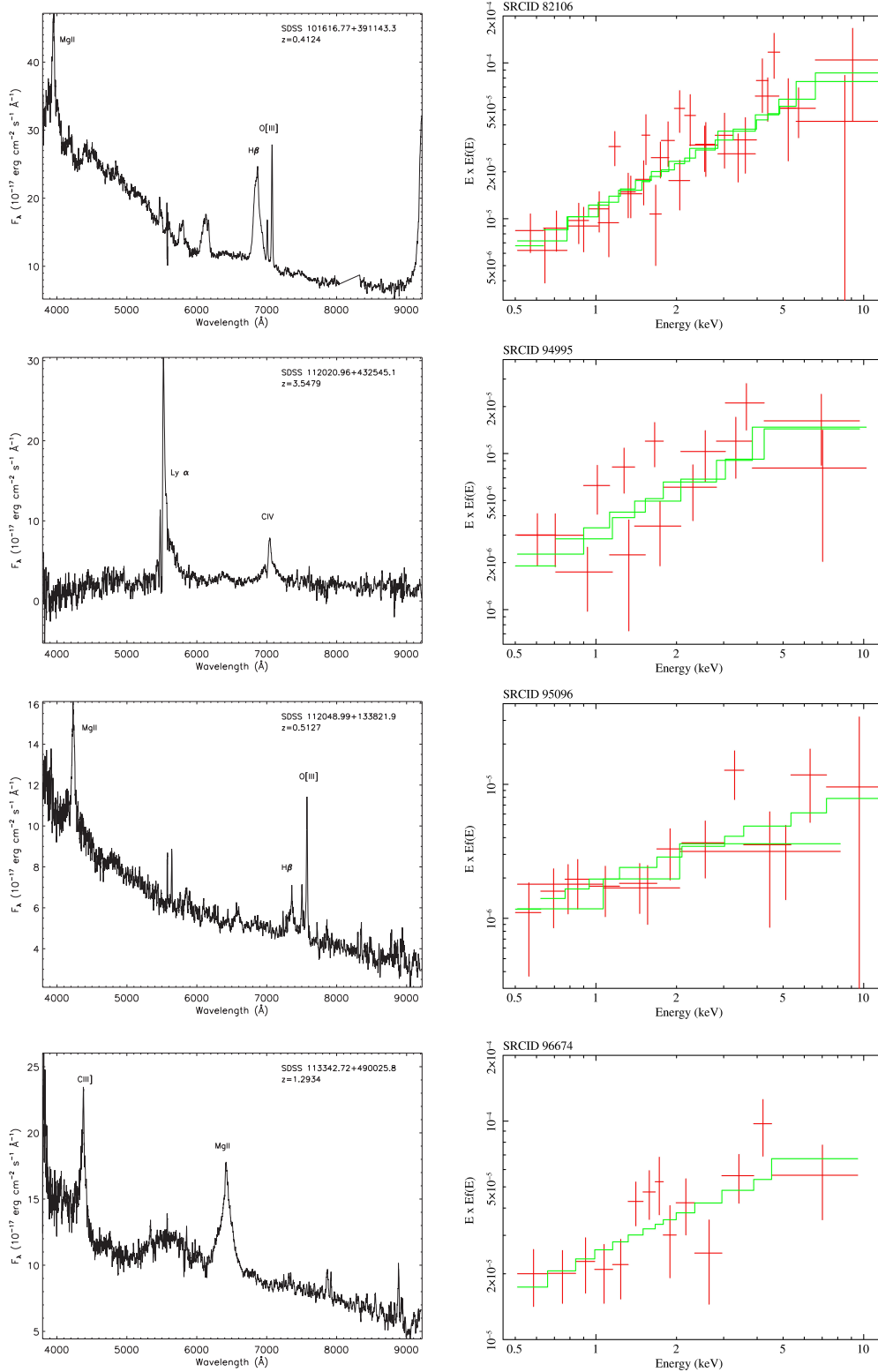


Figure 4.18: Top - SRCID 82106; the flattest of the intrinsic extremes ($\Gamma = 1.095 \pm 0.084$), but also has a low optical extinction ($A_V = -0.52 \pm 0.10$) and hence is very blue. Second - SRCID 94995; this source has a very high X-ray derived Eddington ratio (0.236). Third - SRCID 95096; this source has a very low X-ray derived Eddington ratio (-3.194). Bottom - SRCID 96674; this source has been previously defined as an intrinsically red quasar by Young et al. (2008). Its flat X-ray spectrum ($\Gamma = 1.4_{-0.4}^{+0.5}$) agrees with its red optical spectrum ($A_V = 0.75 \pm 0.03$).

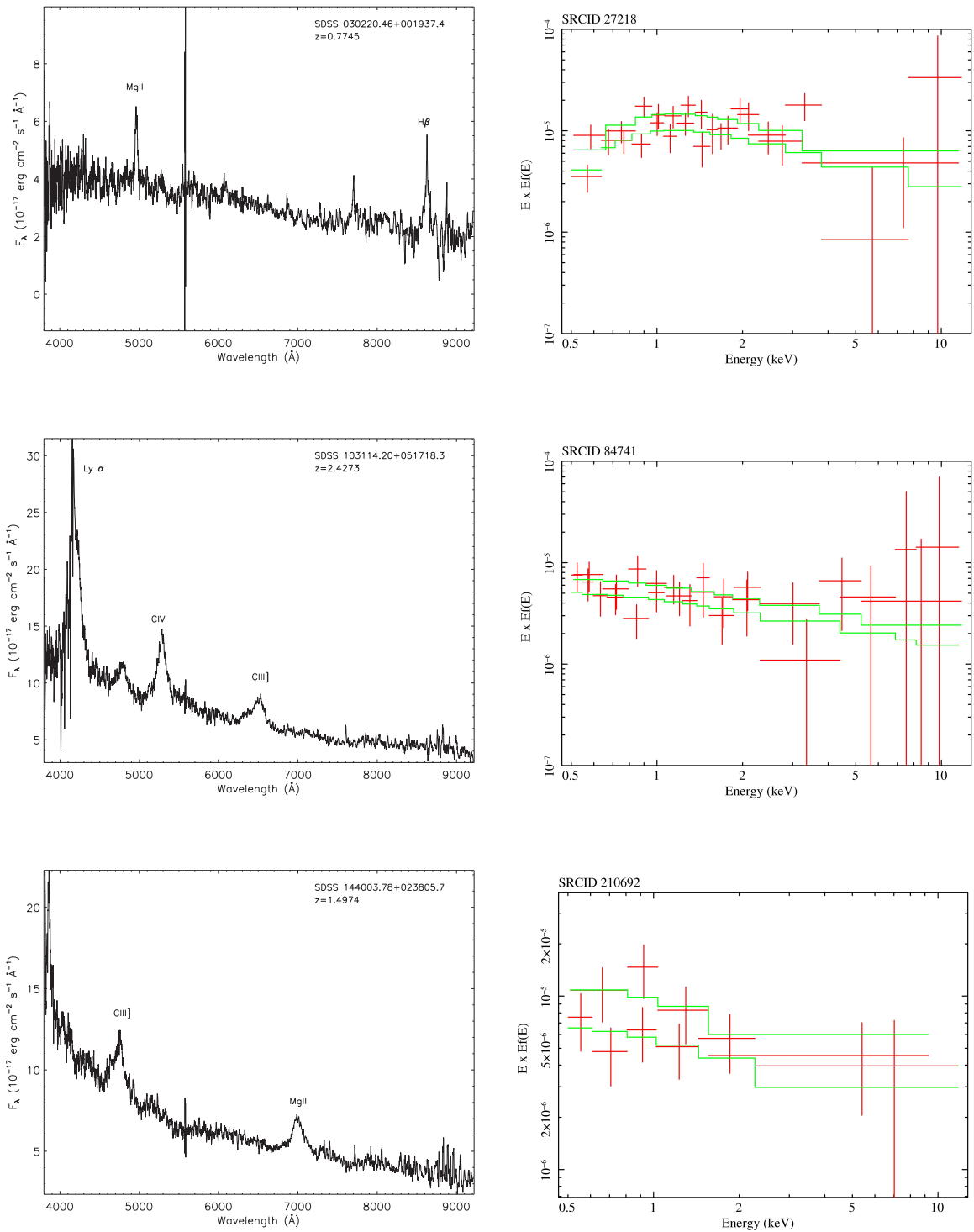


Figure 4.19: Top - SRCID 27218; the steepest of the extreme sources which is unusual in that its optical spectrum appears red and its X-ray spectrum is best-fit with an intrinsically absorbed power law where $N_{\text{H}} = (0.72 \pm 0.26) \times 10^{22}$ cm $^{-2}$. Middle - SRCID 84741; this source has a steep photon index of $\Gamma = 2.482 \pm 0.193$ but an unusually red optical spectrum ($A_V = 0.25 \pm 0.14$). Bottom - SRCID 210692; this source has a steep photon index of $\Gamma = 2.493 \pm 0.265$ but an unusually red optical spectrum with $A_V = 0.18 \pm 0.03$.

4.4.1 Physical Properties

In this section, the physical properties of the intrinsic extreme sample as a whole are studied. Fig. 4.20 plots the Γ values of the intrinsic extreme sources relative to the general population. This shows that the intrinsic extreme sources are not those found in the very extreme wings of the Γ distribution, but still have underlying power-law slopes as flat as $\Gamma \sim 1$ and as steep as $\Gamma \sim 2.7$. The sources which do lie outside of this range have an alternative explanation for their extreme values (such as being better fit with a more complicated model) and it is only their apparent Γ value, rather than their intrinsic Γ value which is extreme. A normalised version of this plot can be seen in Fig. 4.21 (top left).

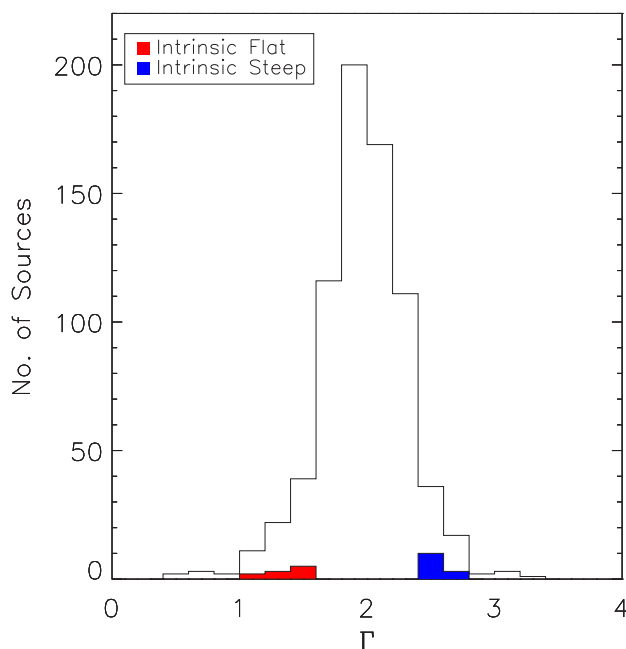


Figure 4.20: The distribution of Γ values for the remaining 23 intrinsic extreme sources (10 flat and 13 steep) compared to the original distribution of 734 sources.

The extreme population is also compared to the general population with regards to the parameters; counts, redshift, 2 – 10 keV X-ray luminosity, black hole mass and X-ray derived Eddington ratio. These distributions can be seen in Fig. 4.21. KS tests again show that the counts distribution of the extreme sources is significantly lower than that of the non-extreme population, expected since the intrinsic sample is a sub-sample of the full extreme sample. Both the luminosity and Eddington ratio distributions of the steep sources are shown to be

significantly different to those of the non-extreme population (KS significances = 0.002 and 0.001, respectively). The Eddington ratio histogram shows a single source (SRCID 95096) with a very low Eddington ratio, occurring due to its low X-ray luminosity ($L_X = 9.5 \times 10^{42} \text{ erg s}^{-1}$). The luminosity histogram also shows some flat sources with low L_X values, contrary to the trend for the full sample. In §3.3.3 a strong anti-correlation between Γ and L_X was found, implying that the low L_X sources tend to have steeper Γ values. However the spread in Γ values is very large at low L_X , meaning there are some low L_X sources with flat Γ values despite the general trend. The histograms of black hole masses show that all 3 sub-samples have very similar distributions.

Fig. 4.22 shows the location in counts/redshift space of the intrinsic flat and steep sources compared to the sources in the general population and the original full sample of extreme sources. With the exception of 2 flat sources (SRCIDs 94995 and 137426) at high redshift ($z > 3$), the distributions appear to be similar.

The sample of sources considered in this section have been chosen for having intrinsically flat or steep power-law values which cannot be explained away simply by using a more complicated spectral model. This makes them ideal for studying trends of Γ with basic physical properties such as L_X , M_{BH} and λ_{Edd} ; properties which are all expected to be correlated. These correlations can be seen in Fig. 4.23. The tightest correlations are between X-ray luminosity and black hole mass and X-ray luminosity and the Eddington ratio. There is no significant correlation ($< 2\sigma$) between Eddington ratio and black hole mass. The bolometric luminosity estimates were determined from the measured L_X values (see §3.3.7). Therefore a correlation is expected between L_X and M_{BH} as indicated by Equation 1.1. Similarly, the definition of the Eddington ratio as the ratio of the bolometric and the Eddington luminosities suggests a correlation between λ_{Edd} and L_X .

In Fig. 4.23, the extreme sources (both flat and steep) occupy a similar area to the sources in the general population. This suggests that their extreme Γ values are not dependent on the combination of these parameters. However, in Chapter 3 the dependence of Γ on these individual properties has already been investigated. In particular, a strong anti-correlation was found between Γ and L_X . The correlation of Γ with Eddington ratio was found to switch

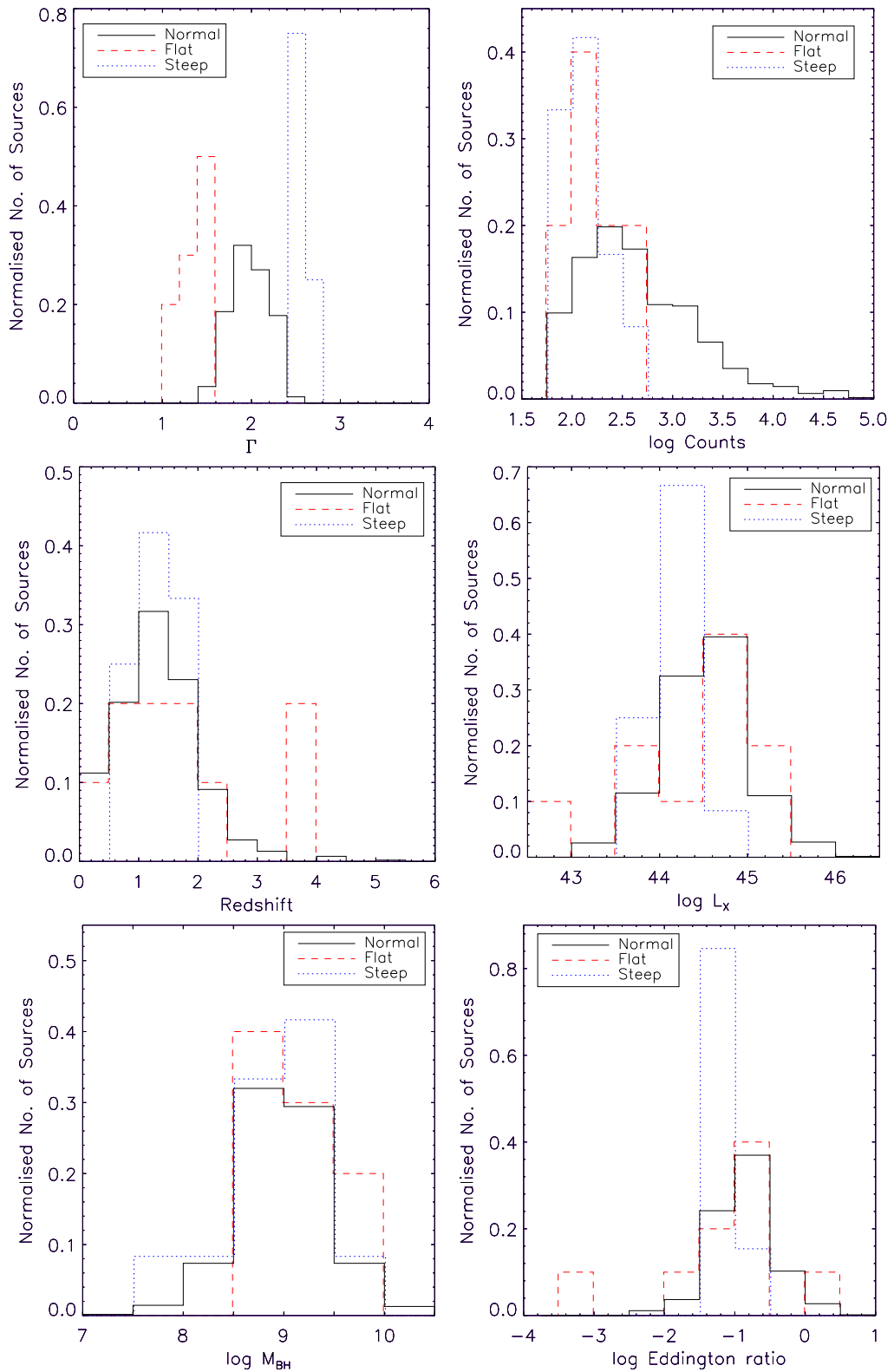


Figure 4.21: These figures compare the distributions of Γ , counts, redshift, 2–10 keV X-ray luminosity, black hole mass and Eddington ratio for the remaining flat (red, dashed) and steep (blue, dotted) samples with the original population of sources with non-extreme (black, solid) Γ values.

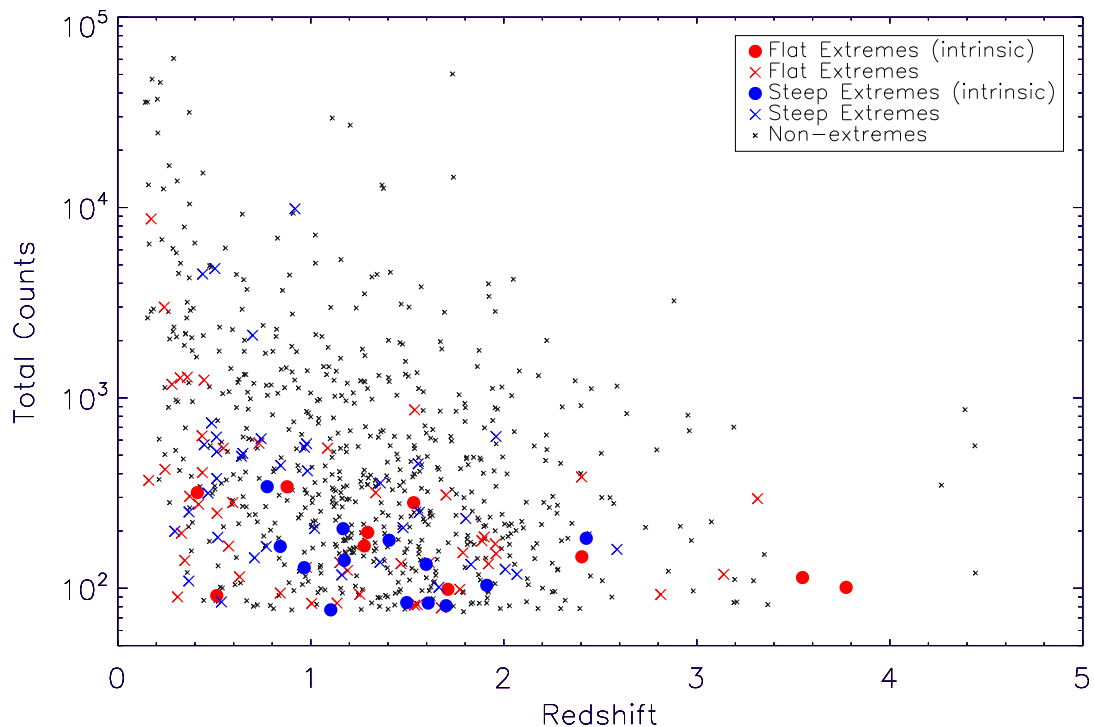


Figure 4.22: This shows the counts/redshift distribution of the sources with non-extreme Γ values (small black crosses) compared with the intrinsic flat (red circles), intrinsic steep (blue circles) and original full extreme sample (red and blue crosses).

direction depending on which broad line was used to estimate the back hole mass (see §3.3.7). This therefore also divides the sources by redshift. When the $H\beta$ line is used, only sources at $z < 0.7$ are included, giving a positive correlation implying that sources with higher Eddington ratios tend to have steeper Γ values. When the MgII line is used, corresponding to sources at $0.7 < z < 1.9$, no correlation is found, and an anti-correlation is seen when the CIV line is used (sources with $z > 1.9$). The average redshift of the 13 steep sources is $z = 1.4 \pm 0.2$ with a spread of $0.77 - 2.43$, meaning all except one of the sources falls into the MgII regime. Therefore, a correlation between Γ and Eddington ratio is not expected. The 10 flat sources show a much larger spread in redshift from $0.33 - 3.77$ ($z_{av} = 1.6 \pm 0.4$) and therefore 3 sources lie in the $H\beta$ regime, 4 in the MgII and 3 in the CIV. A trend between Γ and Eddington ratio is therefore also not expected for this combination of sources.

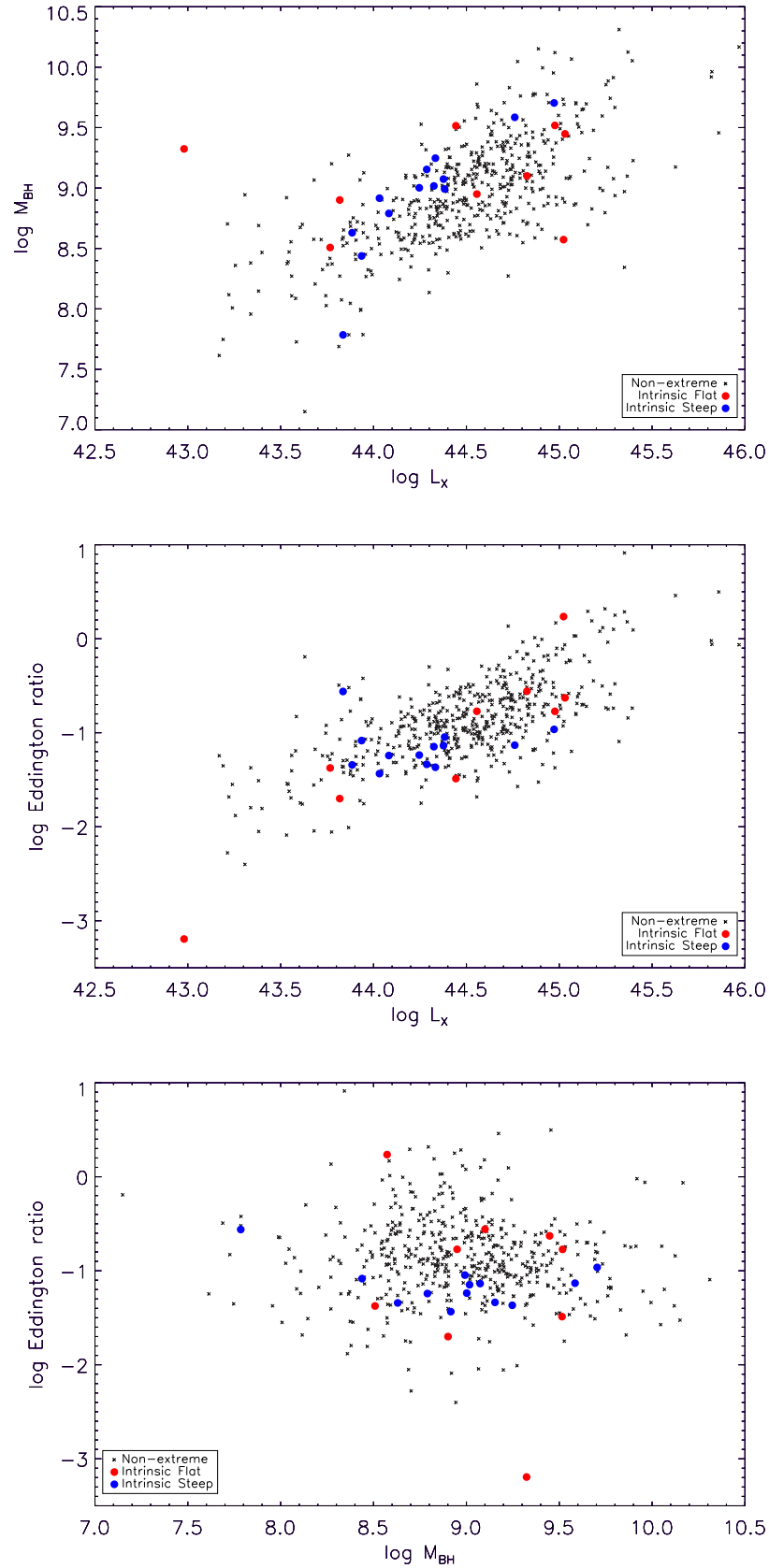


Figure 4.23: These figures show (in 2D) the area of 3D parameter space (M_{BH} , L_X , λ_{Edd}) occupied by the sources in the general population (black crosses). The extreme sources are shown to occupy a similar area, with the exception of SRCID 95096 (flat).

4.5 Discussion

In Chapter 3 the X-ray spectral fitting of a sample of 761 sources was described. In this Chapter, a sub-sample of 109 extreme sources with $\Gamma < 1.54$ or $\Gamma > 2.44$ were considered. Of these sources, 44 could be fit with a more complex model in which a spectral complexity such as cold absorption or a soft excess was included in the fit. These components had not been significantly required in the fit from the original analysis, due to the low quality of the spectra. However, if they are included the Γ values are no longer extreme. 15 sources were well fit with a model including either a partially ionised or partially covering absorbing column. These models had not been considered in the original analysis. 20 of these sources were classified as particular sub-types of type 1 AGN such as NLS1, BALQSO or RLQ, which are all known to show unusual X-ray spectra as their intrinsic emission is modified by winds and jets before it reaches the observer. 7 other sources were removed from the full sample of extremes because their spectra were combined from multiple detections, or had known absorption systems in the line of sight. This left a final sample of 23 sources, thought to have intrinsically extreme power-law slopes. This corresponds to $\sim 21\%$ of the extreme sample and $\sim 3\%$ of the full sample.

This analysis shows that within a sample of serendipitously detected AGN which have X-ray spectra with typically low numbers of counts, $\sim 14\%$ will show apparently extreme power-law slopes, but only $\sim 3\%$ of these are expected to be intrinsically extreme. It is therefore important to check unusual spectral fitting results obtained via automated fitting routines. Young et al. (2009), who use a similar sample of sources to those described here, find a range of Γ values from 0.4 – 4.3. These are therefore likely to be extreme simply due to the low quality of the X-ray spectra and not due to a physical effect. Their sample has an intrinsic dispersion of $\sigma = 0.37$, larger than the $\sigma = 0.30 \pm 0.01$ found for this sample. When the Γ distribution is reconsidered having removed NLS1, BALQSO and RLQ, the intrinsic dispersion is $\sigma = 0.26 \pm 0.01$. This falls to $\sigma = 0.24 \pm 0.01$, once the extremes which can be explained with a more complex model are taken into account.

The Γ values in the intrinsic sample range from $\Gamma = 1.10 \pm 0.08$ (flattest, SRCID 82106) to $\Gamma = 2.75 \pm 0.24$ (steepest, SRCID 27218). These sources are more extreme than the typical

observed range of $\Gamma \sim 1.5 - 2.5$. The flattest source has a comparable spectral index to sources already in the literature such as LBQS 0109+0213 ($\Gamma = 1.23 \pm 0.12$, Shemmer et al. 2008), PHL 909 ($\Gamma = 1.11 \pm 0.11$, Reeves & Turner 2000), PKS 2251+113 ($\Gamma = 0.95 \pm 0.24$, Reeves & Turner 2000) and PG 1440+356 ($\Gamma = 1.2_{-0.2}^{+0.4}$, Piconcelli et al. 2005). However the steepest source has a much higher spectral index than sources found in the literature such as IZWI ($\Gamma = 2.37 \pm 0.05$, Reeves & Turner 2000) or PG 1244+0.26 ($\Gamma = 2.48 \pm 0.03$, Piconcelli et al. 2005).

Sources with extreme Γ values are interesting as they may be indicative of peculiar accretion. However, the intrinsic sample that remains includes spectra with only low numbers of counts³ and is therefore not particularly useful for constraining the power-law production mechanism. Nevertheless, any theory must be able to explain the following observational results:

1. Why the most common spectral index is 2.0.
2. Why there is an intrinsic spread of Γ values.
3. Why the spread of Γ values appears to be symmetric.
4. Why some Γ values can be as flat as ~ 1.0 .
5. Why some Γ values can be as steep as ~ 3.0 .

The cascade model of Svensson (1994) predicts an asymmetric distribution of Γ values from ~ 1.5 to a cut-off at 2.0. Whilst this could explain why the most common spectral index is 2 if all cascades are assumed to saturate, it cannot account for the very steepest sources or the symmetric distribution of values.

³The average is 163.

5

Detectability of Low Energy X-ray Spectral Components in Type 1 AGN

In Chapter 3 the X-ray spectral properties of 761 type 1 AGN were presented. The majority were well fit with a simple power law where $\Gamma \sim 2$, but $\sim 8\%$ also required a soft excess component and $\sim 4\%$ required intrinsic cold absorption in the modelling of their X-ray spectra. Since the ease with which additional components can be detected is limited by the quality of the spectra, these values represent lower limits on the intrinsic percentage of sources which include them. This chapter aims to quantify their detectability in order to deduce how common they really are.

5.1 Introduction

There have been many studies in which some type 1 objects have shown evidence for intrinsic X-ray absorption. The typical percentage of such objects is $\sim 10\%$, with many studies quoting a similar value (Page et al., 2003; Perola et al., 2004; Piconcelli et al., 2005; Mateos et al., 2005b; Mainieri et al., 2007; Garcet et al., 2007; Young et al., 2009; Mateos et al., 2010; Corral et al., 2011).

There is a range of values quoted for the percentage of type 1 sources which include a soft excess including 30 – 50% from a study with *EXOSAT* (Turner & Pounds, 1989), $\sim 40\%$ using *ASCA* (Reeves & Turner, 2000) and it has been suggested that soft excesses may be ubiquitous in optically selected PG quasars (Porquet et al., 2004; Piconcelli et al., 2005). However these samples are biased towards bright and low redshift sources. The quoted percentage of soft excesses can be very different depending upon the redshift range being considered. For example, Mateos et al. (2010) find a percentage of only 8% when considering their entire sample, but this is increased to 36% when only sources at $z < 0.5$ are considered. Similarly the CAIXA sample of *XMM-Newton* target sources finds a high percentage of $\sim 80\%$ (Bianchi et al., 2009). This could be because the sample is biased towards low redshift objects and/or good quality spectra in which detecting the spectral component is easier. Winter et al. (2012) show that the detected percentage increases from $\sim 40\%$ to $\sim 90\%$ when only the best quality spectra of low z AGN are considered. Clearly, in order to determine whether the soft excess is present in all sources, the influences of redshift and spectral quality need to be taken into account, using a sample which covers a large range in these properties.

5.2 Data

The X-ray spectral fitting of the sample is described in detail in §3.2.3 and the number of sources best-fit by each spectral model are listed in Table 3.1. Fig. 5.1 shows the counts and redshift distribution of the sample and indicates how the sample is divided into both count and redshift bins which are described later in the Chapter.

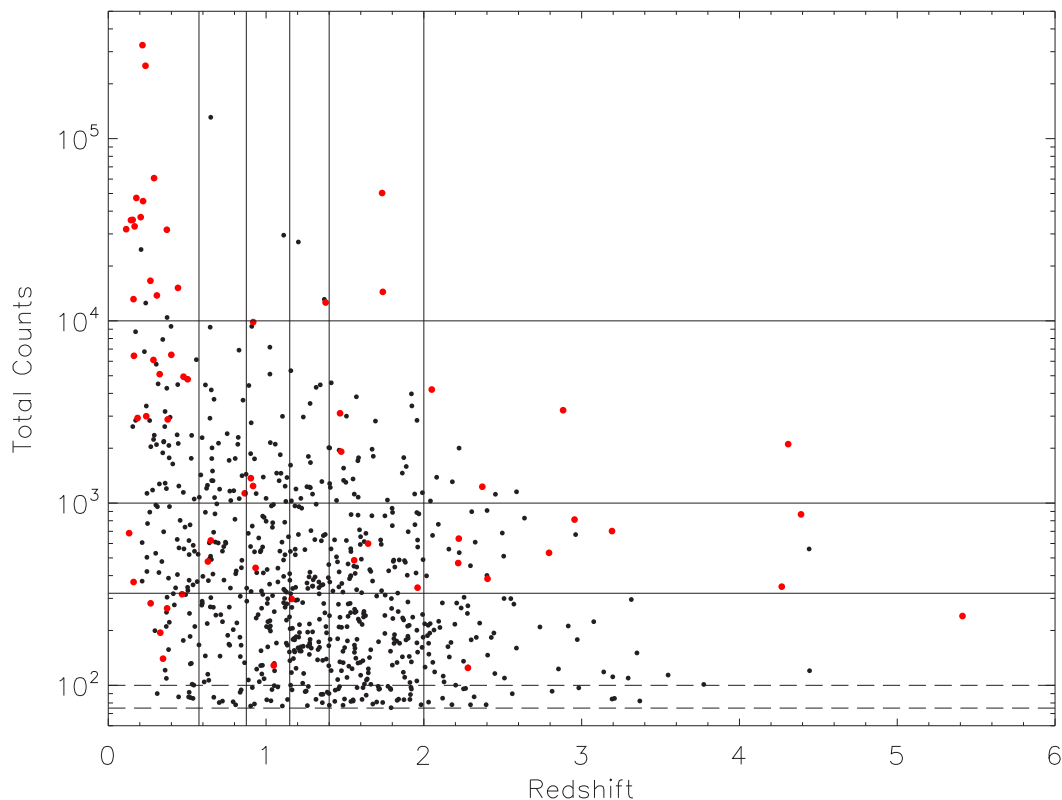


Figure 5.1: The counts and redshift distribution of the sample, with the count and z bins used in this chapter indicated by the black solid lines. Black dashed lines show the lower count limit, which is different when considering soft excess components or absorption. The red points are sources which were the target of the *XMM-Newton* observation.

Fig. 5.2 shows the detected percentages of the soft excess (thick, blue) and absorption (red) components as a function of the total number (MOS+pn) of background subtracted counts in the spectra. The detected percentage of additional components is much lower in spectra with low counts where the statistics are poorer and the features are not detected with enough significance. Since it might be expected that all soft excess components are detected in the highest quality spectra, the intrinsic percentage could be as high as the $\sim 80\%$ found in the top count bin. Fig. 5.2 also shows intrinsic absorption detected in up to $\sim 25\%$ of sources in the higher count bins. Since the sample is drawn from a population of type 1 AGN, such a component is not expected to be required in the modelling of their X-ray spectra. The F-test was used at 99% significance when choosing the best-fitting model for a particular source, therefore 1% of the detections of a specific spectral component can be considered spurious. This 1% level is shown by the dashed line in Fig. 5.2.

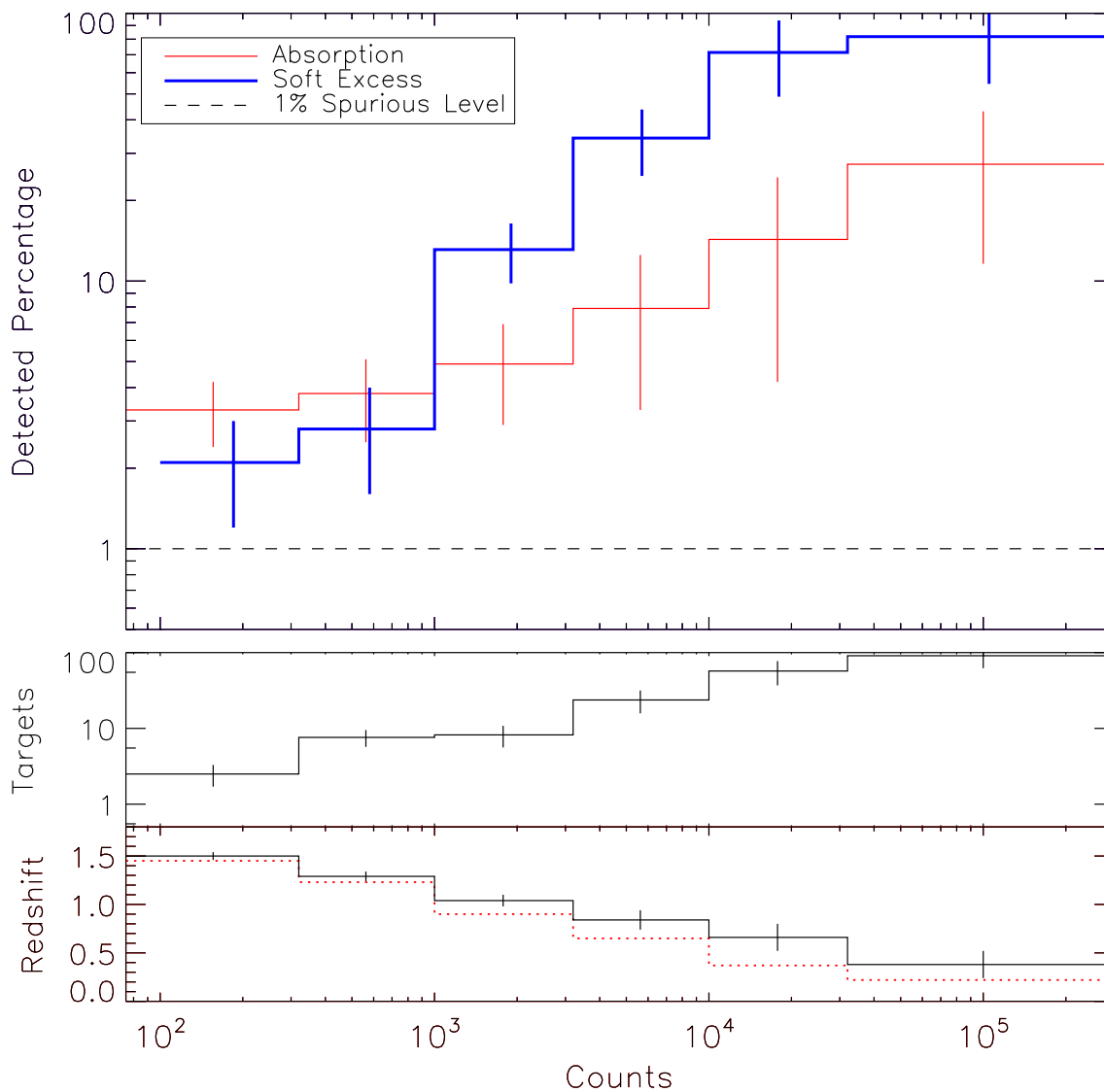


Figure 5.2: The top plot shows how the percentage of sources which require an absorption or soft excess component varies depending on the total number of counts (MOS+pn) that are available in the spectra. The lowest count bin includes sources with between 75 – 320 total counts for absorption and 100 – 320 total counts for the soft excess, since these were the minimum numbers of counts required for fitting that particular spectral component. The sample includes 62 sources which were the target of an *XMM-Newton* observation, rather than a serendipitous detection. The middle plot shows the percentage of sources within each count bin which are target sources. The errors in the top two plots have been calculated using Poissonian statistics. The bottom plot shows how the average redshift of the sources in each count bin varies and includes standard errors on the mean. The red dotted line shows the median redshift of each bin.

The sample contains 62 sources which were the target of an *XMM-Newton* observation and therefore generally contain more counts in their X-ray spectra than the serendipitously detected sources. The percentage of targets in each count bin is shown in Fig. 5.2 and increases towards the higher count bins as expected, with the top bin including almost only target sources. These sources could bias the detection percentages if they were selected for observation due to a previously known soft excess or intrinsic absorption. Therefore the target sources are excluded from the subsequent analysis, leaving 699 sources in the sample (619 with > 100 counts which were fit with models including a soft excess).

For sources at increasing redshifts, the contribution of a soft excess component or absorption in the spectra will decrease as a larger contribution is redshifted outside of the *XMM-Newton* EPIC instrument bandpass (Turner, 2001; Strüder et al., 2001). Therefore the detected percentages of these components are expected to be higher in bins containing mostly low redshift sources. Since these tend to be the bins with higher numbers of counts, the higher detection rate seen may also be due to this redshift bias. The average redshift of the sources in each count bin is plotted in Fig. 5.2 and decreases with increasing counts as expected. However within each count bin the sources cover a large range in redshift. The median redshift within each bin is also plotted on the figure as the dotted red line. These values are consistent with the mean value for the lower count bins, but the difference is larger in the higher count bins due to the low number of sources included.

To further investigate the redshift issue, the sources are split into broad redshift bins of $z < 1$ and $z > 1$. Separate detection curves are created and are shown in Fig. 5.3. In the case of the absorbed sources (top), the detected percentages for the low and high redshift sources appear to be consistent within the error ranges. This is likely due to the large range of N_{H} values found in the sample, which means that absorption can be detected in sources at a reasonably large range of redshifts. The percentage of sources detected with a soft excess component is higher in the low redshift sample than in the high redshift sample as expected. The curve for the $z > 1$ sources shows gaps where the detected fraction falls to zero, due to the low numbers of sources; although soft excesses are detected in the sample up to $z = 2$, the majority (82%) are found in sources with $z \lesssim 1$ as expected.

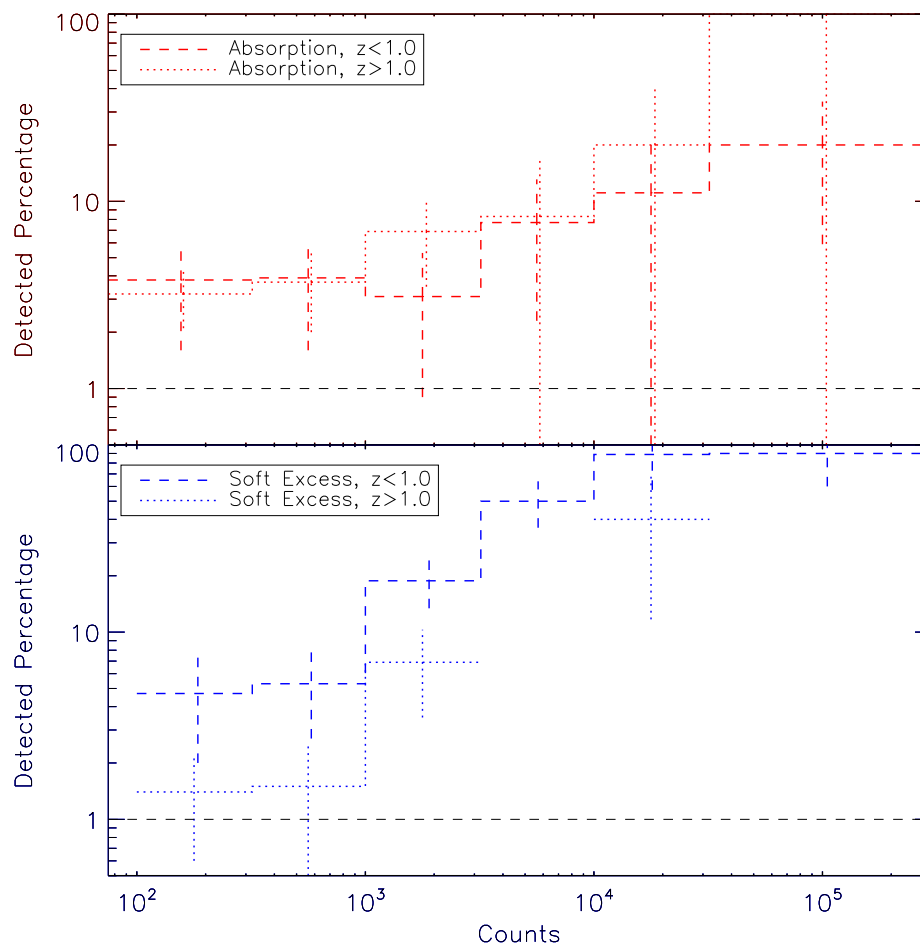


Figure 5.3: These figures show how the detected percentage of absorption (top) and soft excess (bottom) components varies with the number of counts in the spectra, considered in broad redshift bins of $z < 1$ and $z > 1$. There is a clear difference between the two curves in the bottom panel indicating a strong redshift dependence on the detectability of soft excess components.

5.3 Soft Excess Components

5.3.1 Intrinsic Percentage

In order to determine the intrinsic percentage of sources with a soft excess component, multiple sets of simulations are carried out to quantify their detectability. This is done by finding the maximum percentage of components that are expected to be detected in spectra with different numbers of counts.

At each of 5 redshifts and between 7 and 11 different count levels, 1000 spectra are simulated which include a soft excess. Each spectrum is fit over the energy range 0.5 – 12.0 keV with the `po` and `po+bb` models (as described in Chapter 3), and the F-test is used at 99% significance to determine whether the component is statistically required. The percentage of sources in which the component is significantly detected is then determined. By repeating this procedure with sets of spectra at different count levels and redshifts, synthetic detectability curves are constructed from which the maximum detection percentage at any count level can be determined.

The spectra are created using the `fakeit` command in XSPEC which distributes a given number of counts, controlled by varying the exposure time, around a defined model with statistical fluctuations and assigns them Poissonian errors. The model is defined such that it mimics the shape of a typical source in the full sample, both in terms of the shape of the components i.e. the Γ and kT values and the size of the components, particularly the ratio of the blackbody normalisation to that of the power-law normalisation since this will also determine how easy the blackbody is to detect over the power-law continuum. 55 sources required the `po+bb` model in the original analysis. The distribution of power-law slopes and kT values for these sources were each fit with a Gaussian, and the best-fitting mean values with dispersions were $\Gamma = 1.79 \pm 0.46$ and $kT = 0.17 \pm 0.08$ keV. The distribution of blackbody to power-law normalisation ratios are shown in Fig. 5.4 and have a median value of 0.04. Therefore spectra are simulated with $\Gamma = 1.8$, $kT = 0.2$ keV and $bb_{\text{norm}}/pl_{\text{norm}} = 0.04$. These values are intended to represent a ‘typical’ source rather than cover the full range of values, although the distributions of kT and normalisation ratio are reasonably narrow. As shown in Figure 3.27, there is a

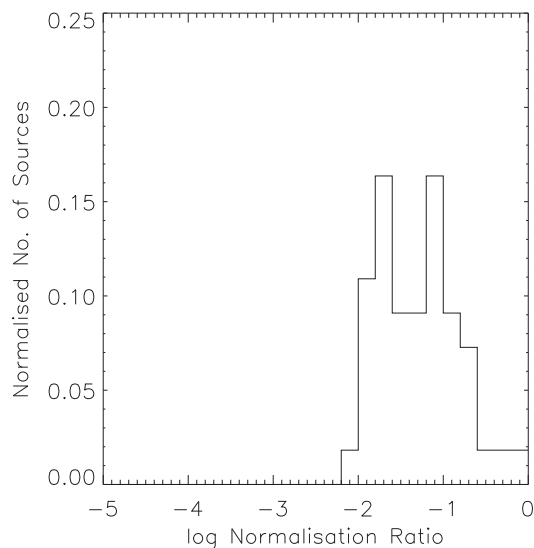


Figure 5.4: The blackbody to power-law normalisation ratios for the sources with a detected soft excess in the original analysis. The median value is 0.04 and the scale is such to allow comparison with Fig. 5.11.

very tight correlation between the luminosities of the blackbody and power-law components. The median normalisation ratio of 0.04 used here corresponds to a luminosity ratio of ~ 0.2 .

Figure 5.5 shows examples of simulated spectra, although in this case all of the counts have been placed in a single MOS spectrum, rather than being divided between a MOS and pn spectrum which are then fit simultaneously, as is done in the actual simulations. On the left is a spectrum with ~ 500 counts in which the soft excess is not significantly detected (F-test = 62.8%). On the right is a spectrum with ~ 8500 counts fit with the po+bb model. In this case $\Gamma = 1.82 \pm 0.03$, $kT = 0.20 \pm 0.01$ keV and F-test = 100% implying the addition of the soft excess component gives an improved fit over that of a simple power law.

As has been previously discussed, the detectability of soft excess components is strongly dependent upon the redshift of the source. Therefore sets of simulations are run at a range of redshifts ($z = 0.4$, $z = 0.75$, $z = 1.0$, $z = 1.3$ and $z = 1.5$) and five separate detectability curves are created. These provide the maximum detection percentage expected for a particular count level if all sources contained this component. If the observed percentages were consistent with this line, it would indicate that the spectral features are present in all of the sources in the sample and it is merely the quality of the spectra that limits their detectability.

The simulated results are fit with linear, quadratic and cubic fits in order to produce de-

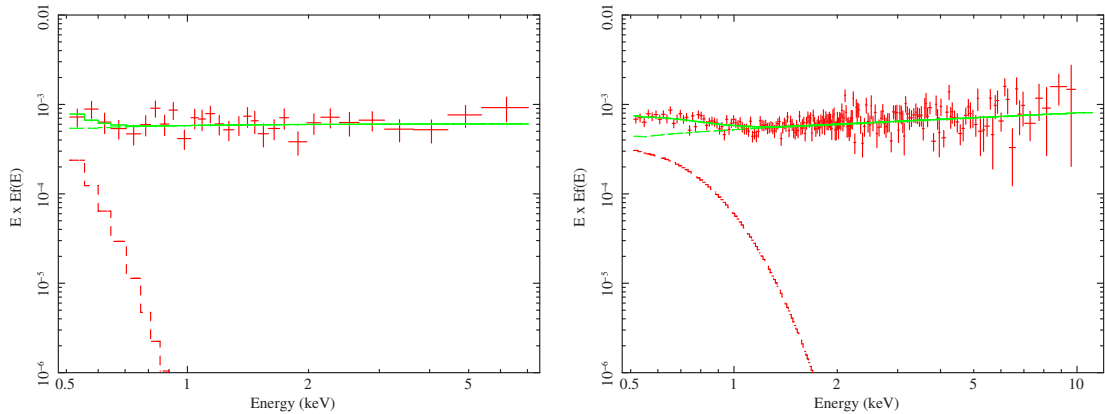


Figure 5.5: This figure shows simulated MOS spectra with ~ 500 counts (left) and ~ 8500 counts (right). They are both shown fit with the po+bb model, although the soft excess is not statistically required in the low count spectrum.

tectability curves. The cubic fit is not statistically required for any curve (according to the F-test used at 99% significance). In the case of the $z = 0.4$ and $z = 0.75$ curves the quadratic fit gives an improvement over a linear fit and for $z = 1.5$, the F-test value is 98.1%. The quadratic curve for $z = 1.3$ has a slightly different curvature from the asymptotic behaviour expected and when the second derivative is forced to be less than or equal to zero, a linear best-fit is returned. Therefore the subsequent analysis uses quadratic fits to the $z = 0.4$, $z = 0.7$, $z = 1.0$ and $z = 1.5$ curves, but a linear fit for $z = 1.3$ as shown in Fig. 5.6. The overall results do not change if different line fittings are used as the uncertainty in the curve fitting is considerably smaller than the error on the observed detected percentages, which dominates. For sources at $z \leq 1$ with $\gtrsim 10,000$ counts, the detectability curves lie at 100%. This suggests that the intrinsic percentage could be as high as $\sim 70\%$; the percentage found in the highest count bin (after removal of the target sources).

The true soft excess detection percentage (corrected percentage) is determined for each count bin by dividing the observed detection percentage by the maximum percentage obtained from the simulated curves which is fixed to lie between the spurious level, 1%, and 100%. As each bin includes sources at a range of redshifts, a corrected percentage is calculated using all five of the detectability curves and a weighted average is determined according to Eqn. 5.1 where the ‘weight’ is the fraction of sources for which each particular redshift curve is appropriate for within that count bin. These redshift bins are marked on Fig. 5.1.

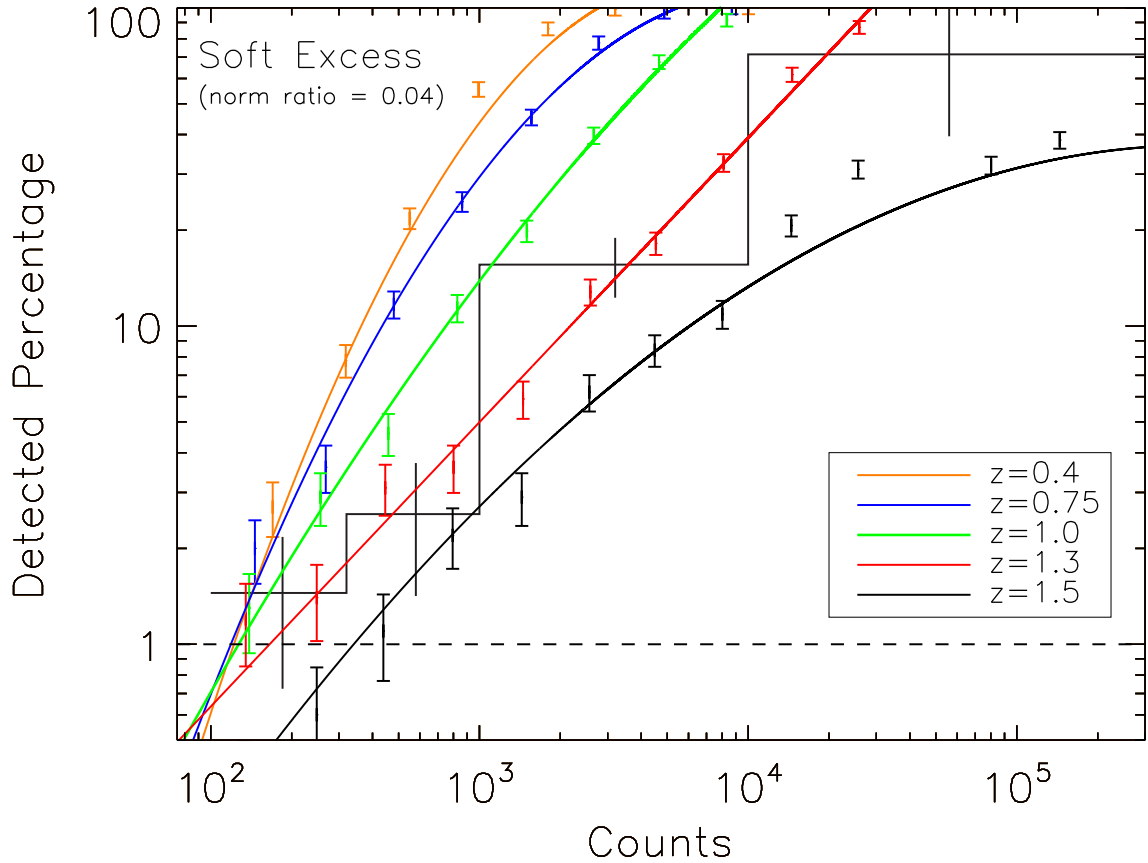


Figure 5.6: The solid black line with error bars shows the observed percentage of soft excess components as a function of counts for the sample after the target sources have been removed, which requires a re-binning of the sources. The coloured curves show the detectability level for a soft excess component with a typical shape and size. Sets of simulations are carried out at different redshifts and count levels as shown by the coloured error bars, where the error is determined from Poissonian statistics. Each of the curves are created from a quadratic fit to at least 7 such results (a linear fit is used for $z = 1.3$).

$$\text{Result} = \sum (\text{weight} \times \text{corrected percentage}) \quad (5.1)$$

For sources at $z > 2$, the maximum percentage is fixed at 1%, as no real soft excesses are expected, but spurious detections may occur. Since the count bins are broad and the sources are not distributed evenly within them, they are further divided into sub-bins. The redshift-corrected percentage is calculated for each as outlined above, and an overall corrected percentage is reconstructed for the full count bin using Eqn. 5.1, where ‘weight’ in this case is the fraction of sources within the particular count sub-bin.

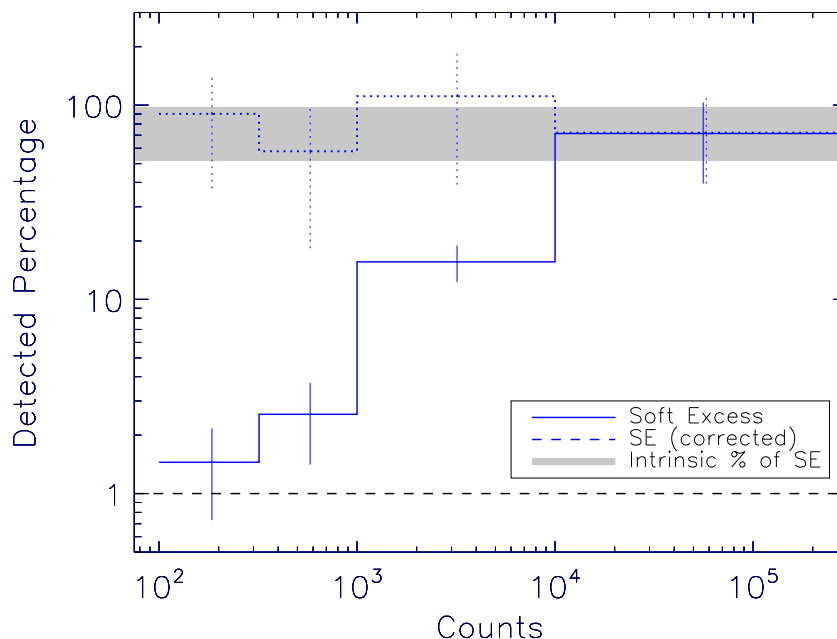


Figure 5.7: The blue solid line shows the observed percentage of soft excess components in the sample (after the target sources have been removed). The dashed line shows the detected percentage determined after the correction for spectral quality. The grey bar indicates the location of the intrinsic percentage of sources with soft excesses, where the width of the bar represents the 1σ error boundary.

The dashed blue line in Fig. 5.7 shows the corrected percentages found from this method. The values are roughly constant after the effect of spectral quality has been removed. In order to determine a value for the intrinsic percentage, χ^2 is calculated for constant percentages between 0 and 100%. The minimum χ^2 occurs for a constant percentage of $75 \pm 23\%$, for which the fit has a null hypothesis probability of $p = 91\%$. This method produces a corrected percentage greater than 100% in the third bin. Whilst this has no physical meaning, its large error bar makes it entirely consistent with the corrected percentages obtained for the other bins. Capping this bin at 100% reduces the intrinsic percentage estimate by only 1%.

To test whether a 1% spurious level is appropriate, spectra which did not include a soft excess were simulated, and the percentage in which this component was incorrectly detected with $> 99\%$ significance was calculated. The simulation results are shown in Fig. 5.8. For the majority of count levels this percentage was consistent with, or lower than 1%. However, for the lowest and highest count levels ($\lesssim 100$ and $\sim 50,000$) the spurious level was somewhat higher (up to $\sim 5\%$), suggesting that both the usual statistical problems affecting simulated fits and some small systematic calibration errors exist. Such simulations were also carried out at higher redshifts and the results were found to be consistent. The count bin most affected

by the spurious level is the lowest, as the simulated curve for $z = 1.5$ sources falls below 1%. Therefore the correction factor is under-estimated if the maximum percentage from the simulated curve is fixed to a minimum of the 1% spurious level. However, excluding this bin from the intrinsic percentage determination gives $71_{-24}^{+26}\%$, which is consistent with the value obtained when the bin is included.

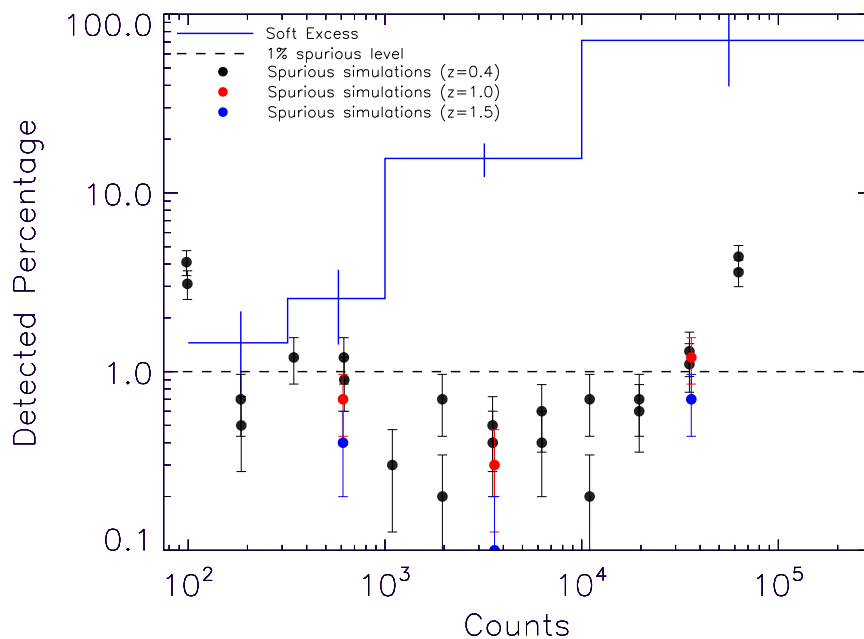


Figure 5.8: The black circles show the results of simulations in order to determine the spurious detection level. Spectra which did not include a soft excess were created at different count levels and the percentage in which this component was incorrectly detected with $> 99\%$ significance was determined. The red and blue circles represent similar simulations carried out at different redshifts.

The detectability of a soft excess component is dependent on both the blackbody temperature and the size of the normalisation with respect to the underlying power law. The spectra that are simulated are intended to represent only a ‘typical’ source in the sample and therefore only a single value has been used for each of these parameters. Here, the effect on the detectability of changing these parameters is briefly considered.

As shown in Fig. 3.24 the distribution of best-fitting blackbody temperatures is rather narrow and can be fit with a Gaussian with mean and dispersion of $kT = 0.17 \pm 0.09$ keV. The simulated spectra are given a temperature of $kT = 0.20$ keV which lies within the 68% error on the mean value. Fig. 5.9 compares the detectability curves for spectra simulated with

temperatures of both $kT = 0.20$ keV (solid line) and $kT = 0.17$ keV (dotted line) at two redshifts; $z = 0.75$ (blue) and $z = 1.3$ (red). The difference in the two lines for $z = 0.75$ is negligible at low numbers of counts but increases to a maximum of $\sim 10\%$ towards higher count levels (> 1000). The difference between the $z = 1.3$ curves increases from $\sim 1\%$ to $\sim 40\%$, but it is only the highest value in the top count bin where the error on the real detected percentage is very high. At most count levels, the difference between the detectability curves caused as a result of varying kT is smaller than the error on the observed detected percentages which is the dominant source of error in the calculation.

Simulations were also run using $kT = 0.20$ keV as in the original analysis, but a lower normalisation ratio of $bb_{\text{norm}}/pl_{\text{norm}} = 0.02$. The resulting detectability curves, each fit with a quadratic function, can be seen in Fig. 5.10 (top). The detectability curves for sources with $z \geq 1$ now consistently lie below the observed detected percentages and the curves for $z = 1.3$ and $z = 1.5$ sources are much less well defined. Fig. 5.10 (bottom) compares how the three lowest redshift detectability curves vary with normalisation ratio by plotting both the original curves (solid lines) and the curves using a lower normalisation ratio (dashed lines). At lower count levels (~ 300) the detection rate changes by only $\sim 4\%$, but this increases to $\sim 40\%$ at higher count levels (~ 3000).

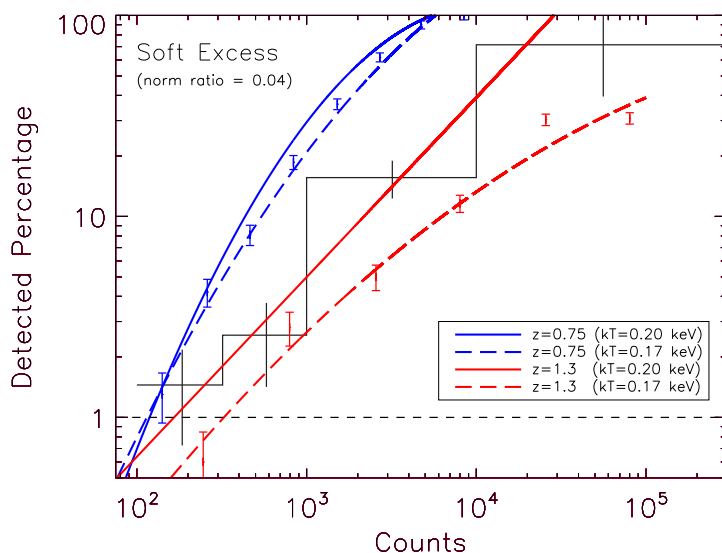


Figure 5.9: This figure reproduces the detectability curves for sources at $z = 0.75$ and $z = 1.3$ with a blackbody to power-law normalisation ratio of 0.04 and a blackbody temperature of $kT = 0.20$ keV (solid lines), as originally shown in Fig. 5.6. Also shown for comparison are the detectability curves of sources with similar parameters, but a temperature of $kT = 0.17$ keV (dashed lines). They were produced from a quadratic fit to simulation runs at 8 ($z = 0.75$) or 6 ($z = 1.3$) different count levels.

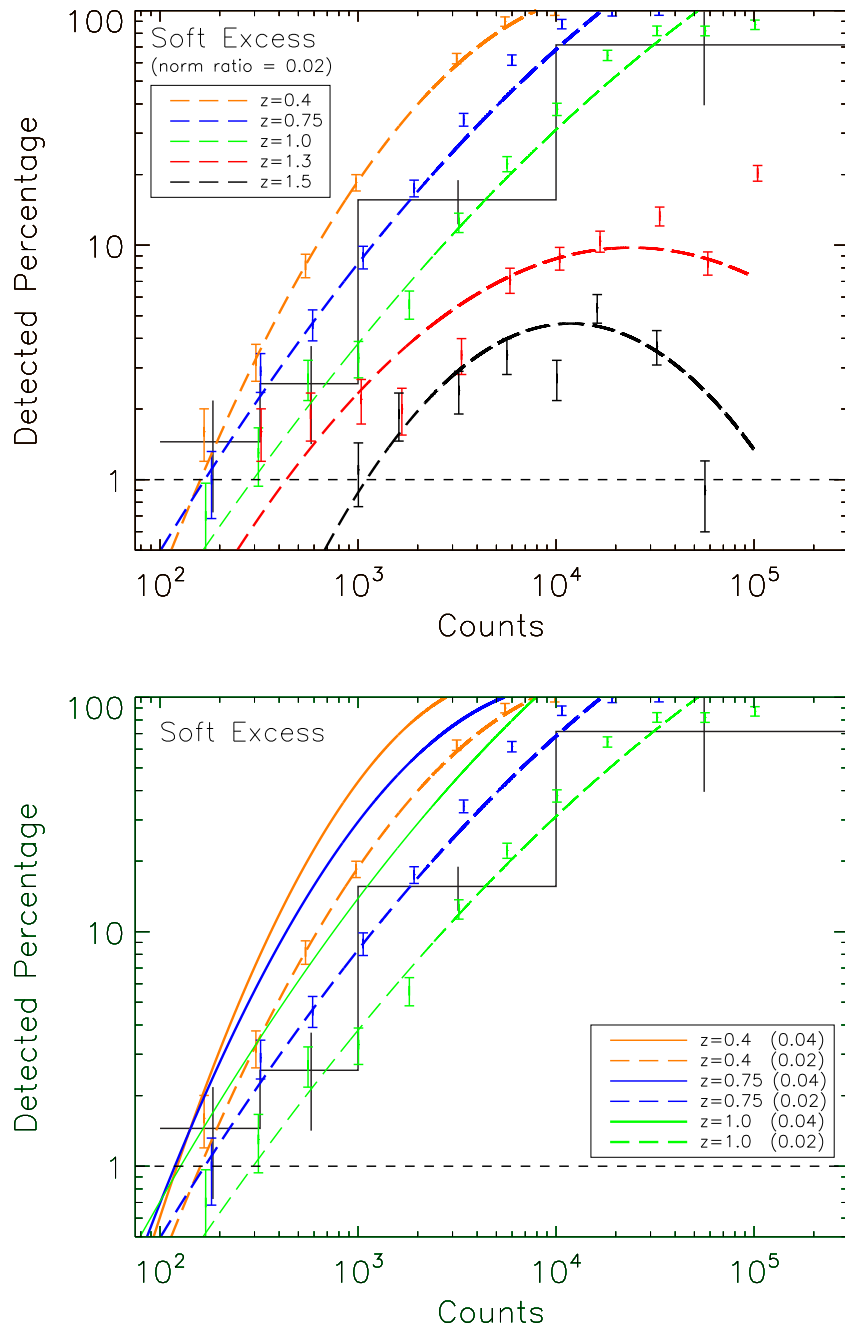


Figure 5.10: Top - This figure shows detectability curves for a soft excess with a typical shape ($kT = 0.20$ keV), but a lower blackbody to power-law normalisation ratio of 0.02. Bottom - This plot reproduces the original detectability curves shown in Fig. 5.6 for sources at $z \leq 1$ (solid lines), and compares them to the detectability curves generated using sources with half the normalisation ratio as shown in the top plot (dashed lines).

5.3.2 Joint Spectral Fitting

The previous section showed that a soft excess component may be ubiquitous in the sample. Spectra with low numbers of counts are now re-analysed in a joint fitting to see if the soft excess feature can be recovered in a combination of spectra where it was previously undetected.

The sample includes 436 sources which were originally fit with a simple power-law model i.e. the soft excess feature was not detected in their spectra with $> 99\%$ significance, and which have < 500 counts. This limit is imposed so that the joint fitting is not dominated by a single object with a high numbers of counts. Samples of ~ 30 sources (~ 50 MOS and/or pn spectra) are created which cover a narrow range in redshift. The resulting groups of spectra include a total of ~ 7000 counts, a level at which a soft excess in a $z < 1$ source is expected to be detected 100% of the time if it is present. This is shown in Fig. 5.6 where the detectability curves for $z = 0.4$ and $z = 0.75$ sources are at 100% at a 7000 count level.

The groups of spectra are jointly fit with the simple power law model, po, in which Γ is free to vary. In each case a best-fitting result of $\Gamma \sim 2$ is found. In the case of the lowest two redshift bins the fit is significantly improved by using the po+bb model, both in terms of a lower χ^2/ν , as listed in Table 5.1, and an F-test comparing the two models which equals 100% in both cases. However the Γ values are lower than 1.8, the value used in the simulations of the previous section. At lower redshifts, cold absorption should be easier to detect (see §5.4) and if a fixed absorption component of $N_{\text{H}} = 10^{21} \text{ cm}^{-2}$ is included in the fit, steeper values of $\Gamma \sim 1.70 \pm 0.05$ are obtained. This does not fully correct for the effect as the resulting continuum from stacking spectra with different levels of absorption is known to be flatter (Mateos et al., 2010).

Each group of spectra is also fit with the po+bb model in which Γ is fixed at 1.8 and kT is tied to the same value for each of the spectra. A single, best-fitting normalisation ratio common to all the spectra is determined by fixing the power-law normalisations at 10^{-5} and tying the blackbody normalisations for each spectrum to a common value. A freely varying constant is added to the model to allow each data set to vary independently. The results can be found in Table 5.1 listed as the model ‘po+bb fix A’. For all except the lowest redshift bin, the average normalisation ratios are consistent with the value of 0.04 used in the simulations of

the previous section. For all except the fifth bin, the kT values are consistent with those found in individual sources with high count spectra.

Each group of spectra is also fit with the $po+bb$ model in which Γ is fixed at 1.8, kT is tied to a common value for each of the spectra and the normalisations of both the blackbody and power-law components are left free to vary. These results are listed in Table 5.1 as the model ‘ $po+bb$ fix B’, and include the median value of the blackbody to power-law normalisation ratios and the percentage of spectra for which the ratio is > 0.01 , which is interpreted as a blackbody component being present. For the three lower redshift bins ($z \lesssim 1$) the inclusion of a blackbody component in the spectral fit results in a better fit and the blackbody temperatures are consistent with the previous values obtained from the individual high count spectra. The normalisation ratios of the blackbody to power-law components are also consistent, both in terms of the median value and a Kolmogorov–Smirnov (KS) test which finds the full distribution of ratios to be not significantly different from those found in single object spectra. The median normalisation ratio of ~ 0.04 is consistent with the value used in the simulations of the previous section and corresponds to a luminosity ratio of ~ 0.2 . Fig. 5.11 shows the blackbody to power-law normalisation ratios for each of the spectra within the 6 samples used in the joint fitting. The 3 left hand panels show the samples at $z < 1$ for which the distribution is consistent with that for sources best-fit with a soft excess in the original analysis (the KS significance values are listed on the figure). The 3 panels on the right show the samples at $z > 1$. Two of them have KS values which indicate they are not consistent with the original sample, also indicated by the different scales (highlighted in red) required to plot the distributions. Sample 6 has a better fit with the ‘ $po+bb$ fix B’ model and gives consistent normalisation ratios, however, the kT value is too high to be consistent with the temperatures observed in individual spectra. Finally, the percentage of spectra which do include a blackbody component (since the fit allows a blackbody normalisation of zero for individual spectra) is consistent with the intrinsic percentage calculated in §5.3.1.

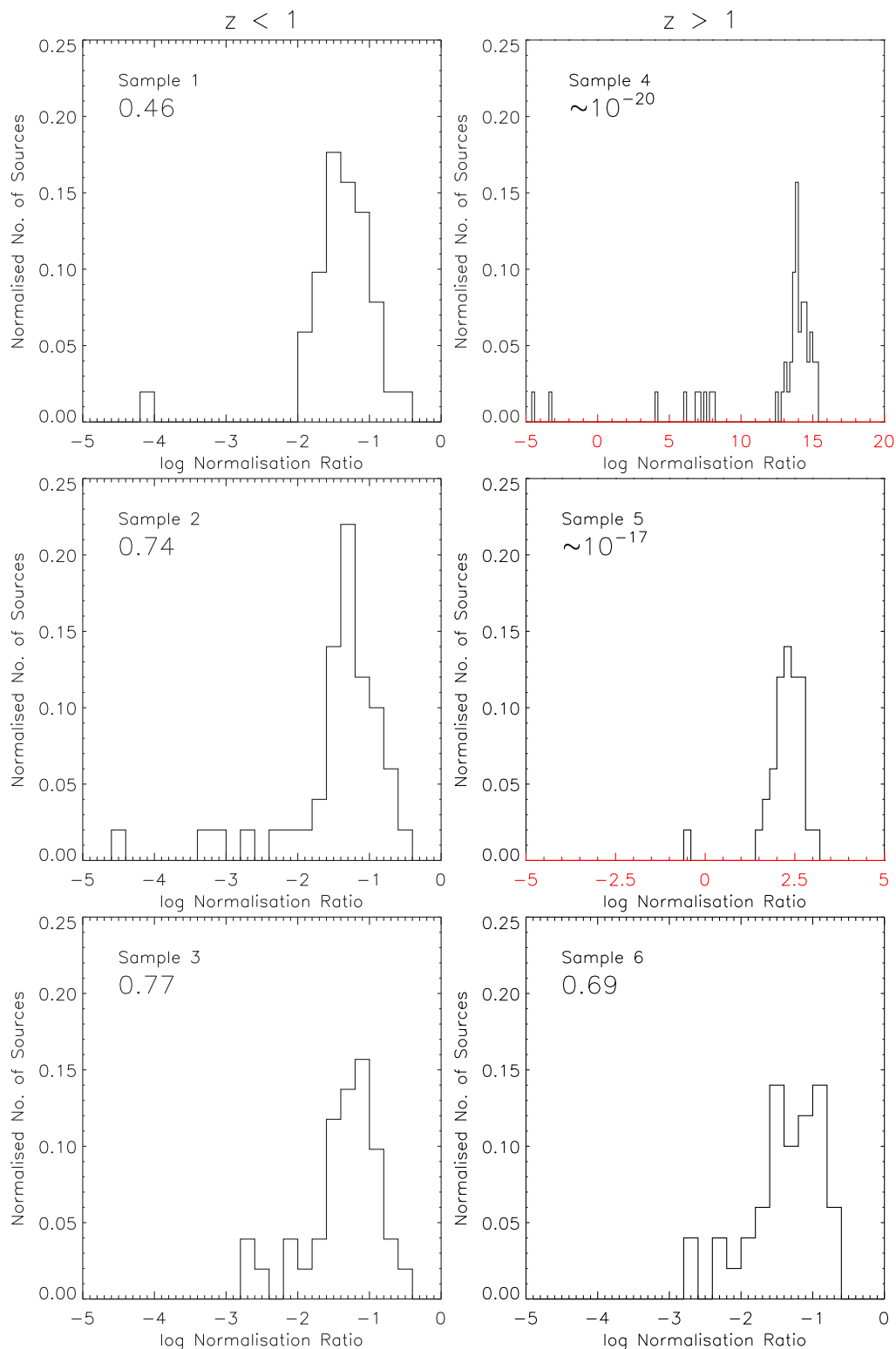


Figure 5.11: These plots show the blackbody to power-law normalisation ratio values for each of the spectra in the 6 samples used in the joint fitting. The scales are consistent with that used in Fig 5.4 to allow a direct comparison, with the exception of samples 4 and 5 as highlighted by the red x axis. The 3 left hand panels show the samples at $z < 1$ and the 3 right hand panels show the samples at $z > 1$. The KS significances from a comparison with the normalisation ratios of the original sources in Fig. 5.4 are listed in each panel.

Sample No.	z range	No. of Sources (Spectra) ^a	Total Counts	Model	χ^2/ν	Γ	kT (keV)	Normalisation Ratio	Percentage with Soft Excess
1	0.21–0.55	34 (51)	8078	po	859/636 (1.351)	$2.10^{+0.04}_{-0.05}$			
				po+bb	664/584 (1.137)	$1.58^{+0.08}_{-0.06}$	$0.23^{+0.01}_{-0.03}$	0.07	78 ± 17
				po+bb fix A	873/635 (1.375)	1.8 (fixed)	$0.23^{+0.03}_{-0.03}$	0.024 ± 0.002	
				po+bb fix B	675/585 (1.154)	1.8 (fixed)	$0.19^{+0.02}_{-0.02}$	0.04	74 ± 16
2	0.56–0.77	30 (50)	7661	po	861/615 (1.400)	$2.07^{+0.05}_{-0.05}$			
				po+bb	682/564 (1.209)	$1.62^{+0.08}_{-0.13}$	$0.24^{+0.03}_{-0.02}$	0.07	84 ± 18
				po+bb fix A	854/614 (1.391)	1.8 (fixed)	$0.19^{+0.04}_{-0.04}$	0.040 ± 0.010	
				po+bb fix B	693/565 (1.227)	1.8 (fixed)	$0.20^{+0.03}_{-0.02}$	0.05	72 ± 16
3	0.77–0.98	33 (51)	7367	po	683/611 (1.118)	$2.03^{+0.05}_{-0.04}$			
				po+bb	624/559 (1.116)	$1.98^{+0.04}_{-0.05}$	$0.044^{+0.002}_{-0.001}$		
				po+bb fix A	681/610 (1.116)	1.8 (fixed)	$0.27^{+0.05}_{-0.05}$	0.036 ± 0.005	
				po+bb fix B	579/560 (1.034)	1.8 (fixed)	$0.28^{+0.03}_{-0.04}$	0.06	63 ± 14
4	0.98–1.12	31 (51)	7583	po	632/629 (1.005)	$2.02^{+0.05}_{-0.04}$			
				po+bb	576/577 (0.998)	$1.97^{+0.04}_{-0.06}$	$0.053^{+0.003}_{-0.002}$		
				po+bb fix A	616/628 (0.981)	1.8 (fixed)	$0.26^{+0.04}_{-0.04}$	0.048 ± 0.008	
				po+bb fix B	629/578 (1.088)	1.8 (fixed)	0.02^b		
5	1.12–1.19	30 (50)	6749	po	604/578 (1.045)	$2.03^{+0.04}_{-0.05}$			
				po+bb	571/527 (1.083)	$1.98^{+0.04}_{-0.06}$	$0.06^{+0.01}_{-0.03}$		
				po+bb fix A	597/577 (1.035)	1.8 (fixed)	$0.35^{+0.05}_{-0.05}$	0.045 ± 0.005	
				po+bb fix B	606/528 (1.148)	1.8 (fixed)	$0.065^{+0.005}_{-0.005}$		
6	1.19–1.28	29 (50)	5614	po	485/509 (0.953)	$1.95^{+0.05}_{-0.05}$			
				po+bb	450/458 (0.983)	$1.89^{+0.05}_{-0.06}$	$0.062^{+0.002}_{-0.002}$		
				po+bb fix A	471/508 (0.927)	1.8 (fixed)	$0.24^{+0.06}_{-0.06}$	0.050 ± 0.030	
				po+bb fix B	416/459 (0.906)	1.8 (fixed)	$0.34^{+0.07}_{-0.06}$	0.04	66 ± 15

Table 5.1: The samples used for the joint fitting and the results from fitting the spectra with the simple power-law model po in which Γ is allowed to vary freely and the po+bb model in which Γ is both fixed at 1.8 and free to vary. ‘po+bb fix A’ refers to the model in which the blackbody to power-law normalisation ratio is kept the same for each spectrum and ‘po+bb fix B’ is the model in which both the blackbody and power-law normalisations are free to vary. In the case of model A, the normalisation ratio quoted is the best-fitting value with a 68% error and for model B it is the median value. The errors on the kT and Γ parameters are 90%. Notes: ^aNot all sources have both a MOS and a pn spectrum available. ^bFor this sample reliable errors cannot be estimated from the fit.

It has been suggested that the soft excess feature is ubiquitous in high accretion rate AGN and that it is this parameter which may determine its presence in the spectra, or the size of the component (e.g. Done et al. 2012). The Eddington ratio, defined as $\lambda_{\text{Edd}} = \log(L_{\text{bol}}/L_{\text{Edd}})$ and calculated in §3.3.7, is used as a proxy for mass accretion rate. As before, only sources with < 500 total counts and those originally best-fit with the model po are used. In addition, only sources at $z < 1$ are used and the remaining sources are split into 3 sub-samples containing roughly equal numbers of sources. The samples are fit with both the ‘po+bb fix A’ and ‘po+bb fix B’ models, the results of which are listed in Table 5.2 along with the properties of each sample. The ‘po+bb fix A’ model finds that a best-fitting normalisation ratio is consistent with the 0.04 found in single spectra for the 2 sub-samples with the highest Eddington ratios. In the case of the lowest λ_{Edd} bin this value is considerably lower, but has a large associated error. A KS test finds the distributions of the normalisation ratios determined from the ‘po+bb fix B’ model to be consistent, however the median values do vary from a lower value than expected in the low λ_{Edd} bin to a higher value than expected in the high λ_{Edd} bin. In addition, the percentage of spectra for which the normalisation ratio is > 0.01 is consistent with the intrinsic percentage in the case of the top 2 bins, but is lower than expected for the lowest λ_{Edd} bin. Whilst the evidence is not strong, this may suggest that soft excesses are smaller and less common in sources with lower accretion rates.

5.4 Absorption Components

Intrinsic cold absorption may also be present in type 1 AGN, suppressing the lower energy emission. The percentage of sources with detected absorption is shown in Fig. 5.2 and appears to be limited by the spectral quality in a similar way to that of the soft excess. However, the effect is not as strong, and the detected percentage decreases by approximately 20% from the higher to lower count bins rather than $\sim 80\%$ in the case of the soft excess. The true percentage of absorbed sources could be as high as the $\sim 25\%$ found in the highest count range, where the spectra might be expected to be of good enough quality to detect any significant absorption if present. However, the highest count bins are heavily contaminated by target sources, resulting

λ_{Edd} range ^a	No. of Sources (Spectra)	Total Counts	Model	χ^2/ν	Γ	kT (keV)	Normalisation Ratio	Percentage with Soft Excess
-2.3 to - 1.3	28 (47)	5613	po+bb fix A	685/498 (1.376)	1.8 (fixed)	$0.15^{+0.16}_{-0.10}$	0.008 ± 0.7	
			po+bb fix B	570/452 (1.261)	1.8 (fixed)	$0.18^{+0.04}_{-0.02}$	0.005	45 ± 12
-1.3 to - 1.0	32 (52)	8383	po+bb fix A	821/660 (1.244)	1.8 (fixed)	$0.25^{+0.03}_{-0.02}$	0.048 ± 0.004	
			po+bb fix B	657/609 (1.079)	1.8 (fixed)	$0.23^{+0.02}_{-0.02}$	0.04	75 ± 16
-1.0 to + 0.2	26 (36)	6536	po+bb fix A	546/500 (1.092)	1.8 (fixed)	$0.18^{+0.04}_{-0.03}$	0.05 ± 0.01	
			po+bb fix B	472/465 (1.015)	1.8 (fixed)	$0.16^{+0.04}_{-0.03}$	0.084	83 ± 21

Table 5.2: The samples created based on Eddington ratio values and the results of the joint spectral fitting. ^a $\lambda_{\text{Edd}} = \log(L_{\text{bol}}/L_{\text{Edd}})$

in a lower detected percentage once they are removed from consideration. Fig. 5.12 shows the detected percentage after target removal. The highest count bin in this plot now suggests that $5.6 \pm 4.0\%$ of type 1 AGN may include an intrinsic absorption component. In the lower count bins (< 3200), the detected percentage of absorbed sources does not vary significantly suggesting that the detectability is not as heavily dependent on spectral quality as it is for the soft excess feature.

The range of rest-frame column densities found in the absorbed sources is very broad, $N_{\text{H}} \sim 10^{21} - 10^{23} \text{ cm}^{-2}$, and the detectability of absorption in the spectra is highly dependent on this N_{H} value. Therefore a single model cannot represent of all the absorbed sources detected, and there are not enough sources to weight detectability curves by both N_{H} and redshift. The detectability of absorption components with different column densities is instead quantified by simulating absorbed spectra at $z = 1$. These detectability curves are shown in Fig. 5.12 by the black curves of different line style. They show that a column of 10^{23} cm^{-2} (equivalent to $2 \times 10^{22} \text{ cm}^{-2}$ at $z = 0$) would be detected in most spectra with > 200 counts, whereas a column of $\sim 3 \times 10^{21} \text{ cm}^{-2}$ (equivalent to $5 \times 10^{20} \text{ cm}^{-2}$ at $z = 0$) is not strong enough to be detected in spectra of this quality at $z = 1$. For the highest count bin ($\gtrsim 3200$ counts), the detectability curves for all but the lowest level of N_{H} shown in Fig. 5.12 are at 100%. This means that all reasonable levels of N_{H} should be detectable and therefore the intrinsic percentage estimate is robust. The fraction of sources with particular N_{H} levels is roughly constant in both different redshift and count bins (the two properties being correlated), and hence the slight decrease in the detected percentage between the top and bottom bins is as expected when objects with lower N_{H} and/or higher redshifts are no longer detectable.

These simulations do not include a soft excess component which could also reduce the detectability of any absorption present. Sources are simulated with both the standard soft excess parameters and two values of N_{H} (shown by the lines of open circles in Fig. 5.12). For $N_{\text{H}} = 10^{22} \text{ cm}^{-2}$ the sensitivity drops by approximately 10% at low count levels (~ 200), increasing to $\sim 25\%$ at higher count levels (~ 1000), making little difference to the conclusions. In the case of $N_{\text{H}} = 3 \times 10^{21} \text{ cm}^{-2}$, at low count levels ($\lesssim 1000$) where the sensitivity to absorption is low anyway, the inclusion of a soft excess makes little difference to its detectability. At

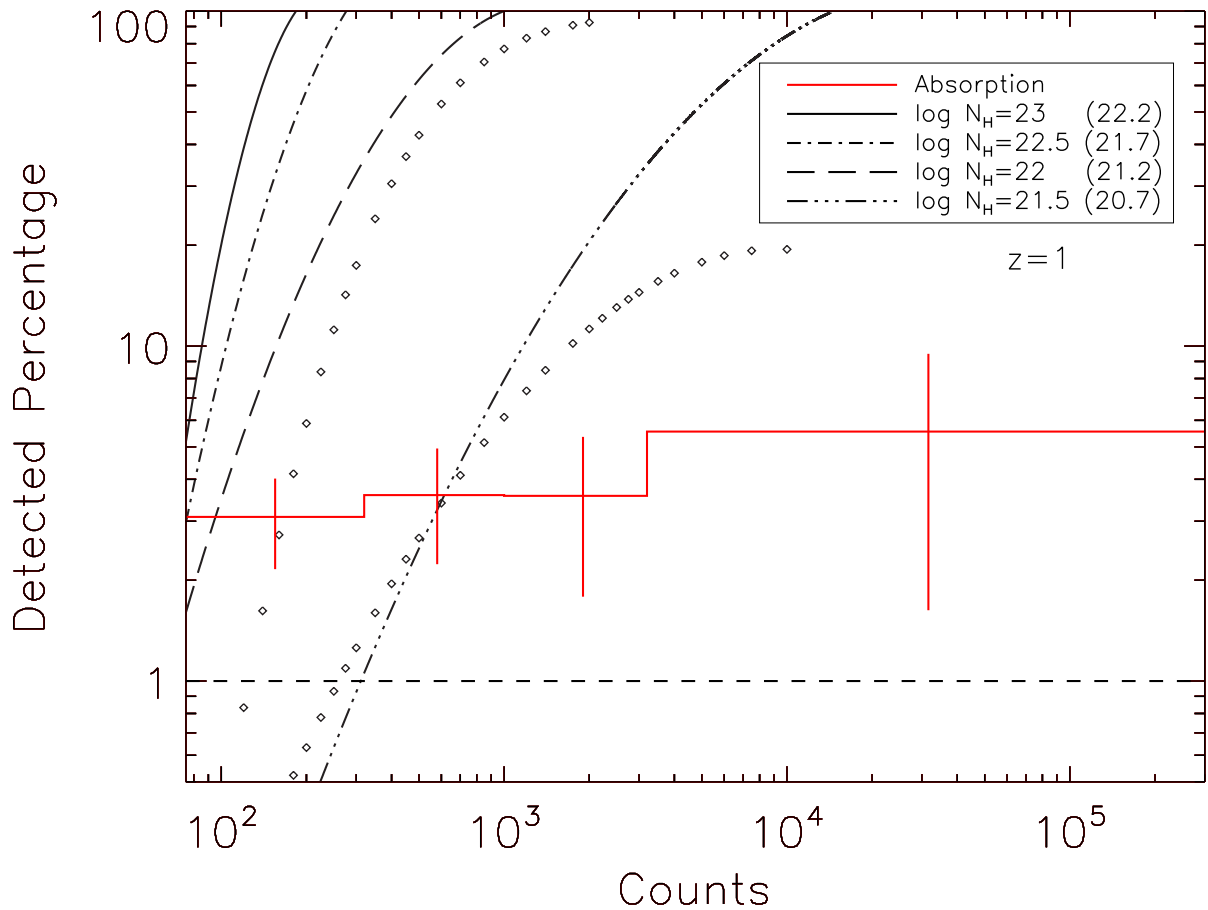


Figure 5.12: This figure shows how the detected percentage of an intrinsic cold absorption component varies with the number of counts in the X-ray spectra (red, solid line). It reproduces Fig. 5.2, but the sources which were the target of an *XMM-Newton* observation have been removed. Due to the reduced number of sources this leaves, the original top three bins are combined. The percentage appears to remain constant at $\sim 3\%$ for spectra with $75 - 32,000$ counts, suggesting the detectability is not as heavily dependent on the spectral quality as is the case for the soft excess. The black lines represent simulated detectability curves for the detection of absorption components with different column densities (shown by the different line styles) in simulated spectra at $z = 1$. The equivalent N_{H} value at $z = 0$ is quoted in brackets on the figure. The open circles show the detectability of absorption of $\log N_{\text{H}} = 22$ and $\log N_{\text{H}} = 21.5$, when a soft excess of typical shape and size is also included in the spectra.

higher counts levels ($\sim 10,000$) where the statistics are better, including the soft excess can reduce sensitivity to the absorption component by $\sim 65\%$.

In §5.3.2, a joint fitting was carried out on groups of low count spectra to see if the soft excess feature could be recovered. Similarly, the apo+bb model is fit to the same samples to see if an absorption component can be recovered in addition to the soft excess already found to be present. The model is implemented with $\Gamma = 1.8$, $kT = 0.2 \text{ keV}$ and both the power law and blackbody normalisations left free to vary. The best-fitting N_{H} values are listed in Table 5.3. An absorption component can be recovered in the low count spectra, but only in

z range	N_{H} ($\times 10^{22}$ cm $^{-2}$)
0.21 – 0.55	$0.57^{+0.27}_{-0.15}$
0.56 – 0.77	$0.83^{+0.22}_{-0.19}$
0.77 – 0.98	< 0.43
0.98 – 1.12	< 0.17
1.12 – 1.19	< 0.53
1.19 – 1.28	< 0.61

Table 5.3: Results from fitting the apo+bb model to the groups of low count spectra described in Table 5.1. In each case, Γ and kT are fixed at 1.8 and 0.2 keV respectively. 90% errors are quoted on the N_{H} value.

the lower redshift bins is this component constrained. Although the N_{H} values are of the order of those seen in single object fits in the sample, the range in column densities means that the values obtained here merely represent an ‘average’ N_{H} value, the exact value of which should be treated with caution.

5.5 Discussion

The origin of the soft excess emission is still a matter of debate and the main theories were described in §1.1.3. The recent model by Done et al. (2012) which suggests that the soft excess may be intrinsic emission from the disc only applies to the lowest mass/highest accretion rate AGN. Since soft excesses are not only found in the high accretion rate sources, this suggests two interpretations are required.

The ubiquity of the soft excess means that any X-ray spectral fitting of type 1 AGN must take this feature into account. It has been shown that leaving this component unmodelled can lead to a Γ value ~ 0.1 too steep. In addition, any attempt to constrain an intrinsic N_{H} value must also include the blackbody component in the fit since they appear in the spectra at a similar energy range. It was found in Chapter 3 that the average Γ values for sources fit with the po+bb model were significantly flatter than those fit with the po model suggesting that the underlying power-law slope in sources with a soft excess is different. However, using a blackbody to model the soft excess component is purely phenomenological - it provides a good representation of the feature seen in spectra of this quality. If the soft excess is actually

a broad spectral feature as suggested by reflection models, this modelling may not be fully accounting for the spectral complexity and the power-law slope at higher energies could still contain some of this component.

This Chapter has confirmed the presence of a population of AGN which are classified as type 1 due to the presence of broad emission lines in their UV/optical spectra, but also show significant X-ray absorption which is unexpected according to the standard orientation based Unified Model. Constraining the fraction of absorbed type 1 sources may aid in interpreting these objects with a ‘clumpy torus’ (Nenkova et al., 2008a,b), regular occultations by clouds in the broad-line region (e.g. Risaliti et al. 2002) or a warped accretion disc (Greenhill et al., 2003; Nayakshin, 2005; Lawrence & Elvis, 2010) as described in Chapter 1.

Whilst it would be interesting to compare how the detection of the low energy spectral components varies with radio loudness, only 6/75 RLQ have a detected soft excess making the statistics poor. However, this is still contrary to previous suggestions that RLQ do not include this component (e.g. Sulentic et al. 2010). Crude estimates of the percentage of RQQ and RLQ with < 500 and > 500 counts which include a soft excess are consistent, suggesting its prevalence is similar regardless of radio loudness. A joint fitting to 29 RLQ which were previously best-fit with the simple power law model and include < 500 total counts in their spectra gives similar results to those found for the full sample which consisted predominantly of RQQ. The ‘po+bb fix A’ model gives a best-fitting normalisation ratio of 0.022 ± 0.004 which is lower than that of the high count sources, but the fit also gives a higher temperature of $kT = 0.31 \pm 0.05$ keV. The ‘po+bb fix B’ model gives a consistent median normalisation ratio of 0.04 and percentage of $76 \pm 18\%$, but again a high temperature of $kT = 0.34^{+0.03}_{-0.02}$ keV.

5.6 Conclusions

This Chapter has quantified the detectability of soft excess components by simulating spectra with a typical spectral shape. The spectra were fit in XSPEC over the energy range 0.5 – 12.0 keV and an F-test was used at 99% significance to test whether the component was statistically required in the fit. By repeating this procedure for spectra with different numbers of counts, maximum detection curves were generated and compared to the observed results from the real data sample in Chapter 3. The effect of redshift on the detectability was also taken into account. Despite the raw percentage of sources with a soft excess being $\sim 8\%$, after correcting for the spectral quality, the intrinsic percentage is $75 \pm 23\%$. This suggests that within the sample, almost all of the sources could include a soft excess component with a shape and size typical of those seen in the highest count spectra, and it is merely the quality of the spectra that limits their detection.

If soft excesses are ubiquitous, then the feature should be recovered in a combination of low count spectra. Groups of ~ 50 spectra (~ 7000 counts) were created in narrow redshift bins, including spectra with < 500 counts and which had no previous evidence for additional spectral features. The groups at $z < 1$ were shown to be better fit with a model including a soft excess, and the temperature and normalisation with respect to the underlying power law of the components required were consistent with those found in individual high count spectra.

A similar simulation procedure to determine the percentage of type 1 AGN which require an intrinsic cold absorption component cannot be conducted. However, its detectability may not be as dependent upon spectral quality as the soft excess. A non-negligible percentage, $\sim 5\%$, of type 1 AGN may include such an absorption feature and therefore any spectral modelling must take the possibility of this feature into account.

6

The Broadband SED Properties of Type 1 AGN

In this Chapter the sample of AGN, which was created from optical and X-ray catalogues, is cross-correlated with archival data at other wavelengths. This gives a flux estimate for each source at up to 17 different frequencies, and correlations between the fluxes at each are considered. Spectral energy distributions (SEDs) are created for each source and a qualitative description of how the mean SED shape changes with varying physical parameters is presented.

6.1 Introduction

As described in Chapter 1, the emission at different wavelengths in the SED is due to different physical processes occurring in and around the AGN. Therefore, studying the output over all wavelengths is necessary in order to create a complete picture of accretion and link these processes together.

A large proportion of an AGN's luminous output is emitted at UV/optical frequencies and is thought to be the signature of the accretion disc. The X-ray emission, whilst contributing a much smaller proportion of L_{bol} , is an important probe of the processes occurring close to the black hole, where it is believed the UV photons from the disc are upscattered to X-ray energies. Therefore, there have been many previous studies which try to understand the link between the emission in these two bands. A commonly used parameter is α_{OX} (see Eqn. 6.1) which relates the amount of emission in the X-ray band to that in the optical (Tananbaum et al., 1979). The X-ray values are commonly taken at 2 keV and the optical at 2500Å.

$$\alpha_{\text{OX}} = \frac{\log[L_{\nu_{\text{X}}}/L_{\nu_{\text{opt}}}]}{\log[\nu_{\text{X}}/\nu_{\text{opt}}]} = 0.38 \log \left(\frac{f_{2\text{keV}}}{f_{2500\text{\AA}}} \right) \quad (6.1)$$

Many studies have found an anti-correlation between α_{OX} and the optical luminosity, $\log l_{2500\text{\AA}}$ i.e. α_{OX} decreases with increasing optical luminosity (Avni & Tananbaum, 1986; Vignali et al., 2003; Strateva et al., 2005; Steffen et al., 2006; Just et al., 2007; Shemmer et al., 2008; Young et al., 2009; Stalin et al., 2010; Lusso et al., 2010). This correlation implies that there is a non-linear relationship between the amounts of X-ray and optical radiation such that at higher luminosities the increase in optical emission is larger than the increase in X-ray. This can be expressed as $L_{\text{X}} \propto L_{\text{opt}}^{\gamma}$ where $\gamma < 1$. A strong correlation between the X-ray and optical emission has been determined by many authors, with most finding $\gamma \sim 0.7 - 0.9$; e.g. $\gamma = 0.75 \pm 0.06$ (Vignali et al., 2003), $\gamma = 0.709 \pm 0.010$ (Just et al., 2007), $\gamma = 0.760 \pm 0.022$ (Lusso et al., 2010), $\gamma = 0.870 \pm 0.001$ (Stalin et al., 2010), $\gamma = 0.85 \pm 0.04$ (Marchese et al., 2012). This correlation still lacks a physical interpretation as it is unclear what mechanism controls the proportion of UV emission that is upscattered to X-rays. The frequencies used to define the α_{OX} parameter, 2 keV and 2500Å, are arbitrary and Young et al. (2010) find that

the slope of the $\alpha_{\text{OX}} - l_{\text{opt}}$ correlation steepens as the X-ray energy used in determining α_{OX} decreases.

The primary emission from the central engine of AGN consists of large amounts of UV radiation and some X-ray emission. This can be reprocessed by any dust present, and be re-emitted in the IR (Rees et al., 1969; Pier & Krolik, 1993). In this scenario correlations are expected between both the X-ray and IR and the UV and IR as the IR emission depends primarily on the luminosity of the central source. The IR and UV humps in AGN SEDs are of a similar size, suggesting that the dust intercepts a large fraction of the ionizing continuum from the nucleus. Early measurements of the mean luminosity ratio found $L_{\text{IR}}/L_{\text{UV}} = 0.4 \pm 0.15$ (Sanders et al., 1989), suggesting the dust covering factor in PG quasars is $\sim 10-30\%$. Continuum thermal emission attributed to dust is correlated with the optical luminosity according to $\lambda L_{\lambda}(6.7 \mu\text{m}) \propto \lambda L_{\lambda}(5100\text{\AA})^{0.82}$. This non-linear relationship was interpreted as a reduction of the dust covering factor as a function of luminosity (Maiolino et al., 2007). Since correlations depend on the nature of the dust, they can be used to test Unification models and constrain the geometry of the torus. Early observations of the correlation between IR and X-rays found it to be consistent between Seyfert 1 and Seyfert 2 sources (Lutz et al., 2004), which is unexpected according to the dusty torus set-up in the standard Unified model and may indicate the IR emission originates from a different dust contribution. The correlation $L_{\text{MIR}} \propto L_{\text{X}}^{\gamma}$ is typically found to have an index of $\gamma \sim 1$ (e.g. Krabbe et al. 2001, Levenson et al. 2009) and $\gamma = 1.60 \pm 0.22$ (Horst et al., 2006), $\gamma = 1.11 \pm 0.07$ (Gandhi et al., 2009) and $\gamma = 0.94 \pm 0.06$ (Matsuta et al., 2012). However, AGN activity is strongly linked to star-formation making it difficult, in high redshift sources, to isolate the IR and UV emission that is solely due to the AGN, and not an associated starburst. Zhu et al. (2008) find the $L_{\text{MIR}}/L_{\text{FUV}}$ ratio in AGN is higher than in star-forming galaxies, but the correlations are consistent.

The X-ray and radio emission from AGN appears to be correlated over several orders of magnitude in both bands, and the correlation is present in both radio-loud and radio-quiet sources (Brinkmann et al., 2000; Panessa et al., 2007; Bianchi et al., 2007a; Li et al., 2008; Laor & Behar, 2008). In radio-loud sources, the radio emission is thought to be a result of synchrotron emission in the jet (Begelman et al., 1984). In §3.3.6, the RL sources were found to

have flatter X-ray power-law slopes and higher X-ray luminosities than their RQ counterparts. This was interpreted as Synchrotron Self Compton (SSC) emission occurring in the jet, producing an additional X-ray component and would naturally explain a correlation between the radio and X-ray emission in these sources. However, since radio-quiet sources do not generally contain powerful jets, the origin of their radio emission is less clear. The correlation between radio and X-ray emission suggests a common, and possibly nuclear, origin. Some suggestions include free-free emission in the optically thin part of an accretion disc wind (Blundell & Kuncic, 2007) or magnetically heated coronal activity (Laor & Behar, 2008). A strong correlation between the radio and X-ray emission has also been observed in X-ray binaries in the low/hard state (Gallo et al., 2003). Since the correlation is therefore common to both stellar and super-massive black holes, a ‘fundamental plane’ including mass as a third parameter was suggested (see Eqn. 6.2; Merloni et al. 2003).

$$\log L_R = (0.60^{+0.11}_{-0.11}) \log L_X + (0.78^{+0.01}_{-0.09}) \log M_{\text{BH}} + (7.33^{+4.05}_{-4.07}) \quad (6.2)$$

6.2 Data

The sample of 761 objects presented in Chapter 3 was created by a cross-correlation of the optical SDSS quasar catalogue and 2XMMi, an X-ray catalogue of serendipitous sources. In this section the sample is cross-correlated with catalogues at other wavelengths. In each case the optical positions are used in the matching since they have a lower positional error than the X-ray positions, typically $0.2''$ in each co-ordinate as opposed to $1 - 2''$. Table 6.1, at the end of this section, lists the percentage of the sample which have a flux measurement in each of the wavebands discussed below.

6.2.1 X-ray

Each of the sources in the sample has an X-ray spectrum obtained from *XMM-Newton*. The spectral fitting of these spectra is described in detail in Chapter 3 and the X-ray fluxes obtained from this fitting are used in this Chapter. The unabsorbed X-ray fluxes are calculated in the

energy bands 0.5 – 2.0 keV and 2.0 – 10.0 keV from the best-fitting spectral model. Separate estimates are obtained for the MOS and pn spectra so an average is determined, weighted by the number of counts in each. In order to compare with monochromatic flux estimates at other wavelengths, the broadband fluxes are divided by the frequency width of each band and converted to Jy. These estimates give the flux at a central energy within the band. These energies are determined by calculating the expectation value of the normalised flux distribution over each band, assuming a power law spectrum with $\Gamma = 2$. They are found to be 1.08 keV for the soft band and 4.97 keV for the hard band.

6.2.2 Optical

Since the initial quasar sample is taken from the SDSS DR5 quasar catalogue (Schneider et al., 2007), each of the sources includes optical photometry in the 5 SDSS *ugriz* bands¹. The magnitudes given in the catalogue are first corrected for Galactic extinction using values from the maps of Schlegel et al. (1998) and then converted into the AB system (Oke & Gunn, 1983). Typical A_u values are ~ 0.12 mag with A_g, A_r, A_i and A_z values decreasing to ~ 0.03 mag. The magnitudes (and their associated errors) are converted into a flux density by Eqn. 6.3 where $F_0 = 3631$ Jy. In the case of 4 of the sources, the error on the *u* band flux is larger than the flux estimate itself, making it an upper limit. Three of the sources for which this occurs lie at high redshift, where the Ly- α forest is redshifted into the *u* and *g* bands (see §6.4).

$$\text{Flux (Jy)} = F_0 \times 10^{\frac{\text{Magnitude}}{-2.5}} \quad (6.3)$$

6.2.3 Radio

As described in Chapter 3, the sample was cross-correlated with the FIRST (Becker et al., 1995) radio catalogue which gives the integrated flux in mJy at 1.4 GHz. A 20'' matching radius was used in order to ensure any extended emission from the source was included, and the fluxes from any multiple matches were summed. 104 sources had a detection in FIRST and

¹with the exception of SRCID 32486 which only includes *r* and *i* band magnitudes due to its proximity to a bright foreground star, and SRCID 122294 which doesn't include a magnitude in any band due to its proximity to the *Whirlpool Galaxy*, but it does have an optical spectrum.

for the 613 sources with no detection, $5 \times$ RMS at the source position was used as an upper limit on the flux. 44 sources did not lie in the area covered by the FIRST survey. For sources with a detection, the error on the integrated flux was taken to be the RMS value at the source position. However, it should be noted that for extended sources this estimate is likely too low. In the case of multiple detections, the RMS values for each are added in quadrature.

6.2.4 Near-Infrared (NIR)

The sample was cross-correlated with the 2MASS Point Source Catalog (Cutri et al., 2003) using a $5''$ matching radius. 170 matches were found, with no sources having duplicate detections. The magnitudes and corresponding errors given in the catalogue were converted to fluxes using Eqn. 6.3 where F_0 for each of the 3 bands is; J: $F_0 = 1594 \pm 27.8$ Jy, H: $F_0 = 1024 \pm 20.0$ Jy, K: $F_0 = 666.7 \pm 12.6$ Jy. Approximately 75% of the source detections are part of the ‘faint extension’ and have magnitudes as faint as 17.6 (J), 17.8 (H) and 16.3 (K). Some detections were flagged as having poor photometry, either as a result of confusion or galaxy contamination. This affected 6 unique sources, only 1 of which has bad photometry in each of the 3 bands. 28 of the sources only have an upper limit in one of the bands.

6.2.5 Mid-Infrared (MIR)

The sample was cross-correlated with the All Sky Data Release (Cutri et al., 2012) from *WISE*. A $5''$ matching radius was used which gave 819 matches corresponding to 754 unique objects. In cases where 2 *WISE* detections were matched to the same SDSS co-ordinates, the one with the largest separation was excluded, provided the closer match had a separation $< 1''$. In some cases multiple detections of the same *WISE* source were returned. Provided the magnitudes of the 2 detections were similar, one was excluded. These cuts resulted in only 3 quasars with double matches and as the separations of the detections were below the resolution limit, $6''$, all were excluded. This gave a final sample in which 754 sources have a *WISE* detection, 98% of which have a separation $< 2''$ from the optical position. *WISE* gives magnitudes and associated errors in 4 broad bands, which can be converted to fluxes by Eqn. 6.3 where the zero point fluxes for the 4 bands are; W1: $F_0 = 306.682 \pm 4.600$ Jy, W2: $F_0 = 170.663 \pm 2.600$ Jy,

W3: $F_0 = 29.045 \pm 0.436$ Jy and W4: $F_0 = 8.284 \pm 0.124$ Jy. These values assume a spectrum with the shape $f_\nu \propto \nu^{-2}$ through the bandpass. The majority of the spectral indices calculated between the W1 and W2 bands lie between -3 and -1 , and the peak is at -2 . If a colour correction is applied, the average change in the flux estimates are < 0.04 Jy ($< 0.4\%$). Since these are much smaller than the variations in SED shape between sources, no colour correction is applied to any *WISE* flux estimate. In some of the detections, the photometry was poor and so was no longer used. This could be due to scattered light from nearby sources, diffraction spikes or multiple components contributing to the PSF. 46 sources were affected in at least one of the *WISE* bands, but only 16 unique sources were affected in all 4.

6.2.6 Ultraviolet (UV)

The sample was also cross-correlated with GR6 data from *GALEX* using CASJobs². A matching radius of $2''$, as recommended by Morrissey et al. (2007), yielded 1664 matches to 645 unique sources. As GR6 includes observations taken as part of many different programs such as the guest observer program (GII), or the Deep Imaging Survey (DIS) and the all sky surveys AIS (All Sky Imaging Survey) and MIS (Medium Survey), $\sim 70\%$ of the sources have multiple detections. The detection list is limited to only the MIS and AIS observations since their magnitude limits are well defined, unlike GII or DIS observations which have variable exposure times and are biased towards ‘interesting’ objects. This leaves 1025 detections of 590 unique sources. In order to select the most appropriate detection corresponding to each individual source, the likelihood ratio is determined (Sutherland & Saunders, 1992). This is defined as

$$L = \frac{Q(< m) \exp(-r^2/2)}{2\pi\sigma_1\sigma_2 N(< m)}, \quad (6.4)$$

where r is the separation between the source and detection positions, σ_1 is the positional error of the source, in this case assumed to be $0.2''$, the typical error on SDSS positions and σ_2 is the positional error on the NUV detections, which range from $0.47''$ to $1.88''$, with the majority ($\sim 80\%$) less than $0.8''$. NUV detections, rather than FUV are considered since a

²<http://galex.stsci.edu/casjobs/>

higher percentage of detections have an NUV measurement, but not an FUV, than vice versa. $Q(< m)$ is defined as the probability of finding a counterpart above the magnitude m . In this case, Q is set to 1.0 by considering the probability distribution function (PDF) presented in Fig. 6.1 (Bianchi et al., 2007a). The faintest NUV detections in the AIS are at ~ 23 mag which is where the turn-off in the PDF occurs. Above this turn-off it is expected that a UV source will be detected if it is present. Similarly the turn-off in the PDF for MIS occurs at ~ 24 mag, and all the detections are brighter than this value. The PDFs from Bianchi et al. (2007a) are converted into cumulative density functions (CDFs) in order to determine $N(< m)$, the cumulative number density of objects brighter than an NUV magnitude m . The reliability of each detection being the correct match is determined using Eqn. 6.5, which simply normalises the likelihood values to a total of 1 for each individual source if Q is assumed to be 1.

$$R_j = \frac{L_j}{\sum L_i + [1 - Q(< m)]} \quad (6.5)$$

The detection with the highest value of R is chosen as the most appropriate, and all detections have $R > 50\%$. If there are detections in both MIS and AIS, the MIS detection is kept. This gives a final sample of 590 unique sources; 222 with a MIS detection and 368 with an AIS detection. The UV magnitudes are corrected for Galactic reddening using the reddening law $A_V = R_V E(B - V)$ (Cardelli et al., 1989) where the $E(B - V)$ values were obtained from the maps of Schlegel et al. (1998) and $R_V = 8.24$ (Wyder et al., 2007). UV fluxes are calculated using Eqn. 6.3 where $F_0 = 3630$ Jy. 358 sources have a detection in both the NUV and FUV bands, 224 sources only have a detection in the NUV and 8 have FUV data only.

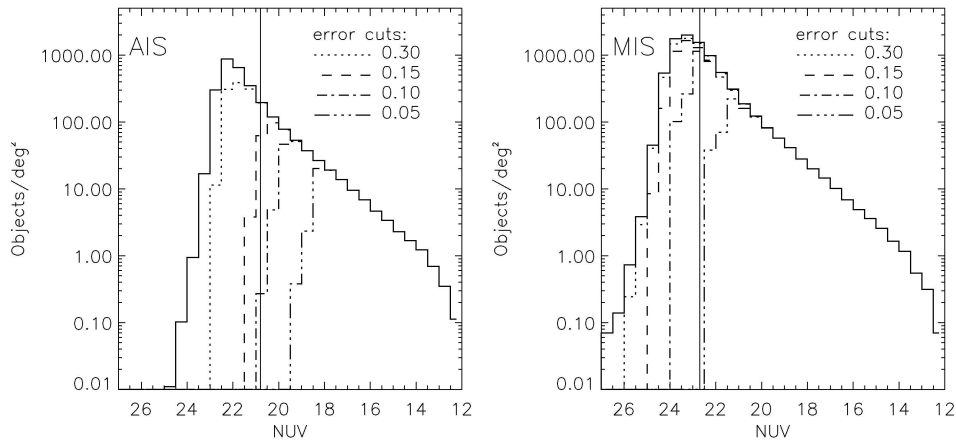


Figure 6.1: Reproduction of the *GALEX* PDF presented in Bianchi et al. (2007a)

	Waveband	Frequency (Hz)	Percentage with flux measurement	
X-ray	Hard	4.97 keV	1.20×10^{18}	100%
	Soft	1.08 keV	2.61×10^{17}	100%
UV	FUV	1539Å	1.95×10^{15}	48%
	NUV	2316Å	1.30×10^{15}	76%
Optical	<i>u</i>	3500Å	8.57×10^{14}	99%
	<i>g</i>	4800Å	6.25×10^{14}	~ 100%
	<i>r</i>	6250Å	4.80×10^{14}	~ 100%
	<i>i</i>	7700Å	3.90×10^{14}	~ 100%
	<i>z</i>	9100Å	3.30×10^{14}	~ 100%
NIR	J	1.25μm	2.40×10^{14}	21%
	H	1.65μm	1.82×10^{14}	20%
	K	2.17μm	1.38×10^{14}	20%
MIR	W1	3.4μm	8.82×10^{13}	94%
	W2	4.6μm	6.52×10^{13}	95%
	W3	12μm	2.50×10^{13}	89%
	W4	22μm	1.36×10^{13}	65%
Radio		1.4 GHz	1.43×10^9	14%

Table 6.1: The frequencies of the 17 wavebands used in the multiwavelength catalogues and the percentage of the sample of 761 sources with a flux measurement in each. Upper limits and detections with bad photometry are not included in these numbers.

6.3 Flux Correlations

The flux estimates obtained in §6.2 are converted into the source rest frame according to $F_{\nu, \text{rest}} = F_{\nu, \text{obs}}(1 + z)$. Correlations between the monochromatic fluxes in each waveband are calculated and are listed in Table 6.2. N gives the number of sources used in each correlation. Sources where the photometry was poor, or the flux was an upper limit were excluded. ρ is the Spearman rank correlation coefficient, which takes values between -1 and $+1$, with 0 indicating no correlation. The significance of the correlation is also listed, with small values indicating a high significance. With the exception of some correlations with the radio flux, all of the correlations are significant at $> 3\sigma$. This is perhaps expected if for the majority of sources the variations between the amount of output in each band is not large i.e. a source bright in one band will still be bright in another. Since the sample is flux limited and incomplete, a redshift bias is present meaning that higher redshift sources generally show the lowest fluxes. In the flux-flux plots in this section, the sources found in the top right corner with a high flux in both bands are mostly low redshift sources. The high redshift sources only lie in the bottom left corner (although they are joined by some low redshift sources), creating an apparent trend. Some of the more physically interesting correlations are reconsidered in broad redshift bins ($0.1 < z < 0.9$, $0.9 < z < 1.5$ and $1.5 < z < 2.3$) to test for this effect, the results of which are listed in Table 6.3. A regression analysis is carried out following the bisector method of Isobe et al. (1990). Two least squares regression lines are calculated in which the parameters taken as the dependent and independent variable are swapped. These are shown in the figures as dashed lines. The best-fitting trend line is then taken as the bisector of these, shown by the solid black line in each figure. This method is useful when there is no prior understanding of the relationship between two variables. Solid red lines in the figures represent 1:1 correspondence lines. In some cases, a correlation between the monochromatic luminosities is also considered. Although these are more strongly affected by a redshift bias, in each case a significant flux correlation has already been confirmed. The monochromatic luminosities are calculated by $L_{\nu} = 4\pi d_L^2 f_{\nu, \text{rest}}$ where d_L is the luminosity distance calculated from the redshift of the source assuming a flat cosmology with $H_0 = 70 \text{ km s}^{-1} \text{ Mpc}^{-1}$, $\Omega_M = 0.3$ and $\Omega_{\Lambda} = 0.7$ (Spergel et al., 2003).

	Hard X-ray	Soft X-ray	FUV	NUV	u	r	z	J	K	W1	W2	W3	W4
Soft X-ray	$N = 704$ $\rho = 0.82$ $< 10^{-46}$												
FUV	$N = 357$ $\rho = 0.52$ 1×10^{-25}	$N = 357$ $\rho = 0.59$ 3×10^{-34}											
NUV	$N = 566$ $\rho = 0.38$ 3×10^{-21}	$N = 566$ $\rho = 0.48$ 1×10^{-33}	$N = 349$ $\rho = 0.84$ $< 10^{-46}$										
u	$N = 702$ $\rho = 0.33$ 9×10^{-20}	$N = 702$ $\rho = 0.37$ 1×10^{-24}	$N = 566$ $\rho = 0.65$ 2×10^{-44}	$N = 566$ $\rho = 0.72$ $< 10^{-46}$									
r	$N = 703$ $\rho = 0.38$ 6×10^{-25}	$N = 703$ $\rho = 0.37$ 1×10^{-24}	$N = 357$ $\rho = 0.63$ 2×10^{-40}	$N = 566$ $\rho = 0.71$ $< 10^{-46}$	$N = 702$ $\rho = 0.95$ $< 10^{-46}$								
z	$N = 702$ $\rho = 0.42$ 1×10^{-31}	$N = 702$ $\rho = 0.38$ 2×10^{-25}	$N = 357$ $\rho = 0.62$ 2×10^{-39}	$N = 566$ $\rho = 0.61$ $< 10^{-46}$	$N = 702$ $\rho = 0.88$ $< 10^{-46}$								
J	$N = 151$ $\rho = 0.40$ 5×10^{-7}	$N = 151$ $\rho = 0.29$ 3×10^{-4}	$N = 110$ $\rho = 0.62$ 6×10^{-13}	$N = 131$ $\rho = 0.60$ 4×10^{-14}	$N = 151$ $\rho = 0.84$ 7×10^{-41}	$N = 151$ $\rho = 0.88$ $< 10^{-46}$	$N = 151$ $\rho = 0.89$ $< 10^{-46}$						
K	$N = 144$ $\rho = 0.54$ 5×10^{-12}	$N = 144$ $\rho = 0.45$ 2×10^{-8}	$N = 104$ $\rho = 0.73$ 1×10^{-18}	$N = 123$ $\rho = 0.61$ 5×10^{-14}	$N = 144$ $\rho = 0.74$ 2×10^{-26}	$N = 144$ $\rho = 0.78$ 4×10^{-30}	$N = 144$ $\rho = 0.83$ 4×10^{-37}	$N = 140$					
W1	$N = 665$ $\rho = 0.51$ 1×10^{-44}	$N = 665$ $\rho = 0.50$ 6×10^{-44}	$N = 340$ $\rho = 0.72$ $< 10^{-46}$	$N = 542$ $\rho = 0.68$ $< 10^{-46}$	$N = 664$ $\rho = 0.60$ $< 10^{-46}$	$N = 664$ $\rho = 0.69$ $< 10^{-46}$	$N = 664$ $\rho = 0.72$ $< 10^{-46}$	$N = 145$ $\rho = 0.66$ 1×10^{-19}	$N = 136$ $\rho = 0.86$ 4×10^{-40}				
W2	$N = 668$ $\rho = 0.46$ 4×10^{-36}	$N = 668$ $\rho = 0.46$ 7×10^{-36}	$N = 340$ $\rho = 0.72$ $< 10^{-46}$	$N = 545$ $\rho = 0.72$ $< 10^{-46}$	$N = 667$ $\rho = 0.66$ $< 10^{-46}$	$N = 667$ $\rho = 0.76$ $< 10^{-46}$	$N = 667$ $\rho = 0.76$ $< 10^{-46}$	$N = 145$ $\rho = 0.69$ 1×10^{-21}	$N = 136$ $\rho = 0.81$ 2×10^{-33}	$N = 664$	$N = 612$ $\rho = 0.96$ $< 10^{-46}$		
W3	$N = 627$ $\rho = 0.36$ 6×10^{-21}	$N = 627$ $\rho = 0.34$ 3×10^{-18}	$N = 330$ $\rho = 0.67$ 3×10^{-44}	$N = 519$ $\rho = 0.63$ $< 10^{-46}$	$N = 625$ $\rho = 0.68$ $< 10^{-46}$	$N = 626$ $\rho = 0.77$ $< 10^{-46}$	$N = 625$ $\rho = 0.80$ $< 10^{-46}$	$N = 143$ $\rho = 0.78$ 4×10^{-30}	$N = 137$ $\rho = 0.81$ 1×10^{-32}	$N = 612$ $\rho = 0.84$ $< 10^{-46}$	$N = 613$ $\rho = 0.90$ $< 10^{-46}$		
W4	$N = 465$ $\rho = 0.34$ 1×10^{-13}	$N = 465$ $\rho = 0.32$ 3×10^{-12}	$N = 258$ $\rho = 0.59$ 4×10^{-26}	$N = 386$ $\rho = 0.50$ 3×10^{-26}	$N = 463$ $\rho = 0.61$ $< 10^{-46}$	$N = 464$ $\rho = 0.67$ $< 10^{-46}$	$N = 463$ $\rho = 0.72$ $< 10^{-46}$	$N = 141$ $\rho = 0.71$ 3×10^{-23}	$N = 133$ $\rho = 0.74$ 4×10^{-24}	$N = 454$ $\rho = 0.71$ $< 10^{-46}$	$N = 455$ $\rho = 0.76$ $< 10^{-46}$	$N = 456$ $\rho = 0.87$ $< 10^{-46}$	
Radio	$N = 95$ $\rho = 0.38$ 2×10^{-4}	$N = 95$ $\rho = 0.30$ 3×10^{-3}	$N = 45$ $\rho = -0.07$ 0.64	$N = 69$ $\rho = -0.02$ 0.88	$N = 95$ $\rho = 0.15$ 0.15	$N = 95$ $\rho = 0.13$ 0.22	$N = 95$ $\rho = 0.06$ 0.59	$N = 40$ $\rho = 0.08$ 0.61	$N = 37$ $\rho = -0.08$ 0.64	$N = 91$ $\rho = -0.09$ 0.90	$N = 91$ $\rho = -0.11$ 0.29	$N = 88$ $\rho = -0.051$ 0.63	$N = 69$ $\rho = -0.08$ 0.49

Table 6.2: This table lists the Spearman rank correlation coefficients (ρ) and significances for correlations between fluxes in each of the different wavebands available. The number of sources (N) included in each correlation is listed (upper limit measurements or estimates with poor photometry are not included). N.B. The SDSS bands g and i and 2MASS H have been omitted from this table for clarity, but the correlation results are similar to those for adjacent bands.

Correlation	Low z	Mid z	High z
Hard X-ray & FUV	$N = 170$ $\rho = 0.56$ 4×10^{-15}	$N = 121$ $\rho = 0.40$ 7×10^{-6}	$N = 66$ $\rho = 0.13$ 0.31
Soft X-ray & FUV	$N = 170$ $\rho = 0.63$ 7×10^{-20}	$N = 121$ $\rho = 0.47$ 4×10^{-8}	$N = 66$ $\rho = 0.19$ 0.13
Hard X-ray & NUV	$N = 194$ $\rho = 0.54$ 6×10^{-16}	$N = 215$ $\rho = 0.25$ 2×10^{-4}	$N = 157$ $\rho = -0.01$ 0.89
Soft X-ray & NUV	$N = 194$ $\rho = 0.60$ 2×10^{-20}	$N = 215$ $\rho = 0.33$ 8×10^{-7}	$N = 157$ $\rho = 0.23$ 4×10^{-3}
Hard X-ray & W1	$N = 213$ $\rho = 0.54$ 9×10^{-18}	$N = 241$ $\rho = 0.43$ 4×10^{-12}	$N = 211$ $\rho = 0.30$ 7×10^{-6}
Soft X-ray & W1	$N = 213$ $\rho = 0.54$ 3×10^{-17}	$N = 241$ $\rho = 0.37$ 5×10^{-9}	$N = 211$ $\rho = 0.36$ 8×10^{-8}
W2 & FUV	$N = 161$ $\rho = 0.78$ 3×10^{-34}	$N = 117$ $\rho = 0.65$ 2×10^{-15}	$N = 62$ $\rho = 0.47$ 1×10^{-4}
W2 & NUV	$N = 186$ $\rho = 0.81$ 1×10^{-43}	$N = 206$ $\rho = 0.69$ 1×10^{-30}	$N = 153$ $\rho = 0.53$ 2×10^{-12}
Hard X-ray & Radio (RLQ)	$N = 22$ $\rho = 0.37$ 0.09	$N = 28$ $\rho = 0.78$ 9×10^{-7}	$N = 19$ $\rho = 0.81$ 3×10^{-5}

Table 6.3: This table lists the number of sources used in the correlations, N , the Spearman rank correlation coefficients, ρ , and significances for some correlations. They are split into 3 broad redshift bins; $0.1 < z < 0.9$, $0.9 < z < 1.5$ and $1.5 < z < 2.3$, in order to test whether the correlations are simply an artifact of using a flux limited sample.

6.3.1 UV and X-ray

A correlation between the X-ray and UV emission has been found by many authors in the literature (see §6.1) and is expected if the X-ray emission in AGN is due to the inverse Compton scattering of UV photons from the disc. Each of the four combinations of the hard and soft X-ray bands and NUV and FUV bands gives a highly significant correlation ($\text{sig} \leq 3 \times 10^{-21}$). In Fig. 6.2 (top) the correlations with the soft X-ray flux are shown. This shows that most sources are $\sim 500 - 8000\times$ brighter in the FUV (the range with NUV is much broader) than soft X-rays. In general the sources whose X-ray spectra were best-fit with the po+bb model lie in the top right of the plot where the emission in both the soft X-rays and the FUV is greater. This is perhaps expected if the soft excess is related to the disc emission. However, this could also be another effect of the redshift bias, as the soft excess component is more efficiently detected in low redshift sources (see Chapter 5). The outliers on the left of the plot are also sources whose X-ray spectra were best-fit with the po+bb model, which is surprising given their relatively low soft X-ray flux. However, they do have FUV fluxes higher than the rest of the sources, consistent with the explanation that the soft excess is related to the disc. If the sources were high redshift, it could be that the soft excess signature was mostly redshifted out of the *XMM-Newton* bandpass, but the larger disc emission was still detected in *GALEX*. However the sources all lie at $z \sim 0.3$.

The sources are split into 3 broad redshift bins, and the correlations are tested again (see Table 6.3). The redshift bias due to the flux limited sample is clearly present in each of the 4 combinations as the significance of the correlations decreases in the higher redshift bins, and is no longer significant in the highest. However, the correlations do remain highly significant in the lowest redshift bin, suggesting that some of the correlation observed is likely to be a real physical effect. The best-fitting trendlines shown in Fig. 6.2 are determined using the bisector method and imply $F_{1\text{keV}} \propto F_{1539\text{\AA}}^{0.96 \pm 0.04}$ and $F_{1\text{keV}} \propto F_{2316\text{\AA}}^{1.00 \pm 0.03}$.

Fig. 6.2 (bottom) shows correlations between the soft X-ray and UV luminosities. They both show a highly significant correlation ($\text{sig} < 10^{-46}$) and the best-fitting trendlines imply the relations $L_{1\text{keV}} \propto L_{1539\text{\AA}}^{0.98 \pm 0.04}$ and $L_{1\text{keV}} \propto L_{2316\text{\AA}}^{0.91 \pm 0.03}$. Direct comparisons with results in the literature are not possible as the frequencies at which the UV and X-ray fluxes have been

measured are not the same. Whilst the NUV frequency is similar to 2500\AA , the X-ray energy used here is lower than the 2 keV value typically used. However, Young et al. (2010) find the slope of the $\alpha_{\text{OX}} - l_{\text{opt}}$ correlation steepens as X-ray energy used decreases, and the value found here is indeed slightly steeper (0.91 ± 0.03) than those seen in the literature ($0.7 - 0.9$).

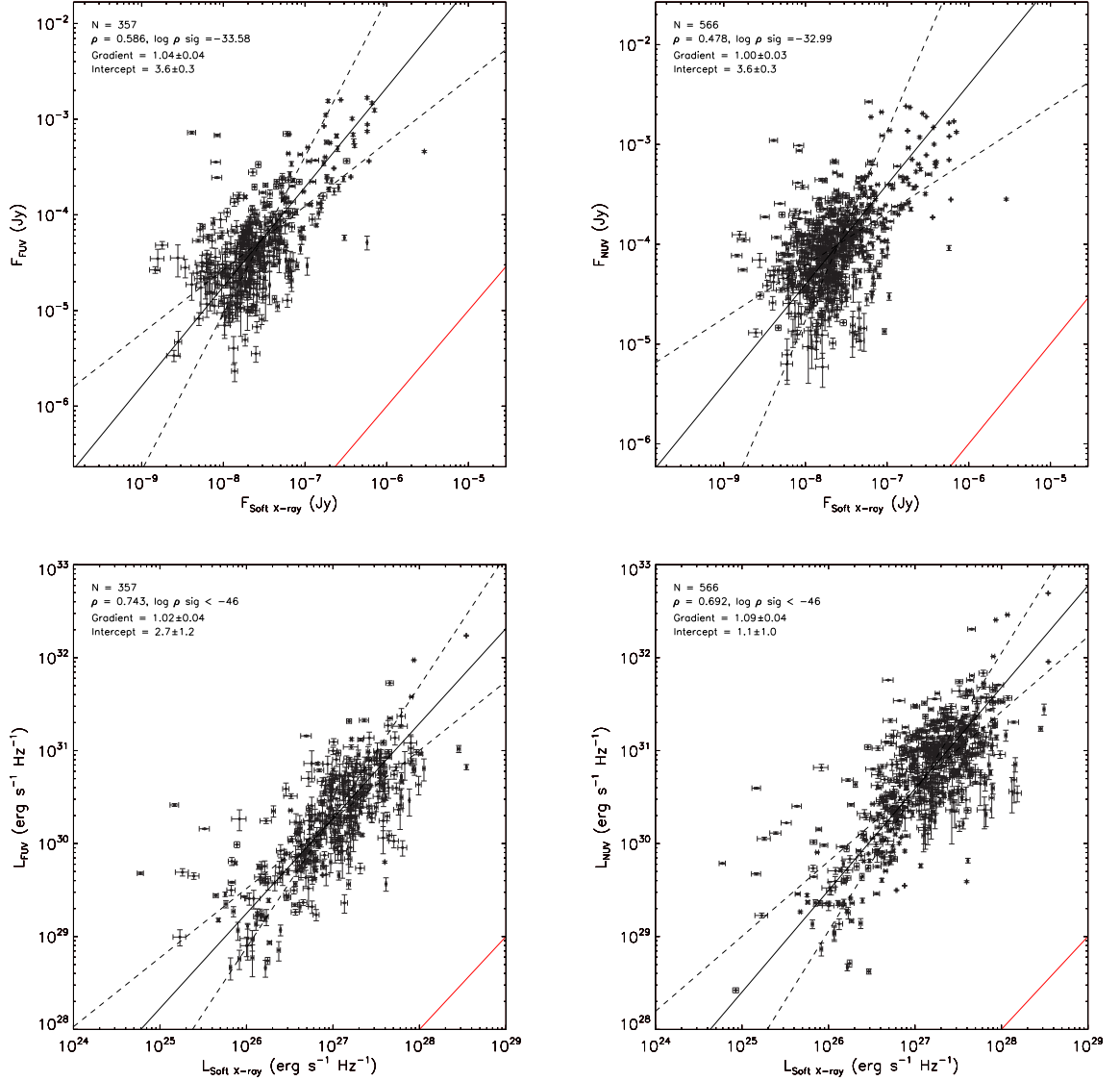


Figure 6.2: Top - The correlations between the flux in the soft X-ray band (at 1.0 keV) and the FUV band (1539\AA , left) and NUV band (2316\AA , right). Spearman's rank correlation coefficients suggest highly significant correlations; $\rho = 0.59/0.48$, significance = $3 \times 10^{-34}/1 \times 10^{-33}$. Bottom - The correlation between the soft X-ray and FUV (left) & NUV (right) luminosities. Both correlations are highly significant: $\rho = 0.74/\rho = 0.69$, significance $< 10^{-46}$ for both. The red solid lines show a 1:1 correspondence

6.3.2 X-ray and IR

The IR emission is thought to be a result of the primary emission being reprocessed by dust. Therefore, correlations between the X-ray and IR bands are expected, particularly if the fraction reprocessed is approximately the same for each source. Correlations with both the hard and soft X-ray fluxes are strongest with the MIR (*WISE* bands), than with the NIR (2MASS bands) and in each case the strongest correlation is with W1 ($3.4\ \mu\text{m}$), $\text{sig} < 3 \times 10^{-44}$, as shown in Fig. 6.3 (top). The dust sublimation temperature $T \sim 2000\ \text{K}$ corresponds to a wavelength of $1.45\ \mu\text{m}$, meaning the shortest wavelength NIR bands may not be probing dust.

Fig. 6.3 shows that the majority of sources have fluxes between $7000\times$ and $60,000\times$ higher at W1 than at 1 keV (soft X-ray) and between $30,000\times$ and $500,000\times$ higher than at 5 keV (hard X-ray) and there is a broad variation in the fraction of emission converted from X-ray to IR. Outliers in the flux correlations include SRCID 211185 which is known to have a very high X-ray count rate and SRCID 202938 which shows a higher than expected IR emission for its given X-ray flux. The significance of the correlation does decrease in higher redshift bins, indicating that a redshift bias is present, however, it remains significant in each sub-bin, suggesting a real physical correlation. Given this, the correlation is also re-considered with the sample split into broad L_X bins; $L_X < 44$, $44 < L_X < 45$ and $L_X > 45$. The correlations remain highly significant for each of the bins, suggesting no dependence on this parameter. Similarly, the correlations are still significant in Eddington ratio sub-bins ($\lambda_{\text{Edd}} < -1.5$, $-1.5 < \lambda_{\text{Edd}} < -0.5$ and $\lambda_{\text{Edd}} > -0.5$). The bisectors shown in Fig. 6.3 imply the relations: $F_{3.4\mu\text{m}} \propto F_{1\text{keV}}^{0.93 \pm 0.03}$ and $F_{3.4\mu\text{m}} \propto F_{5\text{keV}}^{0.92 \pm 0.03}$ and these do not show any significant change within the sub-bins.

Fig. 6.3 (bottom) shows correlations between the W1 and X-ray luminosities. They both show highly significant correlations ($\text{sig} < 10^{-46}$) and the best-fitting trendlines imply the relations $L_{3.4\mu\text{m}} \propto L_{1\text{keV}}^{0.94 \pm 0.03}$ and $L_{3.4\mu\text{m}} \propto L_{5\text{keV}}^{0.91 \pm 0.02}$. These are similar to the results presented in the literature for nearby Seyferts, where $L_{\text{MIR}} \propto L_X$. The plot comparing the soft X-ray luminosity to the W1 luminosity shows a group of outliers above the trend of the general population. Three of these objects have X-ray spectra that were best-fit with an absorbed power-law model, and the average X-ray power-law slope of the remaining sources is very flat

($\Gamma \sim 1.2$), suggesting they include an unmodelled absorption component. This would explain why their soft X-ray luminosities are lower than expected given their MIR luminosity. The bottom right plot of Fig. 6.3 shows an outlier identified as SRCID 211185 which is known to have a high X-ray count rate, and hence shows a high hard X-ray luminosity in comparison with its MIR luminosity. The outlier to the left of the trend is SRCID 202938, which has a very low hard X-ray luminosity and a very flat broadband SED, likely due to a dominating contribution from its host galaxy.

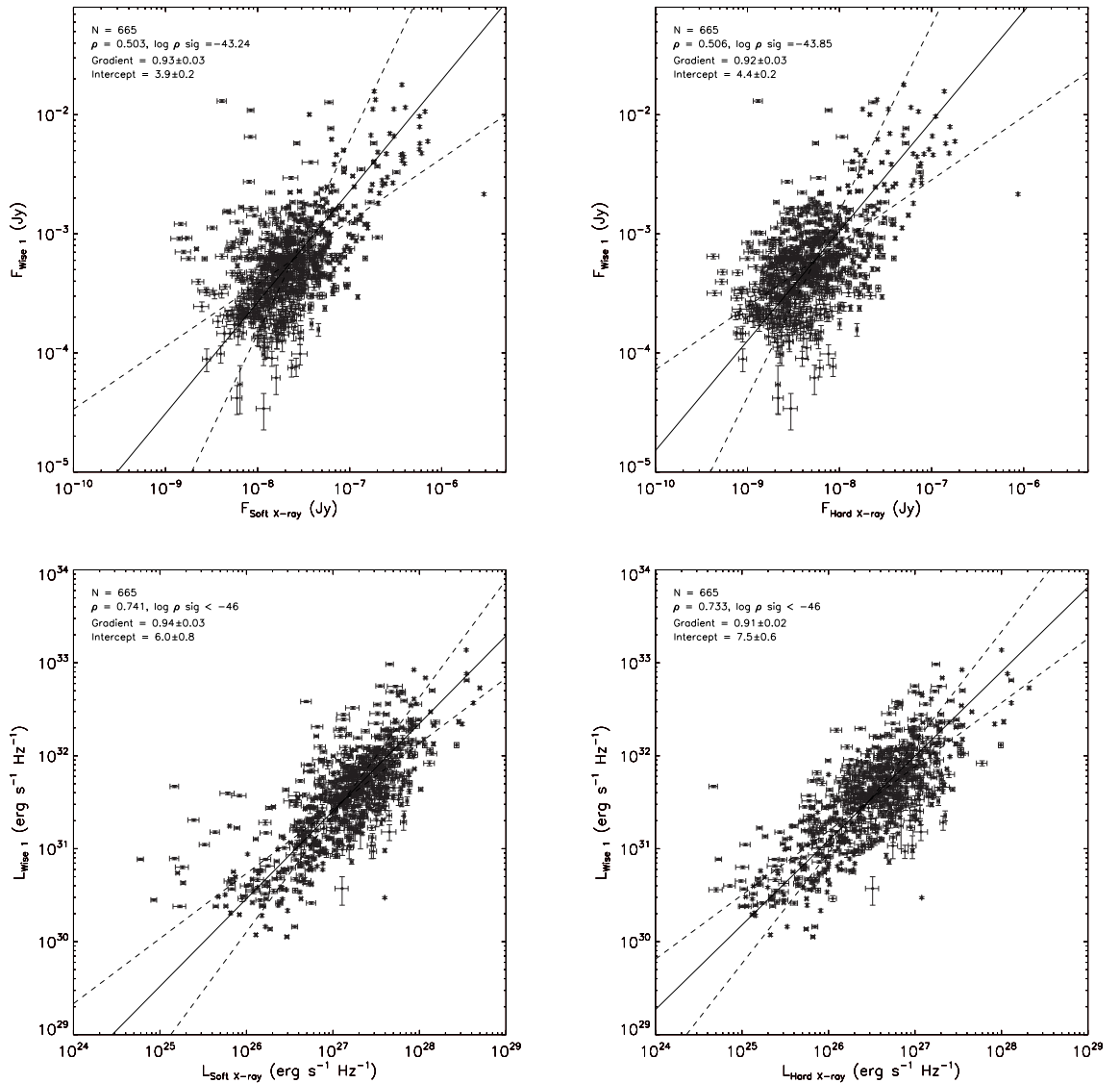


Figure 6.3: Top - The correlations between the flux in the W1 band ($3.4 \mu\text{m}$) and the soft (left) and hard (right) X-ray bands. Spearman's rank correlation coefficients suggest highly significant correlations; $\rho = 0.50/0.51$, $\text{sig} = 6 \times 10^{-44}/1 \times 10^{-44}$. Bottom - The correlation between the W1 and Soft X-ray (left) & Hard X-ray (right) luminosities. Both correlations are highly significant: $\rho = 0.73/\rho = 0.74$, significance $< 10^{-46}$ for both.

6.3.3 UV and IR

The primary emission that is reprocessed into IR, consists of both X-ray and UV. Therefore, correlations between UV and IR emission are also expected. The strongest correlations are again with the MIR rather than with the NIR and in each case the strongest correlations are with W2 ($4.6 \mu\text{m}$), $\text{sig} < 10^{-46}$, as shown in Fig. 6.4 (top).

The plots show a greater amount of emission in the IR band than in the UV, although the sources lie just above a 1 : 1 correspondence, shown by the red lines. The sources cover a narrow band with the majority being between $5\times$ and $100\times$ brighter in FUV than W2 and $4\times$ and $40\times$ brighter in NUV. These are the tightest correlations in the sample, but there is a scatter caused by high redshift sources lying above the rest of the population with a high IR flux for their given NUV emission. The correlations are also re-considered with the sources binned into broad redshift bins. The correlation between W2 and FUV is no longer significant when only the highest redshift sources are considered but the correlation with NUV is still highly significant albeit with a lower significance. The correlations for each are significant in all 3 L_X bins and all 3 λ_{Edd} bins. The best-fitting trendlines shown on Fig. 6.4 by the solid black line give the relations $F_{4.6\mu\text{m}} \propto F_{1500\text{\AA}}^{0.83\pm 0.03}$ and $F_{4.6\mu\text{m}} \propto F_{2300\text{\AA}}^{0.91\pm 0.02}$. The bisectors do change within the L_X bins, but this is simply a result of the outlying sources with high redshift. There is no change within the λ_{Edd} sub-bins.

Fig. 6.4 (bottom) shows correlations between the W2 and UV luminosities. They both show a highly significant correlation ($\text{sig} < 10^{-46}$) and the best-fitting trendlines imply the following relations: $L_{4.6\mu\text{m}} \propto L_{1500\text{\AA}}^{1.04\pm 0.03}$ and $L_{4.6\mu\text{m}} \propto L_{2300\text{\AA}}^{0.95\pm 0.02}$. The bottom right plot shows some outlying sources above the trend of the general population, some of which have absorbed X-ray spectra. If absorbing material is present it is likely responsible for the lower NUV luminosity observed.

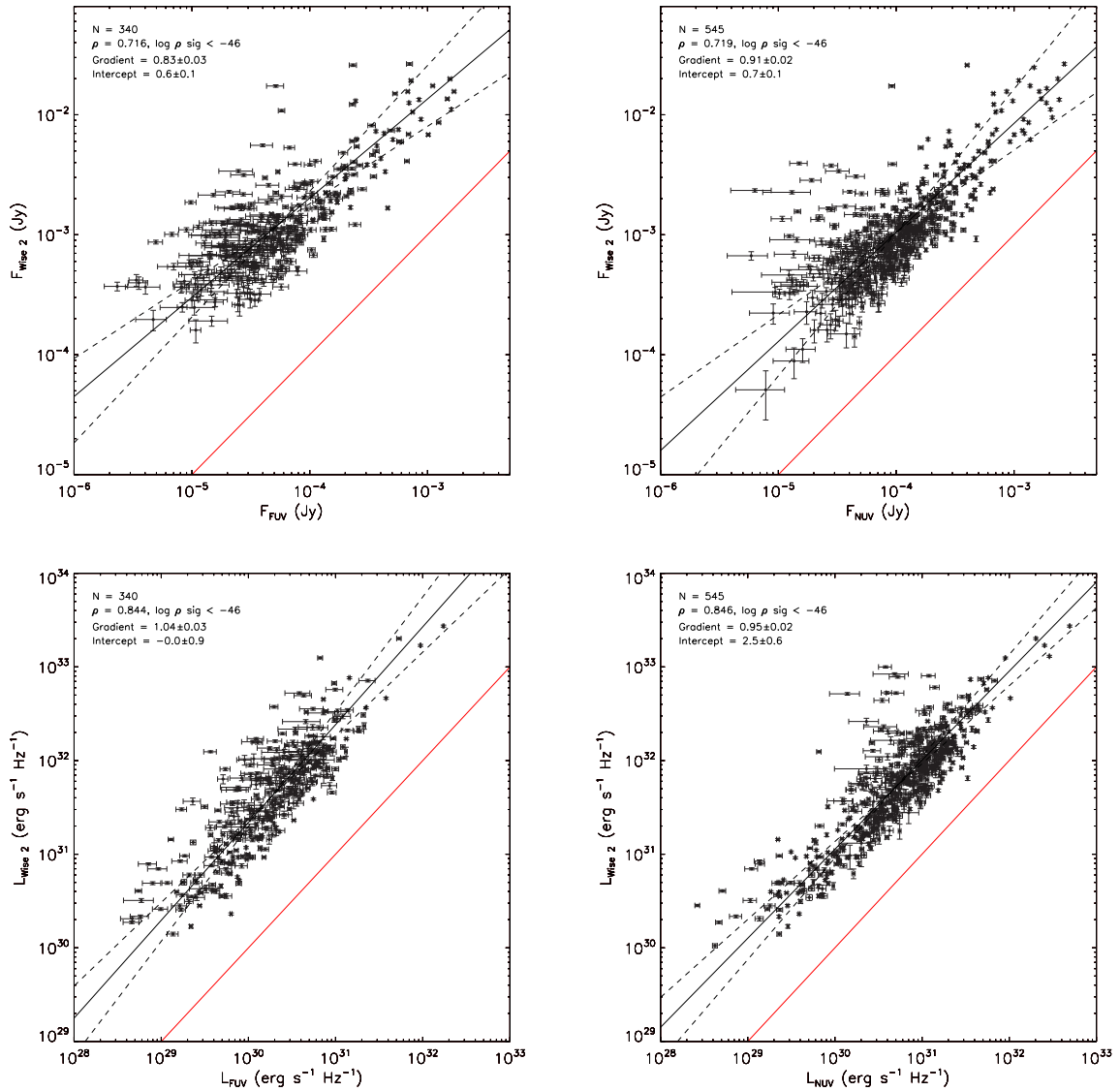


Figure 6.4: Top - The correlations between the flux in the FUV (left) and NUV (right) and W2 ($4.6 \mu\text{m}$). Spearman's rank correlation coefficients suggest highly significant correlations; $\rho = 0.72$, significance $< 10^{-46}$ for each. Bottom - The correlation between the W2 and FUV (left) and NUV (right) luminosities. Both correlations are highly significant: $\rho = 0.84/\rho = 0.85$, significance $< 10^{-46}$ for both. The red solid lines show a 1:1 correspondence.

6.3.4 X-ray and Radio

As discussed in §6.1, previous studies have reported a correlation between the X-ray and radio emission and a significant correlation between the hard X-ray flux and the radio flux was found for this sample (see Table 6.2). However, when the sample is split into RQ and RL sub-samples, the correlation is no longer significant for RQ sources (see Fig 6.5, top right).

The bisector in the RL figure implies the relation $F_{1.4\text{GHz}} \propto F_{5\text{keV}}^{1.5 \pm 0.2}$.

Fig. 6.5 (bottom) shows the correlation between the monochromatic hard X-ray luminosity and the radio luminosity for RL sources (left) and RQ (right). A significant correlation is found in both cases ($\text{sig} = 3 \times 10^{-12} / 4 \times 10^{-6}$), although given the lack of a flux correlation in the case of the radio-quiet sources, this is probably an artefact of the redshift bias. The bisector in the RL figure implies the relation $L_{1.4\text{GHz}} \propto L_{5\text{keV}}^{1.7 \pm 0.1}$.

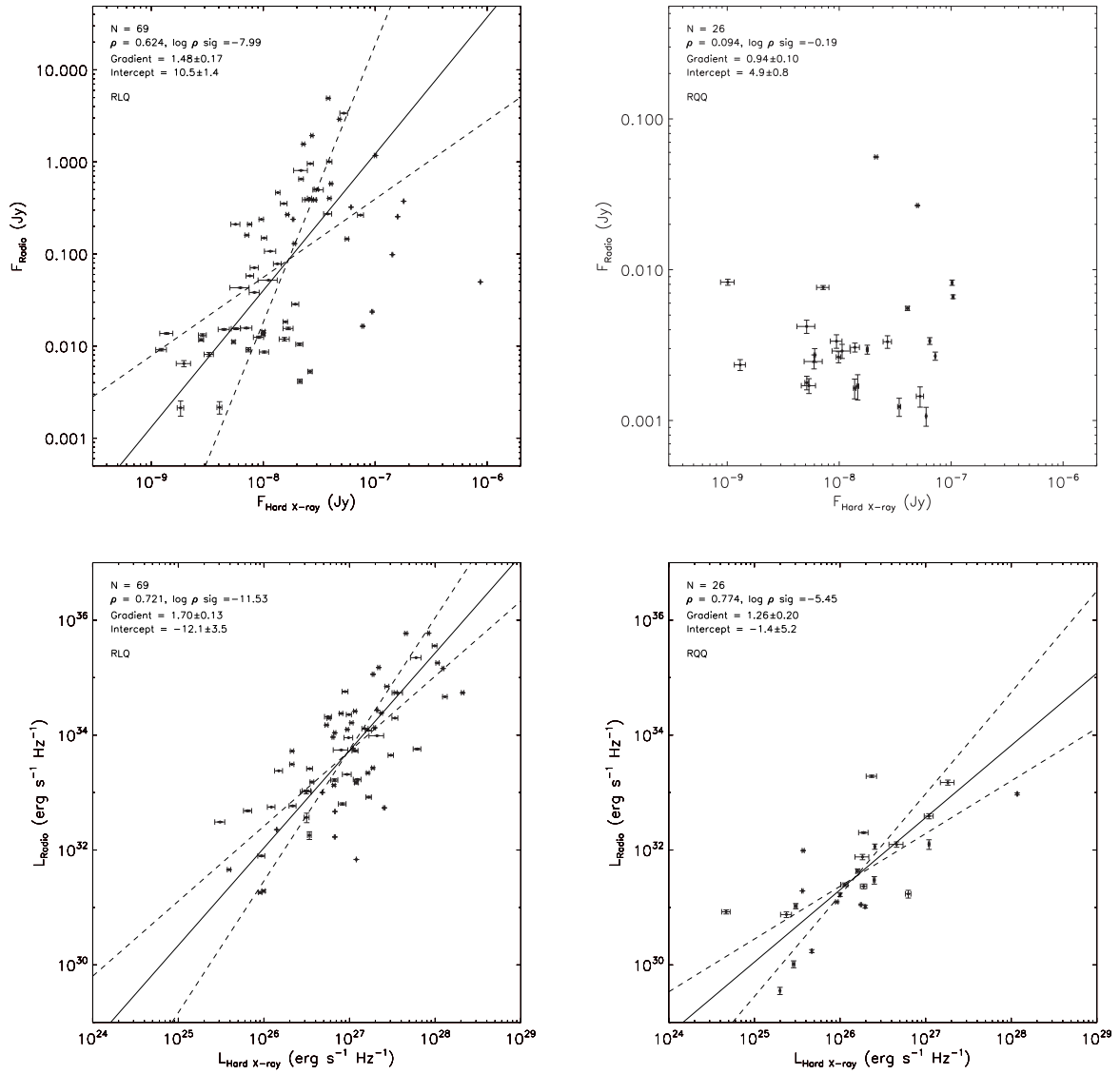


Figure 6.5: Top - The correlation between the flux in the hard X-ray band (at 5.0 keV) and the radio band (1.4 GHz) for RLQ (left) and RQQ (right). Spearman's rank correlation coefficient suggests a significant correlation in the case of the RLQ, $\rho = 0.62$, $\text{sig} = 10^{-8}$, but not in the case of the RQQ. Bottom - The correlation between the luminosities in the hard X-ray and radio band. Both correlations are significant: $\rho = 0.72/\rho = 0.77$, significance = $3 \times 10^{-12}/4 \times 10^{-6}$.

6.4 Spectral Energy Distributions

The fluxes in each waveband are multiplied by the observed frequency (listed in Table 6.1) and corrected into the rest-frame (νF_ν) using Eqn. 6.6 where $\nu' F'_\nu$ is the observed frame. The frequencies plotted on the x axis are also converted into the rest frame using $\nu = \nu'(1 + z)$.

$$\nu F_\nu = \nu' F'_\nu (1 + z)^2 \quad (6.6)$$

An example of an SED is shown in Fig. 6.6. Flux measurements with errors are plotted in different colours depending on the source of the data. Those with bad photometry flags are excluded, whilst upper limits are plotted as triangles. It clearly shows many of the typical features expected in the SED of a type 1 AGN including: Power-law emission in the X-ray regime, in this case with a flat spectral slope of $\Gamma \sim 1.6$, a gap in the SED between the X-ray and UV emission which cannot be sampled due to absorption by the Milky Way, the ‘big blue bump’ (BBB; Shields 1978) at (log) frequencies of 14.5 – 15.5, an inflection point in the NIR at $\log \nu \sim 14.5$, which is thought to correspond to the sublimation temperature of dust grains (Sanders et al., 1989), the IR hump at frequencies lower than $\log \nu = 14.5$, which appears to be due to the superposition of two blackbodies with different peak temperatures, another gap in the SED between the MIR and the radio bands, and a radio upper limit indicating this source is radio quiet.

For high redshift sources, Ly- α (rest-frame wavelength 1216Å) is redshifted into the SDSS photometric bands. This results in an absence of flux in bands bluewards of this due to absorption in the Ly- α forest. This affects the u band for sources with $z \sim 2.3$, g for $z \sim 3.5$ and r for $z \sim 4.8$. Figure 6.7 shows the SED for SRCID 67854 which is at $z = 4.444$. The fluxes in the u and g bands appear significantly lower than might be expected, highlighting this effect. The optical spectrum from SDSS shows Ly- α redshifted into the r band. A redshift cut of $z < 2.3$, which removes $\sim 7\%$ of sources, is applied to the sample in order to remove these effects.

Some of the SEDs indicate absorption in the source. They show a decrease in flux through the SDSS photometric bands despite being at a low redshift, and where available, the UV photometry from *GALEX* is also lower than might be expected. The X-ray spectrum of SRCID

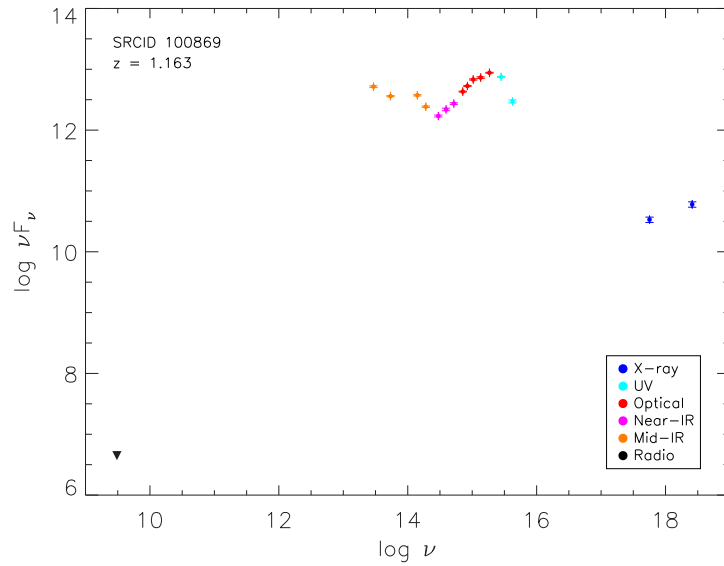


Figure 6.6: The spectral energy distribution of SRCID 100869. It includes radio data from FIRST (black), MIR data from *WISE* (orange), NIR data from 2MASS (pink), optical data from SDSS (red), UV data from *GALEX* (light blue) and X-ray data from *XMM-Newton* (dark blue). Filled circles with error bars correspond to secure flux measurements. Triangles denote upper limit estimates. Any flux measurements with a bad photometry flag in the raw catalogues are excluded.

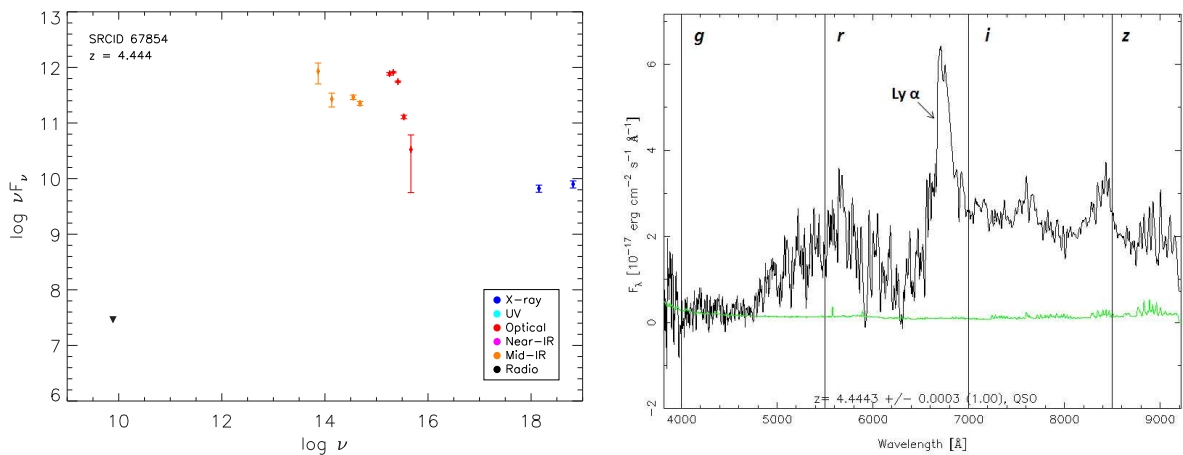


Figure 6.7: Left - the SED of SRCID 67854 which lies at $z = 4.444$. The SDSS photometry in both the *u* and *g* bands appears to be significantly lower than might be expected. Right - the SDSS optical spectrum of the same source. This shows that the photometric bands *u* and *g* are suppressed by the Ly- α forest.

6501 (Fig. 6.8, top left) was originally best-fit with an absorbed power-law model with an intrinsic absorbing column density of $N_{\text{H}} = 1.87_{-0.54}^{+0.57} \times 10^{22} \text{ cm}^{-2}$ and the reddening estimate of $A_{\text{V}} = 3.20 \pm 0.54$ from Hutton et al. (in preparation) also suggests that absorption is present. Similarly, the X-ray spectrum of SRCID 68220 (Fig. 6.8, top right) was fit with an absorbed power-law model where $N_{\text{H}} = (0.17 \pm 0.03) \times 10^{22} \text{ cm}^{-2}$ and the optical spectrum gave a reddening estimate of $A_{\text{V}} = 1.3 \pm 0.2$ (Hutton et al. in prep). The optical spectrum also suggests there may be strong contamination from the host galaxy. SRCID 96216 (Fig. 6.8, bottom left) was not fit with absorption, but does have a very flat power-law of $\Gamma = 0.55 \pm 0.04$ suggesting that unmodelled absorption may be present. There may also be host galaxy contamination present in this source. Richards et al. (2006) use a low redshift cut at $z = 0.3$ in order to remove sources whose optical spectra are contaminated by their host galaxies. The SEDs of the 39 sources at $z < 0.3$ are visually examined, and only those already highlighted show any signs of problems with their optical or UV photometry. Therefore, no lower redshift cut is applied to the sample. The X-ray spectrum of SRCID 194880 (Fig. 6.8, bottom right) was neither fit with an absorbed power-law model, nor is the power law particularly flat; $\Gamma = 1.67 \pm 0.15$. These 4 sources are excluded from further sub-samples.

In the following analysis, the mean SEDs of various sub-sets of sources are created. Interpolation of the individual SEDs is carried out with an initial sampling of 20 points in a straight line between each pair of consecutive flux measurements. A second interpolation using 5000 x points is then determined across the entire SED. Upper limits are not included in this interpolation. In order to create the mean SED, the average $\log \nu F_{\nu}$ value is determined at each rest-frame frequency (sampled by the 5000 interpolation points). The error on this value is plotted as the standard error on the mean, $\alpha = \sigma/\sqrt{N}$, where $\sigma = \sqrt{\frac{1}{N-1} \sum (\nu F_{\nu} - \overline{\nu F_{\nu}})^2}$. As the average SEDs are created from sources with different bolometric luminosities, the dispersion in the plots is due to a combination of two effects; sources having comparable SED shapes, but different normalisations, and sources with different SED shapes. The rest-frame frequency range covered by each source's SED is very similar, but varies slightly due to their redshift. This means that at either end of the SED, the number of sources used to determine the average decreases from $N \rightarrow 0$, which gives an increased dispersion and hence a large

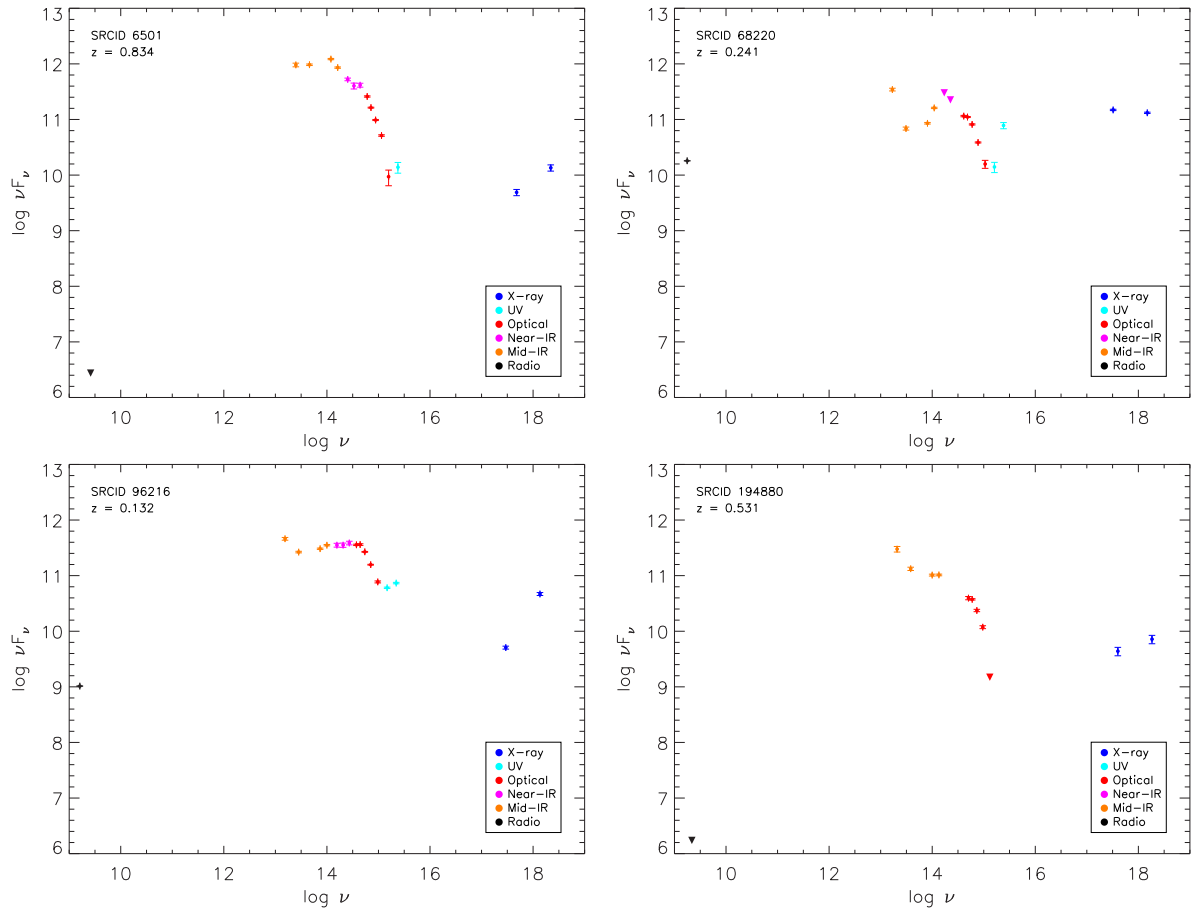


Figure 6.8: The SEDs of four sources with probable intrinsic absorption.

error on the average SED. In mean SEDs created from small numbers of sources, this effect is particularly strong at the high frequency end, so these portions of the SED are trimmed. Between the radio band and W4, and similarly between the FUV band and the soft X-rays, the majority of the SED only consists of interpolation points and no real flux measurements. Therefore, the portions which do not include a contribution from any real flux measurement have also been omitted from the figures.

Three sub-samples of sources are considered based on their data quality. Sample 1 includes 26 sources which have a complete SED with a measured flux (no upper limits or poor photometry) in each of the 17 wavebands considered. This number is low as only 14% of sources have a FIRST radio detection. Sample 2 includes 75 sources which have a complete SED in 16 wavebands but no radio detection (radio upper limits are included as they are not used in the interpolation). Sample 3 consists of all 704 sources, the majority of which do not have a complete SED.

The mean SED of the sources in sample 1 is shown in Fig. 6.9. The BBB is visible at (log) frequencies of 14.5 – 15.5 and the IR hump can be seen between 13 – 14. As was already evident in the individual SED shown in Fig. 6.6, and appears in others in the sample, the MIR regime appears to show a ‘double hump’ shape manifested as a seemingly low W3 flux. Calderone et al. (2012) model this feature with a superposition of 2 blackbodies with different temperatures, ~ 300 K and ~ 1500 K, which could represent emission from the hot, inner edge and the outer, colder edge of the torus.

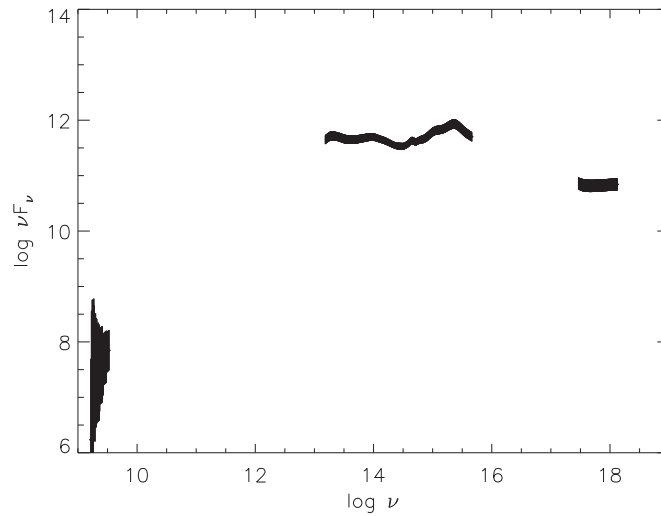


Figure 6.9: The mean SED of the 26 sources with a flux measurement in each of the wavebands. The portions of the SED which do not include any real flux measurement are removed. The SED is also cut off at the high frequency end when the number of sources used in the averaging begins to decrease, giving a large artificial dispersion.

6.4.1 Luminosity Sub-samples

Further sub-sets of sources are defined based on different physical parameters. Here they are binned according to their hard X-ray luminosity as determined from the spectral fitting in Chapter 3. Three bins are defined: $\log L_X < 44.0$, $44.0 < \log L_X < 45.0$ and $\log L_X > 45.0$. The mean SEDs for each of these sub-sets are shown in Fig. 6.11. Separate panels for the 3 different data quality sub-sets are also shown.

All three samples clearly show the X-ray part of the SED is lower in the low L_X samples, as expected. The BBB is more prominent in the higher L_X samples, whereas the IR–UV SED shape appears to be rather flat in the lower L_X samples. The peak of the BBB occurs at a higher value ($\nu F_\nu = 12.6 \pm 0.1$) in the high L_X sample than in the low L_X sample ($\nu F_\nu = 11.48 \pm 0.09$) for data samples 2 and 3, but not for sample 1. This indicates that in general sources which are bright in X-rays are also bright in the UV, suggesting a relationship between the emission in each part of the SED. However, the shape of the SED appears to change as a function of L , not just the amplitude. The slope between the BBB and the X-rays is flatter in the mean SED of the low L_X sources and steeper for the high L_X sample for data sample 2. This suggests that α_{OX} is dependent on L_X . Steffen et al. (2006) and Just et al. (2007) do find that α_{OX} depends on $l_{2\text{keV}}$, but in general most literature results quote the anti-correlation between α_{OX} and $l_{2500\text{\AA}}$ which says that if L_X increases, there is an even larger increase in L_{UV} giving a steeper SED shape between the two frequencies. This relationship agrees with the behaviour seen in the mean SEDs for sample 2 but is not seen in sample 3, despite the SEDs showing increases in both optical and X-ray emission.

The νF_ν values at optical and X-ray frequencies are extracted from the 3 average SEDs in data sample 2 and the $\alpha_{\text{OX}} - l_{\text{opt}}$ anti-correlation is reproduced in Fig. 6.10. The black data points use the X-ray frequency at 1 keV and the optical frequency at 2316Å in order to allow comparison with the flux correlation in §6.3.1 which used soft X-ray and NUV frequencies. The best-fitting trend line (shown by the solid line) was determined from a χ^2 minimization, and the 1σ uncertainty boundary is shown by the dotted black lines. The slope is -0.2 ± 0.2 , which is consistent with zero within 1σ errors, suggesting no trend. However, it gives the relationship $F_{1\text{keV}} \propto F_{2316\text{\AA}}^{0.8 \pm 0.2}$, which agrees with the flux correlation presented in §6.3.1

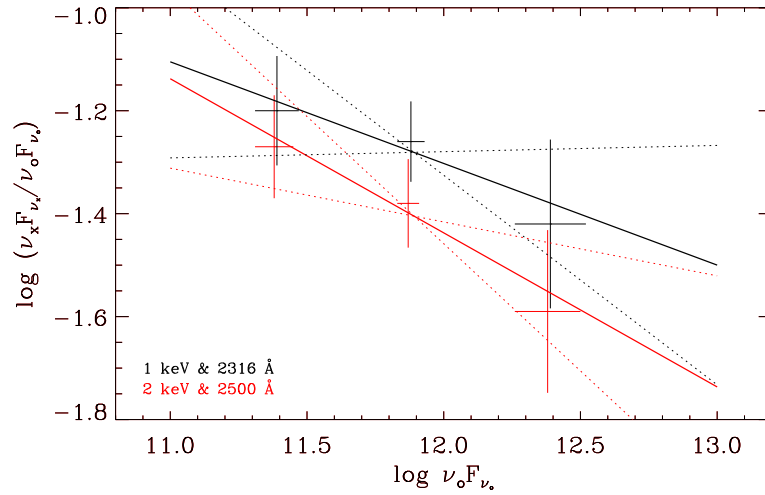


Figure 6.10: A plot of F_X/F_O against F_O with values obtained from the mean SEDs binned according to L_X . The black data points and lines were obtained using data at an X-ray energy of 1 keV and the optical data at a wavelength of 2316Å. The red data points and lines correspond to the typically used values of 2 keV and 2500Å. The solid line represents the best-fitting trend line from a χ^2 minimization, and the dotted lines show the 1σ uncertainty boundary. The difference in optical frequencies has been artificially increased to separate the values on the x axis.

($F_{1\text{keV}} \propto F_{2316\text{\AA}}^{1.00 \pm 0.03}$). In order to compare with results in the literature, values are also extracted at 2 keV and 2500Å and are shown in Fig. 6.10 by the red data points. In this case the best-fitting trendline gives $F_{2\text{keV}} \propto F_{2500\text{\AA}}^{0.7 \pm 0.2}$ but the slope is still consistent with zero within 1.5σ errors and hence there is no significant trend. Young et al. (2010) determined the slope of the $\alpha_{\text{OX}} - l_{\text{opt}}$ correlation using a range of different X-ray energies. Their result obtained at 1 keV (-0.17 ± 0.02) agrees with the result presented here (-0.2 ± 0.2). However, they find the slope gets flatter for higher X-ray energies (-0.12 ± 0.01 at 2 keV), but the results shown here give a steeper slope of -0.3 ± 0.2 . Due to the large errors on this estimate, it is still formally consistent with the Young et al. (2010) result.

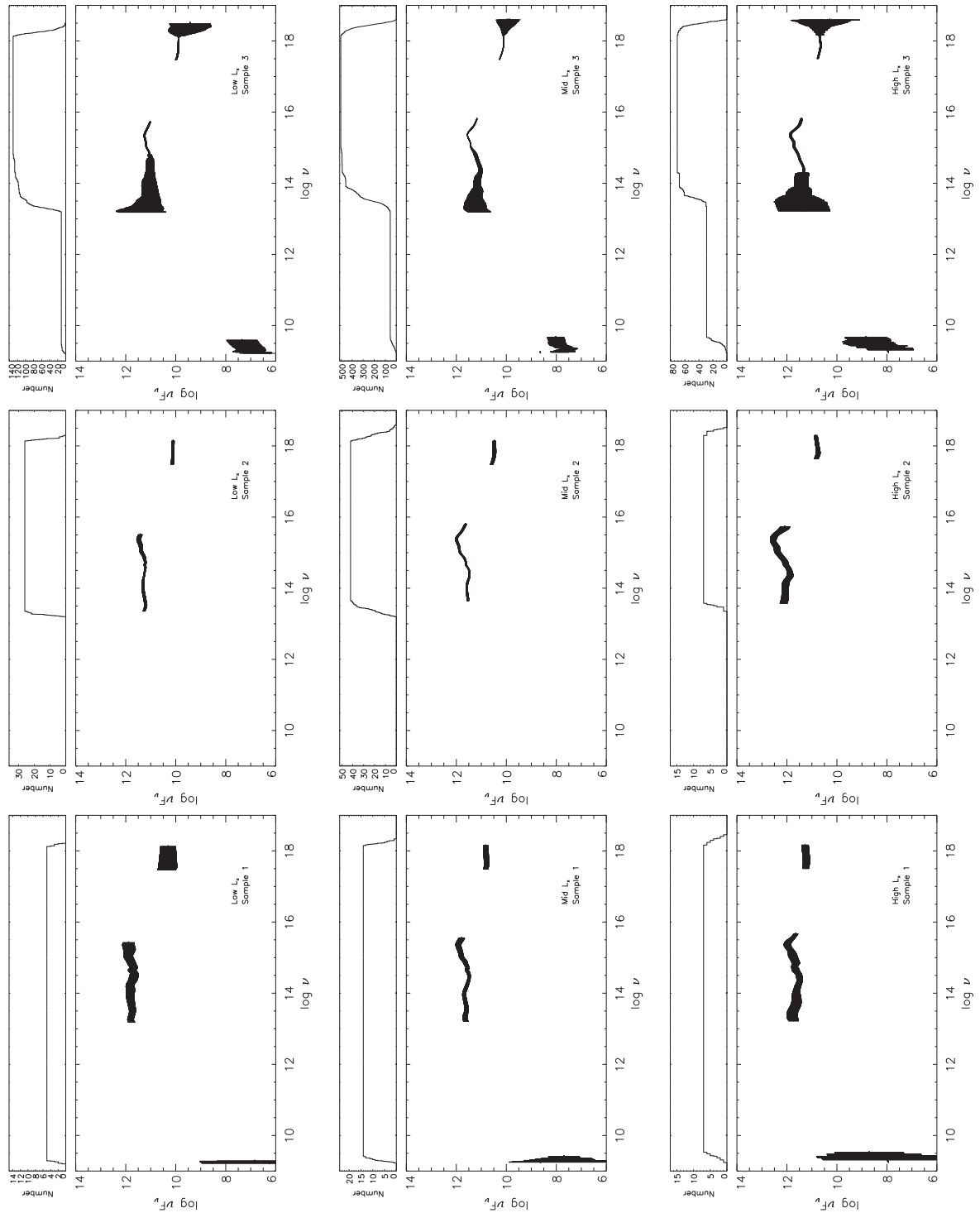


Figure 6.11: These figures show mean SEDs created by averaging the individual SEDs of sources in different sub-sets: Low luminosity ($\log L_X < 44$), medium luminosity ($44 < \log L_X < 45$) and high luminosity ($\log L_X > 45$). In each case, the 3 data quality sub-sets are also considered. The number of sources used in creating the average SED at each frequency is plotted in the panel above each SED.

6.4.2 Eddington Ratio Sub-samples

As the Eddington ratio is a fundamental parameterisation of accretion in AGN, it is likely that the SED shape describing the emission will vary with changes in this parameter. A Principal Component Analysis (PCA; Francis & Wills 1999) of red 2MASS AGN concluded that L/L_{Edd} is the most important factor in determining SED shape (Kuraszkiewicz et al., 2009). Three sub-samples are defined based on the X-ray derived (see §3.3.7) Eddington ratio; $\lambda_{\text{Edd},X} < -1.5$, $-1.5 < \lambda_{\text{Edd},X} < -0.5$ and $\lambda_{\text{Edd},X} > -0.5$. The mean SEDs are shown in Fig. 6.13 and Table 6.4 lists both the νF_ν values at 2 keV and 2500Å and the α_{OX} values calculated from $\alpha_{\text{OX}} = 0.38 \log(f_{2\text{keV}}/f_{2500\text{Å}})$. This shows that for data sample 2, α_{OX} does not change significantly, despite both the optical and X-ray emission increasing. In the case of data sample 3, α_{OX} flattens in sub-samples with increasing $\lambda_{\text{Edd},X}$. This is a result of an increase in X-ray flux (as might be expected since the Eddington ratio is dependent on L_X) but a constant optical flux in the top 2 bins.

Data Sample		Low $\lambda_{\text{Edd},X}$	Mid $\lambda_{\text{Edd},X}$	High $\lambda_{\text{Edd},X}$
Sample 2	2 keV (νF_ν)	9.98 ± 0.11	10.39 ± 0.06	10.80 ± 0.11
	2500 Å (νF_ν)	11.35 ± 0.14	11.77 ± 0.06	11.95 ± 0.18
	α_{OX}	-1.53 ± 0.07	-1.53 ± 0.03	-1.44 ± 0.08
Sample 3	2 keV (νF_ν)	9.75 ± 0.06	10.12 ± 0.01	10.45 ± 0.03
	2500 Å (νF_ν)	11.26 ± 0.07	11.43 ± 0.01	11.40 ± 0.04
	α_{OX}	-1.58 ± 0.04	-1.51 ± 0.01	-1.37 ± 0.02
		Low $\lambda_{\text{Edd},O}$	Mid $\lambda_{\text{Edd},O}$	High $\lambda_{\text{Edd},O}$
Sample 2	2 keV (νF_ν)	10.21 ± 0.20	10.37 ± 0.06	10.50 ± 0.18
	2500 Å (νF_ν)	11.15 ± 0.13	11.74 ± 0.05	12.14 ± 0.16
	α_{OX}	-1.36 ± 0.09	-1.53 ± 0.03	-1.63 ± 0.09
Sample 3	2 keV (νF_ν)	10.14 ± 0.06	10.13 ± 0.01	10.23 ± 0.06
	2500 Å (νF_ν)	11.19 ± 0.05	11.41 ± 0.01	11.64 ± 0.05
	α_{OX}	-1.41 ± 0.03	-1.49 ± 0.01	-1.54 ± 0.03

Table 6.4: The α_{OX} values derived from the flux values in the mean SEDs of sources binned by λ_{Edd} .

Mean SEDs of sub-samples defined by the optically derived Eddington ratios of the sources are shown in Fig. 6.14. The bins are defined as: $\lambda_{\text{Edd},O} < -1.25$, $-1.25 < \lambda_{\text{Edd},O} < -0.5$ and $\lambda_{\text{Edd},O} > -0.5$. The BBB appears to be more prominent in higher Eddington ratio

sub-samples, with its peak value increasing towards the higher ratio sub-samples ($\nu F_\nu = 11.77 \pm 0.06$ compared with 11.23 ± 0.06 in the lower Eddington ratio sub-sample³). This suggests that an increase in accretion rate leads to an increase in the amount of disc emission. However, by definition, the optically defined Eddington ratio depends on the optical luminosity. The amount of X-ray emission appears to be similar in each of the sub-samples. Coupled with the variation in the BBB emission, this naturally results in a steepening of α_{OX} as the Eddington ratio increases, which can be seen in the figures.

Fig. 6.12 plots the α_{OX} values listed in Table 6.4 against the mean Eddington ratio for each sub-sample. Different plotting symbols refer to the different data quality sub-sets. Black data points and lines correspond to the X-ray derived values and red are the optically derived values. The sample of best quality data (sample 2) and the sample including all data (3) are consistent, suggesting that any trend present is likely to be a real physical effect. The best-fitting trendlines shown with the dashed lines were found by χ^2 minimization. For 3 cases the best-fitting gradient obtained is consistent with zero within 3σ , suggesting no significant variation of α_{OX} with λ_{Edd} . For X-ray sample 3, the gradient is significantly different from zero and is plotted as the solid black line, with the black dotted lines indicating the 1σ error boundary. The best-fitting trendline in this case is $\alpha_{\text{OX}} = (0.15 \pm 0.02)\lambda_{\text{Edd}} + (-1.35 \pm 0.02)$. This is consistent with the result of Grupe et al. (2010), but the gradient is flatter than that found by Lusso et al. (2010). It also agrees with the results of Jin et al. (2012) who find that α_{OX} increases with an increased accretion rate. Whilst there appears to be a difference in the direction of the correlation when the optical or X-ray derived bolometric luminosities are used, the gradients of some optical and X-ray sub-samples are consistent with each other. This behaviour might also be expected given that $\alpha_{\text{OX}} \propto L_{\text{X}}/L_{\text{O}}$ and there is at least some dependence of $\lambda_{\text{Edd,X}}$ on L_{X} and $\lambda_{\text{Edd,O}}$ on L_{O} .

6.4.3 Narrow-line Seyfert 1

In §4.3.3 the properties of NLS1 were compared with their broad-line counterparts. The Zhou et al. (2006) catalogue allowed 17 sources to be identified as NLS1s and 169 other sources

³Values for sample 3.

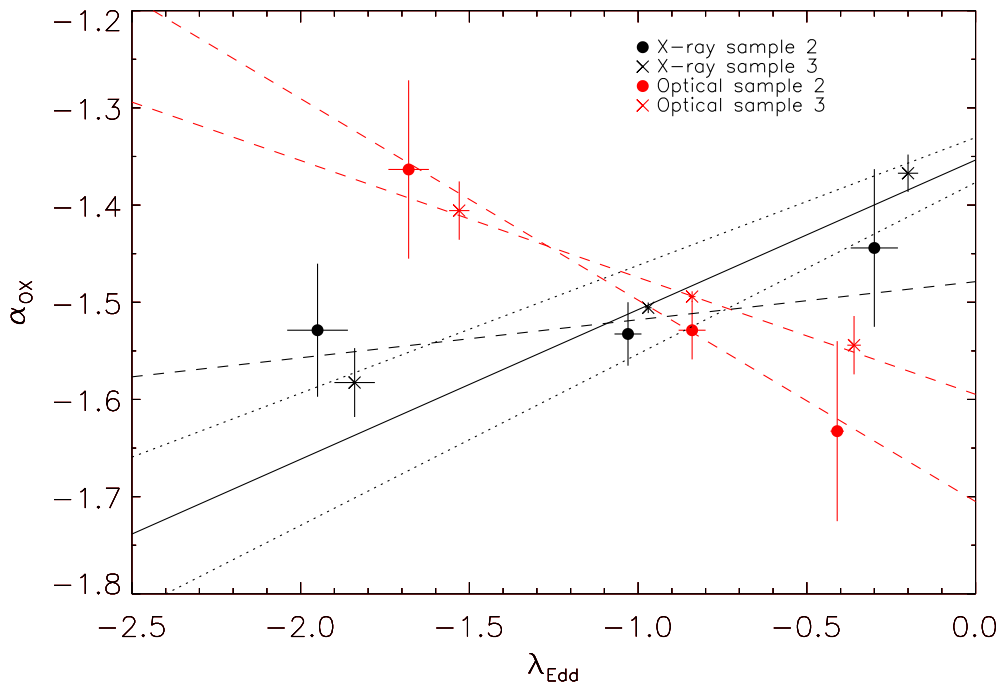


Figure 6.12: The dependence of α_{OX} on Eddington ratio. Different plotting symbols refer to the different data quality sub-sets. Black data points and lines correspond to the X-ray derived values and red are the optically derived values. Dashed lines are best-fitting trend lines found by χ^2 minimization. The solid line is the only trendline for which the gradient is significantly different from zero. The 1σ error bounds are marked by the dotted lines.

were confirmed as non-NLS1. Fig. 6.16 shows the mean SEDs of the NLS1 (left) and non-NLS1 (right). They show a similar SED shape over the IR-UV frequency range, but the optical flux level is higher for the NLS1 indicating an increase in disc emission (BBB peak of $\nu F_\nu = 11.65 \pm 0.11$ compared to 11.37 ± 0.04 for the non-NLS1). However, the X-ray flux level is approximately the same ($\nu F_\nu \sim 10.2$ at 2 keV). This is a likely explanation for the observation made in §4.3.3 that the X-ray derived Eddington ratios of NLS1 and non-NLS1 were not significantly different, as the Eddington ratio is strongly dependent on the X-ray luminosity. When using the optical luminosity, the NLS1 do show a significantly higher Eddington ratios (KS statistic = 0.48, significance = 0.0009, see Fig 6.15), which is consistent with observations in the literature. The increase in the disc emission with an increasing optically derived Eddington ratio agrees with the observations in §6.4.2. The mean SEDs also clearly show a steeper X-ray slope in the NLS1 SED, consistent with the result found in §4.3.3 that NLS1 have significantly steeper Γ .

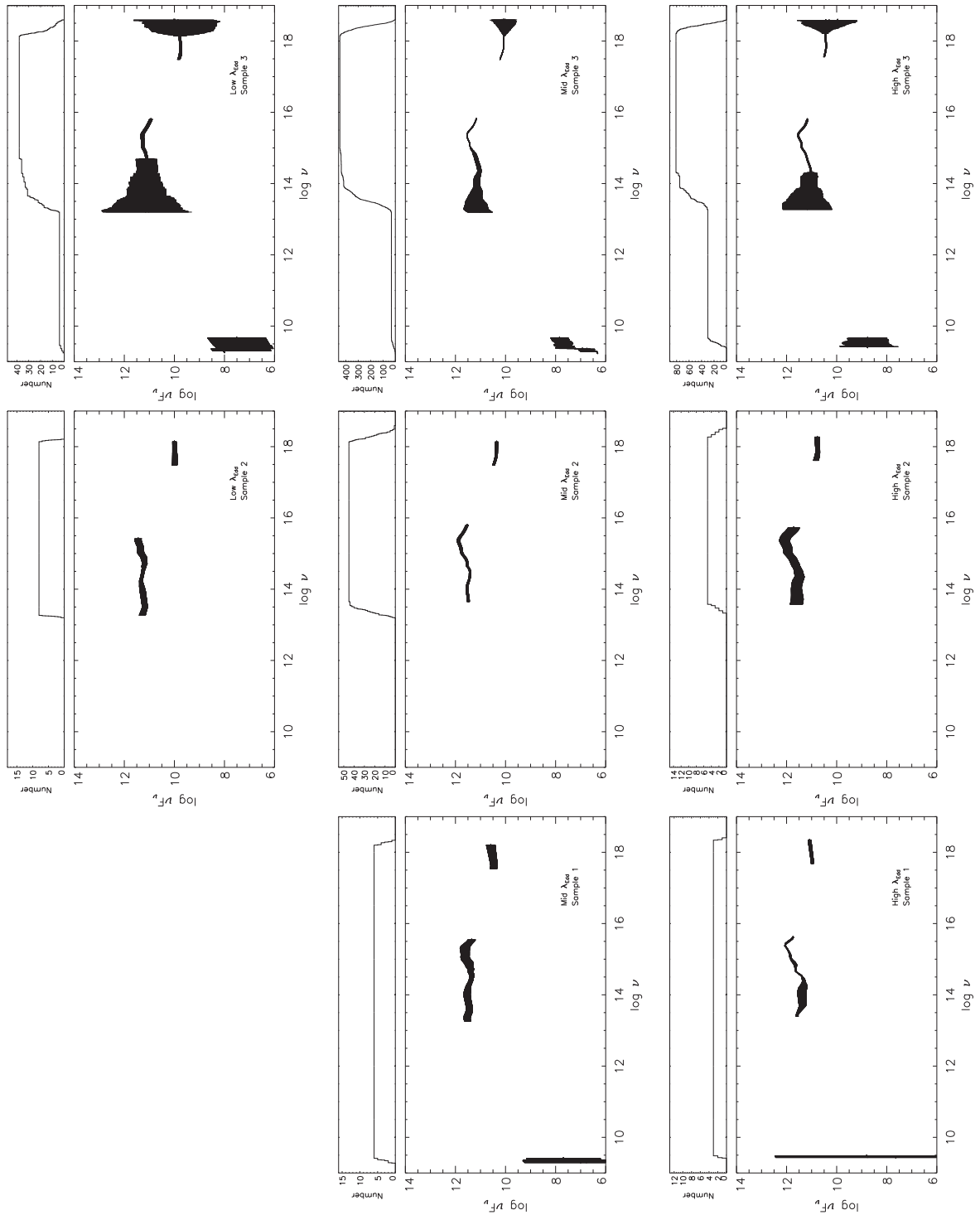


Figure 6.13: The mean SEDs for sub-sets of sources defined by their X-ray derived Eddington ratios: $\lambda_{\text{Edd},X} < -1.5$, $-1.5 < \lambda_{\text{Edd},X} < -0.5$ and $\lambda_{\text{Edd},X} < -1.5$. For each sub-sample, the 3 data quality sub-samples are also considered. The missing panel is due to a lack of sources in sample 1 with an Eddington ratio in the required range.

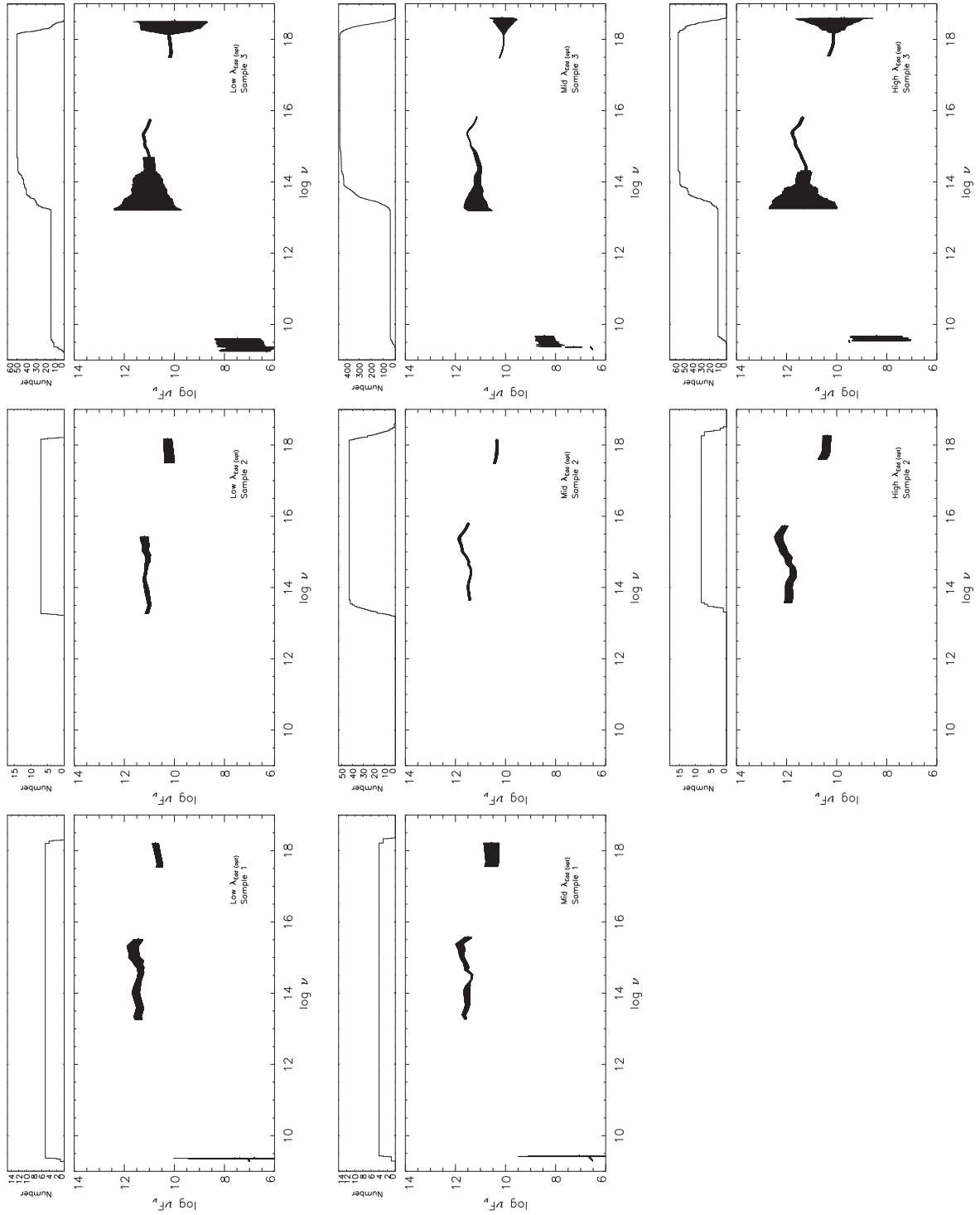


Figure 6.14: The mean SEDs for sub-sets of sources defined by their optically derived Eddington ratios: $\lambda_{\text{Edd},O} < -1.25$, $-1.25 < \lambda_{\text{Edd},O} < -0.5$ and $\lambda_{\text{Edd},O} > -0.5$. For each sub-sample, the 3 data quality sub-samples are also considered. The missing panel is due to a lack of sources in sample 1 with an Eddington ratio in the required range.

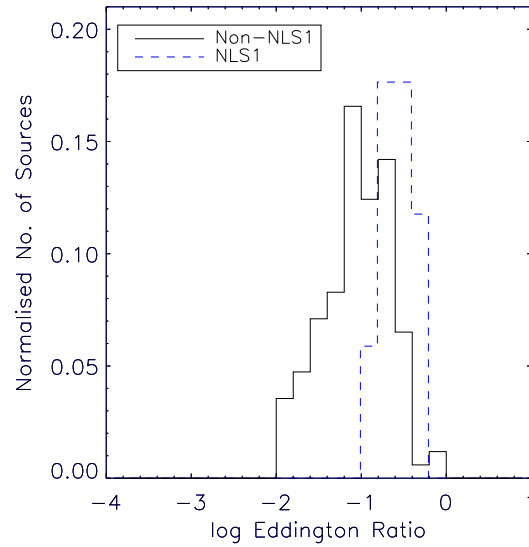


Figure 6.15: This plot compares the optically derived Eddington ratios for 17 NLS1 (blue, dashed) and 169 confirmed non-NLS1 (black, solid).

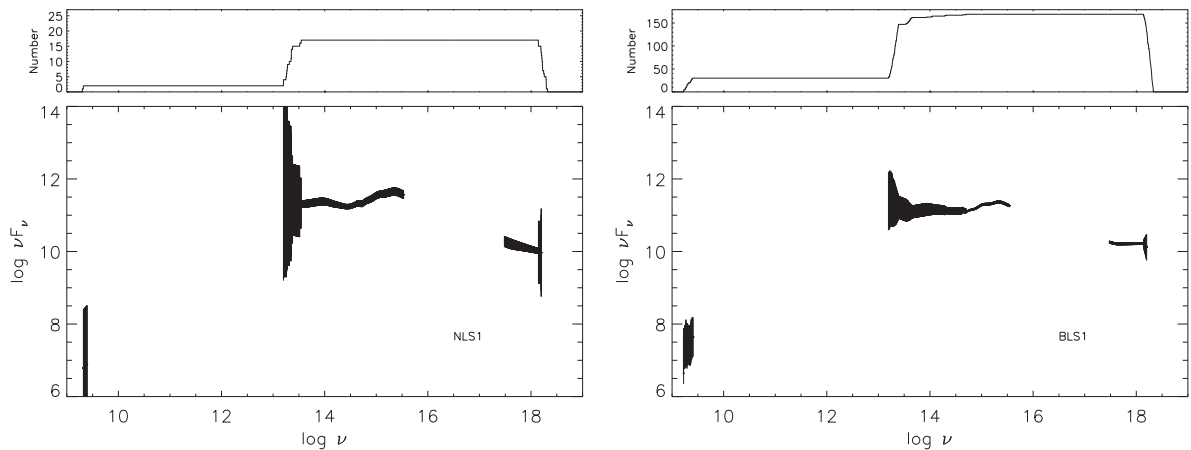


Figure 6.16: Left - The mean SED for 17 sources defined as NLS1 by Zhou et al. (2006; see Chapter 4). Right - The mean SED for 169 sources at $z < 0.8$ and hence covered by the Zhou et al. (2006) catalogue, but not defined as NLS1.

6.4.4 Radio Loudness Sub-samples

Fig. 6.17 shows the mean SEDs of sub-samples of RQQ and RLQ. Sample 2 is not included as it is comprised of sources with no radio detection and therefore the radio loudness cannot be determined. The IR–UV SED shape of both sub-samples appears to be similar, but the RLQ clearly have more radio emission than the RQQ sources. They also show more X-ray emission, $\nu F_\nu = 10.57 \pm 0.05$ at 2 keV compared with $\nu F_\nu = 10.16 \pm 0.02$ for radio quiet, but have a similar amount of optical emission ($\nu F_\nu \sim 11.48$ at 2500Å), as was already found in §3.3.6. This implies that α_{OX} values of RLQ should be flatter than those in RQQ and this is clearly shown in the figures (RLQ: $\alpha_{\text{OX}} = -1.36 \pm 0.03$, RQQ: $\alpha_{\text{OX}} = -1.51 \pm 0.01$). These results imply that RL sources are fundamentally the same as RQ sources and hence produce the same broadband emission, but the presence of a jet gives the additional X-ray and radio emission observed.

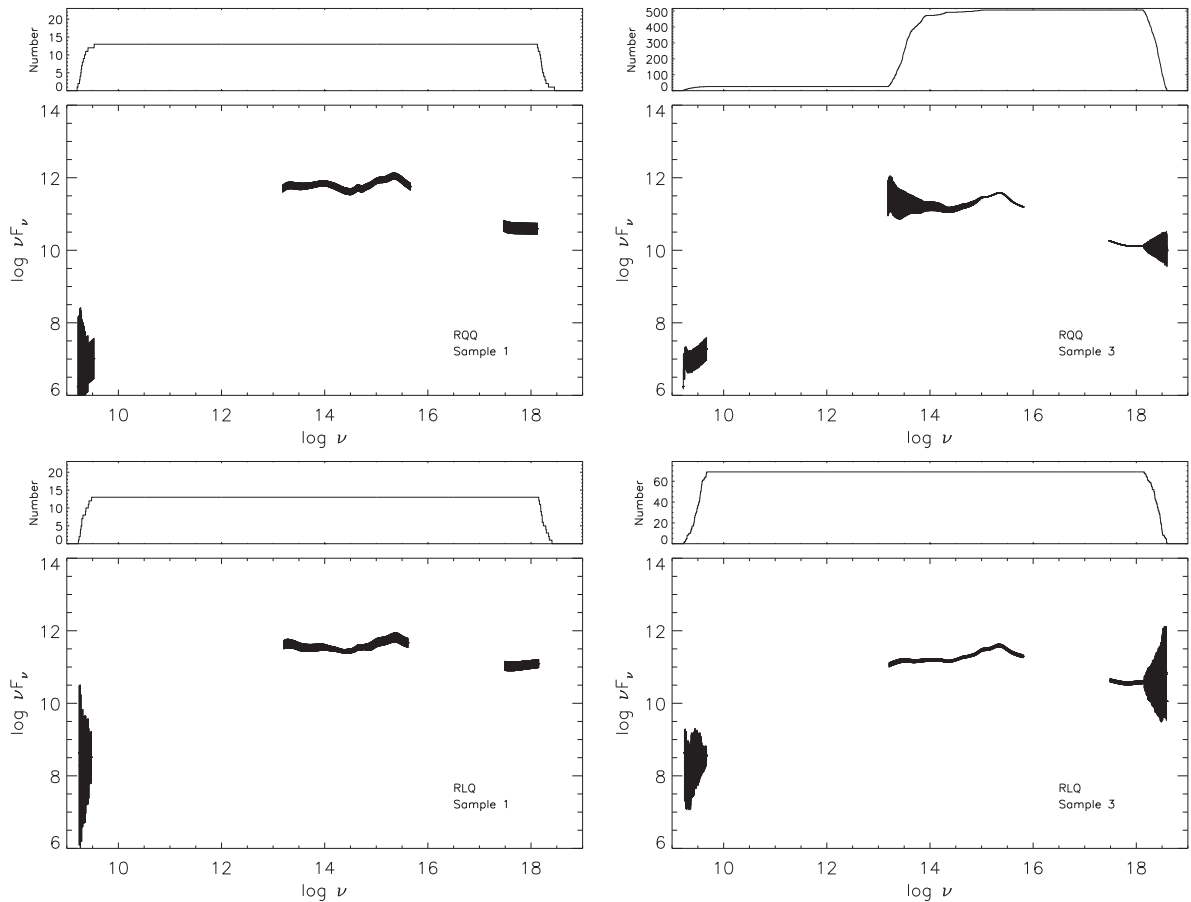


Figure 6.17: The top plots show the mean SEDs created from sub-samples of RQQ. The bottom panels show the mean SEDs of RLQ samples.

6.4.5 X-ray Power-law Slope Sub-samples

Sub-samples are also defined based on the X-ray power-law slope of the sources. ‘Very flat’ sources have $\Gamma < 1.54$, ‘flat’ sources have $1.54 < \Gamma < 2.00$, ‘steep’ sources have $2.00 < \Gamma < 2.44$ and ‘very steep’ sources have $\Gamma > 2.44$. The mean SEDs for each of these samples are shown in Fig. 6.18. They show that the slope of the X-ray part of the SED varies between the Γ sub-samples as expected, and within each of the data sub-samples, the slopes are consistent. The peak of the BBB has a similar value in each of the sub-samples ($\nu F_\nu \sim 11.5$) indicating that the disc emission is not dependent on variations in the X-ray power-law slope.

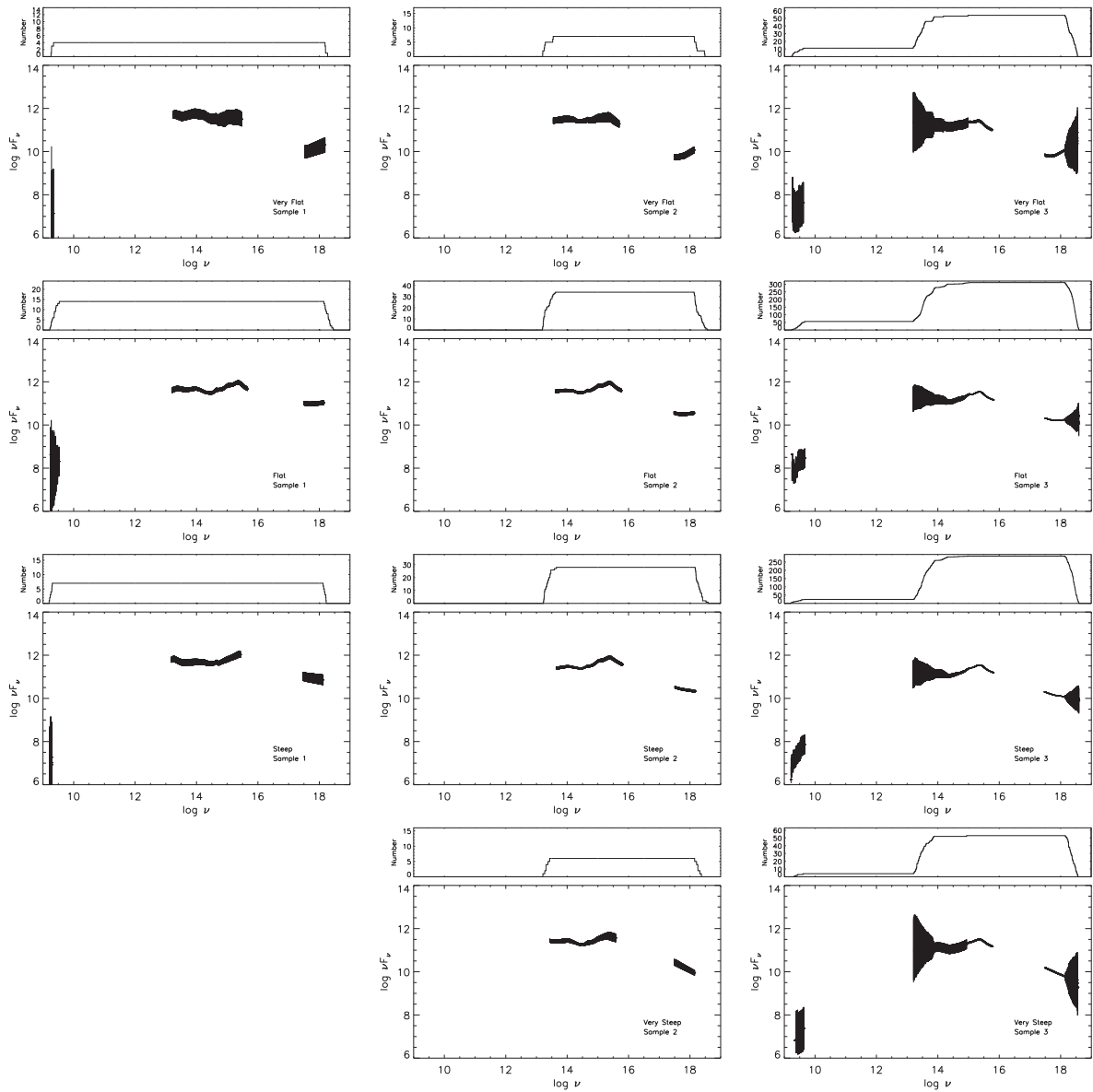


Figure 6.18: The mean SEDs for sub-sets of sources defined by their X-ray power-law slope, Very flat: $\Gamma < 1.54$, flat: $1.54 < \Gamma < 2.00$, steep: $2.00 < \Gamma < 2.44$, very steep: $\Gamma > 2.44$. N.B. No SED is presented for very flat sources in sample 1 as there are no sources which meet this criteria.

6.4.6 Normalised SEDs

The average SEDs in the previous sections included a dispersion which was due to the combination of two effects. In this section, the SED fluxes are normalised at fixed frequencies, so that one of these effects is removed. This means that any remaining dispersion is only due to differences in SED shape between sources, rather than different νF_ν values. The mean SEDs are normalised at the arbitrary frequencies $\log \nu = 10, 14, 15$ and 18 . Fig. 6.19 shows the normalised SEDs for sample 1 (left, 26 sources) and sample 2 (right, 75 sources). Sample 3 is not included as the majority of the sources in this sample do not have a complete SED. This means different numbers of sources would be used at each normalisation frequency due to a lack of data availability. No normalised SED is presented for sample 2 at $\log \nu = 10$ (radio) since the sources in this sample do not include a radio detection.

When normalised at $\log \nu = 10$, the rest of the normalised mean SED for sample 1 shows a large dispersion. This suggests that the radio emission is a poor indicator of the emission in the other parts of the SED i.e. the radio emission is uncorrelated with the other wavebands. This is consistent with the results in §6.3. It is not a surprising result as sample 1 includes 13 RQQ and 13 RLQ which naturally have very different radio fluxes. Normalising these to the same value will clearly result in a large dispersion in the rest of the average SED. When the SEDs are normalised to $\log \nu = 18$ in the X-ray regime, the dispersion in the IR-UV region of the SED is also reasonably high. This suggests a wide variation in X-ray emission properties is possible and so the X-ray band is unlikely to be a good estimator of the bolometric luminosity of sources. Normalising the SEDs to $\log \nu = 14$ (MIR) or $\log \nu = 15$ (optical) does not result in a large dispersion in the rest of the SED, indicating the emission properties of this part of the SED are similar for most sources. This suggests these wavebands can be a good indicator of the emission in the rest of the SED and correlations between these wavebands and others should be tight. This is consistent with §6.3 in which the tightest correlations were observed between W2 and NUV.

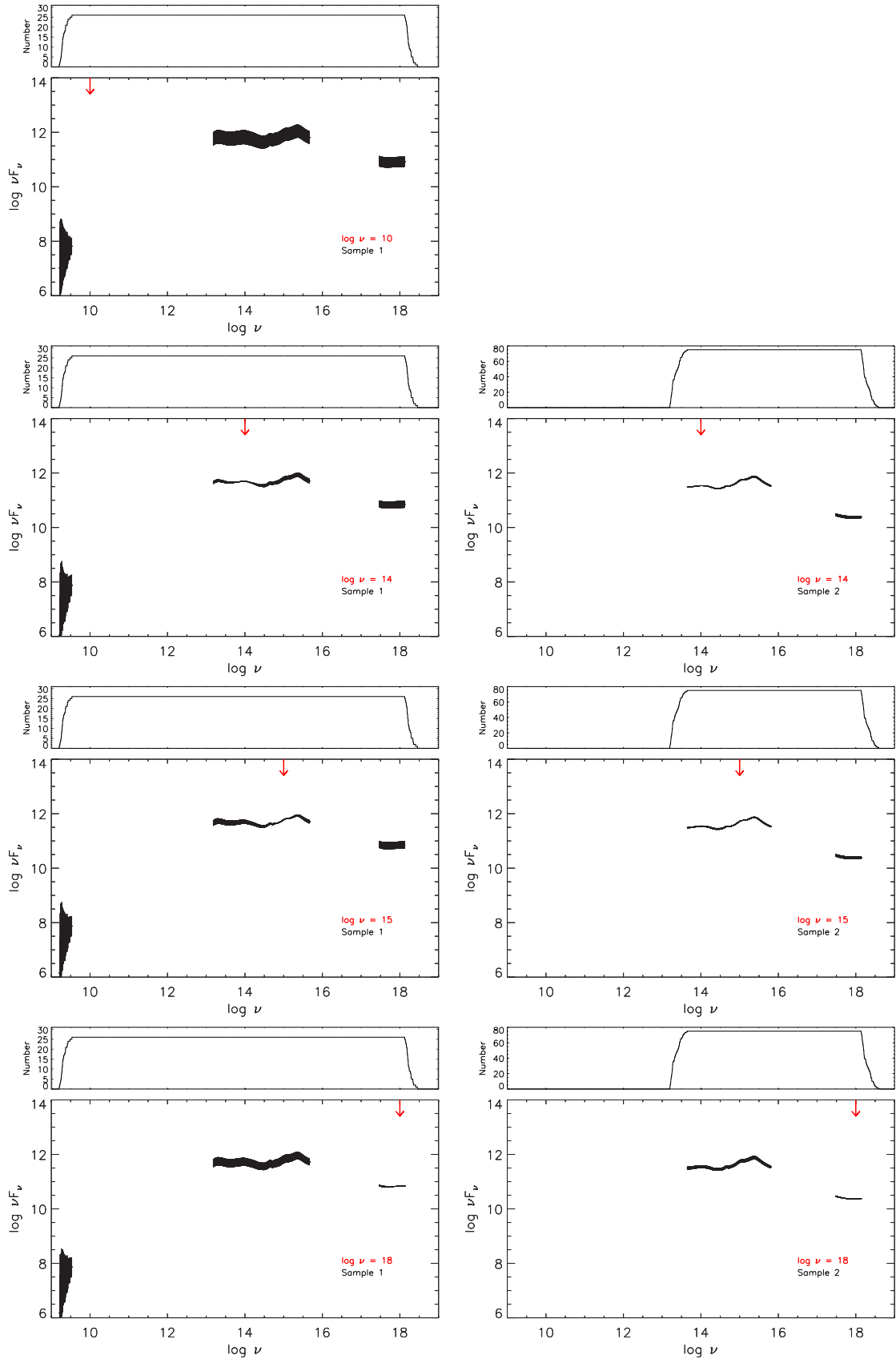


Figure 6.19: These plots show the average SED created after individual SEDs have been normalised to the same flux values at particular frequencies. The top plot is normalised to $\log \nu = 10$ (radio), and the frequency used increases downwards to include $\log \nu = 14$ (MIR), $\log \nu = 15$ (optical) and $\log \nu = 18$ (X-ray). The left panels include the sources in sample 1 and the right panels show sample 2.

6.5 Conclusions

In this Chapter, the shapes of average SEDs and flux correlations were considered in order to find a qualitative description of the broadband emission of AGN. Whilst the SEDs presented here cover a frequency range of $\Delta \log \nu = 10$, there is still a gap between the FUV and the soft X-rays which is unobservable due to absorption by the Milky Way's ISM. Therefore, whilst comments about the SED shape at lower frequencies can be made, it is difficult to form concrete conclusions about the bolometric output of AGN as a major contribution likely lies within this unsampled frequency range.

The IR-UV portion of the SEDs appears to be reasonably similar between objects, as shown by the narrow dispersion in the rest of the SED when normalised at MIR or optical frequencies. This suggests that the processes creating this emission is similar in all sources. The IR-UV SEDs of radio-loud sources are also similar to the radio-quiet sources, suggesting the majority of the AGN emission is not related to its radio loudness in agreement with early results (Sanders et al., 1989). The radio-loud sources simply show additional radio and X-ray components, and a significant correlation between the fluxes in these bands suggests a common origin. This agrees with the results presented in Chapter 3 which were interpreted as a jet producing radio emission via synchrotron and X-ray emission via SSC. No correlation was found between the radio and X-ray fluxes in radio-quiet objects, contrary to the expectation from the literature. However, the sample consists of very few sources with a radio detection (not an upper limit) that are radio quiet. Radio emission is shown to be a poor indicator of the emission at other frequencies by the average SED which has a large dispersion when normalised at radio frequencies, and the lack of any significant correlations with the radio flux (except in the case of hard X-rays for RLQ). This supports the interpretation that the radio emission is unrelated to the majority of the SED and is due to an additional component.

When the average SED is normalised at X-ray wavelengths, there is a large dispersion in the rest of the SED, implying the X-ray emission is not a good indicator of the emission at other frequencies. This suggests that there is a much larger spread in the X-ray emission properties of AGN than there is in the IR-UV properties. This could indicate the accretion processes occurring in the central regions close to the black hole can vary substantially, but

the emission from the accretion disc and torus are generally similar for all AGN. If the X-ray emission is a poor indicator of the emission in the rest of the SED, then it is unlikely to be a good estimator of L_{bol} . This issue was first discussed in Chapter 3, when different results were found depending on whether the X-ray or optical emission was used in the estimation of the Eddington ratio.

In this Chapter, α_{OX} is found to be flatter in sources with a higher X-ray derived Eddington ratio, but is steeper in sources with a higher optically derived Eddington ratio. Sources with a high $\lambda_{\text{Edd,O}}$, including NLS1s, show an increased BBB emission, which does not appear to have a dependence on Γ . α_{OX} is flatter in low L_X sources, likely as a result of the non-linear relationship between the amount of optical and X-ray emission. This was quantified as $F_{1\text{keV}} \propto F_{2316\text{\AA}}^{0.8 \pm 0.2}$ by taking values from mean SEDs of sources binned by L_X , and $F_{1\text{keV}} \propto F_{2316\text{\AA}}^{1.00 \pm 0.03}$ from a flux correlation of individual sources.

7

Conclusions

In this thesis the spectral properties of a large sample of type 1 AGN were studied. In Chapter 3, the X-ray spectral properties were presented, with an emphasis on the distribution of best-fitting spectral indices and their dependence on physical parameters such as z , L_X and λ_{Edd} . Sources with unusually flat or steep spectral slopes were investigated further in Chapter 4. Sources which required additional spectral components such as absorption or a soft excess in their spectral modelling were also discussed, and in Chapter 5 the detectability of these components was quantified using simulated spectra. In Chapter 6, the sample was cross-correlated with multiwavelength catalogues. Correlations between fluxes in different wavebands were considered, and SEDs for each object were created. Variations in the average SED shape with physical parameters were qualitatively discussed. A summary of the main conclusions from this thesis are listed below.

7.1 Summary

1. The 0.5 – 12.0 keV X-ray spectrum of a typical, optically classified type 1 AGN, can be described with a power law plus a soft excess. The spectral index of the power law is typically $\langle \Gamma \rangle = 1.99 \pm 0.01$ and if the soft excess is modelled with a blackbody component, its typical temperature is $\langle kT \rangle = 0.17 \pm 0.09$ keV. The luminosity in these separate spectral components is strongly correlated, with the soft excess luminosity being $\sim 10 - 50\%$ that of the power-law luminosity. This supports a scenario where the soft excess is related to the disc emission and a constant fraction is upscattered to create the X-ray power law.
2. Investigating observational correlations between Γ and physical parameters can provide important constraints for theoretical emission models. A marginal trend for flatter Γ values in higher redshift sources is found when just the sources fit with a simple power-law model are considered. No significant trend is found when considering the full sample which suggests there is no variation in the accretion process with cosmic time. The presence of an unmodelled reflection component in the spectra at high energies is ruled out as a possible cause of the marginal trend observed. A strong trend for flatter Γ values in sources with a higher L_X is observed. As the sample is flux limited, the trend with redshift may simply be a consequence of the trend with L_X . However, when the sample is split into 3 broad redshift bins ($z < 1$, $1 < z < 1.5$, $z > 1.5$) the anti-correlation with L_X is still present.
3. A positive correlation between Γ and λ_{Edd} is also found for the sample suggesting that steeper spectral slopes are a result of greater accretion rates. This implies a strong connection between the accretion rate and the physical conditions in the corona where the X-ray power-law emission is produced, and could help to constrain its geometry and size. However, the calculation of λ_{Edd} relies on black hole mass estimates, determined virially using the width of broad emission lines. The correlation between Γ and λ_{Edd} switches direction depending on which of these lines is used, being positive for H β and negative for CIV. This could be due to a poorer calibration of the CIV line as a mass

estimator, or because CIV is affected by outflowing disc winds and does not accurately represent the virial velocity of the BLR clouds. Alternatively, it could be related to the different redshift of the source sub-samples for which the different lines are used. The correlations also change if the optical luminosity rather than L_X is used to estimate the bolometric luminosity. This suggests that in order to determine an accurate estimate of L_{bol} , a complete SED modelling should be used, rather than relying on generalised bolometric correction factors, which give apparently different results.

4. Although the typical spectral index of the sources is $\Gamma \sim 2$, there is a real intrinsic dispersion on this value of $\sigma_{\langle\Gamma\rangle} = 0.30 \pm 0.01$, which is not simply due to the typical measurement errors ($\Delta\Gamma = 0.13$). Extremely flat, $\Gamma < 1.54$, or steep, $\Gamma > 2.44$, power-law slopes were found in 109 sources. Of these, $\sim 55\%$ can be explained using a more complex spectral model including ionised or partially covering absorption, or by forcing the inclusion of a soft excess which was not detected originally due to the low number of counts in the spectra. A further $\sim 20\%$ of the extreme sources are RLQ, NLS1 or BALQSO, all known to display unusual X-ray spectral slopes. However, $\sim 3\%$ of the original sample are shown to have intrinsically extreme power-law slopes that cannot be explained by other means. This is important for theories of the power-law production method which must be able to explain why the most common spectral index is 2.0, but also why sources can have values as flat as ~ 1.0 and as steep as ~ 3.0 , and why the dispersion of values is symmetric about the mean. The ‘cascade’ models in which scattered photons become the seeds for further interactions, can only explain Γ values up to a limiting value with an asymmetric distribution of values.
5. A soft excess, modelled as a blackbody component, was detected in $\sim 8\%$ of the sample. However, this is a lower limit on the true number of sources which include the component, as its detectability is heavily dependent on redshift and the quality of the spectra. By simulating spectra with typical shapes, these effects were taken into account and an intrinsic occurrence rate of $75 \pm 23\%$ was determined. A soft excess component with a similar kT and normalisation ratio was also recovered in a joint fitting of several low count spectra with no previous evidence for the component. This suggests that

soft excesses are a ubiquitous feature in the X-ray spectra of type 1 AGN. This requires that any theories about its physical origin must be applicable to sources with a range of luminosities, accretion rates and spectral parameters. The blackbody temperature used to model the soft excess correlates with L_X . This perhaps suggests that the soft excess is related to the disc since $T_{\text{disc}} \propto M^{-1/4}(L/L_{\text{Edd}})^{1/4}$ and is created by a non-thermal Compton up-scattering. Despite the strong link between the luminosities in the power law and the soft excess, the power-law emission is correlated with the Eddington ratio, but the soft excess properties kT and L_{bb} are not. This may be because the corona, in which the power-law emission is produced, is closer to the black hole and may therefore be more sensitive to changes in the accretion rate than portions of the disc further away, where the soft excess could be produced.

6. Whilst the majority of the sample appear to have very similar spectral properties, there are some sources with notable differences. 3.4% of the sample require an intrinsic cold absorption component in the modelling of their X-ray spectra, in addition to the Galactic component, which is unexpected according to the standard, orientation based Unified Model. The typical column densities are $N_{\text{H}} = 10^{21} - 10^{23} \text{ cm}^{-2}$ and no trend is present between $N_{\text{H}}^{\text{intr}}$ and z or L_X . There is also no change in the fraction of absorbed sources with z or L_X , suggesting the absorption may be of a different nature to that in type 2 i.e. not the standard torus. It could be due to clumpy torus clouds, the broad line region clouds, a warped accretion disc or an outflow; 19% of the absorbed sources were identified as BALQSOs, sources likely being viewed through an outflowing wind. In addition to the sources with a measured $N_{\text{H}}^{\text{intr}}$, other mis-matches between the optical and X-ray classifications were found. SRCID 82106 has a flat X-ray spectrum, suggesting possible X-ray absorption, but has a very blue optical spectrum. Three sources (SRCIDs 27218, 84741 and 210692) were identified with very steep X-ray spectra, but red optical spectra, showing the reverse scenario. The ability to detect an additional absorption component in the spectra is not as heavily dependent on the number of counts as in the case of the soft excess. In spectra with ~ 200 counts an absorber with $N_{\text{H}} = 5 \times 10^{21} \text{ cm}^{-2}$ (at $z = 0$) can be detected $\sim 100\%$ of the time.

7. The sample includes 72% confirmed radio-quiet AGN and 10% radio-loud AGN. In general, radio-loud AGN appear to be very similar to their radio-quiet counterparts, apart from emission related to their jet. The mean SEDs of RQ and RL sub-samples are very similar over the IR-UV frequency range, but with a significant increase in both the radio and X-ray emission for the RL sources. This naturally results in a flatter α_{OX} parameter. The distributions of z and M_i are the same for RQ and RL sources, but the RL sources show higher L_X values. A correlation between the X-ray and radio flux is also present in RL sources but not RQ sources. This all suggests that an additional X-ray component is present in RL sources and is likely to be related to the radio jet. This component also ‘contaminates’ the original power-law emission, giving the flatter Γ values seen in RL sources. There is no significant trend between the radio loudness parameter and Γ or L_X .
8. Mean SEDs of sub-samples of sources with different physical characteristics were created. In sources with higher L_X , α_{OX} is steeper as a consequence of the non-linear relationship between the X-ray and optical emission. α_{OX} is also steeper in sources with a high optically derived Eddington ratio, this time as a result of an increased flux in the Big Blue Bump. The peak of the BBB emission does not have any dependence on the average Γ value of the sub-samples. In general, the IR-UV portion of the SED is reasonably similar between sources, as shown by the low dispersion generated in the rest of the SED when the fluxes are normalised at either MIR or optical frequencies. There is a much larger dispersion created when the normalisation is done at X-ray frequencies. This suggests that a wider variation in X-ray emission properties are present in the sources, but the disc and torus emission are reasonably similar for all. This could be because the X-ray emission is generated in the very inner regions of the AGN and is therefore more sensitive to changes in physical parameters than the outer regions of the accretion disc and if the IR emission is simply re-processed primary emission, such dependencies may have been eliminated.

7.2 Future Work

The sample studied in this thesis includes 761 type 1 AGN with an X-ray spectrum of sufficient quality for spectral modelling. This is the largest such sample to date, but despite this, much of the analysis presented would benefit from an even larger sample of objects. When sub-sets of the sample are required, e.g. when the sample is binned by redshift, or just those with a detected soft excess are considered, the number of objects falls significantly. Although such sources are inherently unlikely to be observed serendipitously, starting with a larger initial sample will be an advantage. 3XMM, the updated serendipitous source catalogue is due for release at the end of 2012 and is expected to contain $\sim 330,000$ unique X-ray sources. An updated quasar catalogue based on the SDSS DR7 data is already available and contains 105,783 objects (Schneider et al., 2010) for which virially determined black hole mass estimates are available (Shen et al., 2011). However, whilst the *XMM-Newton* sources are distributed over the entire sky, the SDSS footprint only covers $\sim 30\%$ in the northern hemisphere. In order to create the largest samples possible, optical surveys covering the whole sky are required. Pan-STARRS (Panoramic Survey Telescope & Rapid Response System; Kaiser et al. 2010), a ground-based automated telescope which will image $30,000 \text{ deg}^2$ of sky 3 times in each lunar cycle, will begin to resolve this issue. Using even larger samples could help to confirm the conclusions found in this thesis by improving the statistics.

This thesis has largely focused on the X-ray spectral properties of the sources, but each has an optical spectrum and photometry from SDSS, making a more detailed study of the optical properties possible. In particular the α_{OX} parameter could be determined for each individual source, and its dependence on z , L_{X} and λ_{Edd} could be investigated. This would require a careful consideration of the completeness of the sample as currently only sources with > 75 X-ray counts are included in the analysis, imposing a bias against X-ray weak sources. The original cross-correlation gave a sample of 1281 unique AGN. 81 of these were removed in the X-ray screening process, but for 203 an X-ray spectrum with < 30 counts was generated (although not fit) and 237 have an X-ray spectrum with $30 - 75$ counts which can be fit with spectral models in which Γ is a fixed parameter. Using FLIX¹, X-ray upper limits have been

¹<http://www.ledas.ac.uk/flix/flix.html>

obtained for a further 253 sources which are included in the optical catalogue and although they do not appear in 2XMMi, their positions are covered by an *XMM-Newton* observation.

The work detailed in Chapter 6 created a unique data set of 761 type 1 AGN with both X-ray and optical spectra, and photometry in up to 8 additional bands including MIR, NIR and radio. Virially determined mass estimates are also available for $\sim 80\%$ of the sources. A comprehensive SED modelling could be carried out in order to estimate the bolometric luminosity of each object directly. As this would provide a more accurate determination of λ_{Edd} , it would help to confirm the trends with this parameter which were found to vary depending on which waveband had been used in the estimation of L_{bol} . However, the SEDs presented were constructed from non-contemporaneous observations where in some cases the data in different wavebands was taken many years apart. Since AGN are known to display intrinsic long-term variability, the SEDs may be constructed from data points taken when the intrinsic SED shape of the sources was different. Ideally, simultaneous measurements would be used to create a SED which represents a true snapshot of the source at one particular time. *Astrosat* (Agrawal, 2006), due for launch in 2013 will be able to provide simultaneous measurements and monitoring over a broad spectral range covering optical to hard X-rays (1300 Å to 150 keV).

It is necessary to study complete broadband SEDs in order to understand the relationships between the emission at each frequency. However, the emission mechanisms within the AGN depend of a number of parameters (such as z , L_X , λ_{Edd}) which all depend on each other. A Principle Component Analysis (PCA; Francis & Wills 1999) could be used in order to reduce the data set to one described by a smaller number of uncorrelated variables, as was done for 2MASS AGN by Kuraszkiewicz et al. (2009). In order to better understand the causal connections between different stages in the accretion process, interband time lags could be studied.

One particularly important part of the AGN emission is that of the X-ray power-law, thought to be produced in the very central regions near the black hole. Understanding its production mechanism is therefore an important step for further understanding the accretion process. The spectral shape of the emission depends on the optical depth and temperature of the electrons in the plasma but these two quantities cannot be determined independently

without spectra at higher energies. *NuSTAR* (Harrison et al., 2010), expected to launch in June 2012², will be the first focusing hard X-ray mission and will be able to help solve this problem by providing spectra at higher energies, which are required in order to break the degeneracy.

This thesis has reported studies of the X-ray and broadband spectral properties of type 1 AGN. Such research is capable of improving our understanding of the accretion process and the nature of the emission produced. This is important in order to understand the relationship between AGN and their host galaxies, leading to a fundamental understanding of galaxy evolution.

²Successfully launched 13/06/12.



Spectral Fitting Results

Table A.1 contains the results of the spectral fitting of 761 sources from the SDSS/2XMMi sample as described in Chapter 3. It includes the following columns:

1. SRCID as listed in the 2XMMi catalogue
2. SDSS designation as given in the DR5 quasar catalogue
3. Spectroscopic redshift taken from the the quasar catalogue
4. Galactic hydrogen column density in units of 10^{20} cm^{-2} taken from Dickey & Lockman (1990)
5. Photon index, Γ , with 90% errors, from the best-fitting model fit over 0.5 – 12.0 keV
6. Intrinsic N_{H} (in units of 10^{22} cm^{-2}) for sources best fit with the apo model
7. Blackbody temperature, kT, (in units of keV) for the sources best fit with the po+bb model
8. Reduced χ^2
9. Null hypothesis probability (if > 1.0 the fit is taken to be acceptable)
10. Log of the unabsorbed X-ray luminosity in the 2 – 10 keV rest-frame band
11. Best-fitting spectral model
12. MOS and pn counts in the 0.5 – 12.0 keV spectra

Appendix A. Spectral Fitting Results

SRCID	SDSS name	z	$N_{\text{H}}^{\text{Gal}}$ ($\times 10^{20} \text{ cm}^{-2}$)	Γ	$N_{\text{H}}^{\text{intr}}$ ($\times 10^{22} \text{ cm}^{-2}$)	KT (keV)	χ^2/ν	H0	$\log(L_X)$ ($2 - 10 \text{ keV}$)	Model	Counts	
											MOS	pn
5256	003922.44+005951.7	1.989	0.023	$1.91^{+0.15}_{-0.13}$			10.2/18	92.4	44.72	po	123	38
5308	003940.23+004241.5	1.701	0.022	1.47 ± 0.13		0.18 ± 0.04	18.0/26	87.4	44.69	po+bb	142	167
5756	004149.64-094705.0	1.620	0.030	$1.94^{+0.12}_{-0.11}$			27.3/16	3.9	45.29	po	254	
5790	004156.17-094859.8	1.163	0.030	$2.14^{+0.14}_{-0.12}$			21.5/27	76.4	44.61	po	144	123
6107	004247.15+010019.3	1.111	0.023	$2.39^{+0.14}_{-0.12}$			19.3/21	56.6	44.36	po	104	180
6132	004250.54+010205.9	0.600	0.023	$2.39^{+0.11}_{-0.10}$			17.3/26	89.9	43.88	po	182	214
6174	004254.48+005916.5	1.223	0.023	$2.18^{+0.19}_{-0.16}$			11.8/14	62.4	44.20	po	65	89
6184	004255.48+005622.7	1.576	0.023	$1.95^{+0.14}_{-0.13}$			23.7/18	16.5	44.46	po	70	109
6305	004312.70+005605.0	0.902	0.023	1.84 ± 0.07			62.7/39	0.9	44.49	po		578
6351	004319.73+005115.4	0.308	0.023	$1.73^{+0.03}_{-0.04}$		$0.21^{+0.02}_{-0.03}$	371.2/400	84.7	44.44	po+bb	5878	7909
6481	004338.10+004615.9	1.574	0.023	$1.66^{+0.09}_{-0.08}$			13.5/26	97.9	44.74	po	143	192
6501	004341.24+005253.3	0.834	0.023	$1.76^{+0.21}_{-0.17}$	$1.87^{+0.57}_{-0.41}$		8.9/11	63.3	44.28	apo		184
6504	004341.48+005610.0	0.830	0.023	1.84 ± 0.05			66.7/71	62.2	44.60	po	510	549
6510	004342.79+004841.7	0.913	0.023	$1.68^{+0.18}_{-0.16}$			10.2/10	42.6	43.88	po		97
6658	004413.72+005141.0	0.941	0.023	2.04 ± 0.09			24.3/28	66.5	44.55	po	187	228
8536	005548.84+002939.4	0.448	0.028	$2.73^{+0.09}_{-0.08}$			39.6/39	44.4	43.71	po	221	346
10534	010543.51+004003.8	1.074	0.032	$1.87^{+0.21}_{-0.18}$			7.7/7	36.1	44.95	po	36	62
10693	010634.15+140629.7	1.498	0.039	$1.85^{+0.16}_{-0.14}$			15.5/19	69.1	44.49	po	85	76
12003	011824.28-010832.0	0.966	0.035	$2.64^{+0.25}_{-0.20}$			15.0/12	24.2	44.08	po	47	81
12211	012025.29-105439.0	1.339	0.033	$2.07^{+0.12}_{-0.11}$			10.9/21	96.5	44.87	po	123	108
14766	014251.74+133352.6	1.075	0.049	1.83 ± 0.08			14.4/27	97.7	44.68	po	245	124
15526	014814.03+140853.2	0.373	0.051	$1.49^{+0.20}_{-0.21}$		0.17 ± 0.03	7.6/16	96.0	44.23	po+bb	304	
15698	015202.93+010445.2	1.052	0.028	$1.90^{+0.11}_{-0.10}$			23.1/27	68.1	44.40	po	127	127
15858	015245.80+011104.6	1.663	0.028	$1.83^{+0.14}_{-0.13}$			8.7/16	92.4	44.79	po	76	80
15896	015254.04+010434.6	0.570	0.028	2.13 ± 0.08			28.2/36	81.8	43.83	po	242	282
15920	015258.66+010507.4	0.647	0.028	$2.20^{+0.15}_{-0.13}$			24.5/19	17.6	43.78	po	35	235
15981	015509.12+005250.1	1.161	0.028	$2.50^{+0.20}_{-0.17}$			7.4/11	76.7	44.15	po	52	66
16005	015513.28+005307.3	1.399	0.028	$1.96^{+0.19}_{-0.16}$			11.1/9	27.0	44.34	po	48	42
16097	015335.63+010353.5	1.618	0.028	$1.91^{+0.11}_{-0.10}$			12.9/24	96.8	45.08	po	130	107
16314	015653.16-004623.2	0.615	0.026	$2.08^{+0.18}_{-0.16}$			16.4/13	22.8	44.05	po	90	55
16413	015722.81-004254.3	0.770	0.026	$2.56^{+0.17}_{-0.15}$			14.3/15	50.2	44.18	po	66	99
16480	015733.87-004824.4	1.545	0.026	$2.26^{+0.18}_{-0.15}$			8.6/11	66.3	44.84	po	58	65

Appendix A. Spectral Fitting Results

SRCID	SDSS name	z	$N_{\text{H}}^{\text{Gal}}$ ($\times 10^{20} \text{ cm}^{-2}$)	Γ	$N_{\text{H}}^{\text{intr}}$ ($\times 10^{22} \text{ cm}^{-2}$)	KT (keV)	χ^2/ν	H0	$\log(L_X)$ ($2 - 10 \text{ keV}$)	Model	Counts	
											MOS	pn
16706	015950.24+002340.8	0.163	0.026	2.32 ± 0.02			212.5/239	89.0	43.81	po	3203	3227
16712	015957.63+003310.4	0.312	0.026	1.97 ± 0.06			72.7/61	14.6	43.99	po	493	463
16734	020011.52-093126.1	0.361	0.020	1.43 ± 0.04			110.9/83	2.2	44.21	po	856	430
16840	020118.67-091935.7	0.661	0.020	2.07 ± 0.05			141.0/98	0.3	44.36	po	778	722
17608	021000.22-100354.2	1.960	0.022	$1.50^{+0.12}_{-0.11}$			7.6/9	57.4	45.36	po	152	
17701	021100.83-095138.4	0.767	0.022	$2.19^{+0.12}_{-0.11}$			13.4/21	89.5	44.22	po	108	160
17917	021416.95-005229.1	1.796	0.027	1.96 ± 0.11			22.0/20	34.0	44.64	po	264	
17925	021419.62-004215.8	0.972	0.027	$2.19^{+0.13}_{-0.12}$			17.3/18	50.1	44.02	po	265	
17942	021425.69-003859.6	1.726	0.027	$1.90^{+0.07}_{-0.06}$			48.3/43	26.8	44.83	po	627	
17970	021434.78-004242.6	0.437	0.027	2.34 ± 0.04			135.0/97	0.7	43.93	po	2369	
17998	021449.10-005040.9	1.598	0.027	$2.59^{+0.25}_{-0.22}$			14.9/18	66.8	44.03	po	134	
18038	021510.26-003640.4	1.536	0.027	$2.09^{+0.11}_{-0.10}$			27.3/30	60.5	44.71	po	397	
18039	021510.51-004802.2	1.648	0.027	$1.87^{+0.24}_{-0.21}$			11.5/15	71.6	44.20	po	117	
18047	021514.83-003905.0	0.847	0.027	2.14 ± 0.09			25.9/35	86.8	44.11	po	485	
23644	023025.02-004944.1	0.654	0.028	$1.75^{+0.08}_{-0.07}$			28.9/33	67.1	44.40	po	244	246
23731	023057.39-010033.5	0.650	0.028	2.37 ± 0.09			55.1/42	8.4	43.83	po	262	361
23770	023108.49-071824.0	1.874	0.029	$2.14^{+0.24}_{-0.21}$			5.1/8	74.8	44.64	po	83	
23792	023114.93-011002.0	1.275	0.028	$2.08^{+0.13}_{-0.12}$			25.4/22	27.7	44.53	po	104	113
23880	023137.65-072854.4	5.413	0.031	$1.88^{+0.14}_{-0.12}$			22.2/27	72.6	45.35	po	116	124
23917	023148.80-073906.3	2.508	0.031	$1.95^{+0.11}_{-0.10}$			27.0/27	46.2	44.94	po	116	183
24012	023230.42-072644.2	2.551	0.031	1.85 ± 0.10			19.3/27	85.9	45.17	po	131	168
24017	023234.39-073103.6	0.697	0.031	$2.18^{+0.08}_{-0.07}$			53.2/43	13.6	44.30	po		604
24074	023402.08-084314.6	1.264	0.028	$1.96^{+0.13}_{-0.12}$			13.9/13	37.8	44.60	po	196	
24188	023451.43-084005.1	1.608	0.029	$2.57^{+0.28}_{-0.23}$			9.8/8	28.2	44.29	po	84	
25177	024040.82-081309.9	1.844	0.031	2.06 ± 0.08			27.5/41	94.8	44.34	po	209	279
25252	024055.81-081953.3	1.802	0.031	$1.98^{+0.07}_{-0.06}$			74.3/69	31.0	44.46	po	369	520
25302	024105.83-081153.1	0.979	0.031	2.14 ± 0.06			51.4/63	85.2	43.91	po	505	344
25387	024125.89-080935.8	3.077	0.031	$1.79^{+0.13}_{-0.12}$			25.9/30	67.9	44.69	po	77	147
25486	024149.98-000433.8	1.260	0.034	$1.89^{+0.11}_{-0.10}$			24.7/28	64.4	44.32	po	159	205
25518	024157.15+000703.5	1.564	0.034	$1.93^{+0.16}_{-0.15}$			6.9/11	80.9	44.57	po	160	
25532	024200.91+000021.0	1.104	0.034	1.94 ± 0.03			170.4/191	85.5	44.85	po	1194	1798
25547	024204.76+000814.5	0.382	0.035	$2.24^{+0.15}_{-0.13}$			17.2/10	7.0	43.17	po	157	

Appendix A. Spectral Fitting Results

SRCID	SDSS name	z	$N_{\text{H}}^{\text{Gal}}$ ($\times 10^{20} \text{ cm}^{-2}$)	Γ	$N_{\text{H}}^{\text{intr}}$ ($\times 10^{22} \text{ cm}^{-2}$)	KT (keV)	χ^2/ν	H0	$\log(L_X)$ ($2 - 10 \text{ keV}$)	Model	Counts	
											MOS	pn
25560	024207.27+000038.7	0.384	0.035	2.40 ± 0.04			150.2/137	20.8	43.34	po	839	1232
25596	024214.99-000209.5	1.012	0.035	$2.07^{+0.13}_{-0.12}$			11.2/17	84.8	43.93	po	223	
25640	024227.34+000845.4	0.650	0.035	$2.40^{+0.11}_{-0.10}$			23.1/21	33.9	43.55	po	303	
25748	024251.01+001010.9	1.883	0.035	1.73 ± 0.08			24.4/32	82.9	45.03	po	473	
25804	024304.68+000005.4	1.995	0.036	$1.82^{+0.15}_{-0.13}$	$4.93^{+1.73}_{-1.34}$		44.9/33	8.1	45.03	apo	489	
25809	024308.18-000127.0	0.679	0.036	1.91 ± 0.07			37.3/47	84.4	43.54	po	288	323
26678	025528.92-000219.2	1.436	0.064	$1.69^{+0.22}_{-0.19}$			1.9/6	93.2	44.50	po	63	18
26739	025606.03+001634.8	0.627	0.065	$2.08^{+0.17}_{-0.15}$			24.5/21	27.2	43.94	po	115	103
26797	025644.69+001246.0	2.251	0.067	$2.28^{+0.17}_{-0.15}$			8.5/13	80.8	44.97	po	92	43
26804	025650.74+001334.5	1.349	0.067	$1.89^{+0.23}_{-0.19}$			6.5/7	48.7	44.36	po	58	31
26829	025725.08+000114.3	1.248	0.067	$1.64^{+0.19}_{-0.17}$			3.5/7	83.1	44.70	po	35	57
27193	030206.76-000121.3	0.645	0.072	1.85 ± 0.03			155.0/175	85.9	44.53	po	1542	1380
27207	030214.82+000125.3	1.179	0.072	$1.96^{+0.16}_{-0.15}$			5.7/10	84.1	44.15	po	155	
27218	030220.46+001937.4	0.774	0.071	$2.75^{+0.24}_{-0.20}$	$0.72^{+0.26}_{-0.21}$		18.9/22	65.0	43.84	apo	171	171
27224	030222.08+000631.0	3.315	0.072	1.38 ± 0.09			16.9/25	88.7	44.97	po	153	143
27265	030238.16+000203.4	1.349	0.072	$1.69^{+0.16}_{-0.14}$	$1.96^{+0.71}_{-0.54}$		31.4/26	21.2	44.41	apo	97	257
27329	030307.36+001020.4	1.047	0.071	2.15 ± 0.06			69.3/67	39.9	44.41	po	411	570
27335	030309.39-011321.7	1.038	0.071	$2.18^{+0.35}_{-0.26}$			13.9/8	8.4	43.96	po	54	41
27454	030357.45-010907.4	1.520	0.071	$1.90^{+0.09}_{-0.08}$			32.9/30	32.8	44.83	po	186	277
27531	030449.85-000813.4	3.295	0.070	$2.24^{+0.21}_{-0.19}$			12.3/10	26.5	45.74	po	110	
27708	030627.50-001816.3	1.538	0.069	$2.01^{+0.09}_{-0.08}$			41.0/39	38.2	44.87	po	337	205
27747	030639.63+000723.9	2.172	0.070	$2.18^{+0.18}_{-0.16}$			16.2/20	70.4	44.45	po	62	110
27753	030641.67+00108.1	1.397	0.069	2.14 ± 0.09			26.4/36	88.1	44.21	po	210	249
27837	030707.40-000424.0	0.664	0.069	$2.33^{+0.06}_{-0.05}$			111.8/96	12.9	43.83	po	658	668
32486	033639.50+002555.3	1.679	0.080	$2.07^{+0.05}_{-0.04}$			141.4/125	14.9	44.86	po	988	819
32720	033654.24+004016.0	2.638	0.083	1.93 ± 0.06			55.2/62	71.7	45.24	po	401	426
32794	033701.11+004314.0	1.992	0.083	$1.67^{+0.13}_{-0.12}$			24.6/29	70.1	44.37	po	122	123
32863	033711.66+004343.7	1.918	0.083	$2.04^{+0.22}_{-0.19}$			6.5/11	84.0	44.16	po	59	38
32890	033718.81+003303.7	0.437	0.082	1.10 ± 0.06			71.9/56	7.5	43.19	po	330	301
33050	033746.72+003509.8	1.398	0.083	$1.62^{+0.15}_{-0.13}$			11.7/20	92.7	44.22	po	75	90
33080	033754.15+002934.9	2.017	0.082	$1.74^{+0.11}_{-0.10}$			25.3/31	75.2	44.93	po	220	179
33139	033801.88+002718.8	1.583	0.082	$2.14^{+0.22}_{-0.19}$			6.8/14	94.2	44.47	po	63	70

Appendix A. Spectral Fitting Results

SRCID	SDSS name	z	$N_{\text{H}}^{\text{Gal}}$ ($\times 10^{20} \text{ cm}^{-2}$)	Γ	$N_{\text{H}}^{\text{intr}}$ ($\times 10^{22} \text{ cm}^{-2}$)	KT (keV)	χ^2/ν	H0	$\log(L_X)$ ($2 - 10 \text{ keV}$)	Model	Counts	
											MOS	pn
33162	033805.90+003544.8	0.983	0.083	$2.78^{+0.13}_{-0.12}$			31.0/31	46.4	44.22	po	208	206
33180	033810.16+002325.1	1.120	0.081	$2.30^{+0.09}_{-0.08}$			35.4/38	59.1	44.43	po	238	282
33182	033810.57+001854.8	2.587	0.080	$2.46^{+0.19}_{-0.17}$			18.8/17	34.2	44.90	po	72	88
33229	033818.71+001153.6	1.592	0.079	$2.19^{+0.17}_{-0.15}$			31.6/25	17.0	44.64	po	115	110
33281	033828.20+001951.8	2.037	0.081	$2.23^{+0.19}_{-0.17}$			24.6/22	31.9	44.63	po	95	99
33373	033842.62+002128.4	2.236	0.081	$1.67^{+0.12}_{-0.11}$			14.5/21	84.5	45.10	po	195	71
33469	033908.27+002924.9	1.488	0.083	$1.66^{+0.27}_{-0.24}$			6.0/7	53.8	45.04	po	78	
33479	033910.48+002916.6	0.537	0.083	$3.12^{+0.43}_{-0.33}$			12.3/9	19.9	43.03	po	29	56
34689	035255.57+000102.2	0.549	0.118	$2.12^{+0.13}_{-0.13}$			14.6/14	40.5	43.90	po	163	48
61832	073601.47+434455.3	1.814	0.059	$2.29^{+0.17}_{-0.15}$			11.3/12	50.2	44.83	po	190	
62350	074020.22+311841.2	0.296	0.041	$3.34^{+0.22}_{-0.20}$			16.6/13	21.6	43.56	po	199	
62413	074110.70+311200.2	0.631	0.041	1.81 ± 0.07			32.7/30	33.5	44.98	po	478	
62504	074222.34+494147.2	0.927	0.057	$1.69^{+0.10}_{-0.11}$			84.0/103	91.4	44.56	po+bb	1749	
62514	074227.83+290000.4	1.132	0.041	$1.59^{+0.16}_{-0.15}$		$0.30^{+0.02}_{-0.03}$	10.0/17	90.3	44.63	po+bb	280	
63837	075148.46+501711.8	0.792	0.051	$2.38^{+0.18}_{-0.15}$			28.7/21	12.1	43.91	po	81	121
63872	075216.55+500251.3	0.263	0.051	$1.63^{+0.11}_{-0.12}$		$0.14^{+0.02}_{-0.02}$	51.4/56	64.8	43.89	po+bb	431	461
63910	075429.52+215908.3	1.066	0.055	$2.22^{+0.16}_{-0.15}$			11.6/11	39.3	44.29	po	171	
63950	075524.85+215333.8	1.551	0.055	$1.88^{+0.17}_{-0.16}$			5.0/7	66.4	44.90	po	83	
63968	075547.84+220450.1	2.319	0.055	$2.42^{+0.21}_{-0.18}$			2.2/8	97.3	45.15	po	86	
65229	080608.13+244421.0	0.358	0.039	2.35 ± 0.04			148.0/156	66.5	43.93	po	1263	1366
65479	080711.01+390419.7	0.369	0.052	2.00 ± 0.05			67.4/75	72.1	44.15	po	571	630
65668	080844.12+385053.4	0.765	0.051	$2.03^{+0.17}_{-0.15}$			15.9/10	10.2	44.84	po		168
66076	081014.48+280337.1	0.821	0.037	2.11 ± 0.04			132.4/131	44.8	44.90	po	1053	1050
66136	081030.32+281325.9	0.887	0.037	2.21 ± 0.07			51.3/48	34.7	44.36	po	336	347
66276	081103.27+281621.0	3.369	0.037	$1.83^{+0.31}_{-0.26}$			18.4/9	3.1	44.86	po	36	46
66292	081108.60+280500.6	1.560	0.037	$2.20^{+0.23}_{-0.18}$			21.6/19	30.2	44.25	po	80	86
66511	081422.12+514839.4	0.377	0.044	2.15 ± 0.03			189.6/165	9.2	44.35	po	1373	1505
67460	082257.55+404149.7	0.865	0.048	1.90 ± 0.05			83.7/76	25.6	44.89	po	495	636
67785	082718.92+264505.2	1.463	0.037	1.60 ± 0.07			34.1/28	19.8	44.92	po	419	
67793	082733.73+263715.9	0.688	0.037	2.05 ± 0.05			77.6/60	6.3	44.40	po	990	
67854	083103.01+523533.5	4.444	0.039	$1.88^{+0.31}_{-0.26}$			12.7/19	85.4	44.85	po	45	75
67939	083205.95+524359.3	1.572	0.038	1.97 ± 0.03			203.7/227	86.5	44.62	po	1689	2142

Appendix A. Spectral Fitting Results

SRCID	SDSS name	z	$N_{\text{H}}^{\text{Gal}}$ ($\times 10^{20} \text{ cm}^{-2}$)	Γ	$N_{\text{H}}^{\text{intr}}$ ($\times 10^{22} \text{ cm}^{-2}$)	KT (keV)	χ^2/ν	H0	$\log(L_X)$ ($2 - 10 \text{ keV}$)	Model	Counts MOS	pn
68220	083454.89+553421.1	0.241	0.041	$2.24^{+0.06}_{-0.05}$	0.17 ± 0.03		220.5/159	0.1	44.39	apo	2107	1303
68610	083633.54+553245.0	1.614	0.041	$1.41^{+0.15}_{-0.14}$			12.1/13	52.2	44.83	po	91	46
68846	083740.24+245423.1	1.125	0.036	1.87 ± 0.05			61.5/60	42.2	45.35	po	1021	
68864	083748.99+254412.9	1.912	0.036	$2.47^{+0.19}_{-0.17}$			6.2/10	79.4	44.97	po	104	
69876	084659.32+344825.1	1.582	0.033	2.00 ± 0.04			154.7/111	0.4	44.94	po	1354	355
69933	084710.19+345442.8	2.295	0.033	2.23 ± 0.09			30.9/33	57.4	44.85	po	436	17
70444	084905.07+445714.7	1.259	0.026	2.04 ± 0.05			94.5/93	43.6	44.36	po	425	805
70666	084943.70+450024.2	1.592	0.026	2.22 ± 0.07			62.0/57	30.3	44.56	po	370	343
71401	085522.87+375425.9	2.296	0.029	$2.23^{+0.31}_{-0.25}$			9.4/9	40.0	44.57	po	40	38
71445	085551.24+375752.2	1.929	0.029	1.60 ± 0.11			27.5/26	38.5	44.60	po	118	119
71470	085609.47+374928.8	2.570	0.030	$2.26^{+0.12}_{-0.11}$			20.4/25	72.6	45.09	po	117	162
71597	085723.99+090349.0	1.049	0.043	$1.85^{+0.36}_{-0.29}$	$9.76^{+3.59}_{-2.51}$		5.3/10	87.2	44.77	apo	74	55
71634	085735.43+085328.2	1.136	0.044	$0.99^{+0.17}_{-0.16}$			5.1/6	52.5	44.67	po	56	28
71793	085808.91+274522.7	1.090	0.031	2.05 ± 0.04			86.0/105	91.2	44.70	po	1843	
71980	085851.99+274738.2	1.599	0.031	$2.21^{+0.08}_{-0.07}$			53.3/51	38.6	44.56	po	284	370
72089	085935.15+390121.0	0.957	0.026	$2.17^{+0.24}_{-0.19}$			10.6/10	38.6	43.84	po	40	65
72205	090029.02+390145.2	0.964	0.026	$2.13^{+0.08}_{-0.07}$			41.4/34	18.0	44.64	po	541	
72929	091029.03+542719.0	0.526	0.021	2.23 ± 0.03			221.5/195	9.4	44.15	po		1760
73015	091127.61+055054.0	2.793	0.036	$1.75^{+0.12}_{-0.11}$			40.3/39	41.1	45.72	apo	430	103
73150	091301.03+525928.9	1.377	0.016	1.71 ± 0.01	$6.67^{+1.84}_{-1.51}$		388.9/394	56.3	45.87	po	5571	7036
73154	091302.74+530322.5	0.631	0.016	$0.43^{+0.12}_{-0.13}$			15.8/11	14.8	43.52	po	59	56
73222	091345.48+405628.2	0.442	0.018	1.95 ± 0.02	0.14 ± 0.02		469.5/419	4.4	45.06	apo+line	7065	8108
73299	091528.77+441632.8	1.489	0.015	$1.87^{+0.15}_{-0.13}$			7.6/12	81.6	45.40	po	72	62
73344	091617.53+303037.9	0.215	0.020	$1.87^{+0.04}_{-0.08}$		$0.07^{+0.02}_{-0.01}$	31.0/41	87.1	43.19	po+bb	106	501
74135	092053.77+365830.9	1.083	0.015	$1.67^{+0.11}_{-0.12}$		$0.30^{+0.03}_{-0.04}$	91.4/90	43.8	44.66	po+bb	601	726
74182	092104.36+302030.3	3.350	0.019	$1.57^{+0.16}_{-0.15}$			19.8/19	40.7	44.93	po	46	105
74500	092238.43+512121.2	1.753	0.014	$2.15^{+0.14}_{-0.13}$			13.0/21	91.0	44.56	po	142	51
74525	092247.02+512038.0	0.160	0.014	2.32 ± 0.06	0.14 ± 0.002		245.3/243	44.6	43.35	po+bb	8478	4680
74614	092314.48+510020.7	1.388	0.014	$2.26^{+0.24}_{-0.19}$			5.6/9	77.6	44.40	po	33	58
75084	092633.42+304535.3	1.309	0.019	1.98 ± 0.07			26.3/43	97.9	44.74	po	272	358
75175	092718.49+304538.9	0.527	0.019	$1.52^{+0.25}_{-0.21}$			30.0/13	0.5	43.89	po	132	
75454	093157.80+472720.4	1.277	0.014	$1.93^{+0.15}_{-0.13}$			7.6/16	96.1	44.62	po	70	100

Appendix A. Spectral Fitting Results

SRCID	SDSS name	z	$N_{\text{H}}^{\text{Gal}}$ ($\times 10^{20} \text{ cm}^{-2}$)	Γ	$N_{\text{H}}^{\text{intr}}$ ($\times 10^{22} \text{ cm}^{-2}$)	KT (keV)	χ^2/ν	H0	$\log(L_X)$ ($2 - 10 \text{ keV}$)	Model	MOS	Counts	pn
75475	093205.68+284343.9	1.167	0.020	$2.57^{+0.21}_{-0.17}$			32.7/22	6.6	44.38	po	112	94	
75555	093250.90+472255.0	0.878	0.014	1.79 ± 0.10			24.4/30	75.3	44.29	po	146	144	
75569	093255.45+284036.7	0.547	0.020	1.11 ± 0.07			42.7/35	17.4	44.73	po	544		
75574	093258.98+550433.4	1.513	0.019	$1.62^{+0.20}_{-0.18}$			13.1/12	36.5	44.43	po	110	144	
75633	093353.49+472925.0	0.369	0.014	$2.65^{+0.14}_{-0.12}$			21.6/25	66.1	43.38	po	108	144	
75640	093359.34+551550.7	1.863	0.019	1.82 ± 0.04			108.5/97	20.0	44.99	po	712	749	
75697	093458.31+611234.1	0.245	0.026	$1.23^{+0.21}_{-0.19}$	$2.53^{+0.67}_{-0.54}$		26.4/29	60.4	43.49	apo	225	196	
75731	093531.22+612902.0	1.866	0.027	$2.20^{+0.16}_{-0.15}$			23.3/28	71.7	44.57	po	103	132	
75737	093533.01+612738.6	0.475	0.027	$1.76^{+0.41}_{-0.32}$	$7.77^{+3.04}_{-1.93}$		24.1/18	15.1	43.77	apo	45	131	
75761	093555.39+551240.1	1.800	0.019	$1.84^{+0.20}_{-0.16}$			19.7/15	18.4	44.71	po		129	
75798	093639.12+611918.1	1.330	0.025	$1.56^{+0.12}_{-0.11}$			17.7/18	47.5	44.03	po	59	98	
75885	093922.89+370943.9	0.186	0.014	2.44 ± 0.11		0.15 ± 0.01	140.9/150	69.1	43.38	po+bb	1296	1634	
75936	093952.81+033610.0	0.987	0.036	$2.07^{+0.21}_{-0.19}$			7.3/11	77.8	44.22	po	109		
75997	094009.63+033041.8	0.616	0.037	$1.94^{+0.06}_{-0.05}$			70.0/58	13.5	44.22	po	274	616	
76012	094013.85+034804.0	1.380	0.037	$1.76^{+0.13}_{-0.11}$			8.2/15	91.7	44.86	po		210	
76019	094016.43+033424.2	1.675	0.037	$1.98^{+0.10}_{-0.09}$			34.5/32	35.1	44.64	po	145	229	
76154	094053.93+032442.7	1.326	0.038	$2.30^{+0.19}_{-0.17}$			11.7/14	63.2	44.52	po	138		
76195	094104.00+385351.0	0.616	0.015	1.68 ± 0.05		0.25 ± 0.02	128.3/133	59.8	44.82	po+bb	4451		
76393	094231.92+471121.3	1.789	0.013	$1.41^{+0.13}_{-0.12}$			17.0/17	45.3	44.48	po	71	83	
76595	094345.20+465154.6	1.246	0.012	$1.86^{+0.07}_{-0.06}$			32.6/41	82.2	44.44	po	258	297	
76659	094404.41+480646.6	0.392	0.012	2.15 ± 0.08		0.13 ± 0.01	188.1/175	23.6	43.66	po+bb	1495	1463	
76676	094410.91+475246.3	2.251	0.012	$2.03^{+0.23}_{-0.20}$			5.6/10	84.6	44.71	po	54	41	
76757	094438.00+035935.7	1.335	0.037	$1.73^{+0.11}_{-0.10}$			34.8/25	9.1	44.47	po	171	198	
76759	094439.88+034940.1	0.155	0.038	$1.75^{+0.07}_{-0.08}$		0.12 ± 0.01	178.0/159	14.4	43.26	po+bb	1178	1452	
76768	094446.36+040659.7	1.811	0.036	$2.42^{+0.21}_{-0.19}$			23.3/18	18.0	44.61	po	62	107	
77226	094949.46+392135.3	1.636	0.016	$1.93^{+0.19}_{-0.17}$			6.9/10	73.3	44.91	po	107		
77270	095048.38+392650.5	0.206	0.016	1.96 ± 0.02		0.17 ± 0.01	638.2/611	21.6	44.34	po+bb	15481	21596	
77296	095116.22+393340.4	1.334	0.016	$2.30^{+0.18}_{-0.17}$			15.9/11	14.4	44.54	po	173		
77392	095239.81+080715.6	0.545	0.030	$1.87^{+0.09}_{-0.08}$	$0.31^{+0.10}_{-0.08}$		57.8/65	72.5	44.22	apo	1053		
77440	095253.80+075040.3	1.468	0.030	$1.28^{+0.28}_{-0.23}$	$7.17^{+3.74}_{-2.20}$		7.3/12	83.4	44.62	apo	135		
77540	095521.89+074634.9	1.732	0.030	$2.17^{+0.10}_{-0.09}$			12.2/23	96.7	44.74	po	330		
77638	095552.69+080103.6	1.720	0.030	$1.67^{+0.17}_{-0.16}$			7.5/10	68.2	44.49	po	96		

Appendix A. Spectral Fitting Results

SRCID	SDSS name	z	$N_{\text{H}}^{\text{Gal}}$ ($\times 10^{20} \text{ cm}^{-2}$)	Γ	$N_{\text{H}}^{\text{intr}}$ ($\times 10^{22} \text{ cm}^{-2}$)	KT (keV)	χ^2/ν	H0	$\log(L_X)$ ($2 - 10 \text{ keV}$)	Model	Counts	
											MOS	pn
78393	095726.33+411628.7	1.701	0.011	$2.47^{+0.31}_{-0.25}$			4.3/7	74.9	44.25	po	25	56
78523	095754.11+0225508.4	1.569	0.028	$2.08^{+0.16}_{-0.14}$			12.4/17	77.6	44.40	po		141
78530	095755.09+024806.4	1.111	0.028	$1.97^{+0.08}_{-0.07}$			27.4/38	89.7	44.16	po	195	292
78610	095810.87+014005.1	2.102	0.028	$1.65^{+0.14}_{-0.12}$			20.9/23	58.6	44.77	po	113	94
78635	095815.50+014922.9	1.510	0.028	1.71 ± 0.03			172.6/162	27.0	45.14	po	602	2398
78656	095819.87+022903.5	0.345	0.027	1.91 ± 0.04			121.0/119	43.2	43.40	po	1283	605
78669	095821.65+024628.1	1.403	0.028	2.00 ± 0.04			163.2/132	3.4	44.72	po	759	1249
78672	095822.18+014524.1	1.960	0.028	$2.45^{+0.15}_{-0.13}$			49.0/46	35.5	44.88	apo	178	449
78736	095834.04+024427.1	1.888	0.027	2.06 ± 0.05	$2.10^{+0.61}_{-0.52}$		159.5/115	0.4	44.81	po	651	937
78803	095844.94+014309.0	1.337	0.027	$1.37^{+0.09}_{-0.08}$			40.3/31	12.3	44.05	po	111	207
78833	095848.86+023441.1	1.551	0.027	$2.05^{+0.06}_{-0.05}$			114.9/105	24.0	44.46	po	630	726
78851	095852.15+025156.3	1.407	0.027	$2.22^{+0.06}_{-0.05}$			70.7/92	95.2	44.59	po	511	708
78884	095857.34+021314.5	1.024	0.027	1.75 ± 0.02			313.5/316	53.0	44.96	po	3384	3786
78892	095858.68+020138.9	2.454	0.026	1.94 ± 0.05			73.2/83	76.9	45.11	po	639	479
78917	095902.76+021906.3	0.345	0.027	1.84 ± 0.02			283.5/287	54.8	43.94	po	6062	1844
78948	095908.31+024309.6	1.317	0.026	1.88 ± 0.03			186.4/199	72.9	45.14	po	3519	798
78951	095908.68+025423.9	1.556	0.027	$2.62^{+0.12}_{-0.11}$			40.5/35	24.1	44.64	po	197	254
79011	095918.70+020951.4	1.157	0.026	1.75 ± 0.02			213.0/245	93.1	44.91	po	2499	2829
79049	095924.46+015954.3	1.236	0.026	$2.22^{+0.04}_{-0.03}$			218.9/194	10.6	44.62	po	1151	1816
79231	095946.01+024743.5	1.067	0.026	2.07 ± 0.05			89.4/102	80.9	44.49	po	702	758
79254	095949.40+020140.9	1.753	0.026	$2.34^{+0.07}_{-0.06}$			80.8/68	13.7	44.48	po	407	444
79319	095957.97+014327.3	1.618	0.026	$1.99^{+0.17}_{-0.14}$			33.6/34	48.5	44.12	po	100	147
79353	100001.44+024844.6	0.766	0.026	1.96 ± 0.04			119.5/117	41.8	44.14	po	900	815
79402	100008.14+013306.5	1.171	0.026	$2.16^{+0.21}_{-0.18}$			27.0/23	25.6	43.84	po	57	121
79444	100012.91+023522.8	0.699	0.026	2.47 ± 0.04			152.0/140	23.0	43.98	po	982	1150
79460	100014.13+020054.4	2.497	0.026	$2.01^{+0.09}_{-0.08}$			96.8/56	0.1	44.73	po	325	360
79549	100024.39+015053.9	1.664	0.026	$1.70^{+0.09}_{-0.08}$			23.2/35	93.6	44.32	po	196	226
79553	100024.64+023149.0	1.318	0.026	$2.30^{+0.07}_{-0.06}$			81.7/73	22.6	44.40	po	584	402
79561	100025.24+015852.0	0.373	0.026	1.69 ± 0.04	0.24 ± 0.01		323.8/319	41.5	44.01	po+bb	5591	4846
79711	100043.13+020637.2	0.360	0.026	2.00 ± 0.03			221.3/214	35.2	43.31	po	1251	1931
79812	100055.39+023441.3	1.403	0.025	$1.98^{+0.06}_{-0.05}$			131.3/99	1.7	44.39	po	573	707
79852	100058.84+015400.2	1.559	0.026	1.95 ± 0.05			106.6/89	9.9	44.48	po	606	514

Appendix A. Spectral Fitting Results

SRCID	SDSS name	z	$N_{\text{H}}^{\text{Gal}}$ ($\times 10^{20} \text{ cm}^{-2}$)	Γ	$N_{\text{H}}^{\text{intr}}$ ($\times 10^{22} \text{ cm}^{-2}$)	KT (keV)	χ^2/ν	H0	$\log(L_X)$ ($2 - 10 \text{ keV}$)	Model	Counts	
											MOS	pn
79891	100104.32+553521.6	1.537	0.008	$1.88^{+0.09}_{-0.08}$			28.4/28	44.4	44.74	po	238	162
79963	100114.29+022356.8	1.799	0.025	$2.10^{+0.07}_{-0.06}$			98.1/72	2.2	44.59	po	417	520
79985	100116.78+014053.5	2.055	0.026	$1.93^{+0.08}_{-0.07}$			38.9/52	91.0	44.63	po	319	346
80020	100120.26+023341.3	1.834	0.025	$1.84^{+0.11}_{-0.10}$			31.5/30	39.3	44.31	po	213	108
80027	100120.84+555349.5	1.413	0.008	$2.05^{+0.03}_{-0.02}$			207.1/212	58.2	46.02	po	1717	2854
80089	100130.37+014304.3	1.571	0.026	$1.75^{+0.15}_{-0.13}$			29.5/32	59.3	43.93	po	106	148
80108	100132.16+013420.8	1.360	0.026	$2.45^{+0.13}_{-0.12}$			28.7/36	80.3	44.02	po	146	211
80136	100136.50+025303.5	2.117	0.025	$2.17^{+0.13}_{-0.11}$			15.3/27	96.5	44.79	po	118	165
80212	100145.15+022456.9	2.032	0.025	$2.03^{+0.19}_{-0.16}$			23.2/17	14.1	44.35	po	82	67
80279	100156.41+555440.1	1.152	0.008	$1.77^{+0.13}_{-0.12}$			16.3/23	84.1	44.31	po	107	98
80324	100201.51+020329.4	2.008	0.026	$2.50^{+0.32}_{-0.36}$			18.7/16	28.4	44.08	po	83	43
80330	100202.77+022434.6	0.988	0.025	2.11 ± 0.07			86.0/65	4.2	43.94	po	401	434
80352	100205.36+554257.9	1.151	0.008	$0.48^{+0.11}_{-0.12}$			6.8/12	87.2	44.50	po	92	44
80394	100210.72+023026.1	1.161	0.025	2.02 ± 0.06			67.3/75	72.5	44.31	po	549	479
80440	100219.49+015537.0	1.509	0.026	2.16 ± 0.08			47.4/50	57.9	44.31	po	339	284
80496	100226.33+021923.1	1.294	0.026	2.03 ± 0.05			83.0/82	44.9	44.44	po	364	757
80537	100232.13+023537.3	0.658	0.025	2.25 ± 0.04			169.3/133	1.8	43.96	po	1116	893
80554	100234.32+015011.1	1.506	0.026	2.24 ± 0.05			120.4/97	5.4	44.57	po	506	794
80572	100236.70+015948.6	1.516	0.026	$1.76^{+0.15}_{-0.13}$			18.1/21	64.4	44.01	po	62	113
80583	100238.25+013746.5	2.506	0.027	1.90 ± 0.09			44.6/38	21.5	44.93	po	200	312
80648	100248.95+325130.9	1.537	0.014	$2.12^{+0.08}_{-0.07}$			58.4/41	3.8	44.84	po	470	92
80685	100254.52+324039.0	0.829	0.015	1.78 ± 0.02			270.9/276	57.5	45.37	po	1937	4968
80735	100302.92+015208.5	1.800	0.026	1.88 ± 0.07			42.1/58	94.3	44.83	po	373	379
80773	100309.21+022038.3	1.956	0.026	$1.77^{+0.19}_{-0.17}$			5.9/12	92.1	44.51	po	34	71
80775	100309.43+554134.6	0.674	0.008	2.13 ± 0.06			67.1/74	70.1	44.12	po	619	453
80821	100324.56+021831.3	0.518	0.026	$2.26^{+0.08}_{-0.07}$			66.8/54	11.3	43.91	po	62	760
80825	100325.12+325307.0	2.511	0.015	$1.59^{+0.16}_{-0.15}$			7.5/12	82.1	44.56	po	62	48
80946	100420.13+051300.4	0.161	0.024	$0.60^{+0.09}_{-0.11}$	0.07 ± 0.01		21.9/23	52.5	42.87	po+bb	151	218
80979	100434.91+411242.8	1.740	0.011	1.76 ± 0.01			446.8/430	27.8	45.86	po	6533	7893
80993	100440.98+410944.1	1.022	0.011	$1.66^{+0.09}_{-0.08}$			14.5/28	98.3	43.89	po	156	203
81102	100553.93+411436.8	0.593	0.012	$2.11^{+0.14}_{-0.12}$			19.8/21	53.6	43.77	po	220	275
81137	100640.35+125147.1	0.815	0.037	$2.17^{+0.15}_{-0.14}$			26.9/14	2.0	44.21	po	220	275

Appendix A. Spectral Fitting Results

SRCID	SDSS name	z	$N_{\text{H}}^{\text{Gal}}$ ($\times 10^{20} \text{ cm}^{-2}$)	Γ	$N_{\text{H}}^{\text{intr}}$ ($\times 10^{22} \text{ cm}^{-2}$)	KT (keV)	χ^2/ν	H0	$\log(L_X)$ ($2 - 10 \text{ keV}$)	Model	Counts	
											MOS	pn
81203	100717.24+124543.9	1.281	0.037	2.22 ± 0.05			82.0/79	38.6	44.80	po	507	708
81225	100726.10+124856.2	0.241	0.037	1.35 ± 0.02			193.5/189	39.5	43.71	po	1314	1684
81232	100728.69+534326.7	1.772	0.007	$1.45^{+0.18}_{-0.16}$			4.8/9	85.0	44.50	po	48	50
81414	100921.89+534925.6	0.388	0.007	2.36 ± 0.06			58.2/64	68.0	43.54	po	427	530
81418	100926.74+533424.4	1.730	0.008	1.86 ± 0.07			45.6/41	28.5	45.11	po	249	345
81588	101144.33+554103.1	2.813	0.008	$1.09^{+0.15}_{-0.14}$			4.3/9	89.2	44.62	po	25	68
81596	101148.98+554101.6	1.533	0.008	1.26 ± 0.08			16.8/24	85.8	44.44	po	114	167
82010	101537.90+390154.0	0.510	0.014	$1.82^{+0.20}_{-0.17}$			5.8/9	75.8	43.55	po		86
82106	101616.77+391143.3	0.412	0.014	1.10 ± 0.08			26.0/27	52.0	43.77	po	140	178
82319	101720.67+385738.1	0.629	0.014	$1.88^{+0.05}_{-0.04}$			107.2/84	4.4	44.25	po	258	994
82427	101755.29+390430.7	0.844	0.014	$2.49^{+0.10}_{-0.09}$			36.1/31	24.2	43.97	po	201	241
82550	101850.52+411508.1	0.577	0.011	2.34 ± 0.06			61.1/60	43.5	44.37	po	1077	
82563	101857.49+412549.2	2.123	0.011	$1.60^{+0.18}_{-0.17}$			5.3/12	94.7	44.73	po	112	
82671	102003.81+081837.3	2.094	0.030	$2.19^{+0.14}_{-0.13}$			13.0/14	52.7	45.23	po	207	17
82712	102103.22+130834.3	2.030	0.039	$1.55^{+0.20}_{-0.18}$			2.4/7	93.7	44.68	po	63	17
82721	102117.74+131545.9	1.565	0.039	$2.15^{+0.09}_{-0.08}$			21.6/27	75.8	44.91	po	190	222
82734	102124.95+130115.5	1.007	0.039	$1.96^{+0.09}_{-0.08}$			24.9/33	84.2	44.40	po	305	127
82801	102147.45+130850.4	0.656	0.040	1.87 ± 0.04			110.3/114	58.1	44.36	po	786	970
82902	102223.14+125740.8	2.178	0.040	$1.74^{+0.25}_{-0.20}$			7.1/7	41.6	44.94	po	23	55
83205	102350.94+041542.0	1.809	0.030	1.81 ^a		$0.20^{+0.05}_{-0.04}$	35.7/34	38.6	44.46	po+bb	198	289
83599	102623.31+383701.7	1.226	0.014	1.72 ± 0.05			54.2/64	80.5	44.75	po	418	520
84504	103026.55+053816.7	1.412	0.032	1.98 ± 0.08			34.0/43	83.4	44.56	po	241	319
84534	103031.64+052454.9	1.183	0.032	2.20 ± 0.06			53.3/61	74.9	44.48	po	965	
84657	103059.09+310255.8	0.178	0.020	1.72 ± 0.02		0.19 ± 0.01	811.8/757	8.2	44.35	po+bb	19435	27822
84741	103114.20+051718.3	2.427	0.032	$2.48^{+0.19}_{-0.17}$			11.5/23	97.7	44.76	po	79	104
84914	103216.14+505119.6	0.173	0.012	1.28 ± 0.02		0.08 ± 0.01	216.4/224	63.0	43.65	po+bb	8718	
84939	103227.93+573822.5	1.969	0.006	1.78 ± 0.06			78.0/62	8.2	45.02	po	325	548
85135	103357.21+005324.8	1.710	0.050	$1.50^{+0.18}_{-0.16}$			6.0/7	53.8	45.03	po	31	68
85186	103413.88+58252.8	0.745	0.007	2.29 ± 0.08			35.3/41	72.1	44.31	po	357	245
85331	103518.53+392934.9	0.877	0.015	$1.45^{+0.10}_{-0.09}$			30.1/30	45.8	43.82	po	172	169
85704	103848.92+533757.0	0.351	0.012	2.11 ± 0.04			166.5/147	12.9	43.34	po	1030	1135
85709	103850.89+415512.7	1.469	0.013	$2.18^{+0.13}_{-0.12}$			12.4/16	71.9	45.06	po	156	80

Appendix A. Spectral Fitting Results

SRCID	SDSS name	z	$N_{\text{H}}^{\text{Gal}}$ ($\times 10^{20} \text{ cm}^{-2}$)	Γ	$N_{\text{H}}^{\text{intr}}$ ($\times 10^{22} \text{ cm}^{-2}$)	KT (keV)	χ^2/ν	H0	$\log(L_X)$ ($2 - 10 \text{ keV}$)	Model	Counts	
											MOS	pn
85769	103922.67+643417.4	2.128	0.012	$1.67^{+0.23}_{-0.19}$			10.9/8	21.0	44.73	po	49	56
85790	103935.76+533038.7	0.229	0.011	2.05 ± 0.02			265.2/284	78.2	43.73	po	3159	3619
86030	104032.47+643329.5	1.956	0.012	$1.50^{+0.15}_{-0.14}$		$0.08^{+0.03}_{-0.02}$	7.0/14	93.5	44.80	po+bb	95	76
86063	104039.54+061521.5	1.584	0.028	1.92 ± 0.05			77.4/75	40.3	44.92	po	470	608
86412	104155.74+061256.3	1.478	0.028	$2.84^{+0.21}_{-0.18}$			19.2/25	78.9	44.08	po	101	107
88240	104542.18+525112.6	1.058	0.011	1.86 ± 0.03			137.1/129	29.7	45.29	po	1307	798
88355	104609.92+530008.5	1.179	0.011	$1.95^{+0.18}_{-0.16}$			12.6/13	48.3	44.35	po	153	28
88367	104613.73+525554.2	0.503	0.011	$3.06^{+0.14}_{-0.13}$		0.15 ± 0.01	189.3/173	18.8	44.09	po+bb	2566	2216
89017	105014.80+331013.1	1.011	0.020	$2.17^{+0.18}_{-0.16}$			13.1/10	22.1	44.45	po	163	
89129	105039.54+572336.6	1.447	0.006	2.08 ± 0.06			100.5/81	7.0	44.49	po	449	585
89181	105050.14+573820.0	1.281	0.006	2.25 ± 0.05			145.4/130	16.8	44.43	po	647	1022
89424	105142.51+335009.3	0.503	0.018	$2.17^{+0.11}_{-0.10}$			12.4/23	96.4	43.75	po	345	
89433	105143.89+335926.7	0.167	0.018	1.84 ± 0.02		$0.17^{+0.005}_{-0.01}$	684.6/596	0.7	44.02	po+bb	15057	17944
89507	105201.35+441419.8	1.791	0.011	$1.69^{+0.37}_{-0.29}$	$10.53^{+5.45}_{-3.30}$		3.0/7	88.3	44.79	apo	36	59
89519	105204.56+440152.6	1.525	0.011	$2.38^{+0.24}_{-0.20}$			11.4/12	49.3	44.46	po	89	38
89585	105220.91+440439.0	0.968	0.011	$2.62^{+0.10}_{-0.09}$			34.4/38	63.6	44.17	po	278	272
89605	105224.94+441505.2	0.444	0.011	2.12 ± 0.04			131.1/133	53.0	44.16	po	852	1271
89665	105239.60+572431.4	1.112	0.006	2.09^a		unconstrained	666.5/648	29.9	44.75	po+bb	13734	15786
89703	105246.98+335619.8	0.927	0.019	$2.11^{+0.09}_{-0.08}$			35.7/39	62.0	44.51	po	251	290
89731	105253.84+340557.4	0.637	0.019	$2.18^{+0.19}_{-0.17}$			6.4/10	77.9	44.19	po	107	
89790	105316.75+573550.8	1.205	0.006	$1.65^{+0.03}_{-0.02}$	< 0.124	$0.38^{+0.02}_{-0.04}$	577.2/604	77.7	45.03	apo+bb	17900	9189
89916	105404.10+574019.7	1.101	0.006	1.77 ± 0.08			48.9/48	43.8	44.23	po	420	190
89962	105422.55+572031.0	2.972	0.006	$2.21^{+0.20}_{-0.18}$			27.9/24	26.6	44.69	po	98	81
91089	110320.14+380930.8	1.753	0.019	$2.01^{+0.15}_{-0.14}$			18.8/23	71.4	44.30	po	242	
91100	110323.57+405004.2	2.982	0.013	$1.95^{+0.23}_{-0.18}$			10.3/9	32.6	45.03	po	49	48
91149	110334.75+355107.6	1.200	0.021	$2.41^{+0.13}_{-0.12}$			22.0/27	73.9	43.91	po	138	156
91395	110400.27+380230.9	1.622	0.019	$1.80^{+0.09}_{-0.08}$			50.8/63	86.5	44.28	po	489	126
91823	110426.65+404621.2	2.560	0.013	$2.04^{+0.21}_{-0.17}$			6.0/7	53.9	44.94	po	28	62
92164	110449.13+381811.6	1.942	0.014	2.04 ± 0.06			84.7/82	39.8	44.74	po	938	183
92522	110547.15+380947.6	1.154	0.014	2.04 ± 0.07			52.2/46	24.6	44.41	po	129	414
93094	111038.64+483115.6	2.955	0.013	1.91 ± 0.06			68.5/57	14.1	45.32	po	348	464
93253	111121.70+482045.9	0.281	0.013	1.38 ± 0.04			99.2/81	8.3	43.71	po	531	648

Appendix A. Spectral Fitting Results

SRCID	SDSS name	z	$N_{\text{H}}^{\text{Gal}}$ ($\times 10^{20} \text{ cm}^{-2}$)	Γ	$N_{\text{H}}^{\text{intr}}$ ($\times 10^{22} \text{ cm}^{-2}$)	KT (keV)	χ^2/ν	H0	$\log(L_X)$ ($2 - 10 \text{ keV}$)	Model	Counts	
											MOS	pn
93299	111135.76+482945.3	0.558	0.013	1.83 ± 0.05		0.23 ± 0.02	231.8/251	80.3	44.73	po+bb	2600	3524
93636	111452.84+531531.7	1.213	0.009	$1.58^{+0.14}_{-0.13}$			7.0/14	93.5	44.75	po	72	83
93682	111506.01+424948.8	0.301	0.017	2.04 ± 0.09			44.2/35	13.6	43.38	po	530	
93708	111512.44+525601.5	1.103	0.010	$2.56^{+0.29}_{-0.24}$			5.1/6	52.7	44.32	po	48	29
93873	111606.97+423645.4	0.670	0.018	1.55 ± 0.02			209.8/224	74.3	44.57	po	1781	1931
93878	111609.62+441846.0	0.954	0.018	1.96 ± 0.07			35.1/42	76.6	44.61	po	643	
94028	111706.39+441333.3	0.144	0.018	1.60 ± 0.01	0.83 ± 0.01	$0.07^{+0.0007}_{-0.0002}$	976.1/879	8.5	44.11	apo+bb+line	15918	19785
94184	111747.36+075400.2	1.961	0.034	1.76 ± 0.08			61.5/54	22.6	44.38	po	267	307
94223	111753.33+412016.3	2.221	0.019	$1.65^{+0.06}_{-0.05}$			32.1/41	83.9	45.59	po	307	331
94371	111816.95+074558.1	1.735	0.035	1.93 ± 0.01	$1.00^{+0.05}_{-0.04}$		926.8/883	14.9	45.82	apo	22472	27828
94446	111828.67+403517.7	1.635	0.019	$1.93^{+0.24}_{-0.22}$			7.8/8	45.4	44.64	po	88	
94456	111830.28+402554.0	0.155	0.019	2.31 ± 0.02		0.15 ± 0.004	580.9/516	2.5	43.92	po+bb	15546	20282
94521	111840.56+075324.1	1.463	0.036	1.97 ± 0.04			124.9/139	79.8	44.59	po	1076	876
94567	111848.67+402647.7	1.128	0.019	$1.99^{+0.16}_{-0.14}$			9.5/11	57.4	44.70	po		170
94576	111849.74+402228.4	1.265	0.019	$2.26^{+0.10}_{-0.09}$			18.6/23	72.7	44.61	po		340
94601	111853.50+074945.9	2.042	0.036	2.22^a		unconstrained	79.0/81	54.3	44.62	po+bb	513	514
94676	111904.79+401911.3	1.864	0.019	$2.28^{+0.22}_{-0.19}$			18.7/15	22.7	44.65	po	74	70
94787	111928.38+130251.0	2.401	0.022	1.98 ± 0.05			77.7/56	2.9	45.71	po	910	
94854	111946.94+133759.2	2.023	0.022	$1.87^{+0.16}_{-0.14}$			26.0/22	25.3	44.55	po	107	81
94995	112020.96+432545.1	3.548	0.021	$1.19^{+0.18}_{-0.16}$			19.4/11	5.4	45.02	po	53	61
95020	112026.20+134024.6	0.982	0.022	2.17 ± 0.05			105.3/91	14.5	44.53	po		1389
95096	112048.99+133821.9	0.513	0.023	$1.37^{+0.23}_{-0.20}$			5.9/11	87.9	42.98	po	21	70
95129	112104.93+432141.6	2.027	0.021	$1.84^{+0.14}_{-0.13}$			31.3/22	9.1	44.96	po	106	108
95131	112106.07+133824.9	1.944	0.023	1.81 ± 0.06			44.9/54	80.7	45.25	po	482	280
95417	112317.51+051803.9	1.000	0.044	$2.05^{+0.07}_{-0.06}$			41.5/50	79.8	44.96	po	795	
95427	112320.73+013747.4	1.469	0.041	1.87 ± 0.05	$2.21^{+0.23}_{-0.21}$		205.4/192	24.1	45.39	apo	1493	1618
95476	112338.14+052038.5	2.181	0.044	1.64 ± 0.04			91.8/87	34.2	45.63	po	646	663
95486	112340.22+385129.2	1.034	0.020	2.21 ± 0.06			64.5/64	45.8	44.81	po	567	398
95769	112534.69+383848.3	1.788	0.021	$1.93^{+0.24}_{-0.21}$			9.0/10	53.6	44.64	po	96	
96216	113021.41+005823.0	0.132	0.031	0.55 ± 0.04			71.1/44	0.6	43.35	po	367	317
96243	113034.49+312422.7	1.810	0.020	$2.17^{+0.17}_{-0.15}$			18.0/18	45.5	44.89	po	75	106
96325	113109.48+311405.5	0.290	0.020	1.78 ± 0.01		0.21 ± 0.01	893.0/822	4.3	44.84	po+bb	27171	33555

Appendix A. Spectral Fitting Results

SRCID	SDSS name	z	$N_{\text{H}}^{\text{Gal}}$ ($\times 10^{20} \text{ cm}^{-2}$)	Γ	$N_{\text{H}}^{\text{intr}}$ ($\times 10^{22} \text{ cm}^{-2}$)	KT (keV)	χ^2/ν	H0	$\log(L_X)$ ($2 - 10 \text{ keV}$)	Model	Counts	
											MOS	pn
96459	113154.35+311137.7	1.806	0.020	$1.97^{+0.08}_{-0.07}$			31.5/34	59.1	44.71	po	270	209
96502	113205.02+530727.5	1.840	0.011	$1.83^{+0.25}_{-0.21}$			3.0/7	88.4	44.54	po	36	48
96546	113224.00+525157.6	0.837	0.011	$1.84^{+0.15}_{-0.14}$			6.8/14	94.1	44.05	po	43	101
96674	113342.72+490025.8	1.295	0.016	$1.47^{+0.12}_{-0.11}$			12.5/12	40.3	44.98	po	197	
97108	113803.73+031457.7	2.444	0.024	1.64 ± 0.11			9.3/12	68.0	45.56	po	194	96
97219	113841.09+032318.1	2.265	0.024	$1.79^{+0.23}_{-0.19}$			11.4/9	24.7	44.94	po		
97644	114038.95+031429.5	1.606	0.023	$1.99^{+0.10}_{-0.09}$			18.2/23	74.8	44.89	po	157	165
98091	114522.37+472433.7	1.181	0.022	$2.42^{+0.18}_{-0.16}$			11.3/15	73.2	44.40	po	69	84
98188	114636.88+472313.3	1.895	0.022	$1.89^{+0.09}_{-0.08}$			21.3/26	72.5	45.30	po	247	155
98198	114656.73+472755.6	0.668	0.022	$2.14^{+0.08}_{-0.07}$			53.7/46	20.3	44.40	po	399	293
98226	114856.56+525425.2	1.633	0.014	1.65 ± 0.06			60.9/43	3.7	45.82	po	469	213
98272	115005.36+013850.7	2.325	0.023	2.10 ± 0.08			68.1/42	0.7	45.18	po	283	327
98344	115024.80+015620.3	0.706	0.022	1.64 ± 0.05			68.1/82	86.5	44.30	po	512	680
98968	115711.10+553445.8	1.715	0.012	$1.75^{+0.25}_{-0.20}$			6.9/8	55.2	44.75	po	51	45
98984	115726.17+434953.7	1.597	0.014	$2.16^{+0.10}_{-0.09}$			77.8/45	0.2	44.73	po	246	346
99126	115838.56+435505.8	1.208	0.014	$1.35^{+0.05}_{-0.04}$			107.1/70	0.3	44.25	po	451	506
99163	115851.03+435047.7	0.287	0.014	2.21 ± 0.04			109.5/128	88.0	43.21	po	1878	357
99191	115906.28+434643.8	1.462	0.014	$2.24^{+0.29}_{-0.23}$			7.9/14	89.3	44.67	apo	209	
99199	115911.43+440818.3	1.438	0.014	$2.31^{+0.25}_{-0.21}$			6.4/10	78.4	44.38	po	94	
100172	120450.54+442835.8	1.142	0.013	2.22 ± 0.08			54.7/45	15.3	44.55	po	295	359
100246	120504.39+352208.3	2.279	0.017	$2.04^{+0.22}_{-0.17}$			10.5/11	48.6	44.78	po	60	65
100349	120522.18+443140.4	1.921	0.013	$1.03^{+0.13}_{-0.12}$			10.1/13	68.7	44.49	po	38	97
100716	120721.70+650053.9	1.401	0.018	$1.55^{+0.20}_{-0.18}$			4.6/6	59.9	44.48	po	48	29
100869	120858.01+454035.4	1.163	0.013	1.62 ± 0.09			19.6/20	48.5	45.07	po	298	
100924	120913.61+433920.9	1.398	0.014	1.70 ± 0.03			182.7/127	0.1	45.45	po	1057	957
100939	120917.04+422742.4	1.262	0.017	$2.23^{+0.30}_{-0.27}$			2.6/5	76.3	44.10	po	22	55
101033	120941.24+651219.2	0.310	0.019	$1.28^{+0.21}_{-0.18}$			3.7/8	87.9	43.13	po	55	35
101044	120943.34+393642.6	2.332	0.020	$1.85^{+0.14}_{-0.13}$			6.0/14	96.7	44.87	po		183
101147	121001.72+392150.8	2.962	0.020	1.73 ± 0.06			47.8/50	56.4	45.06	po	247	424
101451	121043.97+390802.3	0.663	0.019	$2.24^{+0.11}_{-0.10}$			34.1/31	32.2	44.24	po	132	276
101568	121102.08+390706.3	0.837	0.019	$2.05^{+0.12}_{-0.10}$			20.5/25	72.0	44.08	po	157	151
101613	121111.18+393320.7	1.529	0.020	$2.18^{+0.12}_{-0.11}$			42.6/36	20.8	44.08	po	272	113

Appendix A. Spectral Fitting Results

SRCID	SDSS name	z	$N_{\text{H}}^{\text{Gal}}$ ($\times 10^{20} \text{ cm}^{-2}$)	Γ	$N_{\text{H}}^{\text{intr}}$ ($\times 10^{22} \text{ cm}^{-2}$)	KT (keV)	χ^2/ν	H0	$\log(L_X)$ ($2 - 10 \text{ keV}$)	Model	Counts	
											MOS	pn
101676	121122.44+130937.2	0.324	0.025	1.40 ^e		0.30 ± 0.03	74.5/81	68.1	44.04	po+bb	718	556
101707	121129.36+392513.6	1.671	0.020	2.27 ^{+0.07} _{-0.06}			78.8/63	8.6	44.50	po	467	385
101973	121342.95+025248.9	0.641	0.018	2.74 ^{+0.11} _{-0.10}			28.1/35	79.1	43.50	po	223	270
102133	121423.02+024252.8	2.223	0.018	1.56 ± 0.03			128.9/129	48.6	45.88	po	950	1054
102140	121426.52+140258.9	1.279	0.027	1.71 ± 0.02			150.9/158	64.3	45.16	po		3521
102230	121507.47+522055.7	1.212	0.018	1.83 ^{+0.16} _{-0.15}			30.3/19	4.8	44.86	po	54	140
102234	121509.46+135449.7	0.848	0.028	2.29 ± 0.05			90.5/97	66.6	44.50	po		1413
102326	121613.62+524246.2	0.270	0.018	2.17 ± 0.04			138.5/118	9.5	44.16	po	1128	911
102394	121640.56+071224.3	0.586	0.015	2.21 ± 0.05			102.1/74	1.7	44.74	po	1427	
102452	121700.17+471511.7	1.296	0.012	2.07 ± 0.10			37.7/24	3.7	44.70	po	350	
102484	121713.15+070236.5	1.203	0.015	2.13 ^{+0.15} _{-0.14}			6.5/10	77.6	44.77	po	161	
102490	121715.34+471213.9	1.133	0.012	1.92 ± 0.05			126.6/95	1.7	44.66	po	626	755
102543	121732.69+465829.3	1.991	0.012	1.92 ± 0.05			94.3/78	10.1	45.33	po	519	622
102573	121739.80+375240.5	1.189	0.017	1.99 ± 0.05			82.8/90	69.1	44.30	po	546	649
102693	121808.49+471612.7	0.398	0.012	1.92 ± 0.02			386.4/318	0.5	43.89	po	4325	5001
102875	121836.09+054628.0	0.795	0.015	1.58 ± 0.05			83.6/91	69.7	44.20	po	657	512
103069	121902.78+141439.5	1.915	0.028	1.91 ^{+0.23} _{-0.19}			10.7/8	21.8	44.68	po	43	46
103116	121908.59+141039.2	1.676	0.028	1.47 ^{+0.23} _{-0.19}			5.4/8	71.3	44.95	po		79
103136	121911.18+470707.6	1.901	0.012	1.90 ± 0.07			62.2/55	23.6	44.62	po	337	359
103305	121938.69+064022.4	1.188	0.015	2.15 ± 0.11			14.2/27	97.9	44.50	po	81	264
103356	121952.31+472058.5	0.653	0.012	1.64 ± 0.02			177.8/225	99.1	44.39	po	1647	2531
103449	122018.43+064119.6	0.286	0.016	1.79 ^{+0.04} _{-0.05}		0.18 ^{+0.02} _{-0.03}	229.5/245	75.4	44.46	po+bb	3297	2805
103906	122158.07+142409.8	2.400	0.027	2.06 ^{+0.10} _{-0.09}			28.3/32	65.4	44.86	po	188	212
104378	122436.89+131732.3	0.521	0.026	1.93 ^{+0.20} _{-0.18}			8.8/9	46.0	43.56	po	86	
104405	122442.25+332939.9	0.776	0.013	1.88 ^{+0.06} _{-0.05}			52.1/78	98.9	44.27	po	149	883
104453	122453.33+123916.3	0.368	0.026	2.74 ^{+0.25} _{-0.21}			3.3/10	97.2	43.13	po	34	75
104572	122511.91+125153.6	1.255	0.026	1.32 ^{+0.23} _{-0.21}			17.8/9	3.8	44.95	po		93
104608	122515.65+124441.0	1.664	0.026	2.50 ^{+0.28} _{-0.22}			9.0/10	53.6	44.66	po	57	45
104707	122528.44+131725.4	1.794	0.026	2.06 ^{+0.13} _{-0.11}			33.1/26	16.0	44.66	po	102	197
104920	122556.21+130656.2	1.350	0.026	1.88 ± 0.07			71.2/50	2.6	44.39	po	320	301
104923	122556.62+003535.1	1.221	0.019	1.63 ^{+0.14} _{-0.12}			10.8/14	70.4	44.62	po	84	79
105178	122637.02+013016.0	1.552	0.018	1.18 ^{+0.16} _{-0.15}			6.6/6	35.8	44.54	po	33	49

Appendix A. Spectral Fitting Results

SRCID	SDSS name	z	$N_{\text{H}}^{\text{Gal}}$ ($\times 10^{20} \text{ cm}^{-2}$)	Γ	$N_{\text{H}}^{\text{intr}}$ ($\times 10^{22} \text{ cm}^{-2}$)	KT (keV)	χ^2/ν	H0	$\log(L_X)$ ($2 - 10 \text{ keV}$)	Model	Counts	
											MOS	pn
105261	122656.48+013124.2	0.732	0.018	$1.44^{+0.12}_{-0.11}$	$2.98^{+0.44}_{-0.37}$		51.3/36	4.7	44.65	apo	284	293
105291	122703.37+125402.0	1.278	0.026	$1.85^{+0.09}_{-0.08}$			34.6/38	63.0	44.19	po	183	235
105448	122742.98+013438.2	1.279	0.018	$1.84^{+0.15}_{-0.13}$			16.7/18	54.4	44.54	po	92	86
105706	122853.71+441152.8	1.277	0.014	$1.49^{+0.15}_{-0.13}$			14.6/16	55.7	44.56	po	83	84
105882	122923.73+075359.2	0.854	0.016	1.57 ± 0.03			223.0/209	24.1	44.57	po	1600	2070
105936	122931.19+015248.0	0.770	0.018	$1.66^{+0.06}_{-0.05}$		$0.04^{+0.01}_{-0.004}$	72.5/82	76.4	43.62	po+bb	1153	11
105981	122934.72+015658.1	1.921	0.018	2.06 ± 0.03			165.2/159	35.2	45.01	po	3906	70
106079	122951.54+105826.1	1.846	0.021	$1.77^{+0.16}_{-0.14}$			13.3/16	64.9	44.37	po		170
106562	123035.47+153510.7	0.803	0.024	2.23 ± 0.06			50.0/54	62.8	44.43	po	444	371
106827	123049.78+640848.2	1.040	0.020	$2.35^{+0.07}_{-0.06}$			48.1/53	66.5	44.17	po	328	408
106850	123050.98+154306.5	2.161	0.024	$2.15^{+0.19}_{-0.16}$			10.0/13	69.6	44.92	po	74	69
106917	123054.11+110011.2	0.236	0.022	1.94 ± 0.01		0.17 ± 0.002	1900.7/1423	0.0	44.30	po+bb	99798	151282
107235	123110.35+161257.9	1.453	0.023	$1.68^{+0.09}_{-0.08}$			45.2/34	9.4	44.91	po	256	220
107458	123126.44+105111.4	0.304	0.021	2.27 ± 0.07		0.15 ± 0.01	274.1/238	5.4	43.37	po+bb	3800	1980
107465	123127.41+135447.9	0.511	0.025	$2.58^{+0.09}_{-0.08}$			51.2/41	13.2	43.93	po	272	351
107482	123129.03+154609.7	0.512	0.024	$2.55^{+0.12}_{-0.11}$			22.3/23	50.1	43.91	po	206	172
107662	123147.11+123835.3	0.292	0.026	2.18 ± 0.04			177.9/155	10.0	43.52	po	1284	1073
107891	123228.08+141558.7	0.427	0.025	1.97 ± 0.09			31.7/24	13.5	43.88	po	270	73
107894	123229.67+641115.1	0.743	0.020	$2.51^{+0.15}_{-0.17}$		0.10 ± 0.03	35.0/41	73.5	44.01	po+bb	276	335
108068	123335.07+475800.4	0.382	0.012	$1.96^{+0.09}_{-0.08}$			19.4/22	61.9	44.72	po	387	
108072	123337.60+073132.7	1.185	0.016	1.88 ± 0.07			20.3/35	97.8	45.13	po	559	
108108	123356.11+074755.9	0.371	0.017	1.95 ± 0.03			257.2/212	1.8	44.13	po	1774	2495
108159	123413.34+475351.3	0.373	0.012	2.10 ± 0.10			10.5/16	83.7	44.34	po	264	
108198	123426.77+373643.6	1.623	0.014	$2.16^{+0.22}_{-0.19}$			3.5/8	89.7	44.41	po	41	61
108383	123508.19+393020.0	0.968	0.015	$2.26^{+0.17}_{-0.15}$			4.7/11	94.3	43.90	po	155	
108434	123516.52+373306.8	1.357	0.014	$2.33^{+0.25}_{-0.21}$			3.6/7	82.5	44.44	po	80	
108512	123527.36+392824.0	2.158	0.015	1.88 ± 0.07			51.1/39	9.3	45.01	po	223	336
108599	123540.19+123620.7	3.208	0.026	$2.15^{+0.32}_{-0.25}$			7.3/10	69.4	44.70	po	36	49
108952	123622.94+621526.6	2.587	0.015	1.82 ± 0.05			98.4/88	21.1	44.67	po	640	514
109244	123715.99+620323.3	2.068	0.014	$2.64^{+0.63}_{-0.38}$	$9.28^{+3.97}_{-2.47}$		14.1/17	66.2	44.35	apo	51	67
109405	123759.56+621102.3	0.910	0.014	1.79 ± 0.02			350.2/327	18.1	44.60	po	4153	5174
109409	123800.91+621336.0	0.440	0.015	2.46 ± 0.03			203.2/219	77.0	43.41	po	775	3694

Appendix A. Spectral Fitting Results

SRCID	SDSS name	z	$N_{\text{H}}^{\text{Gal}}$ ($\times 10^{20} \text{ cm}^{-2}$)	Γ	$N_{\text{H}}^{\text{intr}}$ ($\times 10^{22} \text{ cm}^{-2}$)	KT (keV)	χ^2/ν	H0	$\log(L_X)$ ($2 - 10 \text{ keV}$)	Model	Counts	
											MOS	pn
109443	123816.12+620207.8	1.004	0.014	$1.21^{+0.21}_{-0.18}$			11.6/13	56.3	43.52	po	199	83
109701	124006.70+474003.3	1.559	0.012	1.76 ± 0.07			43.1/32	9.1	45.26	po	77	286
109825	124058.45+473302.0	0.368	0.012	$2.01^{+0.15}_{-0.13}$			15.8/21	78.1	43.63	po	1169	134
110183	124206.11+141921.0	1.957	0.022	2.13 ± 0.03			221.3/186	3.9	45.07	po	185	1676
110201	124207.80+333117.3	0.515	0.013	$1.26^{+0.09}_{-0.08}$			25.4/19	14.9	43.62	po	368	248
110251	124214.06+024224.0	1.604	0.018	$2.20^{+0.09}_{-0.08}$			40.8/37	30.5	44.50	po	241	307
110294	124219.16+023118.3	0.480	0.018	1.84 ± 0.07			30.0/40	87.5	43.75	po	484	193
110301	124220.07+023257.6	2.224	0.018	$2.10^{+0.09}_{-0.08}$			41.1/40	42.3	45.00	po	278	293
110520	124244.58+022954.3	0.937	0.018	1.83 ± 0.05			88.5/80	24.2	44.40	po	1791	644
110643	124255.31+024956.9	1.459	0.018	$2.07^{+0.14}_{-0.13}$			31.5/21	6.6	44.53	po	96	2665
111146	124406.96+113524.2	1.344	0.022	1.98 ± 0.02			244.5/232	27.4	44.81	po	776	998
111417	124516.04-001859.3	1.586	0.017	1.85 ± 0.04			161.3/120	0.7	45.03	po	1203	124
111432	124520.72-002128.2	2.354	0.017	$2.07^{+0.25}_{-0.21}$	$8.09^{+3.25}_{-2.18}$		16.9/24	85.3	44.78	apo	444	1616
111490	124540.99-002744.8	1.693	0.017	1.75 ± 0.03			192.8/177	19.7	45.30	po	418	780
111519	124555.11-003735.4	1.042	0.018	$2.23^{+0.07}_{-0.06}$			45.9/54	77.5	44.65	po	394	595
111557	124615.79+673032.8	1.769	0.019	1.92 ± 0.05			74.2/73	43.9	45.10	po	418	644
111692	124728.48+671725.0	1.220	0.019	1.92 ± 0.06			91.1/75	10.0	44.46	po	191	93
113473	125456.83+564941.4	1.273	0.013	$1.69^{+0.09}_{-0.08}$			16.4/24	87.4	45.01	po	130	163
113492	125502.97+564953.0	1.232	0.013	$1.98^{+0.12}_{-0.11}$			17.2/22	75.3	44.61	po	88	145
113561	125524.94+565613.6	1.188	0.013	$2.26^{+0.12}_{-0.11}$			18.9/25	80.3	44.22	po	94	106
113603	125535.11+565239.6	1.804	0.013	$2.50^{+0.15}_{-0.14}$			26.2/24	34.3	44.47	po	81	24
113878	125642.10+564720.6	1.956	0.013	$2.23^{+0.19}_{-0.16}$			26.6/21	18.5	44.63	po	1004	454
114855	125903.93+344702.4	0.608	0.012	$1.83^{+0.20}_{-0.18}$			4.4/10	92.6	43.95	po	105	15
115080	125930.97+282705.5	1.094	0.009	$1.69^{+0.12}_{-0.10}$	$5.06^{+1.59}_{-0.74}$	$0.18^{+0.10}_{-0.04}$	100.6/113	79.3	44.38	apo+bb	65230	65734
115360	130002.79+345043.4	1.054	0.012	$2.44^{+0.26}_{-0.22}$			10.4/12	58.2	44.37	po	611	2802
115572	130028.53+283010.1	0.649	0.009	$1.86^{+0.005}_{-0.004}$			1593.7/1219	0.0	45.08	po	5858	7265
115669	130048.11+282320.7	1.924	0.009	2.01 ± 0.03			232.5/187	1.3	44.81	po	127	127
115798	130120.13+282137.2	1.369	0.009	1.84 ± 0.01			441.4/434	39.2	45.18	po	72	56
116161	130257.68+673006.6	1.837	0.019	$1.84^{+0.12}_{-0.11}$			18.2/27	89.7	44.84	po	251	336
116386	130423.02+673953.5	0.977	0.019	$1.48^{+0.17}_{-0.15}$			10.9/12	54.0	44.05	po	188	127
116492	130454.34+673006.4	0.539	0.019	2.15 ± 0.08			34.1/40	73.1	43.72	po	81	24
117526	130835.06-013835.2	0.490	0.018	2.19 ± 0.10			22.8/25	58.8	44.07	po	1004	454

Appendix A. Spectral Fitting Results

SRCID	SDSS name	z	$N_{\text{H}}^{\text{Gal}}$ ($\times 10^{20} \text{ cm}^{-2}$)	Γ	$N_{\text{H}}^{\text{intr}}$ ($\times 10^{22} \text{ cm}^{-2}$)	KT (keV)	χ^2/ν	H0	$\log(L_X)$ ($2 - 10 \text{ keV}$)	Model	Counts	
											MOS	pn
117906	130937.34-014950.4	0.703	0.018	$2.11^{+0.25}_{-0.20}$			5.7/7	57.3	43.86	po	40	40
118322	131055.58-012724.5	1.003	0.018	$2.23^{+0.16}_{-0.14}$			28.0/23	21.7	43.87	po	86	124
119582	131817.64+324052.9	1.647	0.011	2.02 ± 0.07			24.7/38	95.2	45.12	po	277	323
119757	131931.39+331815.3	1.028	0.010	$2.03^{+0.22}_{-0.20}$			39.7/21	0.8	44.13	po	52	147
119777	131938.76-004940.0	0.891	0.020	1.77 ± 0.02			241.4/195	1.3	45.22	po	2232	2187
120433	132307.69+655446.3	0.648	0.020	$3.08^{+0.12}_{-0.11}$			37.0/34	33.0	43.84	po	511	
120482	132330.44+545955.6	2.208	0.013	$1.82^{+0.17}_{-0.15}$			12.6/17	76.1	45.49	apo	283	
120586	132359.51+652540.7	0.446	0.020	$2.31^{+0.23}_{-0.19}$	$4.02^{+1.86}_{-1.38}$		5.2/8	73.5	43.56	po		86
120593	132401.53+032020.6	0.927	0.020	$-0.29^{+0.17}_{-0.22}$			15.7/5	0.8	44.00	po	67	12
120832	132447.65+032432.6	0.306	0.020	2.07 ± 0.04			87.6/86	43.1	44.18	po	2094	
121147	132531.79+301715.6	1.777	0.012	$2.28^{+0.09}_{-0.08}$			30.6/30	43.5	44.72	po	181	244
121397	132607.08+655543.5	1.513	0.020	$1.93^{+0.12}_{-0.11}$			12.0/15	67.9	44.56	po		210
121508	132623.10+011501.1	1.232	0.019	$2.17^{+0.22}_{-0.19}$			3.5/9	93.9	44.19	po	43	60
121792	132711.13+011009.7	0.971	0.018	1.96 ± 0.10			37.1/24	4.3	44.38	po	76	254
122068	132827.07+581836.9	3.140	0.014	0.66 ± 0.15			8.5/17	95.3	44.57	po	44	74
122294	132938.57+471854.6	1.027	0.015	1.97 ± 0.04			155.4/150	36.4	44.34	po	904	1243
122385	132956.08+114240.0	1.190	0.019	$1.26^{+0.18}_{-0.16}$			8.9/13	78.3	44.23	po	65	59
122589	133027.51-014203.2	1.268	0.024	1.90 ± 0.04			134.5/117	12.8	45.09	po	817	986
122978	133135.19-014430.2	1.462	0.024	$2.11^{+0.11}_{-0.10}$			20.6/25	71.3	44.70	po	176	171
123144	133205.51+111621.0	0.950	0.019	$2.18^{+0.11}_{-0.10}$			17.9/23	76.5	44.34	po	133	111
123255	133229.11+291223.1	1.575	0.012	$1.67^{+0.09}_{-0.08}$			48.7/32	2.9	44.71	po	180	266
123468	133314.81+504526.1	1.173	0.011	$2.65^{+0.23}_{-0.19}$			8.2/17	96.1	43.94	po	72	68
124163	133534.22+515822.3	2.196	0.011	$2.22^{+0.13}_{-0.12}$			18.5/25	82.1	44.62	po	106	110
124254	133551.01+515346.3	1.739	0.011	$1.78^{+0.28}_{-0.22}$			8.1/9	52.3	43.91	po	13	68
124268	133553.61+514744.1	1.830	0.011	$2.72^{+0.50}_{-0.33}$	$6.10^{+3.97}_{-1.99}$		11.0/13	61.2	44.54	apo	66	68
124679	133720.80+520227.7	1.563	0.011	$2.73^{+0.17}_{-0.15}$			18.6/28	91.1	44.24	po	116	134
124759	133735.65+520530.7	0.842	0.011	$2.52^{+0.22}_{-0.20}$			12.2/11	35.1	43.88	po	166	
124865	133753.11+482729.4	0.595	0.017	1.83 ± 0.11			25.0/19	16.0	44.14	po	289	
124917	133759.86+281704.9	0.888	0.011	$1.85^{+0.20}_{-0.18}$			8.2/10	61.1	43.97	po	50	57
124955	133807.47+280509.8	1.088	0.011	1.08 ± 0.05			39.9/37	34.1	44.66	po	278	267
124986	133812.97+391527.1	0.438	0.009	$1.22^{+0.08}_{-0.07}$			19.1/26	83.1	44.28	po	405	
125173	133859.17+272702.2	1.792	0.011	$1.66^{+0.21}_{-0.18}$			2.4/7	93.8	44.56	po	48	27

Appendix A. Spectral Fitting Results

SRCID	SDSS name	z	$N_{\text{H}}^{\text{Gal}}$ ($\times 10^{20} \text{ cm}^{-2}$)	Γ	$N_{\text{H}}^{\text{intr}}$ ($\times 10^{22} \text{ cm}^{-2}$)	KT (keV)	χ^2/ν	H0	$\log(L_X)$ ($2 - 10 \text{ keV}$)	Model	Counts	
											MOS	pn
125205	133909.71+280526.4	1.117	0.011	$2.02^{+0.11}_{-0.10}$			12.9/24	96.8	44.31	po	129	171
125216	133913.38+271818.2	0.682	0.011	$2.39^{+0.16}_{-0.14}$			21.9/15	11.0	44.30	po	243	
125477	134044.52-004516.6	0.386	0.021	1.76 ± 0.12		0.24 ± 0.02	109.3/109	47.4	43.95	po+bb	768	1003
125566	134113.93-005315.0	0.237	0.022	1.74 ± 0.03		0.21 ± 0.02	361.6/362	49.7	44.42	po+bb	5711	6817
125973	134252.95+403201.5	0.906	0.009	1.61 ± 0.03			184.6/172	24.2	44.73	po	1170	1589
125987	134256.51+000057.2	0.804	0.019	1.77 ± 0.04			133.3/115	11.7	44.67	po	854	903
126022	134304.68+403218.2	0.476	0.009	2.42 ± 0.06			75.5/64	15.4	43.87	po	1145	
126111	134323.65+001223.3	0.873	0.019	2.02 ± 0.05			107.3/96	20.2	44.64	po	690	750
126219	134349.10+402722.0	1.907	0.009	1.63 ± 0.11			23.8/22	35.8	44.95	po	146	68
126291	134412.88-003005.4	0.709	0.021	$2.88^{+0.21}_{-0.18}$			11.6/12	48.1	43.73	po	79	65
126386	134447.55+554656.8	0.938	0.011	$1.81^{+0.11}_{-0.10}$			23.8/15	6.8	44.41	po	234	
126416	134459.44-001559.5	0.245	0.021	$2.26^{+0.11}_{-0.10}$			50.6/30	1.1	43.58	po	504	
126430	134507.93-001900.9	0.419	0.021	$1.19^{+0.17}_{-0.15}$	$1.08^{+0.34}_{-0.26}$		11.9/19	89.2	44.27	apo	105	171
126445	134512.06+554759.6	1.168	0.011	$2.11^{+0.10}_{-0.09}$			12.4/24	97.5	44.83	po		340
126952	134740.99+581242.2	2.050	0.013	1.86 ± 0.02			230.4/211	17.2	45.66	po	1859	2339
126999	134747.49+600640.3	1.921	0.018	$1.60^{+0.22}_{-0.19}$			10.1/9	33.9	44.69	po	40	55
127011	134749.86+582109.3	0.646	0.013	1.73 ± 0.04		0.28 ± 0.01	295.6/322	85.1	45.09	po+bb	2625	6606
127306	134834.28+262205.9	0.918	0.012	$2.70^{+0.08}_{-0.07}$		0.18 ± 0.01	284.2/283	46.8	44.61	apo+bb	3848	5996
127400	134848.24+262219.2	0.595	0.012	2.32 ± 0.08		0.13 ± 0.01	75.5/86	78.4	43.97	po+bb	2285	
127410	134850.23+262504.2	2.915	0.012	$1.97^{+0.14}_{-0.12}$			18.6/27	88.5	44.65	po	87	124
127970	135038.58+601901.7	1.165	0.018	$2.15^{+0.19}_{-0.18}$			6.4/9	70.1	44.30	po	94	
128647	135418.09+635704.8	1.614	0.021	$2.06^{+0.26}_{-0.22}$			6.4/11	84.7	44.23	po	57	41
128660	135420.52+401238.5	1.382	0.010	$1.83^{+0.14}_{-0.13}$			6.1/14	96.4	44.53	po	66	73
129151	135639.13+051950.9	1.394	0.021	1.94 ± 0.08			26.7/27	48.1	44.83	po	213	176
129372	135810.69+653739.6	1.111	0.020	$2.14^{+0.11}_{-0.10}$			19.6/27	84.7	44.55	po	236	160
129447	135842.92+652236.6	3.197	0.020	$2.00^{+0.20}_{-0.17}$			11.3/12	50.2	44.98	po	23	88
129592	140001.69-014924.8	1.755	0.039	$1.84^{+0.12}_{-0.11}$			29.7/29	43.0	44.76	po	177	135
129714	140045.00+621814.5	0.542	0.019	$2.20^{+0.27}_{-0.21}$			11.7/9	23.3	44.03	po	100	
129945	140146.53+024434.7	4.442	0.024	$1.80^{+0.08}_{-0.07}$			41.7/52	84.7	45.37	po	309	251
130487	140349.53+432009.9	0.666	0.012	$2.08^{+0.13}_{-0.12}$			33.1/21	4.5	44.11	po	209	59
130833	140541.16+432538.5	0.520	0.012	$2.13^{+0.16}_{-0.16}$			15.2/14	36.6	43.58	po	113	18
131828	141325.92+435146.4	1.520	0.012	$2.18^{+0.12}_{-0.11}$			15.9/19	66.6	44.54	po	84	155

Appendix A. Spectral Fitting Results

SRCID	SDSS name	z	$N_{\text{H}}^{\text{Gal}}$ ($\times 10^{20} \text{ cm}^{-2}$)	Γ	$N_{\text{H}}^{\text{intr}}$ ($\times 10^{22} \text{ cm}^{-2}$)	KT (keV)	χ^2/ν	H0	$\log(L_X)$ ($2 - 10 \text{ keV}$)	Model	Counts	
											MOS	pn
132308	141528.76-002633.2	1.155	0.032	2.23 ± 0.05			111.2/102	25.1	45.12	po	775	840
132498	141624.57+445156.4	1.995	0.012	$2.12^{+0.15}_{-0.14}$			14.7/12	25.8	45.02	po	184	
132585	141642.42+521812.7	1.285	0.013	$1.68^{+0.12}_{-0.11}$	$3.20^{+0.66}_{-0.53}$		48.0/50	55.6	44.44	apo	363	343
132613	141647.20+521115.2	2.153	0.013	$2.24^{+0.18}_{-0.18}$			21.7/11	2.7	44.70	po	163	
132680	141700.81+445606.3	0.114	0.012	2.10 ± 0.02	0.15 ± 0.004		607.0/526	0.8	43.55	po+bb	12255	19594
133099	141838.36+522359.3	1.118	0.013	2.30 ± 0.08			79.8/57	2.5	44.34	po	346	439
133240	141937.27+062414.6	1.912	0.022	$2.21^{+0.24}_{-0.21}$			11.4/8	17.9	44.81	po	84	
133435	142325.46+384032.8	0.249	0.009	2.56 ± 0.07			72.5/47	1.0	43.40	po	772	
133442	142335.86+383408.1	1.487	0.009	$2.33^{+0.22}_{-0.19}$			25.5/15	4.4	44.22	po	89	64
133464	142355.50+383150.5	1.205	0.009	$2.10^{+0.08}_{-0.07}$			56.7/46	13.3	44.62	po	336	336
133480	142406.74+383714.3	1.561	0.009	$2.32^{+0.12}_{-0.10}$			15.4/17	56.6	44.84	po	38	224
133517	142435.97+421030.4	2.218	0.013	$1.90^{+0.08}_{-0.07}$			43.5/30	5.3	45.28	po	226	242
133541	142455.53+421407.6	0.316	0.013	2.09 ± 0.05	0.13 ± 0.02		216.3/208	33.2	44.21	po+bb	2545	1965
133589	142539.38+375736.7	1.897	0.009	$2.29^{+0.31}_{-0.24}$	$5.39^{+1.74}_{-1.30}$		20.3/21	50.1	44.97	apo	104	108
133717	142737.72+424449.9	1.955	0.014	2.17 ± 0.07			93.3/66	1.5	44.70	po	887	
134109	142939.17+473949.7	1.480	0.019	2.40 ± 0.10			27.0/24	30.4	44.76	po	362	
134127	142943.07+474726.2	0.221	0.019	1.99 ± 0.02	$0.17^{+0.005}_{-0.01}$		717.4/668	9.1	44.20	po+bb	18322	27091
134160	142953.79+425110.5	1.877	0.014	2.12 ± 0.08			31.2/35	65.1	45.05	po	155	328
134182	142959.90+475523.8	1.816	0.019	$2.04^{+0.08}_{-0.07}$			35.2/37	55.5	44.83	po	120	326
134239	143025.78+415956.6	0.352	0.014	1.65 ± 0.03			151.5/142	27.7	43.74	po	1035	1144
134410	143424.93+033911.4	1.120	0.025	$1.92^{+0.12}_{-0.11}$			20.3/26	77.6	44.39	po	265	66
134414	143426.27+034817.0	2.300	0.025	$1.91^{+0.14}_{-0.13}$			12.0/19	88.7	45.02	po	88	89
134489	143455.38+035030.9	2.853	0.025	$1.92^{+0.22}_{-0.19}$			10.4/12	57.8	45.13	po	47	76
134510	143506.62+033257.2	2.404	0.026	$1.48^{+0.15}_{-0.14}$			15.1/15	44.1	44.83	po	69	78
134536	143513.89+484149.3	1.887	0.021	$1.28^{+0.12}_{-0.11}$			11.7/18	86.3	44.86	po	118	60
134549	143521.33+034803.7	0.905	0.025	$2.10^{+0.11}_{-0.10}$			20.6/22	54.8	44.33	po	158	170
134637	143621.28+484607.5	2.395	0.021	$1.78^{+0.27}_{-0.23}$			5.4/6	48.9	44.91	po	57	22
134762	143822.19+642000.5	1.163	0.017	$2.20^{+0.11}_{-0.10}$			28.5/19	7.4	44.53	po	296	
135643	144414.66+063306.7	0.208	0.025	1.76 ± 0.02	0.21 ± 0.01		551.4/511	10.5	44.48	po+bb	13247	11386
135784	144501.72+062810.1	1.536	0.025	$1.79^{+0.10}_{-0.09}$			19.6/16	23.7	45.18	po	251	
135800	144506.24+063019.6	0.302	0.025	2.05 ± 0.06			79.6/58	3.1	43.99	po	975	
135989	144636.23+402326.6	2.057	0.012	$2.06^{+0.19}_{-0.17}$			11.9/13	53.2	45.11	po	134	

Appendix A. Spectral Fitting Results

SRCID	SDSS name	z	$N_{\text{H}}^{\text{Gal}}$ ($\times 10^{20} \text{ cm}^{-2}$)	Γ	$N_{\text{H}}^{\text{intr}}$ ($\times 10^{22} \text{ cm}^{-2}$)	KT (keV)	χ^2/ν	H0	$\log(L_X)$ ($2 - 10 \text{ keV}$)	Model	MOS	Counts
136011	144645.93+403505.7	0.267	0.013	2.29 ± 0.03		0.17 ± 0.01	399.0/359	7.1	44.10	po+bb	6685	9912
136103	144727.49+403206.3	1.335	0.012	$2.25^{+0.10}_{-0.09}$			18.2/28	92.0	44.58	po	149	194
137406	150148.85+014405.1	0.484	0.042	1.91 ± 0.06		0.19 ± 0.02	237.8/232	38.2	43.81	po+bb	2245	2616
137426	150152.76+014837.4	3.774	0.042	$1.33^{+0.29}_{-0.24}$			19.7/18	34.7	44.61	po	51	50
137870	150319.42+475206.8	0.757	0.022	$2.23^{+0.17}_{-0.16}$			14.0/12	30.3	44.38	po	188	
138385	150431.30+474151.2	0.824	0.022	1.94 ± 0.03			140.8/143	53.7	44.98	po	956	1338
138405	150452.41+474132.3	1.383	0.022	$1.70^{+0.12}_{-0.11}$			11.6/18	86.8	44.72	po	93	101
138431	150545.63+014146.8	1.424	0.043	$1.88^{+0.10}_{-0.09}$			24.4/26	55.5	44.73	po	94	236
138571	150858.89+570627.8	0.669	0.015	$2.12^{+0.26}_{-0.22}$			4.3/8	83.2	43.48	po	34	52
138587	150916.15+332730.6	1.655	0.016	$2.13^{+0.17}_{-0.15}$			11.9/16	75.3	44.59	po	71	71
138635	150948.65+333626.7	0.512	0.016	$2.74^{+0.11}_{-0.10}$			25.9/40	95.8	43.43	po	237	285
138650	151002.93+570243.3	4.309	0.015	1.52 ± 0.03			175.7/134	0.9	46.45	po	917	1189
138765	151126.46+565934.7	1.031	0.015	$1.58^{+0.22}_{-0.19}$			8.0/6	23.8	44.17	po	40	42
139000	151403.00+365700.6	1.406	0.014	$2.45^{+0.16}_{-0.15}$			12.4/20	90.2	44.38	po	87	92
139076	151443.07+365050.4	0.371	0.014	1.80 ± 0.02		0.20 ± 0.01	632.1/622	38.1	44.96	po+bb	13829	17793
139113	151453.87+561031.9	1.287	0.014	$1.94^{+0.18}_{-0.16}$			15.9/16	46.3	44.50	po	99	61
139142	151510.10+562834.7	0.724	0.014	2.03 ± 0.08			51.8/40	10.0	43.93	po	310	234
139208	151535.47+365549.7	0.811	0.014	2.04 ± 0.09			17.9/29	94.6	44.42	po	238	186
139575	151651.29+562851.0	1.311	0.014	$1.97^{+0.10}_{-0.09}$			18.1/29	94.3	44.46	po	219	174
139939	151842.85+424934.1	1.465	0.019	$2.25^{+0.43}_{-0.38}$			17.1/9	4.7	44.35	po	53	46
140287	152553.89+513649.1	2.882	0.016	$1.99^{+0.05}_{-0.04}$	$3.78^{+0.49}_{-0.46}$		176.6/194	81.0	45.96	apo	1511	1722
140340	152625.52+361010.2	1.577	0.015	$2.08^{+0.22}_{-0.20}$			6.0/9	73.6	44.57	po	29	68
140438	152801.65+355316.9	1.454	0.016	$2.11^{+0.26}_{-0.20}$			11.5/10	31.8	45.00	po	108	
140895	153438.20+553945.5	1.130	0.013	1.85 ± 0.09			20.3/20	43.9	44.54	po	168	157
141163	153617.23+544710.0	1.446	0.013	$2.35^{+0.10}_{-0.09}$			31.5/41	85.7	44.70	po	180	327
141195	153634.89+544318.2	0.913	0.013	$2.21^{+0.08}_{-0.07}$			44.9/59	91.3	44.14	po	264	485
141208	153641.65+543505.5	0.447	0.013	$1.20^{+0.12}_{-0.11}$	$6.81^{+1.08}_{-0.90}$		110.8/95	12.7	43.94	apo	670	570
141491	154316.42+540526.0	0.245	0.013	1.90 ± 0.09		0.10 ± 0.01	75.4/75	46.5	43.24	po+bb	575	556
141541	154359.44+535903.2	2.370	0.013	1.99 ± 0.08	$2.57^{+0.62}_{-0.55}$		79.5/80	49.6	45.51	apo	683	547
141620	154530.24+484609.0	0.400	0.016	2.39 ± 0.06		$0.16^{+0.01}_{-0.02}$	208.4/209	49.8	44.20	po+bb	4038	2472
141624	154535.84+484713.6	1.404	0.016	$2.31^{+0.11}_{-0.10}$			21.5/30	87.2	44.59	po	241	128
143230	160106.26+084605.7	1.207	0.038	1.77 ± 0.12			5.6/11	89.6	45.05	po	184	

Appendix A. Spectral Fitting Results

SRCID	SDSS name	z	$N_{\text{H}}^{\text{Gal}}$ ($\times 10^{20} \text{ cm}^{-2}$)	Γ	$N_{\text{H}}^{\text{intr}}$ ($\times 10^{22} \text{ cm}^{-2}$)	KT (keV)	χ^2/ν	H0	$\log(L_X)$ ($2 - 10 \text{ keV}$)	Model	Counts	
											MOS	pn
143356	160318.06+430114.9	1.156	0.013	$2.01^{+0.24}_{-0.21}$			3.1/10	97.9	44.16	po	49	51
143409	160418.81+325631.3	2.281	0.024	$1.82^{+0.20}_{-0.18}$			17.5/12	13.3	45.00	po	27	100
143561	160513.17+325829.9	2.255	0.023	$2.12^{+0.10}_{-0.09}$			20.1/23	63.8	44.89	po	304	
143711	160613.65+325554.2	1.872	0.023	$1.58^{+0.12}_{-0.11}$			19.0/17	32.7	44.66	po	228	
143757	160658.30+271705.5	0.934	0.040	$1.77^{+0.08}_{-0.07}$			36.8/28	12.3	45.15	po	441	
143826	160803.47+080638.0	1.360	0.040	$1.88^{+0.20}_{-0.17}$			6.1/8	63.4	44.70	po	89	
146739	162937.14+394100.0	0.724	0.008	$1.63^{+0.22}_{-0.20}$			4.6/7	70.4	44.27	po	49	33
147172	163201.11+373750.0	1.476	0.012	2.14 ± 0.04			120.6/121	49.4	45.26	po	848	1068
147535	163255.52+373459.2	0.655	0.012	2.26 ± 0.05			103.7/86	9.4	44.45	po	603	726
148993	164056.22+363404.9	0.676	0.014	2.03 ± 0.06			71.1/53	4.9	44.74	po	873	
149405	164221.22+390333.4	1.713	0.012	$1.86^{+0.16}_{-0.14}$			14.5/18	69.7	44.82	po	92	82
150741	165430.72+395419.7	0.340	0.018	$2.08^{+0.09}_{-0.08}$			29.3/31	55.1	44.02	po	478	
151345	170100.62+641209.0	2.736	0.027	$1.73^{+0.14}_{-0.13}$			10.4/14	73.5	45.72	po	184	25
152130	170554.00+240640.0	0.902	0.044	$1.62^{+0.23}_{-0.20}$			7.1/7	41.6	44.29	po	77	
152136	170606.15+240305.4	0.791	0.044	$2.04^{+0.21}_{-0.18}$			5.1/8	74.7	43.90	po	81	
152163	170639.26+240606.1	0.836	0.043	$2.30^{+0.37}_{-0.26}$			13.6/9	13.9	43.92	po	92	
153115	171300.68+572530.2	0.360	0.025	$2.28^{+0.29}_{-0.25}$			18.0/10	5.5	43.56	po	65	56
153243	171359.51+640939.5	1.359	0.026	$2.50^{+0.23}_{-0.20}$			16.2/13	24.1	44.61	po	126	11
178050	212328.38-060013.3	1.148	0.056	$1.83^{+0.15}_{-0.14}$			10.7/9	29.4	44.82	po	153	
178463	212909.65+001214.3	1.339	0.043	$2.39^{+0.17}_{-0.15}$			22.1/19	27.8	43.99	po	70	91
178476	212912.24+120751.9	1.149	0.068	$2.33^{+0.14}_{-0.13}$			13.7/18	75.1	44.19	po	237	
180473	215419.70-091753.6	1.212	0.037	$1.93^{+0.13}_{-0.12}$			29.0/24	21.9	44.27	po	94	121
180628	215703.71-073829.8	1.899	0.036	$1.96^{+0.13}_{-0.12}$			39.3/32	17.7	44.81	po	142	145
182370	221640.14+001620.0	1.020	0.047	$2.45^{+0.16}_{-0.15}$			16.2/14	30.2	44.01	po	206	
182450	221708.83+002717.1	1.112	0.046	$2.16^{+0.13}_{-0.12}$			27.2/24	29.7	44.43	po	336	
182477	221715.18+002615.0	0.754	0.047	1.90 ± 0.03			157.2/158	50.3	44.19	po	1089	1315
182489	221719.55-081234.4	1.459	0.053	$1.95^{+0.22}_{-0.19}$			8.5/9	48.3	44.72	po	96	
182537	221729.41-081154.9	1.010	0.053	1.94 ± 0.11			31.3/19	3.8	44.70	po	299	
182571	221738.41+001206.6	1.121	0.047	2.27 ± 0.06			114.9/93	6.2	43.87	po	488	750
182630	221751.29+001146.4	1.491	0.047	$1.95^{+0.05}_{-0.04}$			87.0/96	73.2	44.37	po	553	780
182648	221755.20+001512.3	2.092	0.047	1.72 ± 0.07			90.0/61	0.9	44.50	po	300	465
182686	221806.61+000534.9	2.276	0.048	$1.96^{+0.14}_{-0.13}$			37.3/33	27.6	44.41	po	112	136

Appendix A. Spectral Fitting Results

SRCID	SDSS name	z	$N_{\text{H}}^{\text{Gal}}$ ($\times 10^{20} \text{ cm}^{-2}$)	Γ	$N_{\text{H}}^{\text{intr}}$ ($\times 10^{22} \text{ cm}^{-2}$)	KT (keV)	χ^2/ν	H0	$\log(L_X)$ ($2 - 10 \text{ keV}$)	Model	MOS	Counts	pn
182728	221821.88-081329.8	0.808	0.053	$2.13^{+0.10}_{-0.09}$			20.3/27	81.9	44.48	po	410	410	
183789	223518.33+134008.2	1.025	0.048	1.74 ± 0.11			17.4/22	74.4	44.85	po	113	113	114
183965	223607.68+134355.3	0.326	0.048	2.28 ± 0.04		0.10 ± 0.02	178.7/202	88.0	44.29	po+bb	2407	2407	2691
187727	231733.66+001128.3	0.842	0.041	$1.53^{+0.19}_{-0.18}$			10.0/9	34.9	44.25	po	94	94	
187742	231742.60+000535.1	0.321	0.041	$2.19^{+0.10}_{-0.09}$			28.1/27	40.6	44.03	po	416	416	
187748	231744.51+001102.4	0.505	0.041	2.21 ± 0.10			15.0/26	95.8	43.82	po	220	220	111
189677	233706.36+002132.3	0.713	0.038	$1.95^{+0.13}_{-0.12}$			24.7/24	42.3	44.06	po	120	120	124
189681	233707.23+002006.8	1.901	0.038	$2.27^{+0.16}_{-0.14}$			19.5/17	30.2	44.91	po	93	93	88
189786	233736.43+000950.8	1.135	0.038	$1.97^{+0.13}_{-0.11}$			14.2/16	58.4	44.33	po	41	41	125
190602	234705.67+010630.5	1.052	0.038	$1.96^{+0.18}_{-0.16}$			9.1/12	69.4	44.66	po	132	132	
190636	234715.27+005807.7	1.487	0.038	2.08 ± 0.10			22.9/25	58.2	44.81	po	152	152	173
190639	234715.98+005602.9	0.456	0.038	$2.16^{+0.07}_{-0.06}$			82.7/52	0.4	43.65	po	321	321	483
191937	000355.49+000736.4	1.027	0.032	$1.77^{+0.14}_{-0.13}$			17.2/21	69.6	44.44	po	114	114	98
191967	000442.18+000023.3	1.008	0.032	$2.00^{+0.11}_{-0.10}$			14.7/18	68.5	44.90	po	281	281	77
191979	000456.17+000645.5	1.041	0.031	$1.61^{+0.10}_{-0.09}$			20.2/24	68.5	44.58	po	233	233	77
191987	000512.11+001313.2	1.275	0.031	$2.33^{+0.20}_{-0.17}$			21.6/16	15.7	44.40	po	77	77	71
191988	000512.18+000802.9	1.121	0.031	$1.76^{+0.12}_{-0.11}$			24.4/28	66.0	44.54	po	120	120	148
192005	000531.06+000951.0	0.941	0.031	$1.60^{+0.17}_{-0.16}$			5.7/12	93.3	44.34	po	61	61	62
192021	001010.03+005126.6	0.387	0.029	$2.26^{+0.15}_{-0.14}$			17.2/15	30.6	43.38	po			222
192024	001016.22+004713.3	1.181	0.029	$2.15^{+0.16}_{-0.15}$			16.2/19	64.2	44.35	po	76	76	102
192071	001103.18+005927.2	0.486	0.029	2.50 ± 0.07			47.2/51	62.5	43.62	po	204	204	535
192079	001109.60+004545.6	1.478	0.029	$2.13^{+0.25}_{-0.20}$			18.7/12	9.6	44.40	po	120	120	
192103	001130.40+005751.8	1.492	0.029	1.54 ± 0.04			133.0/104	2.9	45.25	po	692	692	864
192106	001131.42+004718.3	1.879	0.029	$1.91^{+0.19}_{-0.17}$			10.2/11	51.6	44.45	po	31	31	80
192130	001202.35+005314.0	1.641	0.029	$1.58^{+0.17}_{-0.16}$			9.0/11	62.6	44.85	po	108	108	
192138	002155.52+001434.3	1.831	0.027	$1.59^{+0.29}_{-0.24}$			9.2/9	41.7	44.37	po	42	42	40
192150	002209.95+001629.3	0.575	0.027	$1.29^{+0.22}_{-0.19}$			30.6/21	8.0	43.39	po	96	96	71
192174	002237.90+000519.0	1.373	0.027	$1.88^{+0.14}_{-0.13}$			40.9/30	8.8	44.58	po	146	146	104
194803	011440.60+001023.0	2.279	0.034	$1.95^{+0.11}_{-0.10}$			33.7/32	38.6	44.69	po	147	147	126
194839	011513.16+002013.1	2.119	0.034	$2.02^{+0.36}_{-0.26}$			9.6/13	72.8	44.26	po	46	46	39
194853	011517.79+001715.3	1.585	0.034	$2.17^{+0.14}_{-0.12}$			25.4/18	11.4	44.49	po	231	231	
194880	011536.92-000011.0	0.531	0.035	$1.67^{+0.15}_{-0.14}$			7.4/10	68.9	43.68	po	101	101	

Appendix A. Spectral Fitting Results

SRCID	SDSS name	z	$N_{\text{H}}^{\text{Gal}}$ ($\times 10^{20} \text{ cm}^{-2}$)	Γ	$N_{\text{H}}^{\text{intr}}$ ($\times 10^{22} \text{ cm}^{-2}$)	KT (keV)	χ^2/ν	H0	$\log(L_X)$ ($2 - 10 \text{ keV}$)	Model	MOS	Counts	pn
194884	011537.72+002028.6	1.276	0.034	$2.21^{\pm 0.08}$		$0.01_{-0.01}^{+0.08}$	106.8/84	4.7	44.74	po+bb	557	668	
194887	011542.18+002300.2	1.375	0.034	$2.11^{\pm 0.23}$		$0.02_{-0.01}^{+0.23}$	66.4/51	7.3	44.72	po+bb	331	342	
194888	011544.05+002014.9	1.052	0.034	$1.56_{-0.24}^{+0.31}$			15.5/13	27.6	43.68	po	36	63	
194898	011552.59+000601.0	3.193	0.035	$1.65_{-0.22}^{+0.25}$			8.4/9	49.4	44.79	po	26	58	
194905	011557.43+000725.9	1.538	0.035	0.68 ± 0.18			5.7/10	83.8	44.09	po	48	33	
194931	011836.66+003337.9	1.630	0.033	$1.71_{-0.10}^{+0.11}$			23.0/26	63.3	44.70	po	91	150	
194934	011840.40+004004.0	1.599	0.033	$2.19_{-0.17}^{+0.20}$			5.6/12	93.5	44.27	po	60	53	
194956	011905.91+003531.6	1.294	0.033	2.18 ± 0.09			20.8/25	70.6	44.34	po	157	193	
196974	024651.91+005930.9	0.468	0.041	2.50 ± 0.12			23.2/20	27.8	44.26	po	316		
197629	033429.44+000611.0	0.347	0.079	1.36 ± 0.24		0.14 ± 0.03	6.0/12	91.8	43.12	po+bb	69	71	
201729	073635.93+304249.1	1.560	0.045	$1.70_{-0.13}^{+0.14}$			8.8/15	88.7	44.79	po	73	79	
201748	073654.04+302657.5	0.724	0.045	1.68 ± 0.12			34.1/22	4.8	44.22	po	74	149	
201764	073708.12+303914.2	1.402	0.044	$2.04_{-0.12}^{+0.14}$			36.5/26	8.2	44.51	po	125	116	
201771	073712.57+303636.6	0.918	0.044	1.98 ± 0.04			64.0/80	90.5	44.75	po	652	588	
202938	083535.80+245940.1	0.330	0.037	$1.14_{-0.33}^{+0.35}$		0.19 ± 0.03	14.7/20	79.2	42.74	po+bb	79	115	
202949	083543.01+251102.2	1.186	0.037	$2.33_{-0.08}^{+0.09}$			17.6/37	99.7	44.72	po	217	304	
203079	083946.22+511202.8	4.390	0.033	1.58 ± 0.05			65.0/61	33.9	45.97	po	448	419	
203732	090429.45+340544.9	1.299	0.024	$1.97_{-0.09}^{+0.10}$			40.2/31	12.4	44.18	po	195	185	
203734	090432.19+553830.1	0.269	0.028	$2.22_{-0.11}^{+0.12}$			18.1/22	70.1	43.22	po	152	130	
203796	090505.58+341351.7	1.025	0.023	1.64 ± 0.02			193.4/231	96.6	44.99	po	3041	2062	
203817	090516.66+340921.3	1.873	0.023	2.13 ± 0.04			124.4/121	39.9	44.86	po	856	920	
203835	090525.30+341459.8	1.583	0.023	$2.09_{-0.06}^{+0.07}$			77.3/66	16.2	44.49	po	418	441	
204017	090837.09+393533.3	0.409	0.019	1.88 ± 0.04			98.7/115	86.1	43.61	po	762	878	
204175	091557.29+292618.3	0.529	0.021	1.74 ± 0.11		$0.26_{-0.02}^{+0.01}$	148.8/141	31.0	44.10	po+bb	1062	1291	
204202	091613.59+292106.2	1.150	0.021	$1.94_{-0.08}^{+0.09}$			24.4/29	70.8	44.56	po	179	231	
204308	092531.53+362750.2	1.316	0.014	$1.82_{-0.21}^{+0.24}$			4.4/9	88.4	44.23	po	22	62	
204349	092612.00+363531.3	2.040	0.014	$2.26_{-0.13}^{+0.14}$			22.5/24	54.9	44.80	po	89	129	
204379	092633.60+362450.7	1.672	0.014	$1.88_{-0.03}^{+0.04}$			169.2/131	1.4	45.08	po	825	1150	
204414	092654.71+363434.9	1.648	0.014	$1.82_{-0.16}^{+0.19}$			9.7/14	78.1	44.35	po	39	84	
204896	095759.50+020435.9	2.030	0.028	$1.89_{-0.14}^{+0.16}$			19.5/20	49.2	44.46	po	52	118	
204954	095834.74+014502.3	1.899	0.027	1.19 ± 0.11			28.1/23	21.4	44.26	po	63	123	
205336	100251.62+022905.3	2.005	0.025	$1.85_{-0.16}^{+0.19}$			33.8/24	8.8	44.52	po	98	119	

Appendix A. Spectral Fitting Results

SRCID	SDSS name	z	$N_{\text{H}}^{\text{Gal}}$ ($\times 10^{20} \text{ cm}^{-2}$)	Γ	$N_{\text{H}}^{\text{intr}}$ ($\times 10^{22} \text{ cm}^{-2}$)	KT (keV)	χ^2/ν	H0	$\log(L_X)$ ($2 - 10 \text{ keV}$)	Model	Counts	
											MOS	pn
205588	101823.62-000527.7	1.398	0.042	$2.34^{+0.22}_{-0.19}$			8.8/13	78.5	44.34	po	46	82
205593	101827.13-000008.5	0.979	0.042	$1.95^{+0.12}_{-0.11}$			29.7/21	9.9	44.52	po	315	
205729	103056.10+645726.3	1.075	0.012	$2.11^{+0.09}_{-0.08}$			20.6/31	92.2	44.47	po	205	235
205741	103125.51+651058.7	1.268	0.012	$2.09^{+0.23}_{-0.20}$			6.9/9	64.4	44.04	po	53	46
205770	103220.93+650024.8	2.201	0.012	$1.84^{+0.20}_{-0.17}$			7.3/10	69.2	44.37	po	38	62
205894	103934.13+395257.9	1.960	0.014	$1.61^{+0.09}_{-0.08}$			22.4/23	49.8	45.05	po	159	185
206049	105540.04+065551.2	0.596	0.029	0.85 ± 0.09			20.1/21	51.4	43.90	po	282	
206056	105549.47+065541.9	0.902	0.029	1.84 ± 0.04			85.8/106	92.5	44.74	po	1867	
206076	105603.71+070234.9	2.303	0.029	$2.09^{+0.06}_{-0.05}$			59.7/64	63.0	45.10	po	636	261
206110	105622.18+071250.6	1.657	0.028	$1.89^{+0.09}_{-0.08}$			31.0/29	36.6	45.00	po	431	
206609	110913.57+613524.1	0.733	0.007	1.89 ± 0.10			25.1/30	71.9	44.15	po	105	273
206620	110934.14+611421.4	1.520	0.007	$1.98^{+0.11}_{-0.10}$			24.6/23	37.3	44.59	po	93	187
206634	111003.43+611303.1	1.870	0.007	$1.91^{+0.22}_{-0.19}$			5.6/13	95.8	44.60	po	44	74
206635	111006.94+612521.3	0.262	0.007	1.79 ± 0.09		0.17 ± 0.01	175.9/135	1.0	43.59	po+bb	708	2130
207125	120034.73+065020.3	1.950	0.014	$1.62^{+0.08}_{-0.07}$			22.3/27	72.4	45.17	po	180	233
207187	120150.70+064400.5	1.267	0.014	$2.21^{+0.18}_{-0.15}$			10.5/16	84.0	44.66	po	67	97
207821	123433.62+153004.0	1.434	0.023	$1.98^{+0.08}_{-0.07}$			44.3/44	46.0	44.74	po	252	376
208208	125030.48+002000.0	1.151	0.016	2.09 ± 0.10			26.1/24	34.6	44.97	po	187	190
208821	130050.96+585927.4	1.156	0.012	$2.04^{+0.10}_{-0.09}$			12.8/20	88.8	44.83	po	318	
208835	130112.93+590206.7	0.477	0.012	2.13 ± 0.04		$0.12^{+0.01}_{-0.005}$	229.6/207	13.5	44.49	po+bb	1969	2970
208859	130207.81+585431.3	0.807	0.012	$1.88^{+0.21}_{-0.19}$			1.5/5	91.1	44.24	po	49	29
209098	130940.69+573309.9	4.268	0.014	$1.57^{+0.09}_{-0.08}$			41.9/25	1.9	45.35	po	173	174
210523	142616.93+601553.4	1.365	0.016	$1.93^{+0.11}_{-0.10}$			24.3/24	44.4	44.74	po	174	107
210538	142656.17+602550.8	3.192	0.016	1.81 ± 0.06			43.9/48	64.3	45.69	po	423	279
210539	142656.53+602903.2	0.623	0.016	1.91^{α}			75.5/76	49.5	44.26	po+bb	876	330
210692	144003.78+023805.7	1.497	0.030	$2.49^{+0.26}_{-0.23}$			2.7/7	91.3	44.33	po	34	50
210769	144944.23+630656.0	0.519	0.017	$2.69^{+0.20}_{-0.17}$			22.9/17	15.2	43.71	po	78	107
210996	150103.40+421656.9	1.908	0.015	$1.66^{+0.16}_{-0.14}$			22.8/15	8.8	44.40	po	79	65
211083	150140.94+421834.1	0.978	0.015	2.67 ± 0.10			49.9/42	18.9	44.05	po	203	372
211185	150407.51-024816.5	0.217	0.060	$2.03^{+0.003}_{-0.002}$	$0.29^{+0.01}_{-0.001}$	$0.09^{+0.001}_{-0.0006}$	2534.1/1621	0.0	45.29	apo+bb+line	153280	172633
211203	150419.85-023514.7	0.563	0.059	1.82 ± 0.09			23.0/25	57.7	44.33	po	371	
211207	150422.10-024556.8	2.064	0.060	$1.82^{+0.12}_{-0.11}$			14.1/15	51.7	44.86	po	201	

Appendix A. Spectral Fitting Results

SRCID	SDSS name	z	$N_{\text{H}}^{\text{Gal}}$ ($\times 10^{20} \text{ cm}^{-2}$)	Γ	$N_{\text{H}}^{\text{intr}}$ ($\times 10^{22} \text{ cm}^{-2}$)	KT (keV)	χ^2/ν	H0	$\log(L_X)$ ($2 - 10 \text{ keV}$)	Model	MOS	Counts	pn
211251	150626.44+030659.9	0.174	0.038	2.14 ± 0.03			130.1/126	38.2	43.69	po	2501	343	
211259	150701.56+010805.4	1.191	0.044	$2.18^{+0.16}_{-0.14}$			7.0/19	99.4	44.54	po	68	117	
211281	150743.32+011324.0	1.354	0.043	$1.62^{+0.07}_{-0.06}$	$0.96^{+0.27}_{-0.23}$		82.4/89	67.7	45.25	apo	579	733	
211318	150819.57+010207.1	1.363	0.043	2.01 ± 0.06			47.7/45	36.2	44.94	po	290	373	
211336	150843.50+010725.5	1.238	0.043	$1.93^{+0.19}_{-0.16}$			8.3/12	75.8	44.61	po	116		
211494	153434.59+574723.6	1.236	0.017	$1.89^{+0.18}_{-0.16}$			13.0/13	44.7	44.30	po	164		
211507	153458.41+575625.7	1.129	0.017	1.96 ± 0.12			14.4/16	57.2	44.44	po	228		
211618	153703.94+533219.9	2.404	0.013	1.42 ± 0.07			32.5/32	44.3	45.26	po	246	139	
211635	153716.30+574838.6	0.641	0.017	2.60 ± 0.12			107.6/43	0.0	43.87	po	605		
212440	162718.13+495511.8	0.904	0.017	1.84 ± 0.04			92.6/88	34.8	44.98	po	756	614	
214255	171029.48+590834.8	0.864	0.023	$1.87^{+0.14}_{-0.13}$			11.2/13	59.5	44.65	po	133		
214282	171126.94+585544.2	0.537	0.023	$2.25^{+0.11}_{-0.10}$			17.2/24	83.8	44.14	po	356		
214424	171815.96+584613.6	1.413	0.026	$2.29^{+0.24}_{-0.21}$			12.0/14	60.5	44.44	po	120		
214426	171818.14+584905.2	0.635	0.026	$2.29^{+0.12}_{-0.11}$			30.2/30	45.7	43.84	po	336	40	
214486	171930.24+584804.7	2.081	0.027	2.04 ± 0.05			90.9/100	73.1	45.28	po	908	477	
214547	172052.30+590153.7	0.351	0.028	1.65 ± 0.06			45.2/51	70.1	43.91	po	239	457	
214578	172130.96+584404.7	1.000	0.028	2.22 ± 0.06			107.5/81	2.6	44.75	po	674	387	
220070	220529.34+003110.6	2.450	0.051	$1.87^{+0.18}_{-0.17}$			14.2/13	36.0	44.75	po	76	40	
220558	231940.16+001008.4	0.973	0.041	2.09 ± 0.22			21.9/11	2.5	44.36	po	115		
220705	232810.56+150012.8	1.539	0.041	1.39 ± 0.05			98.2/70	1.5	44.57	po	415	450	
220878	233254.46+151305.4	0.215	0.039	$1.94^{+0.10}_{-0.09}$			28.8/26	31.9	43.53	po	315	58	
221066	235800.62+000107.5	1.454	0.032	$1.85^{+0.13}_{-0.12}$			7.0/18	99.0	44.81	po	78	102	
221075	235815.45+000327.1	1.828	0.032	$2.06^{+0.14}_{-0.13}$			21.3/17	21.5	44.92	po	43	132	
221105	235844.95+000724.0	1.983	0.032	$2.33^{+0.25}_{-0.22}$			9.0/7	25.2	44.87	po	78		
221106	235845.67+000459.6	1.609	0.032	$1.72^{+0.13}_{-0.12}$			28.4/23	19.9	44.79	po	132	84	

Table A.1: Spectral Fitting Results.

^a The po+bb sources re-fit over 0.5 – 12.0 keV with a fixed Γ from a power-law fit over 2 – 10 keV in the rest frame.

References

- Abramowicz M. A., Czerny B., Lasota J. P., Szuszkiewicz E., 1988, *ApJ*, 332, 646
- Adelman-McCarthy J. K., 2007, *ApJS*, 172, 634
- Agrawal P. C., 2006, *Advances in Space Research*, 38, 2989
- Aharonian F., Akhperjanian A. G., Bazer-Bachi A. R., et al., 2006, *Science*, 314, 1424
- Alexander D. M., Hickox R. C., 2012, *New Astronomy Review*, 56, 93
- Antonucci R., 1993, *ARA&A*, 31, 473
- Antonucci R. R. J., Miller J. S., 1985, *ApJ*, 297, 621
- Arnaud K. A., 1996, in *Astronomical Society of the Pacific Conference Series*, Vol. 101, *Astronomical Data Analysis Software and Systems V*, Jacoby G. H., Barnes J., eds., pp. 17–+
- Arnaud K. A., Branduardi-Raymont G., Culhane J. L., Fabian A. C., Hazard C., McGlynn T. A., Shafer R. A., Tennant A. F., Ward M. J., 1985, *MNRAS*, 217, 105
- Assef R. J., Denney K. D., Kochanek C. S., Peterson B. M., Kozłowski S., et al., 2011, *ApJ*, 742, 93
- Avni Y., Tananbaum H., 1986, *ApJ*, 305, 83
- Bahcall J. N., Kirhakos S., Saxe D. H., Schneider D. P., 1997, *ApJ*, 479, 642
- Balbus S. A., Hawley J. F., 1991, *ApJ*, 376, 214
- Balucinska-Church M., McCammon D., 1992, *ApJ*, 400, 699
- Band D. L., Grindlay J. E., 1986, *ApJ*, 308, 576
- Baskin A., Laor A., 2005, *MNRAS*, 356, 1029
- Bechtold J., Siemiginowska A., Shields J., Czerny B., Janiuk A., Hamann F., Aldcroft T. L., Elvis M., Dobrzycki A., 2003, *ApJ*, 588, 119
- Becker R. H., White R. L., Helfand D. J., 1995, *ApJ*, 450, 559
- Begelman M. C., 2002, *ApJL*, 568, L97
- Begelman M. C., Blandford R. D., Rees M. J., 1984, *Reviews of Modern Physics*, 56, 255
- Bennett A. S., 1962, *MNRAS*, 125, 75
- Bevington P. R., 1969, *Data reduction and error analysis for the physical sciences*, Bevington, P. R., ed.

-
- Bianchi L., Rodriguez-Merino L., Viton M., Laget M., Efremova B., et al., 2007a, *ApJS*, 173, 659
- Bianchi S., Guainazzi M., Matt G., Fonseca Bonilla N., 2007b, *A&A*, 467, L19
- Bianchi S., Guainazzi M., Matt G., Fonseca Bonilla N., Ponti G., 2009, *A&A*, 495, 421
- Blandford R. D., Rees M. J., 1978, *Physica Scripta*, 17, 265
- Blandford R. D., Znajek R. L., 1977, *MNRAS*, 179, 433
- Blundell K. M., Kuncic Z., 2007, *ApJL*, 668, L103
- Blustin A. J., Page M. J., Fuerst S. V., Branduardi-Raymont G., Ashton C. E., 2005, *A&A*, 431, 111
- Boller T., Brandt W. N., Fink H., 1996, *A&A*, 305, 53
- Boroson T. A., 2002, *ApJ*, 565, 78
- Brandt W. N., Mathur S., Elvis M., 1997, *MNRAS*, 285, L25
- Brinkmann W., Laurent-Muehleisen S. A., Voges W., Siebert J., Becker R. H., Brotherton M. S., White R. L., Gregg M. D., 2000, *A&A*, 356, 445
- Calderone G., Sbarrato T., Ghisellini G., 2012, *MNRAS*, L482
- Cardelli J. A., Clayton G. C., Mathis J. S., 1989, *ApJ*, 345, 245
- Carrera F. J., Barcons X., Fabian A. C., Hasinger G., Mason K. O., McMahon R. G., Mittaz J. P. D., Page M. J., 1998, *MNRAS*, 299, 229
- Chevallier L., Collin S., Dumont A.-M., Czerny B., Mouchet M., Gonçalves A. C., Goosmann R., 2006, *A&A*, 449, 493
- Corral A., Della Ceca R., Caccianiga A., Severgnini P., Brunner H., Carrera F. J., Page M. J., Schwope A. D., 2011, *A&A*, 530, A42+
- Croom S. M., Boyle B. J., Shanks T., Smith R. J., Miller L., Outram P. J., Loaring N. S., Hoyle F., da Ângela J., 2005, *MNRAS*, 356, 415
- Crummy J., Fabian A. C., Gallo L., Ross R. R., 2006, *MNRAS*, 365, 1067
- Cutri R. M., Skrutskie M. F., van Dyk S., et al., 2003, 2MASS All Sky Catalog of point sources.
- Cutri R. M., Wright E. L., et al., 2012, Explanatory Supplement to the WISE All-Sky Data Release Products
- Czerny B., Elvis M., 1987, *ApJ*, 321, 305
- Dai X., Chartas G., Eracleous M., Garmire G. P., 2004, *ApJ*, 605, 45
- Darg D. W., Kaviraj S., Lintott C. J., Schawinski K., Sarzi M., et al., 2010, *MNRAS*, 401, 1552
- De Robertis M. M., Yee H. K. C., Hayhoe K., 1998, *ApJ*, 496, 93

-
- den Herder J. W., Brinkman A. C., Kahn S. M., Branduardi-Raymont G., Thomsen K., et al., 2001, *A&A*, 365, L7
- Dickey J. M., Lockman F. J., 1990, *ARA&A*, 28, 215
- Done C., 2010, preprint, arXiv:1008.2287
- Done C., Davis S. W., Jin C., Blaes O., Ward M., 2012, *MNRAS*, 420, 1848
- Done C., Nayakshin S., 2007, *MNRAS*, 377, L59
- Edge D. O., Shakeshaft J. R., McAdam W. B., Baldwin J. E., Archer S., 1959, *Memoirs of the RAS*, 68, 37
- Elvis M., 2000, *ApJ*, 545, 63
- Elvis M., Risaliti G., Nicastro F., Miller J. M., Fiore F., Puccetti S., 2004, *ApJL*, 615, L25
- Elvis M., Wilkes B. J., McDowell J. C., Green R. F., Bechtold J., Willner S. P., Oey M. S., Polomski E., Cutri R., 1994, *ApJS*, 95, 1
- Fabian A. C., Miniutti G., 2005, preprint, arXiv:0507409
- Fanaroff B. L., Riley J. M., 1974, *MNRAS*, 167, 31P
- Ferrarese L., Merritt D., 2000, *ApJL*, 539, L9
- Foltz C. B., Chaffee F. H., Hewett P. C., Weymann R. J., Morris S. L., 1990, in *Bulletin of the American Astronomical Society*, Vol. 22, *Bulletin of the American Astronomical Society*, pp. 806–+
- Franceschini A., Vercellone S., Fabian A. C., 1998, *MNRAS*, 297, 817
- Francis P. J., Wills B. J., 1999, in *Astronomical Society of the Pacific Conference Series*, Vol. 162, *Quasars and Cosmology*, G. Ferland & J. Baldwin, ed., pp. 363–+
- Fukugita M., Ichikawa T., Gunn J. E., Doi M., Shimasaku K., Schneider D. P., 1996, *AJ*, 111, 1748
- Gabor J. M., Impey C. D., Jahnke K., Simmons B. D., Trump J. R., Koekemoer A. M., Brusa M., Cappelluti N., Schinnerer E., Smolčić V., Salvato M., et al., 2009, *ApJ*, 691, 705
- Gallagher S. C., Brandt W. N., Chartas G., Garmire G. P., 2002, *ApJ*, 567, 37
- Gallo E., Fender R. P., Pooley G. G., 2003, *MNRAS*, 344, 60
- Gandhi P., Horst H., Smette A., Hönig S., Comastri A., Gilli R., Vignali C., Duschl W., 2009, *A&A*, 502, 457
- Ganguly R., Brotherton M. S., 2008, *ApJ*, 672, 102
- Ganguly R., Brotherton M. S., Cales S., Scoggins B., Shang Z., Vestergaard M., 2007, *ApJ*, 665, 990
- Garcet O., Gandhi P., Gosset E., Sprimont P. G., Surdej J., et al., 2007, *A&A*, 474, 473

-
- Gebhardt K., Bender R., Bower G., Dressler A., Faber S. M., Filippenko A. V., Green R., Grillmair C., Ho L. C., Kormendy J., Lauer T. R., Magorrian J., Pinkney J., Richstone D., Tremaine S., 2000, *ApJL*, 539, L13
- Gehrels N., Chincarini G., Giommi P., Mason K. O., Nousek J. A., Wells A. A., White N. E., et al., 2004, *ApJ*, 611, 1005
- Georgakakis A., Nandra K., Laird E. S., Cooper M. C., Gerke B. F., Newman J. A., Croton D. J., Davis M., Faber S. M., Coil A. L., 2007, *ApJL*, 660, L15
- Gierliński M., Done C., 2004, *MNRAS*, 349, L7
- Gilli R., Zamorani G., Miyaji T., Silverman J., Brusa M., et al., 2009, *A&A*, 494, 33
- Giustini M., Cappi M., Vignali C., 2008, *A&A*, 491, 425
- Glikman E., Helfand D. J., White R. L., 2006, *ApJ*, 640, 579
- Gofford J., Reeves J. N., Turner T. J., Tombesi F., Braito V., Porquet D., Miller L., Kraemer S. B., Fukazawa Y., 2011, *MNRAS*, 414, 3307
- Green P. J., Aldcroft T. L., Richards G. T., et al., 2009, *ApJ*, 690, 644
- Green P. J., Mathur S., 1996, *ApJ*, 462, 637
- Greene J. E., Peng C. Y., Ludwig R. R., 2010, *ApJ*, 709, 937
- Greenhill L. J., Booth R. S., Ellingsen S. P., Herrnstein J. R., Jauncey D. L., McCulloch P. M., Moran J. M., Norris R. P., Reynolds J. E., Tzioumis A. K., 2003, *ApJ*, 590, 162
- Grogin N. A., Conselice C. J., Chatzichristou E., et al., 2005, *ApJL*, 627, L97
- Grupe D., 2004, *AJ*, 127, 1799
- Grupe D., Beuermann K., Thomas H., Mannheim K., Fink H. H., 1998, *A&A*, 330, 25
- Grupe D., Komossa S., Leighly K. M., Page K. L., 2010, *ApJS*, 187, 64
- Guilbert P. W., Rees M. J., 1988, *MNRAS*, 233, 475
- Gunn J. E., Carr M., Rockosi C., Sekiguchi M., Berry K., et al., 1998, *AJ*, 116, 3040
- Gunn J. E., Siegmund W. A., Mannery E. J., Owen R. E., Hull C. L., et al., 2006, *AJ*, 131, 2332
- Haardt F., Maraschi L., 1993, *ApJ*, 413, 507
- Haas M., Klaas U., Müller S. A. H., Bertoldi F., Camenzind M., Chini R., Krause O., Lemke D., Meisenheimer K., Richards P. J., Wilkes B. J., 2003, *A&A*, 402, 87
- Halpern J. P., 1984, *ApJ*, 281, 90
- Häring N., Rix H.-W., 2004, *ApJL*, 604, L89
- Harrison F. A., Boggs S., Christensen F., Craig W., Hailey C., Stern D., Zhang W., et al., 2010, in Society of Photo-Optical Instrumentation Engineers (SPIE) Conference Series, Vol. 7732

-
- Hasinger G., 2008, *A&A*, 490, 905
- Hine R. G., Longair M. S., 1979, *MNRAS*, 188, 111
- Ho L. C., 2002, *ApJ*, 564, 120
- Holt S. S., McCray R., 1982, *ARA&A*, 20, 323
- Hopkins P. F., Richards G. T., Hernquist L., 2007, *ApJ*, 654, 731
- Horst H., Smette A., Gandhi P., Duschl W. J., 2006, *A&A*, 457, L17
- Hutchings J. B., Frenette D., Hanisch R., Mo J., Dumont P. J., Redding D. C., Neff S. G., 2002, *AJ*, 123, 2936
- Hutchings J. B., Scholz P., Bianchi L., 2009, *AJ*, 137, 3533
- Hutton S., Alexander D. M., Mateos S., Scott A. E., Stewart G. C., Ward M. J., in preparation, *MNRAS*
- Ishibashi W., Courvoisier T. J.-L., 2009, *A&A*, 495, 113
- , 2010, *A&A*, 512, A58+
- Isobe T., Feigelson E. D., Akritas M. G., Babu G. J., 1990, *ApJ*, 364, 104
- Iwasawa K., Fabian A. C., Reynolds C. S., Nandra K., Otani C., Inoue H., Hayashida K., Brandt W. N., Dotani T., Kunieda H., Matsuoka M., Tanaka Y., 1996, *MNRAS*, 282, 1038
- Iwasawa K., Taniguchi Y., 1993, *ApJL*, 413, L15
- Jaffe W., Meisenheimer K., Röttgering H. J. A., Leinert C., Richichi A., et al., 2004, *Nature*, 429, 47
- Jansen F., Lumb D., et al., 2001, *A&A*, 365, L1
- Jiang P., Wang J. X., Wang T. G., 2006, *ApJ*, 644, 725
- Jin C., Ward M., Done C., Gelbord J., 2012, *MNRAS*, 420, 1825
- Jogee S., 2006, in *Lecture Notes in Physics*, Berlin Springer Verlag, Vol. 693, *Physics of Active Galactic Nuclei at all Scales*, D. Alloin, ed., p. 143
- Just D. W., Brandt W. N., Shemmer O., Steffen A. T., Schneider D. P., Chartas G., Garmire G. P., 2007, *ApJ*, 665, 1004
- Kaiser N., Burgett W., Chambers K., Denneau L., Heasley J., Jedicke R., Magnier E., Morgan J., Onaka P., Tonry J., 2010, in *Society of Photo-Optical Instrumentation Engineers (SPIE) Conference Series*, Vol. 7733
- Kaspi S., Smith P. S., Netzer H., Maoz D., Jannuzi B. T., Giveon U., 2000, *ApJ*, 533, 631
- Kauffmann G., Haehnelt M., 2000, *MNRAS*, 311, 576
- Kawaguchi T., Shimura T., Mineshige S., 2001, *ApJ*, 546, 966

-
- Kellermann K. I., Sramek R., Schmidt M., Shaffer D. B., Green R., 1989, *AJ*, 98, 1195
- Kelly B. C., Bechtold J., Siemiginowska A., Aldcroft T., Sobolewska M., 2007, *ApJ*, 657, 116
- Kii T., Williams O. R., Ohashi T., et al., 1991, *ApJ*, 367, 455
- King A., 2003, *ApJL*, 596, L27
- King A. R., 2010, *MNRAS*, 402, 1516
- Kormendy J., Gebhardt K., 2001, in American Institute of Physics Conference Series, Vol. 586, 20th Texas Symposium on relativistic astrophysics, J. C. Wheeler & H. Martel, ed., pp. 363–381
- Kormendy J., Gebhardt K., Richstone D., 2000, in Bulletin of the American Astronomical Society, Vol. 32, American Astronomical Society Meeting Abstracts #196, pp. 702–+
- Kormendy J., Richstone D., 1995, *ARA&A*, 33, 581
- Koss M., Mushotzky R., Veilleux S., Winter L., 2010, *ApJL*, 716, L125
- Krabbe A., Böker T., Maiolino R., 2001, *ApJ*, 557, 626
- Krolik J. H., 2007, *ApJ*, 661, 52
- Kuraszkiewicz J., Wilkes B. J., Schmidt G., Ghosh H., Smith P. S., Cutri R., Hines D., Huff E. M., McDowell J. C., Nelson B., 2009, *ApJ*, 692, 1143
- Lacy M., Laurent-Muehleisen S. A., Ridgway S. E., Becker R. H., White R. L., 2001, *ApJL*, 551, L17
- Lake G., Katz N., Moore B., 1998, *ApJ*, 495, 152
- Laor A., 2000, *ApJL*, 543, L111
- Laor A., Behar E., 2008, *MNRAS*, 390, 847
- Lawrence A., 1991, *MNRAS*, 252, 586
- Lawrence A., Elvis M., 1982, *ApJ*, 256, 410
- , 2010, *ApJ*, 714, 561
- Levenson N. A., Radomski J. T., Packham C., Mason R. E., Schaefer J. J., Telesco C. M., 2009, *ApJ*, 703, 390
- Li Z.-Y., Wu X.-B., Wang R., 2008, *ApJ*, 688, 826
- Lightman A. P., White T. R., 1988, *ApJ*, 335, 57
- Liu Y., Jiang D. R., Gu M. F., 2006, *ApJ*, 637, 669
- Livio M., Ogilvie G. I., Pringle J. E., 1999, *ApJ*, 512, 100
- Lobban A. P., Reeves J. N., Miller L., Turner T. J., Braitto V., Kraemer S. B., Crenshaw D. M., 2011, *MNRAS*, 414, 1965

-
- Lund N., Budtz-Jørgensen C., Westergaard N. J., et al., 2003, *A&A*, 411, L231
- Lusso E., Comastri A., Vignali C., Zamorani G., Brusa M., et al., 2010, *A&A*, 512, A34+
- Lutz D., Sturm E., Genzel R., Spoon H. W. W., Stacey G. J., 2004, *A&A*, 426, L5
- Lynden-Bell D., 1969, *Nature*, 223, 690
- Magdziarz P., Blaes O. M., Zdziarski A. A., Johnson W. N., Smith D. A., 1998, *MNRAS*, 301, 179
- Magorrian J., Tremaine S., Richstone D., Bender R., Bower G., Dressler A., Faber S. M., Gebhardt K., Green R., Grillmair C., Kormendy J., Lauer T., 1998, *AJ*, 115, 2285
- Mainieri V., Hasinger G., Cappelluti N., et al., 2007, *ApJS*, 172, 368
- Maiolino R., Marconi A., Salvati M., Risaliti G., Severgnini P., Oliva E., La Franca F., Vanzani L., 2001, *A&A*, 365, 28
- Maiolino R., Shemmer O., Imanishi M., Netzer H., Oliva E., Lutz D., Sturm E., 2007, *A&A*, 468, 979
- Malkan M. A., Sargent W. L. W., 1982, *ApJ*, 254, 22
- Marchese E., Della Ceca R., Caccianiga A., Severgnini P., Corral A., Fanali R., 2012, *A&A*, 539, A48
- Marconi A., Hunt L. K., 2003, *ApJL*, 589, L21
- Marconi A., Risaliti G., Gilli R., Hunt L. K., Maiolino R., Salvati M., 2004, *MNRAS*, 351, 169
- Mason K. O., Breeveld A., Much R., et al., 2001, *A&A*, 365, L36
- Mateos S., Barcons X., Carrera F. J., Ceballos M. T., Caccianiga A., Lamer G., Maccacaro T., Page M. J., Schwope A., Watson M. G., 2005a, *A&A*, 433, 855
- Mateos S., Barcons X., Carrera F. J., Ceballos M. T., Hasinger G., Lehmann I., Fabian A. C., Streblyanska A., 2005b, *A&A*, 444, 79
- Mateos S., Carrera F. J., Page M. J., Watson M. G., Corral A., Tedds J. A., Ebrero J., Krumpel M., Schwope A., Ceballos M. T., 2010, *A&A*, 510, A35+
- Mateos S., Saxton R. D., Read A. M., Sembay S., 2009, *A&A*, 496, 879
- Matsuta K., Gandhi P., Dotani T., Nakagawa T., Isobe N., Ueda Y., Ichikawa K., Terashima Y., Oyabu S., Yamamura I., Stawarz Ł., 2012, *ApJ*, 753, 104
- Matt G., 2002, Royal Society of London Philosophical Transactions Series A, 360, 2045
- McLure R. J., Dunlop J. S., 2001, *MNRAS*, 327, 199
- , 2002, *MNRAS*, 331, 795
- , 2004, *MNRAS*, 352, 1390
- McLure R. J., Jarvis M. J., 2002, *MNRAS*, 337, 109

-
- Merloni A., Heinz S., di Matteo T., 2003, *MNRAS*, 345, 1057
- Metcalf R. B., Magliocchetti M., 2006, *MNRAS*, 365, 101
- Miller B. P., Brandt W. N., Schneider D. P., Gibson R. R., Steffen A. T., Wu J., 2011, *ApJ*, 726, 20
- Mitsuda K., Bautz M., Inoue H., Kelley R. L., Koyama K., Kunieda H., Makishima K., Ogawara Y., Petre R., Takahashi T., Tsunemi H., White N. E., et al., 2007, *PASJ*, 59, 1
- Mittaz J. P. D., Carrera F. J., Romero-Colmenero E., Mason K. O., Hasinger G., McMahon R., Andernach H., Bower R., Burgos-Martin J., González-Serrano J. I., Wonnacott D., 1999, *MNRAS*, 308, 233
- Molina M., Bassani L., Malizia A., Stephen J. B., Bird A. J., Dean A. J., Panessa F., de Rosa A., Landi R., 2009, *MNRAS*, 399, 1293
- Morrissey P., Conrow T., Barlow T. A., Small T., Seibert M., Wyder T. K., Budavári T., et al., 2007, *ApJS*, 173, 682
- Mullaney J. R., Alexander D. M., Goulding A. D., Hickox R. C., 2011, *MNRAS*, 414, 1082
- Mushotzky R. F., 1982, *ApJ*, 256, 92
- Mushotzky R. F., Done C., Pounds K. A., 1993, *ARA&A*, 31, 717
- Mushotzky R. F., Marshall F. E., Boldt E. A., Holt S. S., Serlemitsos P. J., 1980, *ApJ*, 235, 377
- Myers A. D., Brunner R. J., Richards G. T., Nichol R. C., Schneider D. P., Vanden Berk D. E., Scranton R., Gray A. G., Brinkmann J., 2006, *ApJ*, 638, 622
- Nandra K., Fabian A. C., Brandt W. N., Kunieda H., Matsuoka M., Mihara T., Ogasaka Y., Terashima Y., 1995, *MNRAS*, 276, 1
- Nandra K., Pounds K. A., 1994, *MNRAS*, 268, 405
- Nandra K., Pounds K. A., Stewart G. C., Fabian A. C., Rees M. J., 1989, *MNRAS*, 236, 39P
- Nayakshin S., 2005, *MNRAS*, 359, 545
- Nenkova M., Sirocky M. M., Ivezić Ž., Elitzur M., 2008a, *ApJ*, 685, 147
- Nenkova M., Sirocky M. M., Nikutta R., Ivezić Ž., Elitzur M., 2008b, *ApJ*, 685, 160
- Netzer H., 1990, in *Active Galactic Nuclei*, R. D. Blandford, H. Netzer, L. Woltjer, T. J.-L. Courvoisier, & M. Mayor, ed., pp. 57–160
- Netzer H., Lutz D., Schweitzer M., Contursi A., Sturm E., Tacconi L. J., Veilleux S., Kim D., Rupke D., Baker A. J., Dasyra K., Mazzarella J., Lord S., 2007, *ApJ*, 666, 806
- Oke J. B., Gunn J. E., 1983, *ApJ*, 266, 713
- Oshlack A. Y. K. N., Webster R. L., Whiting M. T., 2002, *ApJ*, 576, 81
- Osterbrock D. E., 1978, *Proceedings of the National Academy of Science*, 75, 540

-
- , 1981, *ApJ*, 249, 462
- Osterbrock D. E., Pogge R. W., 1985, *ApJ*, 297, 166
- Padovani P., Urry C. M., 1992, *ApJ*, 387, 449
- Page K. L., O’Brien P. T., Reeves J. N., Turner M. J. L., 2004a, *MNRAS*, 347, 316
- Page K. L., Reeves J. N., O’Brien P. T., Turner M. J. L., Worrall D. M., 2004b, *MNRAS*, 353, 133
- Page M. J., Loaring N. S., Dwelly T., Mason K. O., McHardy I., Gunn K., Moss D., Sasseen T., Cordova F., Kennea J., Seymour N., 2006, *MNRAS*, 369, 156
- Page M. J., McHardy I. M., Gunn K. F., Loaring N. S., Mason K. O., Sasseen T., Newsam A., Ware A., Kennea J., Sekiguchi K., Takata T., 2003, *Astronomische Nachrichten*, 324, 101
- Panessa F., Barcons X., Bassani L., Cappi M., Carrera F. J., Ho L. C., Pellegrini S., 2007, *A&A*, 467, 519
- Panessa F., Bassani L., 2002, *A&A*, 394, 435
- Perola G. C., Puccetti S., Fiore F., Sacchi N., Brusa M., Cocchia F., et al., 2004, *A&A*, 421, 491
- Peterson B. M., 1993, *Publications of the ASP*, 105, 247
- , 1997, *An Introduction To Active Galactic Nuclei*. Cambridge University Press
- Piconcelli E., Cappi M., Bassani L., Di Cocco G., Dadina M., 2003, *A&A*, 412, 689
- Piconcelli E., Jimenez-Bailón E., Guainazzi M., Schartel N., Rodríguez-Pascual P. M., Santos-Lleó M., 2005, *A&A*, 432, 15
- Pier E. A., Krolik J. H., 1993, *ApJ*, 418, 673
- Porquet D., Reeves J. N., O’Brien P., Brinkmann W., 2004, *A&A*, 422, 85
- Pounds K. A., Done C., Osborne J. P., 1995, *MNRAS*, 277, L5
- Pounds K. A., King A. R., Page K. L., O’Brien P. T., 2003a, *MNRAS*, 346, 1025
- Pounds K. A., Nandra K., Stewart G. C., George I. M., Fabian A. C., 1990, *Nature*, 344, 132
- Pounds K. A., Nandra K., Stewart G. C., Leighly K., 1989, *MNRAS*, 240, 769
- Pounds K. A., Reeves J. N., 2009, *MNRAS*, 397, 249
- Pounds K. A., Reeves J. N., King A. R., Page K. L., 2004, *MNRAS*, 350, 10
- Pounds K. A., Reeves J. N., King A. R., Page K. L., O’Brien P. T., Turner M. J. L., 2003b, *MNRAS*, 345, 705
- Pounds K. A., Vaughan S., 2011, *MNRAS*, 413, 1251

-
- Pozzi F., Vignali C., Comastri A., Bellocchi E., Fritz J., Gruppioni C., Mignoli M., Maiolino R., Pozzetti L., Brusa M., Fiore F., Zamorani G., 2010, *A&A*, 517, A11+
- Predehl P., Schmitt J. H. M. M., 1995, *A&A*, 293, 889
- Pringle J. E., Rees M. J., 1972, *A&A*, 21, 1
- Prochaska J. X., Herbert-Fort S., Wolfe A. M., 2005, *ApJ*, 635, 123
- Rafanelli P., Rifatto A., 2000, *Mem.S.A.It.*, 71, 981
- Rao S. M., Turnshek D. A., Nestor D. B., 2006, *ApJ*, 636, 610
- Rees M. J., Silk J. I., Werner M. W., Wickramasinghe N. C., 1969, *Nature*, 223, 788
- Reeves J., Done C., Pounds K., Terashima Y., Hayashida K., Anabuki N., Uchino M., Turner M., 2008, *MNRAS*, 385, L108
- Reeves J. N., O'Brien P. T., Ward M. J., 2003, *ApJL*, 593, L65
- Reeves J. N., Turner M. J. L., 2000, *MNRAS*, 316, 234
- Reeves J. N., Turner M. J. L., Ohashi T., Kii T., 1997, *MNRAS*, 292, 468
- Reichard T. A., Richards G. T., Hall P. B., Schneider D. P., Vanden Berk D. E., Fan X., York D. G., Knapp G. R., Brinkmann J., 2003, *AJ*, 126, 2594
- Remillard R. A., McClintock J. E., 2006, *ARA&A*, 44, 49
- Reynolds C. S., 1997, *MNRAS*, 286, 513
- Richards G. T., Fan X., Newberg H. J., Strauss M. A., Vanden Berk D. E., Schneider D. P., Yanny B. e. a., 2002, *AJ*, 123, 2945
- Richards G. T., Lacy M., Storrie-Lombardi L. J., Hall P. B., Gallagher S. C., et al., 2006, *ApJS*, 166, 470
- Rieke G. H., 1978, *ApJ*, 226, 550
- Risaliti G., Elvis M., 2004, in *Astrophysics and Space Science Library*, Vol. 308, *Supermassive Black Holes in the Distant Universe*, Barger A. J., ed., pp. 187–+
- Risaliti G., Elvis M., Fabbiano G., Baldi A., Zezas A., Salvati M., 2007, *ApJL*, 659, L111
- Risaliti G., Elvis M., Nicastro F., 2002, *ApJ*, 571, 234
- Risaliti G., Salvati M., Elvis M., Fabbiano G., Baldi A., Bianchi S., Braitto V., Guainazzi M., Matt G., Miniutti G., Reeves J., Soria R., Zezas A., 2009a, *MNRAS*, 393, L1
- Risaliti G., Young M., Elvis M., 2009b, *ApJL*, 700, L6
- Ross R. R., Fabian A. C., 2005, *MNRAS*, 358, 211
- Rózańska A., 1999, *MNRAS*, 308, 751
- Ryabinkov A. I., Kaminker A. D., Varshalovich D. A., 2003, *A&A*, 412, 707

-
- Rybicki G. B., Lightman A. P., 1979, *Radiative Processes in Astrophysics*. John Wiley & Sons, Inc.
- Saez C., Brandt W. N., Shemmer O., Chomiuk L., Lopez L. A., Marshall H. L., Miller B. P., Vignali C., 2011, *ApJ*, 738, 53
- Saez C., Chartas G., Brandt W. N., Lehmer B. D., Bauer F. E., Dai X., Garmire G. P., 2008, *AJ*, 135, 1505
- Sambruna R. M., Eracleous M., Mushotzky R. F., 1999, *ApJ*, 526, 60
- Sanders D. B., Phinney E. S., Neugebauer G., Soifer B. T., Matthews K., 1989, *ApJ*, 347, 29
- Sanders D. B., Soifer B. T., Elias J. H., Madore B. F., Matthews K., Neugebauer G., Scoville N. Z., 1988, *ApJ*, 325, 74
- Scaringi S., Cottis C. E., Knigge C., Goad M. R., 2009, *MNRAS*, 399, 2231
- Schartel N., Rodríguez-Pascual P. M., Santos-Lleó M., Clavel J., Guainazzi M., Jiménez-Bailón E., Piconcelli E., 2005, *A&A*, 433, 455
- Schlegel D. J., Finkbeiner D. P., Davis M., 1998, *ApJ*, 500, 525
- Schmidt M., 1963, *Nature*, 197, 1040
- Schmidt M., Green R. F., 1983, *ApJ*, 269, 352
- Schneider D. P., Hall P. B., Richards G. T., Strauss M. A., Vanden Berk D. E., 2007, *AJ*, 134, 102
- Schneider D. P., Richards G. T., Hall P. B., Strauss M. A., Anderson S. F., Boroson T. A., Ross N. P., Shen Y., et al., 2010, *AJ*, 139, 2360
- Schneider P., 2006, *Extragalactic Astronomy and Cosmology - An Introduction*. Springer Berlin Heidelberg New York
- SDSS-III collaboration: Hiroaki Aihara et al., 2011, *ApJS*, 193, 29
- Seward F. D., Charles P. A., 2010, *Exploring the X-ray Universe*. Cambridge University Press
- Seyfert C. K., 1943, *ApJ*, 97, 28
- Shakura N. I., Sunyaev R. A., 1973, *A&A*, 24, 337
- Shemmer O., Brandt W. N., Netzer H., Maiolino R., Kaspi S., 2006, *ApJL*, 646, L29
- , 2008, *ApJ*, 682, 81
- Shemmer O., Brandt W. N., Vignali C., Schneider D. P., Fan X., Richards G. T., Strauss M. A., 2005, *ApJ*, 630, 729
- Shen Y., Greene J. E., Strauss M. A., Richards G. T., Schneider D. P., 2008, *ApJ*, 680, 169
- Shen Y., Richards G. T., Strauss M. A., Hall P. B., Schneider D. P., et al., 2011, *ApJS*, 194, 45
- Shen Y., Strauss M. A., Oguri M., Hennawi J. F., Fan X., et al., 2007, *AJ*, 133, 2222
-

-
- Shields G. A., 1978, *Nature*, 272, 706
- Sikora M., Stawarz Ł., Lasota J.-P., 2007, *ApJ*, 658, 815
- Skrutskie M. F., Cutri R. M., Stiening R., Weinberg M. D., Schneider S., Carpenter J. M., et al., 2006, *AJ*, 131, 1163
- Snellen I. A. G., Lehnert M. D., Bremer M. N., Schilizzi R. T., 2003, *MNRAS*, 342, 889
- Sobolewska M. A., Done C., 2007, *MNRAS*, 374, 150
- Sobolewska M. A., Siemiginowska A., Gierliński M., 2011, *MNRAS*, 413, 2259
- Spergel D. N., Verde L., Peiris H. V., Komatsu E., Nolte M. R., et al., 2003, *ApJS*, 148, 175
- Stalin C. S., Petitjean P., Srianand R., Fox A. J., Coppolani F., Schwobe A., 2010, *MNRAS*, 401, 294
- Steffen A. T., Strateva I., Brandt W. N., Alexander D. M., Koekemoer A. M., Lehmer B. D., Schneider D. P., Vignali C., 2006, *AJ*, 131, 2826
- Storchi-Bergmann T., González Delgado R. M., Schmitt H. R., Cid Fernandes R., Heckman T., 2001, *ApJ*, 559, 147
- Storchi-Bergmann T., Mulchaey J. S., Wilson A. S., 1992, *ApJL*, 395, L73
- Strateva I. V., Brandt W. N., Schneider D. P., Vanden Berk D. G., Vignali C., 2005, *AJ*, 130, 387
- Streblyanska A., Barcons X., Carrera F. J., Gil-Merino R., 2010, *A&A*, 515, A2+
- Strüder L., Briel U., Dennerl K., Hartmann R., Kendziorra E., Meidinger N., Pfeiffermann E., Reppin C., 2001, *A&A*, 365, L18
- Sulentic J., Zamfir S., Marziani P., 2010, in *Astronomical Society of the Pacific Conference Series*, Vol. 427, *Accretion and Ejection in AGN: a Global View*, L. Maraschi, G. Ghisellini, R. Della Ceca, & F. Tavecchio, ed., pp. 371–+
- Sutherland W., Saunders W., 1992, *MNRAS*, 259, 413
- Svensson R., 1994, *ApJS*, 92, 585
- Tanaka Y., Nandra K., Fabian A. C., Inoue H., Otani C., Dotani T., Hayashida K., Iwasawa K., Kii T., Kunieda H., Makino F., Matsuoka M., 1995, *Nature*, 375, 659
- Tananbaum H., Avni Y., Branduardi G., Elvis M., Fabbiano G., Feigelson E., Giacconi R., Henry J. P., Pye J. P., Soltan A., Zamorani G., 1979, *ApJL*, 234, L9
- Tavecchio F., Maraschi L., Ghisellini G., 1998, *ApJ*, 509, 608
- Titarchuk L., Lyubarskij Y., 1995, *ApJ*, 450, 876
- Tombesi F., Cappi M., Reeves J. N., Palumbo G. G. C., Yaqoob T., Braitto V., Dadina M., 2010, *A&A*, 521, A57

-
- Tozzi P., Gilli R., Mainieri V., Norman C., Risaliti G., Rosati P., Bergeron J., Borgani S., Giacconi R., Hasinger G., Nonino M., Streblyanska A., Szokoly G., Wang J. X., Zheng W., 2006, *A&A*, 451, 457
- Trammell G. B., Vanden Berk D. E., Schneider D. P., Richards G. T., Hall P. B., Anderson S. F., Brinkmann J., 2007, *AJ*, 133, 1780
- Trump J. R., Hall P. B., Reichard T. A., Richards G. T., Schneider D. P., Vanden Berk D. E., et al., 2006, *ApJS*, 165, 1
- Turner M. J. L., 2001, *A&A*, 365, L27
- Turner M. J. L., Williams O. R., Courvoisier T. J. L., Stewart G. C., Nandra K., Pounds K. A., et al., 1990, *MNRAS*, 244, 310
- Turner T. J., Pounds K. A., 1989, *MNRAS*, 240, 833
- Ueda Y., Akiyama M., Ohta K., Miyaji T., 2003, *ApJ*, 598, 886
- Urry C. M., Padovani P., 1995, *Publications of the ASP*, 107, 803
- Vanden Berk D. E., Richards G. T., Bauer A., Strauss M. A., Schneider D. P., Heckman T. M., York D. G., Hall P. B., Fan X., Knapp G. R., et al., 2001, *AJ*, 122, 549
- Vasudevan R. V., Fabian A. C., 2007, *MNRAS*, 381, 1235
- , 2009, *MNRAS*, 392, 1124
- Vaughan S., Boller T., Fabian A. C., Ballantyne D. R., Brandt W. N., Trümper J., 2002, *MNRAS*, 337, 247
- Veilleux S., 2008, *New Astronomy Review*, 52, 289
- Vestergaard M., 2002, *ApJ*, 571, 733
- Vestergaard M., Peterson B. M., 2006, *ApJ*, 641, 689
- Vignali C., Brandt W. N., Schneider D. P., 2003, *AJ*, 125, 433
- Vignali C., Brandt W. N., Schneider D. P., Kaspi S., 2005, *AJ*, 129, 2519
- Vignali C., Comastri A., Cappi M., Palumbo G. G. C., Matsuoka M., Kubo H., 1999, *ApJ*, 516, 582
- Voges W., Aschenbach B., Boller T., Bräuninger H., Briel U., et al., 1999, *A&A*, 349, 389
- Wagner R. M., 2008, *MNRAS*, 385, 119
- Wake D. A., Miller C. J., Di Matteo T., Nichol R. C., Pope A., Szalay A. S., Gray A., Schneider D. P., York D. G., 2004, *ApJL*, 610, L85
- Wang J., Mao Y. F., Wei J. Y., 2009, *AJ*, 137, 3388
- Wardlow J. L., Smail I., Coppin K. E. K., et al., 2011, *MNRAS*, 415, 1479

-
- Watson M. G., Schröder A. C., Fyfe D., Page C. G., Lamer G., Mateos S., Pye J., Sakano M., Rosen S., et al., 2009, *A&A*, 493, 339
- Weisskopf M. C., Tananbaum H. D., Van Speybroeck L. P., O'Dell S. L., 2000, in *Society of Photo-Optical Instrumentation Engineers (SPIE) Conference Series*, J. E. Truemper & B. Aschenbach, ed., Vol. 4012, pp. 2–16
- Weymann R. J., Morris S. L., Foltz C. B., Hewett P. C., 1991, *ApJ*, 373, 23
- Wilkes B. J., Elvis M., 1987, *ApJ*, 323, 243
- Wilms J., Allen A., McCray R., 2000, *ApJ*, 542, 914
- Winkler C., Courvoisier T. J.-L., Di Cocco G., et al., 2003, *A&A*, 411, L1
- Winter L. M., Mushotzky R. F., Reynolds C. S., Tueller J., 2009, *ApJ*, 690, 1322
- Winter L. M., Veilleux S., McKernan B., Kallman T. R., 2012, *ApJ*, 745, 107
- Woo J.-H., Urry C. M., 2002, *ApJL*, 581, L5
- Worrall D. M., Birkinshaw M., 2006, in *Lecture Notes in Physics*, Berlin Springer Verlag, Vol. 693, *Physics of Active Galactic Nuclei at all Scales*, D. Alloin, ed., p. 39
- Worrall D. M., Tananbaum H., Giommi P., Zamorani G., 1987, *ApJ*, 313, 596
- Wright E. L., Eisenhardt P. R. M., Mainzer A. K., Ressler M. E., et al., 2010, *AJ*, 140, 1868
- Wyder T. K., Martin D. C., Schiminovich D., Seibert M., Budavári T., Treyer M. A., et al., 2007, *ApJS*, 173, 293
- York D. G., 2000, *AJ*, 120, 1579
- Young M., Elvis M., Risaliti G., 2008, *ApJ*, 688, 128
- , 2009, *ApJS*, 183, 17
- , 2010, *ApJ*, 708, 1388
- Zamorani G., Henry J. P., Maccacaro T., Tananbaum H., Soltan A., Avni Y., Liebert J., Stocke J., Strittmatter P. A., Weymann R. J., Smith M. G., Condon J. J., 1981, *ApJ*, 245, 357
- Zhou H., Wang T., Yuan W., Lu H., Dong X., Wang J., Lu Y., 2006, *ApJS*, 166, 128
- Zhou X., Zhao Y., 2010, *ApJL*, 720, L206
- Zhu Y.-N., Wu H., Cao C., Li H.-N., 2008, *ApJ*, 686, 155